

PHOTOELECTRON SPECTROSCOPY OF ORGANIC AROMATIC ANIONS

by

Daniel John Nelson

B.S., University of Wisconsin – Madison, 2010

A thesis submitted to the
Faculty of the Graduate School of the
University of Colorado in partial fulfillment
of the requirements for the degree of
Doctor of Philosophy
Chemical Physics
2017

This thesis entitled:

Photoelectron Spectroscopy of Organic Aromatic Anions

written by Daniel John Nelson

has been approved for the Committee on Chemical Physics

by

W. Carl Lineberger

Veronica M. Bierbaum

The final copy of this thesis has been examined by the signatories, and we find that both the content and the form meet acceptable presentation standards of scholarly work in the above mentioned discipline.

DATE: _____

Nelson, Daniel John (Ph.D. Chemical Physics)

Photoelectron Spectroscopy of Organic Aromatic Anions

Thesis directed by Professor W. Carl Lineberger

This dissertation reports and interprets the results of experiments in which photoelectron spectroscopy was performed on a variety of aromatic anions. In addition to these photoelectron studies, the results and conclusions of an experiment in which HCl is scattered off atomically flat Au (111) surfaces are also presented.

Photoelectron spectroscopy of the isomers of methylphenoxide reveals that these molecules display minimal vibrational excitation upon photodetachment, accessing the electronic ground and first excited state of the corresponding radicals. The photoelectron spectra of *p*-methylphenoxide reveal a photon energy dependence arising from electron autodetachment. The slow electron velocity map imaging (SEVI) technique was employed to obtain the electron affinities (EAs) of these radicals with an uncertainty of 1.4 meV. Combining the measured EAs with previously measured O–H bond dissociation energies in a thermodynamic cycle allows for the measurement of the acidities of the methylphenols with an uncertainty that is an order of magnitude smaller than any previous measurement.

The full interpretation of the photoelectron spectra of the isomers of methylenephenoxy presents a far greater challenge with many subtleties. The EAs of *o*- and *p*-methylenephenoxy were measured and shown to be ~1 eV lower in energy than for the methylphenoxy, implying that the electron withdrawing effect of the CH₂ group in the methylenephenoxy attracts electron density from the oxygen site via resonance, as compared to the methylphenoxy. The

singlet–triplet splittings of the diradicals *o*- and *p*-methylenephenoxyl were measured. The acidities of the methylenephenols were measured by acid bracketing. Combining the EAs of the methylenephenoxyls with these acidities allows for a measurement of the weak O-H bond dissociation energy of the methylenephenols.

The photoelectron spectra of indolide were obtained and interpreted. The structure of indolide minimally distorts upon electron photodetachment accessing the electronic ground doublet state of indolyl. The EA of indolyl was measured utilizing the SEVI technique with an uncertainty of 1.7 meV. Ring distortion vibrational modes were found to be excited upon electron photodetachment. The previously measured acidity of indole is combined with our measurement of the EA of indolyl to determine the N–H bond dissociation energy of indole.

DEDICATION

To the memory of my late grandfather, whose name I bear, Daniel W. Nelson.

ACKNOWLEDGEMENTS

The simple truth is that there are far too many people to thank and acknowledge here who have supported me throughout the sometimes grueling course of my graduate education. It was only with the considerable compassion, love, and understanding of these people that I was able to complete this Ph.D.

Of course, my advisor W. Carl Lineberger deserves special recognition. His advice and counsel on both academics and life over the course of these last few years has been invaluable. Carl, if you're reading this, know that I will always treasure what you've taught me. In so many ways, thank you.

Starting at the beginning of my graduate career, I must thank those people who took in an arrogant, idiotic undergrad and transformed him into an experimentalist. Thank you to Joseph Robert Roscioli, the post-doc who first trained me, starting from how to turn on a laser without electrocuting myself. In a similar vein, I also thank David Nesbitt who opened my mind and taught me, for the first time, how to actually understand quantum mechanics. Everyone in the Nesbitt group at that time also deserves a thank you: Tom Baker, Andrej Grubisic, Grant Buckingham, Mia Zutz, Nick Dupuis, Julie Fiore, Andy Gisler, Erik Holmstrom, Melanie Roberts, and Mike Ziemkiewicz. After Rob left the group for new horizons, I would next work with Monika Grütter Kasumaj, a phenomenal scientist I was privileged with the opportunity to learn from.

I would subsequently begin my work in the Lineberger group, and specifically, I teamed up with Wilson K. Gichuhi. Wilson and I would spend the next two years on one of the most difficult projects I have ever been challenged with. Thank you so much for your patience and tenacity, Wilson. I found in Wilson one of the kindest and most hard working people I will ever

know. It was also at this time when I started to collaborate with the Bierbaum group, and everyone there deserves my gratitude, including Charles Nichols, Callie Cole, and especially Veronica M. Bierbaum, herself! Finally, the last post-doc I worked with was Julia H. Lehman. Julia is, without question, one of the finest scientists I have ever met. Julia taught me how to be a better scientist myself, and especially how to be a better writer. Julia would go on to become a personal friend as well as professional colleague. Thank you, Julia. Your support and friendship mean the world to me. In this last year of my studies I have worked with Allan Maple de Oliveira, a fantastically enthusiastic grad student who has also become a friend of mine. Thank you Allan, for your help and support- especially as I've slowly pulled a disappearing act these last several months to try and actually complete this ridiculous document. Other members of the Lineberger group deserve a thank you as well: Elisa M. Miller, Amanda Case, and Yu-Ju Lu.

All the members of the JILA support staff deserve my sincere thanks. You all are far more talented and skilled than even your considerable reputation suggests. Terry Brown in the electronics shop is especially deserving of my thanks. I had the pleasure of working extensively with him to rebuild whole laser systems, and I couldn't have asked for a better man to help in a crisis.

Finally, I want to thank my friends and family. To my mom and dad, Jenny and Doug Nelson, as well as my sisters, Katie Nelson Hardt and Sallie Nelson Haugen, thank you for all the love and support you have given me my whole life. I wouldn't be here without you. To my old friends, Luke Justman, Nick Doremus, and Dylan Jambrek, thank you for keeping me mostly sane through high school and undergrad. I love you guys. And to my new friends, Steve Harshman, Tony Tumminello, Rashawn Griffin, and to the whole Magic club, you've all added so much to my new life out here in Colorado. Thank you.

CONTENTS

Chapter I: Introduction and Background

§ 1.1 Principles and Advantages of Anion Phototelectron Spectroscopy.....	1
§ 1.2 General Background on Aromatic Organic Molecules and Radicals.....	11
§ 1.3 Background on Methylphenoxides and Methylphenoxyls.....	15
§ 1.4 Background on Distonic Radical Anions and Diradicals: Methylenephenoxides and Methylenephenoxyls.....	18
§ 1.5 Background on Deprotonated Indole and Indoline.....	21
§ 1.6 References.....	23

Chapter II: Experimental Background and Methods

§2.1 Introduction and Background.....	31
§2.2 Overview: Continuous Photoelectron Spectrometer.....	36
§2.3 Principles of Operation: Flowing–Afterglow Ion Source	40
§2.4 Principles of Operation: Wien Velocity Filter.....	44
§2.5 Principles of Operation: Argon–Ion Laser System.....	49
§2.6 Principles of Operation: Hemispherical Electron Energy Analyzer.....	68
§2.7 Overview: Pulsed Velocity Map Imaging Photoelectron Spectrometer.....	73
§2.8 Principles of Operation: Dual Pulsed Valve Ion Source.....	76

§2.9 Principles of Operation: Wiley-McLaren Time-of-Flight Mass Spectrometer.....	79
§ 2.10 Principles of Operation: Velocity Map Imaging Photoelectron Spectrometer.....	81
§ 2.11 References.....	85
Chapter III: Anion Photoelectron Spectroscopy of Deprotonated <i>o</i> -, <i>m</i> -, and <i>p</i> -Methylphenol	
§3.1 Introduction and Background.....	87
§3.2 Experimental Specifics.....	89
§3.3 Theoretical Methods and Simulations.....	94
§3.4 Expectations and Error Analysis.....	96
§3.5 Electron Affinities and Term Energies.....	98
§3.6 Vibrational Analysis: <i>ortho</i> -Methylphenoxyl.....	108
§3.7 Vibrational Analysis: <i>meta</i> -Methylphenoxyl.....	115
§3.8 Vibrational Analysis: <i>para</i> -Methylphenoxyl.....	120
§3.9 CH ₃ Deprotonated <i>meta</i> -Methylphenol.....	123
§3.10 Photon Energy Dependence of the <i>para</i> -Methylphenoxide Photoelectron Spectra	127
§3.11 Discussion.....	133
§ 3.12 Conclusions.....	139
§3.13 References.....	140

Chapter IV: Photoelectron Spectroscopy and Thermochemistry of *o*-, *m*-, and *p*-

Methylenephenoxide Anions

§4.1 Introduction and Background.....	143
§4.2 Experimental Specifics.....	145
§4.3 Theoretical Methods and Simulations.....	151
§ 4.4 Results: Overview.....	152
§ 4.5 Results: Photodetachment to the ground S ₀ State of <i>o</i> -, and <i>p</i> -Methylenephenoxyl.....	159
§ 4.6 Results: Photodetachment to the T ₁ State of <i>o</i> -, and <i>p</i> -Methylenephenoxyl.....	167
§ 4.7 Results: Unassigned Features.....	171
§ 4.8 Results: Thermochemistry.....	176
§ 4.9 Discussion.....	179
§ 4.10 Conclusions.....	185
§4.11 References.....	189

Chapter V: Anion Photoelectron Spectroscopy of Deprotonated Indole and Indoline

§5.1 Introduction and Background.....	190
§5.2 Experimental Specifics.....	192
§5.3 Theoretical Methods and Simulations.....	195

§5.4 Results: Overview.....	199
§5.5 Results: Electron Affinity of Indolyl and Photoelectron Angular Distribution of Indolide.....	203
§5.6 Results: Vibrational Analysis of Indolyl.....	206
§5.7 Discussion.....	221
§5.8 Deprotonated Indoline.....	224
§5.9 Conclusions.....	229
§5.10 References.....	230
 Chapter VI: State-Resolved Velocity Map Imaging of Surface-Scattered Molecular Flux	
§6.1 Introduction and Background.....	233
§6.2 Experimental Setup and Apparatus.....	237
§6.3 Collected Velocity Maps.....	246
§6.4 Velocity Map Analysis.....	249
§6.5 Rotational State Distributions and Energy Maps.....	258
§6.6 Conclusions.....	264
§6.7 References.....	265
 Bibliography.....	 268
 Appendix.....	 284

LIST OF TABLES

Table 2.1 Proton Affinities of Gas Phase Bases.....	42
Table 3.1 Calculated Thermochemistry of the Methylphenols.....	90
Table 3.2. Summary of Experimental Results Obtained for the Methylphenoxides.....	106
Table 3.3 Diagrams of the Primary Franck-Condon Active Normal Modes of <i>o</i> -Methylphenoxide Upon Photodetachment.....	113
Table 3.4 Diagrams of the Primary Franck-Condon Active Normal Modes of <i>m</i> -Methylphenoxide Upon Photodetachment.....	118
Table 3.5 Diagrams of the Primary Franck-Condon Active Normal Modes of <i>p</i> -Methylphenoxide Upon Photodetachment.....	122
Table 3.6 Diagrams of the Primary Franck-Condon Active Normal Modes of <i>m</i> -Methylenephenol.....	125
Table 3.7 Summary of Vibrational Results Obtained for the Methylphenoxides.....	126
Table 4.1 Summary of Vibrational Results Obtained for the Methylenephenoxides.....	163
Table 4.2 Diagrams of the Primary Franck-Condon Active Normal Modes for Each Product Studied.	164
Table 4.3 Summary of Acid Bracketing Results.	177
Table 4.4 Summary of All Results Obtained for the Methylenephenoxides.....	178
Table 5.1 Calculated Vibrational Analysis of Indolyl.....	198
Table 5.2 Summary of Experimental Vibrational Assignments.....	210
Table 5.3 Diagrams of the Vibrational Normal Modes of Indolyl in the Ground Electronic State.	212
Table 6.1 Line Positions and State Assignments of (2+1) REMPI Transitions Utilized in HCl.....	243

LIST OF FIGURES

Fig. 2.1 Early measurement of the O^- photoelectron cross section as a function of photon energy.....	32
Fig. 2.2 Diagram of the continuous photoelectron spectrometer.....	37
Fig. 2.3 An idealized schematic of the magnetic and electric fields that a negatively charged particle q , with a velocity v , would encounter upon entering the Wien filter.....	46
Fig. 2.4 A schematic of the experiment prior to converting the laser system to be able to perform UV photoelectron spectroscopy.....	51
Fig. 2.5 Schematic of the full laser system utilized in the current continuous photoelectron spectrometer.....	53
Fig. 2.6 A qualitative schematic of how the laser light is frequency modulated as it impinges upon the build-up cavity.....	57
Fig. 2.7 An example of the FM-to-AM conversion when the dithered laser is scanned over the cavity fringe of the build-up cavity in frequency by monitoring the transmitted light intensity.	59
Fig. 2.8 Qualitative schematic of the form of the error signal utilized in the laser locking system as the laser fringe scans over a build-up cavity fringe.	61
Fig. 2.9 Schematic of the custom bayonet output coupler mount fabricated to accommodate a piezoelectric actuator.	63
Fig. 2.10 Annotated circuit diagrams detailing the specific ways in which the laser servo works	67
Fig. 2.11 Schematic of the electron kinetic energy analyzer system with deceleration, input, and output lens stacks included.....	69
Fig. 2.12 Schematic of the pulsed VMI photoelectron spectrometer experiment.....	74
Fig. 2.13 A schematic of the ion source utilized in the experiments.....	77
Fig. 2.14 Picture of the VMI PE spectrometer, annotated.....	84
Fig. 3.1 The 355 nm photoelectron spectra of the three methylphenoxide anion isomers.	99

Fig 3.2 Photoelectron spectra of the products of methylphenol reacted with hydroxide in the flowing afterglow ion source obtained with a photon energy of 3.40814 eV and collected in a hemispherical energy analyzer.....	101
Fig. 3.3 The Slow Photoelectron Velocity-Map Imaging (SEVI) spectra of <i>o</i> -, <i>m</i> -, and <i>p</i> -methylphenoxide, allowing for the determination of the EAs of the corresponding methylphenoxyls.....	103
Fig. 3.4 The 355 nm anion photoelectron spectra of <i>o</i> -, <i>m</i> -, and <i>p</i> -methylphenoxide, examining the first excited doublet electronic states (\tilde{A}) of the methylphenoxyl radicals.....	105
Fig. 3.5. The anion photoelectron spectra of <i>o</i> -, <i>m</i> -, and <i>p</i> -methylphenoxide, examining the ground doublet electronic states of the methylphenoxyls.....	110
Fig. 3.6 Photoelectron spectrum of <i>ortho</i> -methylphenoxide taken with a photon energy of 2.822 eV, utilizing the VMI photoelectron spectrometer.....	111
Fig. 3.7 The photoelectron spectrum of <i>meta</i> -methylphenoxide taken on the VMI spectrometer with a photon energy of 2.329 eV.....	116
Fig. 3.8 Photoelectron spectrum of methyl deprotonated <i>meta</i> -methylphenol, taken with a photon energy of 3.408 eV and collected with a hemispherical energy analyzer.....	124
Fig. 3.9 Photoelectron spectra of <i>p</i> -methylphenoxide taken at a variety of photon energies, displaying a photon energy dependence as discussed further in the text.....	128
Fig. 3.10 Photoelectron spectra of <i>para</i> -methylphenoxide obtained with the VMI spectrometer with photon energies of 2.329 eV and 2.637 eV.....	129
Fig. 3.11 The photoelectron spectrum of <i>meta</i> -methylphenoxide taken on the VMI spectrometer with photon energies of 3.494 eV and 3.832 eV.....	132
Fig. 4.1 Mass spectra collected on the FA-SIFT instrument of selectively deuterated cresols reacted with O ⁻	153
Fig. 4.2 Photoelectron spectra taken on the VMI photoelectron spectrometer with a photon energy of 3.494 eV of the three isomers of methylenephenoxide.....	157
Fig. 4.3 Photoelectron spectra of the <i>o</i> - and <i>p</i> -methylenephenoxide anions obtained using Instrument A utilizing a photon energy of 3.408 eV.....	160
Fig. 4.4 Photoelectron spectra accessing the first triplet electronic excited states of the <i>o</i> - and <i>p</i> -methylenephenoxyl diradicals.....	168
Fig. 4.5 Photoelectron spectra of <i>m</i> -methylenephenoxide anions obtained on instrument B with two different photon energies, 3.494 and 3.832 eV.....	173

Fig. 4.6 Photoelectron Spectra of the three isomers of the methylenephenoxide anion, collected on the VMI PE spectrometer with a photon energy of 2.330 eV.....	174
Fig. 4.7 Photoelectron spectra obtained with a photon energy of 2.330 eV on instrument B. These spectra were obtained by simply alternating the laser timing to either intersect $m/z = 106$ (methylenephenoxide, black curves) or 107 (methylphenoxide, red curves)	175
Fig. 5.1 The photoelectron spectrum of indolide obtained with a photon energy of 3.494 eV	201
Fig. 5.2 The Slow Electron Velocity–Map Imaging (SEVI) PE spectrum of the origin transition of indolide acquired with a photon energy of 2.4500 eV.....	204
Fig. 5.3 Photoelectron spectra of indolide obtained with three separate photon energies, 2.518 eV (upper panel), 2.588 eV (middle panel), and 2.678 eV (lower panel).....	207
Fig. 5.4 The photoelectron spectrum of the anionic product(s) of $F^- + \text{indoline}$ with a mass to charge ratio of 118.....	226
Fig. 6.1 Experimental setup of the velocity-map imager (VMI) adapted to probe surface scattering dynamics.....	238
Fig. 6.2 Velocity map images of scattered HCl from a 1% HCl/H ₂ incident supersonic jet with $E_{\text{inc}} = 21(5)$ kcal/mol.....	247
Fig. 6.3 Integrated velocity distributions parallel to the scattering plane (along $v_{\text{in-plane}}$) for scattered HCl molecules in $J = 2 - 12$ originating from a 21 ± 5 kcal/mol incident beam	250
Fig. 6.4 Tracking the energy content in various degrees of freedom as a function of J-state.	253
Fig. 6.5 Rotational distribution of molecules scattered from a 1% HCl/H ₂ beam at 21 ± 5 kcal/mol.....	259
Fig. 6.6 Rotational energy map of a scattered HCl beam ($E_{\text{inc}} = 21 \pm 5$ kcal/mol) at every value of $v_{\text{in-plane}}$ and $v_{\text{out-of-plane}}$	261

CHAPTER I

INTRODUCTION AND BACKGROUND

Portions of this chapter have been published or will be published in the Journal of Chemical Physics under the titles of:

“Anion Photoelectron Spectroscopy of Deprotonated *ortho*-, *meta*-, and *para*-Methylphenol”

By, Daniel J. Nelson, Wilson K. Gichuhi, Elisa M. Miller, Julia H. Lehman, *and* W. Carl Lineberger

“Anion Photoelectron Spectroscopy and Thermochemistry of *o*-, *m*-, and *p*-Methylenephenoxide”

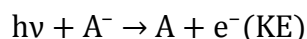
By, Daniel J. Nelson, Wilson K. Gichuhi, Charles M. Nichols, Julia H. Lehman, Veronica M. Bierbaum, *and* W. Carl Lineberger

“Anion Photoelectron Spectroscopy of Deprotonated Indole and Indoline”

By, Daniel J. Nelson, Allan M. Oliveira, *and* W. Carl Lineberger

§ 1.1 Principles and Advantages of Anion Photoelectron Spectroscopy

Anion photoelectron spectroscopy is a form of spectroscopy which is quite distinct from other forms of spectroscopy.^{1,2} In principle, this process is understandable in broad strokes: a photon possessing a known amount of energy interacts with an anion. If the photon possesses more energy than the binding energy of an electron in the anion, there is a chance that the anion will eject that electron and simultaneously absorb the photon. This may be summarized by the deceptively simple formula:



Where A^- represents an anion, which can take the form of an atom or molecule. Since one electron is ejected from the anion in question, it is necessarily the case that either the anion or the corresponding neutral is an open shell radical. As one can see by examining the above formula, there are several methods one might employ to measure the quantum state distribution of the

anion or neutral. Perhaps most intuitively, one might measure the attenuation of the light as it passes through a cloud of anions as a function of the frequency of the light. This is a nearly impossible measurement, however, as one can practically only make very low densities of ions, such that the attenuation of the light through the ion cloud would be so small as to render this type of measurement impossible without herculean efforts. The inverse of this scheme has been utilized however, *i.e.* measuring the attenuation of the ions as they pass through a radiation field. This is a plausible experimental design, as it is possible to measure ion currents with high sensitivity with either a Channeltron or Microchannel Plates (MCPs). Historically, this method has been used to obtain absolute photoelectron cross-sections of anions. As an alternative to these methods, one could instead collect the electrons produced. As these particles are charged, it is again possible to measure them on a single event basis with either a Channeltron or MCPs. In order to obtain quantum state sensitivity, one of two methods must be employed when collecting electrons. Either the photon energy may be scanned and all of the photodetached electrons are collected as a function of photon energy (photodetachment spectroscopy), or a fixed frequency laser is used and the electrons are gathered and then their kinetic energy is measured (photoelectron spectroscopy). This latter process, photoelectron spectroscopy, is utilized throughout this work, and a detailed, theoretical explanation follows.

Before detailing the experimental steps taken (Chapter II), we will first focus on the theory of photoelectron spectroscopy, and how one might analyze and understand the physical meaning of a photoelectron spectrum. Assuming that one is able to measure the kinetic energies of the electrons, and given that we know the photon energy, by simple conservation of energy we must also know the energy which was left in internal states of the remaining neutral molecule or atom. This is achieved simply by subtracting the electron kinetic energy (eKE) from the photon energy to arrive at the electron binding energy (eBE):

$$eBE = h\nu - eKE$$

The only assumption which has been made so far is that upon photodetachment, all of the kinetic energy released will be deposited in the electron. How good is this assumption? This is a straightforward classical mechanics problem. One may accurately model the situation thusly: Upon photodetachment there is a known amount of energy which must be accounted for, namely, the energy of the absorbed photon. Some portion of this energy must be deposited within the internal degrees of freedom of the neutral molecule. This, by definition, cannot affect the center of mass (COM) motion of the particles. This leaves the remaining energy which must be placed in either the kinetic energy of the molecule or the electron. However, there remain two constraints which govern this: conservation of energy and conservation of momentum.

$$\text{(Conservation of Energy)} \quad KE_{TOT} = KE_{mol} + KE_{elec} = \frac{1}{2}Mv_{mol}^2 + \frac{1}{2}mv_{elec}^2$$

$$\text{(Conservation of Momentum)} \quad M\vec{v}_{mol} = m\vec{v}_{elec}$$

It is possible to define the fraction of kinetic energy which will be possessed by the electron.

$$F = \frac{KE_{elec}}{KE_{TOT}} = \frac{\frac{1}{2}mv_{elec}^2}{\frac{1}{2}Mv_{mol}^2 + \frac{1}{2}mv_{elec}^2}$$

Upon the addition of conservation of momentum and some simplification one arrives at:

$$F = \frac{mv_e^2}{mv_e^2\left(\frac{m}{M} + 1\right)} = \frac{1}{\frac{m}{M} + 1}$$

Hence, if one conservatively estimates that the molecular or atomic mass is 50,000 times larger than the electron mass, then $F = 0.99998$. This is a conservative estimate considering that $2,000 \times m_{electron} \sim m_{proton}$.³ It may be concluded then that the assumption that all of the

available kinetic energy is found in the kinetic energy of the electron is appropriate for all cases which are studied in this work.

Interpreting the measured electron binding energy distribution will first be done from a classical perspective in order to facilitate intuition, and then will be considered from the quantum perspective. Assuming that one is considering a molecular anion which is a classical object, one would expect a smooth, continuous distribution of energy which could be placed into internal degrees of freedom of the molecule following photodetachment of the corresponding anion, and thus the kinetic energy of the electron would also possess an analogous distribution. This leads one to question how one might determine into which degrees of freedom this energy is deposited. There are several physical pictures which may be used to motivate this process. Perhaps the most intuitive is as follows: Upon photodetachment, all atoms comprising the molecule will take on new geometrical equilibrium positions, which means that each atom is by definition displaced to varying degrees from equilibrium. If this were a classical problem, we might be tempted to model the force connecting the atoms to each other (the bonds) as harmonic springs each with a separate spring constant and with the initial condition that each atom is displaced just so from the springs' equilibrium positions at time zero. Solving this set of ordinary differential equation (ODE) problems is straightforward, if a bit tedious.⁴ However, it should be intuitively obvious that those atoms which have been displaced further from their respective equilibrium position will obtain more vibrational energy ($\sim \frac{1}{2}k(\vec{r}_o - \vec{r}_{max})^2$) than those displaced less.

Of course, molecules are inherently quantum mechanical systems and not classical ones. As such, we must treat the internal states of the molecule as quantized, not continuous, and rework the same problem with this understanding.⁵⁻⁷ Critically, the same intuitive result from the examination of the classical case will hold. In the anionic state, the atoms within the molecule

experience a potential and from this a particular Hamiltonian may be written. Assuming that the Hamiltonian is separable and the Born-Oppenheimer approximation holds, then the electronic, nuclear, and spin coordinates may be treated separately ($\hat{H}_{tot} \approx \hat{H}_{nuclear} + \hat{H}_{electronic} + \hat{H}_{spin}$). Thus, we may consider only the portion of the Hamiltonian which concerns itself with the nuclear motion of the molecule or anion. Disregarding eigenfunctions/eigenvalues representing either translation or rotation, then solutions may be found for the eigenvalues physically corresponding to the vibrations of the normal modes of the molecule. If at this point an electron is removed from the system, the newly formed neutral molecule exerts a new potential on the nuclei and electrons remaining in the system. This potential defines a new Hamiltonian and consequently new eigenfunctions and eigenvalues as well. Hence, the previous wavefunction of the system is no longer an eigenfunction of the newly formed Hamiltonian. Physically, therefore, the system must have the current state be described by the neutral eigenfunctions. Since the neutral eigenfunctions of the Hamiltonian represent a complete orthonormal set, this is a straightforward process. The anionic eigenfunction must be expanded in the complete orthonormal basis set of the neutral eigenfunctions.

$$|\Psi_{final}\rangle = \sum_{neutral\ states} \langle \Psi_{neutral} | \Psi_{anion} \rangle |\Psi_{neutral}\rangle$$

While a full derivation here is not appropriate, this explanation is sufficient to motivate the fact that the probability that a certain vibrational state will be populated is therefore proportional to $|\langle \Psi_{neutral} | \Psi_{anion} \rangle|^2$. This value is commonly referred to as a Franck-Condon Factor (FCF).^{6,7} Recall that since each of these newly populated quantized states have specific eigenvalues (disregarding degeneracy), or energies, associated with each, then the final quantized

population state distribution of the molecules will be encoded necessarily on the eKE distribution of the measured electrons.

The FCF is an essential tool for predicting and interpreting photoelectron spectra, and has several properties that are important to underscore. First, consider the case where the geometry change between an anion and neutral is very small, with no bond or internal angle changing by more than $\sim 0.01\%$. From a classical picture, it is easy to anticipate that there will be virtually no vibrational excitation. This is borne out in the FCFs as well. Assuming the majority of the anion population is in the vibrational ground state, the overlap integral between the anion and the ground vibrational neutral eigenfunction will approach unity, while the overlap with other states will approach zero. An easy way to intuit this result is as follows: In the extreme case that the potential energy surfaces are the same between the anion and the neutral, then the anion and neutral species will share the same complete orthonormal set of eigenfunctions. Since we assume the anion population is in the vibrational ground state, then by virtue of the orthogonality of the set, the overlap with anything other than the ground state of the neutral will be identically zero. If one imagines making only slight changes to the potential energy surface from this extreme case, it is easy to imagine that, while the overlap between the ground state of the anion and non-ground states of the neutral are no longer identically zero, they remain small compared to the overlap between the two ground states.

The second, and most common case of those molecules studied in this thesis, is that most atoms in the molecule do not change their equilibrium geometry relative to each other, or only do so to an insignificant degree, while only the geometry of a minority of the atoms change to some degree. From the classical picture, it is intuitive to see that the normal modes which incorporate motion along the changed bond lengths/angles will be vibrationally excited, while other normal

modes will remain dormant. This is again consistent with what the FCFs predict in such a scenario. For the internal coordinates with very little change, only the ground vibrational states of both the anion and neutral will have significant overlap with all other states resulting in very small overlap, comparatively. For modes with significant change, the neutral eigenfunction with the greatest overlap with the anion ground vibrational state may correspond to eigenvalues several or even many quanta above the ground state. This will lead to a clear progression of one or several vibrational modes in the photoelectron spectra.

Finally, there is the case of a large geometry change for many of the atoms in the molecule upon photodetachment. This might correspond to a “floppy” molecule whose potential energy surfaces are extremely flat, or a molecule for which several bonds severely weaken upon photodetachment. As one would expect, this will result in a very significant amount of excitation in virtually every normal mode. Indeed, under these circumstances, the normal mode/harmonic approximation is almost certainly incorrect. That is to say Taylor expanding the potential energy surface of the anion and neutral out to only second order about the equilibrium position of each atom comprising the molecule and then solving the Schrödinger equation with this simplified version of the potential energy surface is woefully inadequate to the task of modeling the behavior of the molecule. Even in the classical picture, non-rigid motion is all but virtually impossible to model, often leading to chaotic motion. In the FC picture, this would be equivalent to the opposite of the first case; namely, the overlap between the ground anionic vibrational state and the ground neutral vibrational state will be small compared to the overlap between the ground vibrational anionic state and other non-ground vibrational states of the neutral. This will, in general, result in far more transitions having significant FCFs than in the other two cases, and practically will result in a spectrum wherein no single transition may be individually resolved.

Now that the basic principles of how to interpret a photoelectron spectrum are understood, one might question what benefit this form of spectroscopy offers? The answer to this is several fold. First, by the very nature of PE spectroscopy, one does not necessarily need a tunable laser. (We do utilize several such lasers in this work, but this is due to a design necessity, rather than a fundamental requirement of PE spectroscopy. This is discussed in greater detail in Chapter II.) This is in contrast to most other spectroscopic techniques which require one to scan the frequency of a laser over the spectroscopically active region of a molecule and observe either light absorption or emission as a function of the laser frequency. In principle, for a given photon energy utilized in a PE spectroscopy experiment, the investigator will receive data on all Franck–Condon active transitions with binding energies less than that photon energy. This can be a major advantage, as obtaining tunable light sources over large (1-2 eV) ranges of photon energies can be quite challenging. The second advantage of this form of spectroscopy lies in the molecules which may be investigated. As was previously explained, the information gathered in a PE spectroscopy experiment yields data primarily on the neutral molecule which is formed upon photodetachment. The only requirement on the lifetime of a compound, therefore, is on the lifetime of the anion. Thus, we may investigate short-lived neutrals, *e.g.* neutrals which are transition states, so long as the anionic form of that neutral is long lived.⁸ This allows one to perform spectroscopic measurements of transition states which would be otherwise nearly impossible to measure directly. The third advantage stems from the fact that this form of spectroscopy necessarily removes a source of spin in the molecule, and as such, optically inaccessible neutral states may be investigated. For example, if an anion begins in the ground electronic state with doublet multiplicity, after photodetachment it would be possible to access both the singlet and triplet electronic states of the resulting neutral molecule.

Photoelectron spectroscopy has one final advantage. However, this advantage is not directly due to the spectroscopic data which are collected. Instead, photoelectron spectra inherently allow for another measurement- the photoelectron angular distribution. This distribution and its interpretation was studied first in atomic anions by Cooper and Zare⁹ and later expanded to Molecular Orbital Theory (MOT) by Sanov.¹⁰ This distribution, when measured for molecular systems, often reveals the nature of the molecular orbital from which the photoelectron was detached. The interpretation of this phenomenon may be understood as follows: By its fundamental nature, an electron may possess angular momentum. Certainly, an electron bound within an atomic system will possess different quantities of angular momenta, depending upon the atomic orbital which describes its motion. However, the total angular momentum of an electron bound in a molecule is not a good quantum number. If the molecule happens to be a diatomic molecule, then the projection of the angular momentum on the internuclear axis is a good quantum number. Unfortunately, none of the molecules which are studied in this collection of works will be diatomic, and so this case will not be of use to consider. Hence, we must approximate. MOT suggests that it is possible to describe a molecule by the symmetry-adapted linear combination of the atomic orbitals of the atoms which comprise the molecule in question.¹¹ This leads to the formation of molecular orbitals, which may be approximated to confer angular momentum analogous to the atomic total angular momentum associated with the electrons which occupy them, despite this not being rigorously accurate. When an electron is photodetached, it may therefore possess some amount of angular momentum, limited by the angular momentum characteristic of the molecular orbital from which it was detached. Practically, this translates into a difference in the probability of an electron ejecting oriented either along the plane of the electric field of the laser which photodetached it or perpendicular to the electric field. This difference is characterized as the anisotropy and defined

by the anisotropy parameter, β . In general, ejecting electrons from different electronic states (molecular orbitals) will result in a different value of β . This allows for one to distinguish features in a photoelectron spectrum which arise from different electronic states. This is an especially attractive feature as frequently a spectroscopist must rely on fitting quantum chemical calculations to experimental spectra in order to identify electronic and vibrational transitions, but this allows for an independent verification of different electronic states being accessed in a given spectrum without the reliance on theoretical prediction.

§ 1.2 General Background on Aromatic Organic Molecules and Radicals

In this work, the predominant class of molecules which have been studied are cyclic or polycyclic aromatic anions and radicals. Aromatic molecules are a class of molecules which are characterized by possessing fully occupied cyclic π bonded molecular orbitals, such as in the proto-typical case of benzene. This molecular orbital configuration offers a variety of qualitative differences in reactivity and chemical behavior when compared to non-aromatic species, such as an alkane. Taking benzene as an exemplar, the π bonds which connect each sp^2 hybridized carbon center to its nearest neighbor make the overall ring structure extremely rigid and flat, thus attaining the high symmetry point group D_{6h} .¹² Cyclohexane, the immediate analog of benzene, but a non-aromatic alkane, is far less rigid and possesses almost none of the symmetry of benzene. Cyclohexane is a bent molecule, with either a classic “chair” or “boat” structural configuration. Upon the addition of functional groups onto an aromatic species, the aromatic π structure allows for chemical resonance between the aromatic ring and the functional groups. When two separate functional groups are attached to a benzene ring, this resonance effect allows for the two moieties to influence the others behavior. For example, adding an electron donating group to benzene, such as NH_2 , and an electron withdrawing group, such as $COOH$, to the *para* or 3 position on the benzene ring, will cause electron density to be pulled onto the $COOH$ group from the NH_2 group, thus preparing the $COOH$ group for electrophilic attack. This represents just one way in which an aromatic molecule might behave differently from a non-aromatic species, and the reader is directed to Ref. 12 or another textbook covering organic chemistry for an exhaustive review of this topic.

Radicals are critical to understanding nearly, if not all reaction mechanisms, and play a key role in all fields of chemistry as a result.¹³⁻¹⁵ Molecular radicals are easiest to understand

from a molecular orbital standpoint. They are simply molecules that possess a partially filled molecular orbital, commonly a valence orbital. Due to this orbital being only partially filled, radical species are extremely reactive with short lifetimes, often possessing a reaction rate on the order of the collision rate, if not faster if they undergo unimolecular reactions.¹⁶⁻¹⁸ Thus, it is frequently an experimental challenge to observe them directly, despite radicals frequently playing the role of reaction intermediates. As mentioned previously in § 1.1, when one conducts photoelectron spectroscopy, either the anion or the neutral that results from photodetachment of the anion must be a radical. In the case of the anions studied in this work, the neutrals which result from photodetachment are all radicals, which allows for our experiments to directly probe what would otherwise be a difficult species to spectroscopically observe. The umbrella of “radical” covers many other specific cases. Studied in this work, in addition to the standard radical case, are diradicals, *i.e.* molecules with two molecular orbitals only partially filled, and distonic radical anions, *i.e.* an anion which is also a radical, but the radical site is localized on a different part of the molecule from the site containing the negative formal charge. As one might imagine, these molecules have reactivities which defy simple physical models of their behavior. These will be explained in detail on a case by case basis in the following chapters.

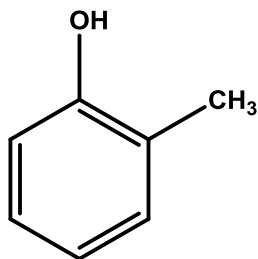
The molecules studied in this dissertation were chosen deliberately for a variety of scholarly reasons. First, cyclic and polycyclic organic aromatic molecules are vitally important to numerous fields of physical chemistry,¹⁹⁻²² analytical chemistry,²³⁻²⁵ astrochemistry,^{26, 27} biochemistry,^{28, 29} combustion chemistry,^{23, 24} organic chemistry,^{30, 31} and biophysics.^{32, 33} While the full list of applications wherein organic aromatics are key reaction intermediates is too large to go into detail, here are several examples: In astrochemistry, polycyclic aromatic hydrocarbons (PAHs) are believed to be major contributors in Diffuse Interstellar Absorption Bands (DIBs).^{26,}
²⁷ In combustion chemistry, they have been shown to be critical intermediates with respect to the

modeling of the removal of oxygen from biomass in order to generate biofuels.^{23, 24} In biochemistry, cyclic and polycyclic organic aromatic molecules comprise the backbone of many biologically relevant molecules and pharmaceuticals.³²⁻³⁵ Second, cyclic and polycyclic organic aromatic structures are geometrically rigid due to the π -bonded aromatic electronic structure which typically requires these molecules to have small geometry changes upon photodetachment.³⁶⁻³⁸ Practically, this translates into photoelectron spectra which are minimally congested, as explained in the previous section. This is especially interesting as this allows for the investigation of large molecules (~15 atoms/molecule), which have typically been avoided in the past since larger molecules possess heavily congested PE spectra. Finally, the aromatic structure allows for the investigation of how substituents affect the electronic structure of these compounds. This would be expected to be different from the behavior of a more standard hydrocarbon, such as an alkane, in that the resonance structures are fundamentally different between aromatic and non-aromatic organic molecules.¹² Due to the π -bonded electronic structure of the molecular orbitals in aromatics there are many resonance structures which may be constructed, and as such, functional groups which are attached to the aromatic structure will interact in far different, and often more long-rang ways than simple alkanes.

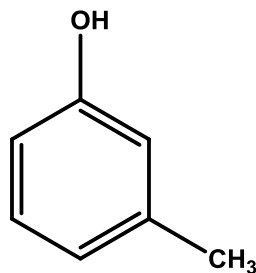
This general background now laid out, we will go into more detail about each of the molecules which have been studied in this work and why they are of interest to the scientific community. What follows is an introduction to the molecules studied in this dissertation and acts as an outline for the upcoming chapters. First, the methylphenoxides and methylphenoxyls are introduced. This will be followed by the methylenephenoxides and methylenephenoxyls, as well as a more general discussion of distonic radical anions and diradicals. The final molecules considered are deprotonated indole and indoline.

§ 1.3 Background on Methylphenoxides and Methylphenoxyls

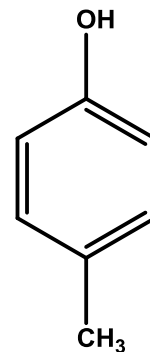
o-methylphenol



m-methylphenol



p-methylphenol



Methylphenols, commonly referred to as cresols, are an important class of molecules in many fields of chemistry.^{19, 23-25, 39-67} They are commonly used as model systems for hydrodeoxygenation in catalytic chemistry for refining biofuels,^{23-25, 40, 41} while the internal rotations of the functional groups are of great interest to many spectroscopists.^{42-46, 68, 69} Their thermochemistry and kinetics have also been studied, *e.g.* King *et al.*⁵⁸ measured the bond dissociation energies of the O-H bond in each isomer of methylphenol to high accuracy (± 0.14 kcal/mol), while McMahon and Kebarle⁶⁶ implemented proton-transfer equilibria studies to measure their gas phase acidities. The study of the thermochemistry of methylphenols is often motivated by the desire to understand the effect of different benzene substitutions on reactivity, particularly in comparison with their simpler counterparts, phenol and toluene. Through these comparisons, insight can be gained into the relative contribution of the OH group (which is strongly electron donating in aromatic systems) compared to the CH₃ group (weakly electron donating), and how these two functional groups work in concert to affect reactivity and electronic structure. Methylphenols have been previously spectroscopically studied utilizing a

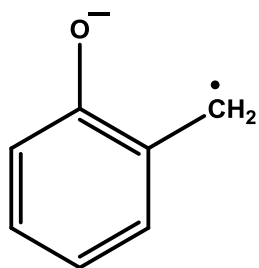
large variety of spectroscopic techniques including microwave absorption,^{42, 68} Laser Induced Fluorescence (LIF),^{43, 44, 46, 53, 69} Resonance Enhanced Multiphoton Ionization (REMPI),^{19, 52, 56} stimulated Raman-UV optical double resonance,⁵⁵ and Hole Burning spectroscopy. In addition to purely spectroscopic probes, these compounds have been ionized and detected using Time of Flight (TOF),^{18,24} and Fourier-Transform Ion Cyclotron Resonance (FT-ICR) mass spectrometry.⁶⁵ However, very little experimental information on the methylphenoxyl radicals or their thermochemistry was previously available prior to the studies contained in this dissertation. Despite the numerous studies and the reliance on methylphenols as a model species in catalytic and combustion chemistry, prior to this work, the electron affinity of *p*-methylphenoxyl had only been measured to an accuracy of ~100 meV,⁶⁶ while there are no measurements for the other isomers, and the gas phase acidities of all three isomers have been measured with a fairly large uncertainty (at least 2 kcal/mol).

This dissertation will present a study utilizing photoelectron spectroscopy to determine accurate electron affinities of the methylphenoxyl radicals, and, in concert with quantum chemical calculations, provide physical insight into the structures of both the methylphenoxide anions and methylphenoxyl radicals. Combining the highly accurate (error of ± 0.14 kcal/mol) O-H bond dissociation energy for each methylphenol isomer from King *et al.*,⁵⁸ as modified by Karsili *et al.*,⁶⁷ with the EAs measured in this study allows for the construction of a thermodynamic cycle that provides accurate gas phase acidities.⁷⁰ The results will also be compared with the previous work on the phenoxide^{36, 71} and benzyl anions,³⁶ which were also studied using anion photoelectron spectroscopy. One might ask if the methylphenoxyls will display a combination of attributes previously shown by those two anions, or will the chemistry and spectroscopy have qualitatively different behavior? For example, one major difference

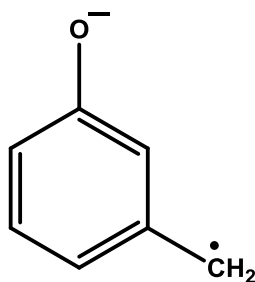
between the *ortho*, *meta*, and *para* isomers of methylphenol is based on possible resonance structures, which will likely influence the derived chemical properties.

§ 1.4 Background on Distonic Radical Anions and Diradicals: Methylenephenoxides and Methylenephenoxyls

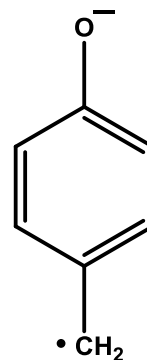
o-methylenephenoxide



m-methylenephenoxide



p-methylenephenoxide



The next set of molecules studied with anion photoelectron spectroscopy in this dissertation are the three isomers of methylenephenoxide. These anions are in fact distonic radical anions which form diradicals upon photodetachment. The study of diradicals is of interest to the many diverse fields of chemistry, biology, and physics.^{34, 72-79} Due to their frequently unstable and short lived nature, as well as their complicated electronic structure,⁸⁰⁻⁸⁹ they are challenging to investigate both experimentally and theoretically. Despite this difficulty, they have proven important as reaction intermediates as seen in experiments, and predicted to be important for many more. For instance, the Bergman cyclization reaction is used to produce the diradical *p*-benzyne from enediyne, and this diradical proceeds to strand cleavage in DNA, leading to cell apoptosis.³⁴ Thus, a diradical is responsible for one of the most potent subsets of anticancer drugs to date.

The field of distonic radical ions, which is to say an ion that has a radical site localized separate from the charged site on the ion, is of equal interest to the scientific community.⁹⁰⁻¹⁰³ Radical ions may react as either a radical or an ion, opening the door to any number of reaction

schemes. Their initial study is largely due to the pioneering work of Kenttämäa and coworkers and their efforts towards understanding distonic radical cations in the gas phase.¹⁰² Distonic radical anions have also been extensively studied.^{92, 94, 97} As the study of these radical ions continues, they have been shown to be relevant in reaction mechanisms, often in zwitterion chemistry, with a famous example being the McLafferty rearrangement of molecular ions in carbonyl compounds.

In some of the initial studies, distonic radical anions were created in the condensed phase, and studied with Electron Spin Resonance (ESR) spectroscopy.⁹¹ This, however, was limited to those distonic radical anions and/or diradicals which were long lived in the condensed phase, on the order of minutes or hours. Later, both diradicals and distonic radical anions became the focus of gas phase studies, with many groups in the mass spectrometry field taking an interest. Time of flight mass spectrometry, Fourier Transform Ion Cyclotron Resonance mass spectroscopy, and Collision Induced Dissociation (CID) have all been utilized to this end.^{91, 92, 102}

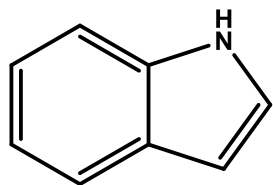
The study presented in this dissertation is an investigation via photoelectron spectroscopy of all three isomers of methylenephenoxy. While a wealth of information may exist on the methylphenols (see § 1.3), the methylenephenoxyes are not well understood as of yet, and present an opportunity to study both distonic radical anions and diradicals by way of photodetachment.

In addition to anion PE spectroscopy, the thermodynamic properties of the methylenephenoxy isomers are studied using a Flowing Afterglow – Selected Ion Flow Tube (FA-SIFT) mass spectrometer in conjunction with the acid bracketing procedure,²⁸ thus providing information on the acidities of the methylenephenoxy radicals. Together with the

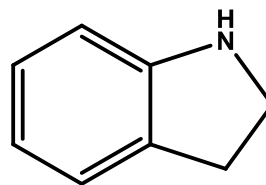
Electron Affinities (EAs) provided by PE spectroscopy, acidities from the FA-SIFT machine, and a thermodynamic cycle, bond dissociation energies are also measured.

§ 1.5 Background on Deprotonated Indole and Indoline

Indole



Indoline



The final molecules which were investigated with PE spectroscopy are deprotonated indole and indoline. The bicyclic molecules indole and indoline are of interest to the fields of biophysics and biochemistry.^{32, 33} This is primarily due to the fact that indole acts as a chromophore in tryptophan and therefore dominates much of the spectroscopy performed on numerous biological systems. Indoline is less studied, and has primarily been utilized as an analog of indole with a less complex electronic structure.¹⁰⁴ The importance of indole as a chromophore of tryptophan has symbiotically inspired numerous spectroscopic studies of indole and indole clustered with various partners.^{20, 21, 32, 35, 105-119} While this scrutiny from the spectroscopic community is partially due to the related biological interest, indole also provides unique spectroscopic challenges due to the complex nature of its vibronic structure.^{120, 121} Indole is a low symmetry molecule belonging to the C_s point group, and the two lowest level electronic states (1L_a and 1L_b) have been shown to be strongly coupled, due in part to belonging to the same representation. This has made indoline an attractive analog of indole as the 1L_a and 1L_b states of indoline are further separated in energy than in the case of indole.

Despite this interest in both indole and indoline, there is relatively little known of their thermodynamic properties. Similarly, neither deprotonated indole or indoline have been studied

extensively, spectroscopically or otherwise. The gas phase acidity of indole, referring to deprotonation from the N–H site, was studied in 1988 by means of proton transfer equilibria,¹²² $^{123} \Delta_{acid} H_{600\text{ K}}^0(\text{N–H}) = 352 \pm 2 \text{ kcal/mol}$, and has not been updated since that time. The gas phase acidity of indoline has not been studied. The electron affinity (EA) of indolyl may be inferred by means of a thermodynamic cycle¹²⁴ from the work of Taft *et al.*¹²² with relatively large uncertainty, $2.52 \pm 0.20 \text{ eV}$, and was updated recently, though with only a modest improvement in the error bar, by McKay *et al.*,¹²⁵ $2.31 \pm 0.15 \text{ eV}$. The EAs of any of the other radical isomers associated with deprotonated indole have not been studied. Finally, an upper bound was placed on the bond dissociation energy of the N–H bond in indole by Nix *et al.*¹²⁶ by way of photofragment translational spectroscopy: $D_0(\text{N–H}) \leq 91.2 \text{ kcal/mol}$. No analogous studies of indoline have been conducted to date that directly measure these thermodynamic properties. We believe that these previous studies present an opportunity to obtain the EAs of these molecules with significantly improved error bars and explore both the electronic and vibrational structure by means of anion photoelectron (PE) spectroscopy.

§ 1.6 References

- 1) W. C. Lineberger, H. Hotop and T. A. Patterson, edited by H. Kleinpoppen, and M. McDowell (Plenum, New York, 1976), pp. 125-132.
- 2) K. M. Ervin and W. C. Lineberger, in *Advances in Gas Phase Ion Chemistry*, edited by N. G. Adams, and L. M. Babcock (JAI Press, Greenwich, 1992), pp. 121-166.
- 3) D. R. Burgess and J. E. Bartmess, *Thermochemical Data in NIST Chemistry WebBook, NIST Standard Reference Database Number 69*, Eds. P.J. Linstrom and W.G. Mallard, <http://webbook.nist.gov/chemistry/>
- 4) L. D. Landau and E. M. Lifshitz, *Mechanics* (Elsevier Ltd., 2010), 3rd edn., Vol. 1, Course of Theoretical Physics.
- 5) R. Shankar, *Principles of Quantum Mechanics* (Springer, 2008), 2nd edn.
- 6) J. E. Bright Wilson, J. C. Decius and P. C. Cross, *Molecular Vibrations: The Theory of Infrared and Raman Vibrational Spectra* (Dover Publications, Inc., New York, 1980).
- 7) G. Herzberg, *Molecular Spectra and Molecular Structure* (Krieger Publishing Co., New York, 1989), 2nd edn.
- 8) A. M. Oliveira, J. H. Lehman, A. B. McCoy and W. C. Lineberger, *J. Phys. Chem. A* **120**, 1652-1660 (2016).
- 9) J. Cooper and R. N. Zare, *J. Chem. Phys.* **48**, 942-943 (1968).
- 10) A. Sanov, *Annu. Rev. Phys. Chem.* **65**, 341-363 (2014).
- 11) C. C. J. Roothaan, *Rev. Mod. Phys.* **23**, 69-89 (1951).
- 12) J. McMurry, *Organic Chemistry* (Brooke/Cole Publishing Company, Belmont, California, 1992).
- 13) P. D. Lightfoot, R. A. Cox, J. N. Crowley, M. Destriau, G. D. Hayman, M. E. Jenkin, G. K. Moortgat and F. Zabel, *Atmospheric Environment. Part A. General Topics* **26**, 1805-1961 (1992).

- 14) G. S. Tyndall, R. A. Cox, C. Granier, R. Lesclaux, G. K. Moortgat, M. J. Pilling, A. R. Ravishankara and T. J. Wallington, *Journal of Geophysical Research: Atmospheres* **106**, 12157-12182 (2001).
- 15) A. Studer and D. P. Curran, *Angew. Chem. Int. Ed.* **55**, 58-102 (2016).
- 16) P. Neta, R. E. Huie and A. B. Ross, *J. Phys. Chem. Ref. Data* **17**, 1027-1284 (1988).
- 17) C. Chatgililoglu, K. U. Ingold and J. C. Scaiano, *J. Amer. Chem. Soc.* **103**, 7739-7742 (1981).
- 18) R. Atkinson, C. N. Plum, W. P. L. Carter, A. M. Winer and J. N. Pitts, *J. Phys. Chem.* **88**, 1210-1215 (1984).
- 19) R. Tembreull and D. M. Lubman, *Anal. Chem.* **56**, 1962-1967 (1984).
- 20) B. J. Fender, D. M. Sammeth and P. R. Callis, *Chem. Phys. Lett.* **239**, 31-37 (1995).
- 21) J. Hager, M. Ivanco, M. A. Smith and S. C. Wallace, *Chem. Phys. Lett.* **113**, 503-507 (1985).
- 22) H. Nakai and Y. Kawamura, *Chem. Phys. Lett.* **318**, 298-304 (2000).
- 23) C. Wang, D. Wang, Z. Wu, Z. Wang, C. Tang and P. Zhou, *App. Catal. A* **476**, 61-67 (2014).
- 24) V. M. L. Whiffen, K. J. Smith and S. K. Straus, *App. Catal. A* **419-420**, 111-125 (2012).
- 25) C. Wang, Z. Wu, C. Tang, L. Li and D. Wang, *Catal. Comm.* **32**, 76-80 (2013).
- 26) B. T. Draine and L. Aigen, *Astrophys. J.* **657**, 810 (2007).
- 27) B. T. Draine, D. A. Dale, G. Bendo, K. D. Gordon, J. D. T. Smith, L. Armus, C. W. Engelbracht, G. Helou, R. C. Kennicutt, Jr., A. Li, H. Roussel, F. Walter, D. Calzetti, J. Moustakas, E. J. Murphy, G. H. Rieke, C. Bot, D. J. Hollenbach, K. Sheth and H. I. Teplitz, *Astrophys. J.* **663**, 866 (2007).
- 28) M. A. Kurinovich and J. K. Lee, *J. Am. Soc. Mass Spectrom.* **13**, 985-995 (2002).
- 29) D. J. Hopper, *Biochem. J.* **175**, 345-347 (1978).

- 30) W. T. Read, *Industrial Chemistry* (Chapman and Hall, Limited, London, 1947).
- 31) X. Liu, M. Liu, X. Guo and J. Zhou, *Catal. Comm.* **9**, 1-7 (2008).
- 32) E. H. Strickland, J. Horwitz and C. Billups, *Biochemistry (Mosc.)* **9**, 4914-4921 (1970).
- 33) J. T. Vivian and P. R. Callis, *Biophys. J.* **80**, 2093-2109 (2001).
- 34) B. Breiner, K. Kaya, S. Roy, W.-Y. Yang and I. V. Alabugin, *Org. Biomolec. Chem.* **10**, 3974-3987 (2012).
- 35) C. K. Teh, J. Sipior and M. Sulkes, *J. Phys. Chem.* **93**, 5393-5400 (1989).
- 36) R. F. Gunion, M. K. Gilles, M. L. Polak and W. C. Lineberger, *Int. J. Mass Spectrom. Ion Processes* **117**, 601-620 (1992).
- 37) M. L. Weichman, J. B. Kim and D. M. Neumark, *J. Phys. Chem. A* **119**, 6140-6147 (2015).
- 38) D. J. Nelson, W. K. Gichuhi, E. M. Miller, J. H. Lehman and W. C. Lineberger, *J. Chem. Phys.* **146**, 074302 (2017).
- 39) M. Haeberlein and T. Brinck, *J. Phys. Chem.* **100**, 10116-10120 (1996).
- 40) E. O. Odebunmi and D. F. Ollis, *J. Catal.* **80**, 56-64 (1983).
- 41) V. M. L. Whiffen and K. J. Smith, *Ener. & Fuels* **24**, 4728-4737 (2010).
- 42) A. Hellweg, C. Hattig, I. Merke and W. Stahl, *J. Chem. Phys.* **124**, 204305 (2006).
- 43) H. Mizuno, K. Okuyama, T. Ebata and M. Ito, *J. Phys. Chem.* **91**, 5589-5593 (1987).
- 44) T. Aota, T. Ebata and M. Ito, *J. Phys. Chem.* **93**, 3519-3522 (1989).
- 45) K. Suzuki, Y. Emura, S.-i. Ishiuchi and M. Fujii, *J. Electron. Spectrosc. Relat. Phenom.* **108**, 13-20 (2000).
- 46) A. Oikawa, H. Abe, N. Mikami and M. Ito, *J. Phys. Chem.* **88**, 5180-5186 (1984).

- 47) M. Pohl and K. Kleinermanns, *Z. Phys. D: At., Mol. Clusters* **8**, 385-392 (1988).
- 48) C.-M. Tseng, Y. T. Lee, C.-K. Ni and J.-L. Chang, *J. Phys. Chem. A* **111**, 6674-6678 (2007).
- 49) J. S. Wright, D. J. Carpenter, D. J. McKay and K. U. Ingold, *J. Amer. Chem. Soc.* **119**, 4245-4252 (1997).
- 50) J. L. Lin, C. Li and W. B. Tzeng, *J. Chem. Phys.* **120**, 10513-10519 (2004).
- 51) H. S. Biswal, P. R. Shirhatti and S. Wategaonkar, *J. Phys. Chem. A* **113**, 5633-5643 (2009).
- 52) J. Huang, K. Huang, S. Liu, Q. Luo and W. Tzeng, *J. Photochem. Photobiol. A* **188**, 252-259 (2007).
- 53) M. Ito and A. Oikawa, *J. Mol. Struct.* **126**, 133-140 (1985).
- 54) H. M. Relles, D. S. Johnson and J. S. Manello, *J. Amer. Chem. Soc.* **99**, 6677-6686 (1977).
- 55) T. Ebata and M. Ito, *J. Phys. Chem.* **96**, 3224-3231 (1992).
- 56) M. Gerhards, B. Kimpfel, M. Pohl, M. Schmitt and K. Kleinermanns, *J. Mol. Struct.* **270**, 301-324 (1992).
- 57) R. J. Lipert and S. D. Colson, *J. Phys. Chem.* **93**, 3894-3896 (1989).
- 58) G. A. King, A. L. Devine, M. G. D. Nix, D. E. Kelly and M. N. R. Ashfold, *Phys. Chem. Chem. Phys.* **10**, 6417-6429 (2008).
- 59) L. A. Angel and K. M. Ervin, *J. Phys. Chem. A* **110**, 10392-10403 (2006).
- 60) A. Chandra and T. Uchimaru, *Int. J. Mol. Sci.* **3**, 407-422 (2002).
- 61) R. M. B. d. Santos and J. A. M. Simoes, *J. Phys. Chem. Ref. Data* **27**, 707-739 (1998).
- 62) L. S. Richard, C. E. S. Bernardes, H. P. Diogo, J. P. Leal and M. E. Minas da Piedade, *J. Phys. Chem. A* **111**, 8741-8748 (2007).

- 63) S. A. Kudchadker, A. P. Kudchadker, R. C. Wilhoit and B. J. Zwolinski, *J. Phys. Chem. Ref. Data* **7**, 417-423 (1978).
- 64) J. D. Cox, *Pure Appl. Chem.* **2**, 125-128 (1961).
- 65) M. Fujio, R. T. McIver and R. W. Taft, *J. Amer. Chem. Soc.* **103**, 4017-4029 (1981).
- 66) T. B. McMahon and P. Kebarle, *J. Amer. Chem. Soc.* **99**, 2222-2230 (1977).
- 67) T. N. V. Karsili, A. M. Wenge, B. Marchetti and M. N. R. Ashfold, *Phys. Chem. Chem. Phys.* **16**, 588-598 (2014).
- 68) A. Hellweg and C. Hattig, *J. Chem. Phys.* **127**, 24307 (2007).
- 69) G. Myszkiewicz, W. L. Meerts, C. Ratzner and M. Schmitt, *Phys. Chem. Chem. Phys.* **7**, 2142-2150 (2005).
- 70) K. M. Ervin and V. F. DeTuri, *J. Phys. Chem. A* **106**, 9947-9956 (2002).
- 71) J. B. Kim, T. I. Yacovitch, C. Hock and D. M. Neumark, *Phys. Chem. Chem. Phys.* **13**, 17378-17383 (2011).
- 72) M. Bendikov, H. M. Duong, K. Starkey, K. N. Houk, E. A. Carter and F. Wudl, *J. Amer. Chem. Soc.* **126**, 7416-7417 (2004).
- 73) W. T. Borden, *Diradicals* (John Wiley and Sons, New York, 1982).
- 74) D. Doehnert and J. Koutecky, *J. Amer. Chem. Soc.* **102**, 1789-1796 (1980).
- 75) H. K. Hall and A. B. Padias, *Acc. Chem. Res.* **23**, 3-9 (1990).
- 76) R. Hoffmann, D. B. Boyd and S. Z. Goldberg, *J. Amer. Chem. Soc.* **92**, 3929-3936 (1970).
- 77) K. N. Houk, J. Liu, N. C. DeMello and K. R. Condroski, *J. Amer. Chem. Soc.* **119**, 10147-10152 (1997).
- 78) R. Huisgen, *The Journal of Organic Chemistry* **41**, 403-419 (1976).

- 79) P. G. Wenthold and R. R. Squires, *J. Amer. Chem. Soc.* **116**, 6401-6412 (1994).
- 80) G. E. Davico, R. L. Schwartz, T. M. Ramond and W. C. Lineberger, *J. Amer. Chem. Soc.* **121**, 6047-6054 (1999).
- 81) E. Goldstein, B. Beno and K. N. Houk, *J. Amer. Chem. Soc.* **118**, 6036-6043 (1996).
- 82) J. Gräfenstein, A. M. Hjerpe, E. Kraka and D. Cremer, *J. Phys. Chem. A* **104**, 1748-1761 (2000).
- 83) L. Koziol, V. A. Mozhayskiy, B. J. Braams, J. M. Bowman and A. I. Krylov, *J. Phys. Chem. A* **113**, 7802-7809 (2009).
- 84) R. Lindh, T. J. Lee, A. Bernhardsson, B. J. Persson and G. Karlstroem, *J. Amer. Chem. Soc.* **117**, 7186-7194 (1995).
- 85) W. C. Lineberger and W. T. Borden, *Phys. Chem. Chem. Phys.* **13**, 11792-11813 (2011).
- 86) A. Rajca, *Chem. Rev.* **94**, 871-893 (1994).
- 87) E. Ramos-Cordoba and P. Salvador, *Phys. Chem. Chem. Phys.* **16**, 9565-9571 (2014).
- 88) V. Vanovschi, A. Krylov and P. Wenthold, *Theoretical Chemistry Accounts* **120**, 45-58 (2008).
- 89) G. P. F. Wood, L. Radom, G. A. Petersson, E. C. Barnes, M. J. Frisch and J. A. Montgomery, *J. Chem. Phys.* **125**, 094106 (2006).
- 90) X. Asensio, À. González-Lafont, J. Marquet, J. M. Lluch and M. Geoffroy, *Journal of Molecular Structure: THEOCHEM* **913**, 228-235 (2009).
- 91) M. Born, S. Ingemann and N. M. M. Nibbering, *Mass Spectrom. Rev.* **16**, 181-200 (1997).
- 92) S. Gronert, *Chem. Rev.* **101**, 329-360 (2001).
- 93) G. Gryn'ova and M. L. Coote, *J. Amer. Chem. Soc.* **135**, 15392-15403 (2013).

- 94) B. T. Hill, J. C. Poutsma, L. J. Chyall, J. Hu and R. R. Squires, *J. Am. Soc. Mass Spectrom.* **10**, 896-906 (1999).
- 95) T. Ichino, S. M. Villano, A. J. Gianola, D. J. Goebbert, L. Velarde, A. Sanov, S. J. Blanksby, X. Zhou, D. A. Hrovat, W. T. Borden and W. C. Lineberger, *J. Phys. Chem. A* **115**, 1634-1649 (2011).
- 96) M. Lin and J. J. Grabowski, *Int. J. Mass spectrom.* **237**, 149-165 (2004).
- 97) D. C. Magri and M. S. Workentin, *Chemistry – A European Journal* **14**, 1698-1709 (2008).
- 98) K. K. Morishetti, P. Stripadi, V. Mariappanadar and J. Ren, *Int. J. Mass spectrom.* **299**, 169-177 (2011).
- 99) K. Pius and J. Chandrasekhar, *J. Chem. Soc. [Perkin 2]* 1291-1295 (1988).
- 100) D. R. Reed, M. Hare and S. R. Kass, *J. Amer. Chem. Soc.* **122**, 10689-10696 (2000).
- 101) D. R. Reed, M. C. Hare, A. Fattahi, G. Chung, M. S. Gordon and S. R. Kass, *J. Amer. Chem. Soc.* **125**, 4643-4651 (2003).
- 102) K. M. Stirk, L. K. M. Kiminkinen and H. I. Kenttamaa, *Chem. Rev.* **92**, 1649-1665 (1992).
- 103) N. R. Wijeratne and P. G. Wenthold, *J. Am. Soc. Mass Spectrom.* **18**, 2014-2016 (2007).
- 104) M. W. Allen, J. R. Unruh, B. D. Slaughter, S. J. Pyszczyński, T. R. Hellwig, T. J. Kamerzell and C. K. Johnson, *J. Phys. Chem. A* **107**, 5660-5669 (2003).
- 105) J. R. Carney and T. S. Zwier, *J. Phys. Chem. A* **103**, 9943-9957 (1999).
- 106) J. R. Carney, F. C. Hagemester and T. S. Zwier, *J. Chem. Phys.* **108**, 3379-3382 (1998).
- 107) G. A. Bickel, D. R. Demmer, E. A. Outhouse and S. C. Wallace, *J. Chem. Phys.* **91**, 6013-6019 (1989).
- 108) J. Hager and S. C. Wallace, *J. Phys. Chem.* **87**, 2121-2127 (1983).
- 109) S. Arnold and M. Sulkes, *J. Phys. Chem.* **96**, 4768-4778 (1992).

- 110) G. Berden, W. L. Meerts and E. Jalviste, *J. Chem. Phys.* **103**, 9596-9606 (1995).
- 111) M. J. Tubergen and D. H. Levy, *J. Phys. Chem.* **95**, 2175-2181 (1991).
- 112) C. Unterberg, A. Jansen and M. Gerhards, *J. Chem. Phys.* **113**, 7945-7954 (2000).
- 113) W. Caminati and S. Di Bernardo, *J. Mol. Struct.* **240**, 253-262 (1990).
- 114) R. D. Suenram, F. J. Lovas and G. T. Fraser, *J. Mol. Spectrosc.* **127**, 472-480 (1988).
- 115) Y. Nibu, H. Abe, N. Mikami and M. Ito, *J. Phys. Chem.* **87**, 3898-3901 (1983).
- 116) W. B. Collier, *J. Chem. Phys.* **88**, 7295-7306 (1988).
- 117) S. Albert, K. K. Albert, P. Lerch and M. Quack, *Faraday Discuss.* **150**, 71-99 (2011).
- 118) J. M. Hollas, *Spectrochimica Acta* **19**, 753-767 (1963).
- 119) R. Bersohn, U. Even and J. Jortner, *J. Chem. Phys.* **80**, 1050-1058 (1984).
- 120) L. Serrano-Andrés and B. O. Roos, *J. Amer. Chem. Soc.* **118**, 185-195 (1996).
- 121) J. Kupper, D. W. Pratt, W. Leo Meerts, C. Brand, J. Tatchen and M. Schmitt, *Phys. Chem. Chem. Phys.* **12**, 4980-4988 (2010).
- 122) R. W. Taft and F. G. Bordwell, *Acc. Chem. Res.* **21**, 463-469 (1988).
- 123) M. Meot-Ner, J. F. Liebman and S. A. Kafafi, *J. Amer. Chem. Soc.* **110**, 5937-5941 (1988).
- 124) K. M. Ervin and V. F. DeTuri, *J. Phys. Chem. A* **106**, 9947-9956 (2002).
- 125) A. R. McKay, M. E. Sanz, C. R. S. Mooney, R. S. Minns, E. M. Gill and H. H. Fielding, *Rev. Sci. Instrum.* **81**, 123101 (2010).
- 126) M. G. D. Nix, A. L. Devine, B. Cronin and M. N. R. Ashfold, *PCCP* **8**, 2610-2618 (2006).

CHAPTER II

EXPERIMENTAL BACKGROUND AND METHODS

§ 2.1 Introduction and Background

Photoelectron (PE) spectroscopy has been performed by researchers for a number of years, though the technology and methodologies have evolved considerably. Perhaps one of the earliest examples of the use of PE spectroscopy, in the form of a photodetachment study, was performed by Branscomb and Smith¹ in 1955. At the time, the electron affinity (EA) of the oxygen atom was a contested issue with most of the experiments that attempted to measure this quantity relying on calculating the EA from thermodynamic measurements of electron attachment to hot tungsten filaments.² History is a harsh judge; these measurements would be shown to be quite inaccurate, far beyond the error bars reported in those early works. Branscomb and Smith resolved to measure the EA more directly by exposing a mass selected beam of O⁻ anions to a bright lamp (a 1 kW movie theater projector) with a water-cooled doped-glass plate, capable of filtering out known wavelengths of light, interposed between the lamp and the anionic oxygen beam. If the photons which passed through the filter were energetically capable of detaching the electrons, then the electrons would be ejected, collected, and measured by lock-in detection. By changing the wavelength filtering plates, they were able to measure a crude version of the photoelectron cross-section as a function of photon energy. See Fig. 2.1.

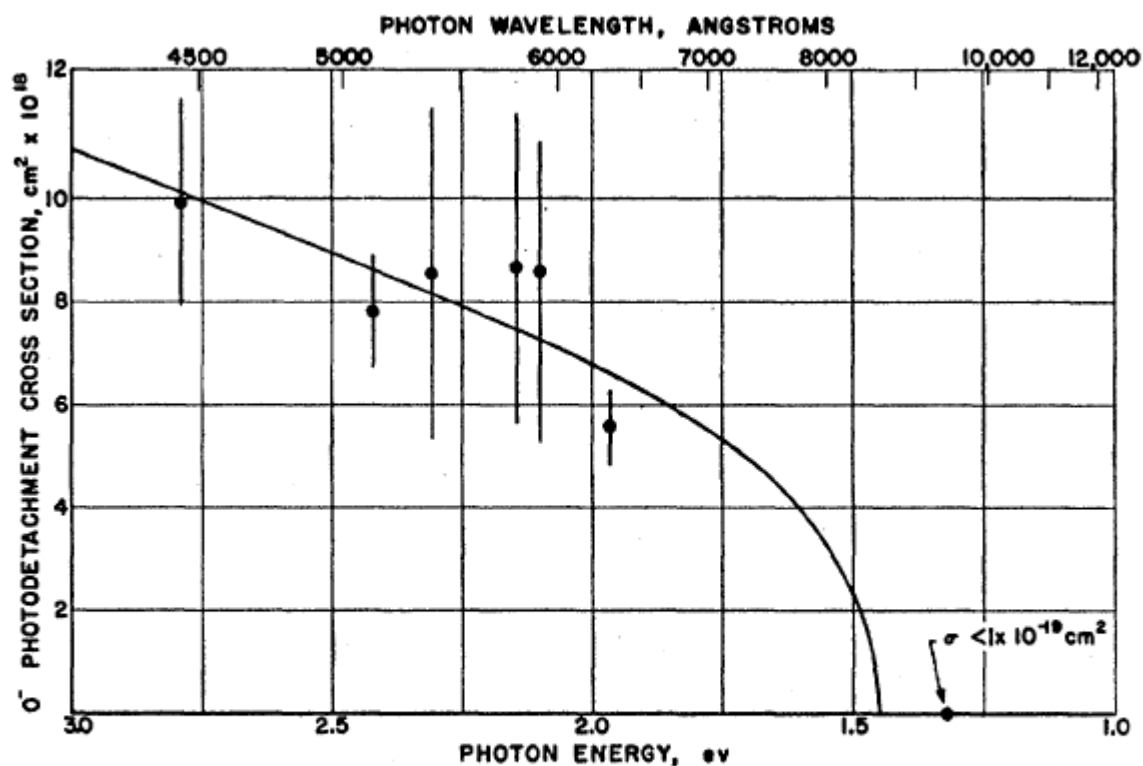


FIG. 2. Cross section for photodetachment of electrons from O^- . The solid curve is not extrapolated, but is the best fit to the data of Table I for a monotonic function and is thus not uniquely determined.

Fig. 2.1 Early measurement of the O^- photoelectron cross section as a function of photon energy. This figure is reprinted from Ref. 1.

As one can see from Fig. 2.1, the experimental data was quite sparse and had large errors associated with the measurements. Even more extraordinary is the theoretical fit to the data; so extraordinary, in fact, that it likely had been viewed with healthy skepticism as the authors used this fit to extrapolate out to the threshold of photodetachment, which would be equal to the EA. By this method, the authors claimed to measure the EA of the oxygen atom as 1.45 ± 0.15 eV. Disregarding the validity of such an extrapolation, this measurement would be later confirmed as correct, within its reported error, by far more sensitive and rigorous investigations.³

After this initial foray into utilizing a light source to photodetach electrons from anions, several attempts to refine the methodology of lamps and filters were made;⁴ however this quickly proved to be fatally limited by both the low power non-coherent light which could not be efficiently focused and the broad continua of wavelengths which filters must inherently transmit. At this same time, a new technology was waxing strongly which would revolutionize the way photodetachment spectra were collected: organic dye lasers. These lasers allowed for the first measurements of photodetachment spectra of atomic anions with enough resolution to resolve the fine structure of those atoms.⁵ Later, this would allow for the measurement of vibrational states in molecular anions as well.

While photodetachment studies offer the same information as photoelectron spectra, in principle, they differ in several important ways. Photodetachment studies require a tunable light source whose frequency is scanned across and then above the detachment threshold of a particular anion, and all ejected electrons are collected as a function of the photon energy. The kinetic energies of these electrons (eKE) are not analyzed directly in this process. PE spectra are instead obtained with a fixed frequency of laser light, after which, the ejected electrons are collected and then their kinetic energy is measured by some means. This has the advantage of not

requiring a tunable laser which must be accurately and smoothly scanned across some frequency range, and, in the case of organic dye lasers, Amplified Spontaneous Emission (ASE) must also be effectively eliminated lest the laser turn back into a lamp. Considering the advantages available to PE spectroscopy the only obstacle was how to accurately measure the kinetic energy of photodetached electrons. This was first overcome by means of the device known as a hemispherical electron energy analyzer, then called an “electron monochromator,”⁶ and thus the first photoelectron spectra were obtained in 1972 and subsequently in 1974.^{7, 8}

In principle, the primary limitation on the resolution in PE spectroscopy is set by the method used to analyze the electron kinetic energy. As such, considerable effort would be expended in the following years to improve and refine the hemispherical electron energy analyzer, allowing it to attain a resolution of ~ 3 meV under the correct circumstances and conditions. While improving the hemispherical electron energy analyzer was pursued, so were alternative methods. The magnetic bottle electron energy analyzer⁹ and the Velocity Map Imaging (VMI) photoelectron spectrometer^{10, 11} were later developed.

These various methods all have unique advantages and weaknesses. The hemispherical electron energy analyzer has the advantage of possessing a constant spectral resolution, regardless of electron kinetic energy. As such, this method enjoys the full benefit of PE spectroscopy in that one need only employ the highest photon energy laser possible, with virtually no need to ever change the laser color. However, this piece of equipment is greatly limited by the collection efficiency of the photoelectrons. In the hemispherical electron analyzer utilized in the studies presented in this dissertation, for example, of the photoelectrons being ejected in the total 4π steradians of solid angle, only those electrons within $\sim 1/2000$ steradians are collected for analysis. This places a strong restriction on the apparatus that the source of

photoelectrons must be large enough to overcome this limitation. Practically, this requires an intense light source. (This will be discussed further in § 2.4) The magnetic bottle, on the contrary, is nearly the inverse of the hemispherical electron energy analyzer in terms of strengths and weaknesses. The magnetic bottle, or Time-Of-Flight (TOF) electron spectrometer, enjoys nearly 100% collection efficiency of photoelectrons. However, the spectral resolution of this method decreases with increasing electron kinetic energy and generally possesses lower spectral resolution than the hemispherical energy analyzer. For a magnetic bottle to attain resolution on par with the hemispherical electron energy analyzer requires a TOF Ultra-High-Vacuum (UHV) tube often several stories tall. The VMI photoelectron spectrometer offers an attractive compromise between the two previous instruments. While the VMI PE spectrometer also has a spectral resolution which is a function of the kinetic energy of the photoelectrons, it is also capable of meeting or exceeding the resolution of the hemispherical electron energy analyzer at low kinetic energies.¹² Additionally, the VMI PE spectrometer is a physically small and uncomplicated device, especially when compared to the magnetic bottle regarding size or the hemispherical electron energy analyzer regarding complexity.

The photoelectron studies presented in this dissertation have been collected on two separate machines. The first instrument combines a Flowing-Afterglow (FA) ion source with a Wien Velocity Filter (WVF), which mass selects the anions of interest, a hemispherical electron energy analyzer, and finally a light build-up cavity locked to an argon ion laser system. The second experiment utilizes a novel dual pulsed valve plasma entrainment ion source, a Wiley-McClaren TOF mass spectrometer, VMI PE spectrometer, and a nanosecond tunable pulsed laser system. The following sections will describe and discuss all of these components in detail, first addressing the former instrument followed by the latter.

§ 2.2 Overview: Continuous Photoelectron Spectrometer

The first instrument to be discussed is best summarized in Fig. 2.2.

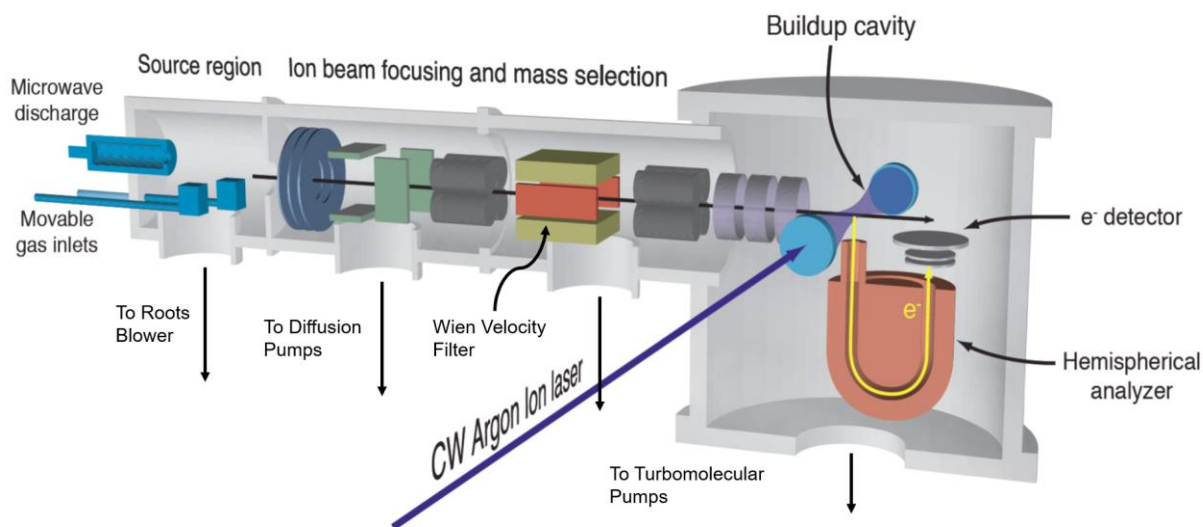


Fig. 2.2 Diagram of the continuous photoelectron spectrometer. Continuous ion generation takes place on the left hand side of the instrument in a flowing afterglow microwave plasma source. The ions are extracted through a small orifice, accelerated to a kinetic energy of 735 eV, mass selected in a Wien velocity filter, decelerated to a kinetic energy of 35 eV, intersected by a cw Ar ion laser, and the photoelectrons collected and their kinetic energies analyzed via a hemispherical photoelectron energy analyzer.

The anions to be studied are generated in a flowing afterglow ion source (§ 2.3) and then extracted into a differentially pumped region and accelerated to a kinetic energy of 735 eV. The ion beam, consisting of many different anions, is introduced to a Wien velocity filter (§ 2.4) where anions of a single mass-to-charge ratio (m/z) are selected. The mass selected anions are then decelerated to a kinetic energy of 35 eV and intersect a build-up cavity of light generated with an Ar ion laser. (§ 2.5) Upon encountering the radiation within the build-up cavity, the anions undergo photodetachment, and the photoelectrons are subsequently collected and fed into a hemispherical energy analyzer. (§ 2.6) All of these components are discussed in detail in their respective sections, which follow this section.

Taken as a whole, the strengths and weakness of this experimental design may be summarized as follows. Utilizing a flowing afterglow ion source gives this experiment access to multi-step rational ion synthesis, by sequentially introducing reagents to the gas flow. The FA source is also capable of generating large continuous ion currents, up to 40 nA prior to mass selection, however this comes at the cost of a very heavy gas load of up to 25 sccm of helium. This is both monetarily expensive, and requires a roots blower based pumping system to adequately remove the helium. The Wien velocity filter benefits from being spacially compact, does not require exceptionally powerful magnetic or electric fields, and offers low loss of ion current through the device, compared to a mass selecting quadrupole, for instance. The limitation of the Wien velocity filter is found in the fact that it generally possesses a lower mass resolution than other mass selecting devices. The hemispherical electron energy analyzer is a complex device with a long history of scientific use, as discussed in the previous section, but the primary advantage could arguably be said to be the constant resolution of the device across the entire photoelectron spectrum of a given anion. The primary disadvantage is the low collection

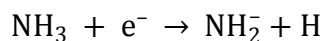
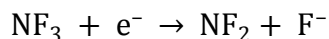
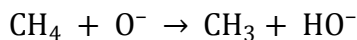
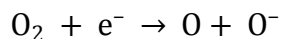
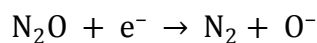
efficiency of photoelectrons, necessitating the use of a laser build-up cavity to boost the photoelectron yield.

A discussion of the specific components utilized in this experiment and their respective principles of operation follows.

§ 2.3 Principles of Operation: Flowing–Afterglow Ion Source

A Flowing–Afterglow plasma has been shown to be an effective method for the generation of a continuous flow of atomic and molecular anions possessing many advantages.^{13,}
¹⁴ The first key advantage is temperature control. The FA He plasma used in these experiments is at high pressure, ~ 0.5 Torr, with only trace amounts of reagent. If the formation of an anion of interest is exothermic, the excited ion can be collisionally cooled by He, which is thermally equilibrated with the walls of the chamber, for several milliseconds. This implies that any anion of interest generated in the apparatus will have a well-defined thermal temperature in all degrees of freedom. The second advantage is the ability to perform sequential rational ion synthesis by injecting reagents separated spatially along the flow. In theory, multi-step syntheses are possible via this route, and may be easily controlled by varying the spacing of the reagent inlet ports in relation to one another in the flow.

In the experiments examined in this dissertation, the specific flowing afterglow apparatus utilized has been described in detail previously, and as such only a generalized discussion will be given here.¹⁵ This FA ion source utilizes a flow of helium which is converted into a plasma by a resonant microwave cavity which engulfs the flow tube, which itself is made of glass. The plasma of He^+ and e^- is then utilized to perform any number of chemical reactions with a given reagent. While it is sometimes possible to encounter a reagent which is capable of directly interacting with the plasma to form the desired product anion, this is rare and not the case for any of the studies displayed in this work. Instead, the first step in the anion synthesis is the generation of a strong Lewis base in the gas phase which is then reacted with a neutral molecule that will subsequently be deprotonated. Some common reactions to generate these bases are as follows:



Note that in the case of generating hydroxide, this must be done in a two-step process; first generating atomic oxygen anions via either N_2O or O_2 and then subsequently introducing methane into the flow after the first step, adjusting the methane flow to fully titrate the oxygen anions.

The only question which remains is how to choose the proper base for a given molecular system which is to be investigated. As was discussed in the prior chapter, aromatic hydrocarbons were the focus of the studies of this dissertation, and as such, many of these molecules have multiple sites which could, in principle, be deprotonated. This implies that the choice of base used may be critical to the success of an experiment, as choosing too strong of a base might result in multiple deprotonated isomers, which cannot be distinguished via mass selection. To this end, the acidity of all of the sites on the molecules studied were theoretically calculated (see the individual chapters regarding any specific molecule for more detail) and compared to the known proton affinities of the bases produced in the reactions shown above.

Table 2.1 This table details the proton affinities of the gas phase bases which were most commonly utilized to generate the anions of interest in the studies of this dissertation.¹⁶

Proton Affinities of Common Bases in the Gas Phase	
F ⁻	372 kcal mol ⁻¹
O ⁻	382.6 kcal mol ⁻¹
OH ⁻	390.3 kcal mol ⁻¹
NH ₂ ⁻	403.4 kcal mol ⁻¹

Following the ion generation step in the FA plasma source, the negatively charged products are extracted through a nosecone ($r \sim 0.5$ mm) and into a differentially pumped region. Subsequently, the newly formed beam of anions are focused, steered and accelerated to 735 eV towards the Wien velocity filter. Of course, the synthesis of the anions which are intended to be studied are not unique and a number of byproducts are also produced in the FA plasma source. As such, it is necessary to physically separate the anions of interest from all other anions before performing PE spectroscopy. This is accomplished by way of the Wien velocity filter, which will be discussed next.

§ 2.4 Principles of Operation: Wien Velocity Filter

Wien Velocity Filters (WVFs) have been utilized for some time with the express purpose of separating out particles of a single velocity from a continuous beam of charged particles.¹⁷ There are several features of the WVF which make it particularly attractive in the application of PE spectroscopy. First, as was previously discussed, the collection efficiency of a hemispherical electron energy analyzer, which is the detection instrument employed on the continuous experiments, is quite low, and as such we cannot afford to lose any possible signal. The WVF offers high throughput, meeting this design need. Additionally, the WVF ideally does not deflect or in any way alter the course of the ions of the desired mass, which further reduces any design needs to steer and focus the mass selected ion beam after passing through the filter.

The other two obvious options for mass selecting a continuous beam of anions were not employed for several reasons. The first choice is the quadrupole mass filter.¹⁸ This is a device which alternates between two large ($V_{\max} \sim 15$ kV) saddle point potentials orthogonally oriented to the direction of motion of the incoming ion beam at radio frequencies. The two potentials are simply the same potential rotated $\pi/2$ radians from each other about the axis of the incoming ion motion. This causes the ions to travel in a helical trajectory through the quadrupole, where the trajectories' radius is a function of the mass of the ions, assuming all of the ions which entered the filter had the same kinetic energy. By also applying a DC field, one is able to select a specific mass to have a stable trajectory through the filter.¹⁹ However, this method has two key flaws for this application. First, the exit trajectory of the mass selected ions is helical and therefore quite difficult to re-collimate and focus without loss of overall ion signal following mass selection. Second, the throughput of quadrupole mass filters is generally lower than for WVFs. The other option for mass selecting the ion beam would be a magnetic bend.²⁰ This type

of setup would enjoy the same high throughput of the WVF, but large magnetic fields (far larger than those employed in the WVF) are required to operate this equipment. As we are performing PE spectroscopy, and therefore trying to measure the kinetic energy of electrons, having an external magnetic field acting upon the photoelectrons to any appreciable degree would be unacceptable. For example, the hemispherical electron energy analyzer must be shielded from the magnetic field of the earth with μ -metal, as that is already disruptive to the electron trajectories. Additionally, this method is in general a larger and more costly setup than a WVF.

The WVF setup is intuitive and relies on basic physical ideas to operate. The setup is as follows. Charged particles, each moving at an arbitrary speed, though all have the same direction of motion, enter a region of space intersected by two orthogonally oriented fields; one electric and one magnetic. See Fig. 2.3.

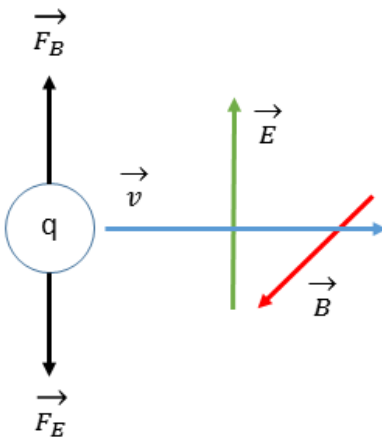


Fig. 2.3 An idealized schematic of the magnetic and electric fields that a negatively charged particle q , with a velocity v , would encounter upon entering the Wien filter. Also displayed are the resulting force vectors acting upon the negatively charged particle resulting from these fields.

As Fig. 2.3 demonstrates pictorially for the idealized case of a negatively charged particle q entering a Wien filter with a velocity v , the Lorentz force on the particle will be given as

$$\overrightarrow{F_{Lorentz}} = q\vec{E} + q\vec{v} \times \vec{B}$$

The ion beams used in the experiments are comprised of a collection of particles (molecular anions) all possessing $-1e$ of total charge, accelerated to the same kinetic energy, 735 eV, and possessing different masses. Since all of these particles possess the same kinetic energy, but have different mass, particles of different masses will attain different speeds.

$$KE_i = \frac{1}{2} m_i v_i^2 \rightarrow |\vec{v}_i| = \sqrt{\frac{2KE}{m_i}}$$

Rewriting the Lorentz force with this substitution

$$\overrightarrow{F_{Lorentz}} = q\vec{E} + q \sqrt{\frac{2KE}{m_i}} \hat{v}_i \times \vec{B}$$

Since we design the apparatus such that the electric and magnetic forces are antiparallel to each other, by setting a constant electric field and therefore constant electric force, and then choosing a magnetic field such that the Lorentz force on particles of a particular mass is zero, we have selected one set of particles of mass m_i to pass through the Wien filter without being deflected at all. Necessarily, this requires all other particles of mass not equal to m_i to be deflected. An aperture is placed ~ 30 cm after the exit of the Wien filter, and all particles which have been deflected by an amount greater than or equal to the radius of this aperture are thus discarded. This aperture defines the mass resolution of the instrument, which in our case is $m/\Delta m \sim 70$.

Of course, the real instrument deviates from the idealized model on display in Fig. 2.3. The largest obstacle in the design of a Wien filter lies in the construction of truly parallel electric field lines. Truly parallel field lines may only be achieved with infinitely large conducting plates laid parallel to each other and charged to different potentials. Infinitely large plates are not possible in the experiment, and finite plates, for which even approximating them as infinite plates is inappropriate, are used instead. Due to the effects of fringe fields in non-infinite plates, one must use other methods to create these parallel fields within the limited space of the Wien filter. This was achieved in this case by placing glass plates that were coated in vapor-deposited silicon along the edges of and perpendicular to the metal plates providing the electric field. This provided a gradient of potential along the resistive silicon which worked to counteract the fringe fields exerted by the edges of the metal plates. This setup was the focus of a previous graduate student's work and is explained in detail elsewhere.²¹ This is not as significant a problem for the creation of parallel magnetic field lines, as magnetic fields penetrate common metals such as 304 steel without significantly attenuating or distorting due to low magnetic susceptibility, and as such, one may place a large electromagnet exterior to the vacuum chamber without being limited by chamber dimensions. This allows for greatly increased surface area of the magnet faces, and so the parallel field approximation is valid.

Following mass selection in the Wien filter, the ion beam is steered, focused, and decelerated into the interaction region of the hemispherical electron energy analyzer.

§ 2.5 Principles of Operation: Argon–Ion Laser System

Once the ion beam has been decelerated to a kinetic energy of 35 eV, down from 735 eV, and is focused into the interaction region of the hemispherical electron energy analyzer, the beam is intersected by a linearly polarized UV cw laser beam generated by an argon–ion laser orthogonally oriented to the ion beam. This causes the desired photodetachment of electrons, which are then collected and their kinetic energies analyzed.

As previously discussed, the low collection efficiency of the analyzer necessitates a high level of photoelectron production in the interaction region in order to obtain practically useful levels of photoelectron signal. Photoelectron production of a well aligned ion and laser beam in the interaction region is proportional to the product of the laser power and the ion beam current. Considering this, one seeks to maximize both of these quantities. This has already been accomplished with regard to the ion beam, by utilizing a high amperage ion source in the flowing afterglow and a high throughput, minimum deflection mass selector in the Wein velocity filter. This now leaves the task of maximizing the laser power in the interaction region of the analyzer. A high power cw laser beam, at least on the ~50 W, and ideally on the ~100 W scale, has been determined as necessary in order to obtain practically useful levels of photoelectron signal, for typical ion beam currents. For context, when the instrument is configured to select only O^- , typical ion currents in the interaction region range from 10–20 nA.

Generating a cw UV laser beam with 50-100 W of output power is not practical by conventional methods, such as purchasing a commercial laser with such a rated output power. In the past incarnations of this experiment, this obstacle was overcome by using an argon–ion laser for green (488 nm) light. While commercial lasers of this type can achieve ~50 W at this wavelength, the previous design sought to drastically increase this power further. By removing

the output coupler of the laser and placing the remaining components in front of the windows into the vacuum chamber and finally placing a spherical high reflector after the hemispherical electron energy analyzer interaction region, one was able to essentially create a laser with extremely low output power, but extremely high circulating in-cavity power, ~ 1 kW.²² See Fig. 2.4. In essence, this made the vacuum chamber housing the interaction region of the hemispherical electron energy analyzer a lossy component of a laser cavity. This was possible to do with an Ar-ion plasma tube as a gain medium for 488 nm laser light, as the gain is extremely high at this wavelength, and so lasing was achievable even with the added loss that the vacuum chamber represented. To give a sense of the amount of gain available at this wavelength, typical output couplers of green Ar-ion lasers are only $\sim 66\%$ reflective.

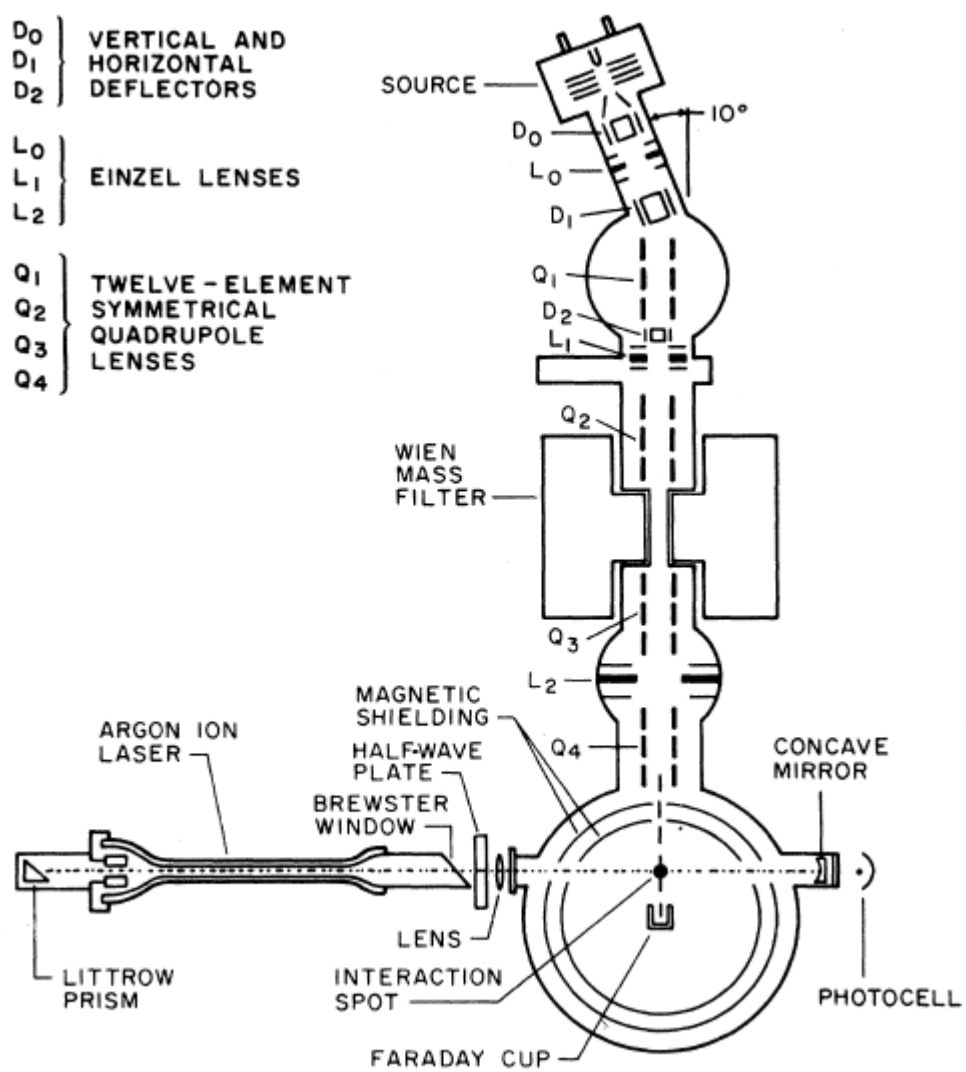


Fig. 2.4 A schematic of the experiment prior to converting the laser system to be able to perform UV photoelectron spectroscopy. Reprinted from Ref. 22.

This technique is not an option, however, if one wishes to perform UV photoelectron spectroscopy, as the gain of an Ar-ion laser plasma tube on either of the two strongest UV lasing transitions ($\lambda = 364$ or 351 nm) is far lower than for the green wavelengths. For reference, the output coupler on a typical Ar-ion laser lasing in the UV is $\sim 97\%$ reflective.

Given this fact, the system was designed to instead transform the windows of the vacuum chamber into a near-confocal cavity and then to lock the frequency of the UV laser light to a fringe of the chamber cavity. See Fig. 2.5. By injecting the frequency servo-locked laser light into the chamber with proper mode matching, one may achieve a large buildup of power within the chamber cavity: $P_{cavity} \sim P_{laser} \mathfrak{F}$, where \mathfrak{F} is the finesse of the chamber cavity. The full details of how this was accomplished are explained below.

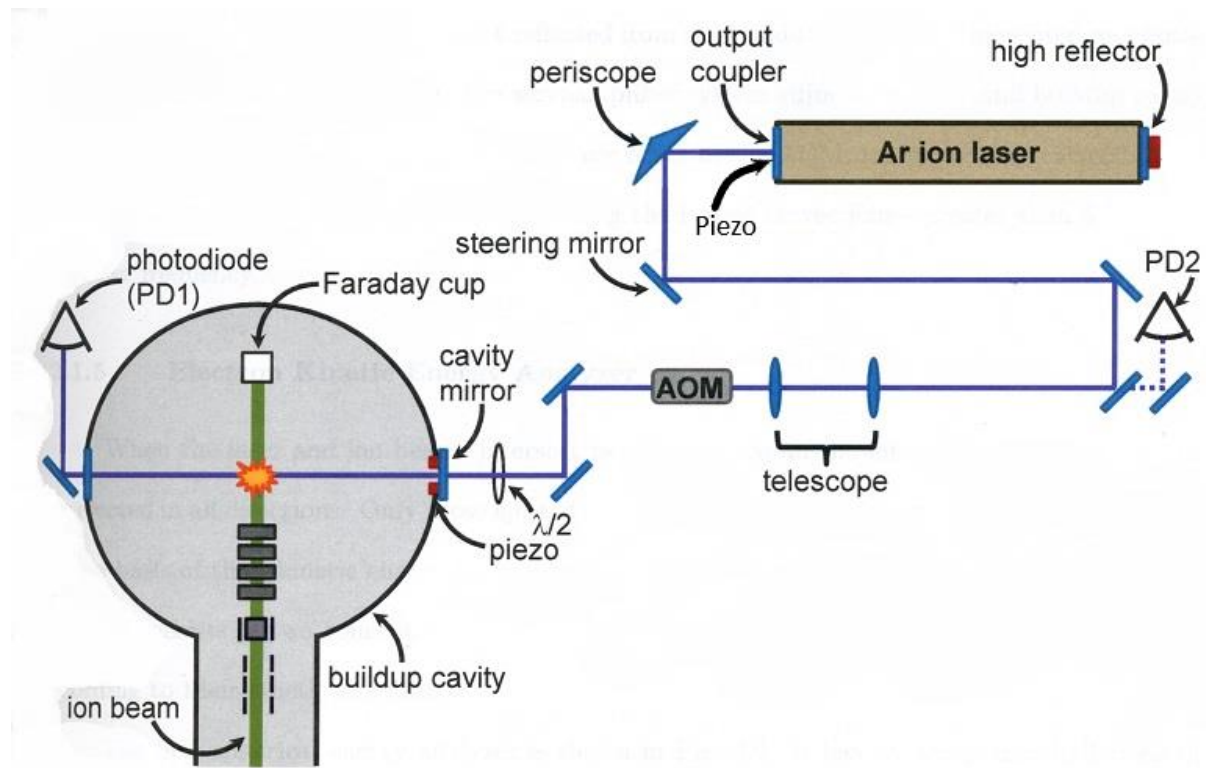


Fig. 2.5 Schematic of the full laser system utilized in the current continuous photoelectron spectrometer.

The first component in this laser system is a commercial Ar-ion laser. This laser has 3 Brewster windows in order to stabilize the horizontal laser polarization; two windows fused to the 1.5 meter long beryllium-ceramic plasma tube and one after the output coupler. There is an internal iris aperture that can be constricted to maximize the TEM(0,0) component of the beam. In order to precisely select the laser frequency, two components are required; a prism for selecting the lasing transition and an etalon to select the specific cavity fringe on which to lase. The etalon is necessary because we will be attempting to lock this cavity to another cavity, and power not contained within the overlap of the two fringes of the laser and chamber cavities in frequency space will be lost. Once the lasing transition and cavity fringe have been selected, typically the 364 nm lasing transition, the light is fed into the chamber build-up cavity.

A general description of the behavior of laser light coupling into an optical cavity follows: The cavity formed about the interaction region of the electron energy analyzer, designated the build-up cavity, intrinsically has a free spectral range ($FSR = \frac{c}{2L_{cavity}}$) and finesse associated with forming a standing light wave within it. In order to accumulate photons within the cavity such that the photon flux within it increases to a steady state value larger than that of the input laser, one must inject photons whose frequency is resonant with the maximum of one of the cavity fringes associated with the FSR of the build-up cavity. If the frequency of the laser light overlaps with a cavity fringe of the build-up chamber in frequency space to within the Full Width at Half Maximum (FWHM) of the build-up cavity fringe, ~ 400 kHz, and the laser FWHM, ~ 10 kHz, then the two cavities may be said to be resonant and photons will rapidly accumulate and reach a steady state population within the build-up cavity. Under these circumstances, considering that the finesse of the build-up cavity is ~ 450 , the steady-state power within the build-up cavity will be approximately $P_{cavity} \sim P_{laser} 450$. If the lasing and build-up

cavity fringes do not overlap, the cavities will not be resonant, and comparatively few photons will accumulate within the buildup cavity.

In an idealized world then, one might consider that one could manufacture the laser and build-up cavity lengths to be such that the lasing cavity fringe and a cavity fringe of the build-up cavity are perfectly resonant, and thus the problem of locking the frequencies of the cavities to be resonant would be solved. This, however, is not possible as it does not account for the real-world problems of noise and frequency drift. While one might be able to manufacture both optical cavities with enough precision to have them be resonant, length changes within either the laser or the build-up cavity on the order of one micron are enough to lose the resonance. Since there will always be acoustic noises in a lab, which might easily vibrate a cavity mirror with a displacement of one micron or more, plasma density fluctuations causing slight frequency shifts of the amplified photons through the gain medium of the Ar-ion laser, or any other of a host of small disturbances which might break the resonance of the two cavities, another method must be developed. We seek a method to actively adjust the FSR of both the laser and build-up cavities in real time with piezoelectric actuators to counteract these spurious motions utilizing home-built electronics in conjunction with an Acousto-Optic Modulator (AOM) to more finely tune the frequency of the laser light at high speed.

The method used to perform this active intervention has been described previously and is known as Pound-Drever-Hall (PDH) frequency stabilization.²³ The first step to utilizing this technique is to create an electronic error signal. This must take the form of some voltage which the electronics will check against a desired value and then send voltage(s) to outputs which connect to devices that alter aspects of the experiment which thereby change the error signal. This cycle continues indefinitely and ideally maintains the error signal at some value. In this

case, an error signal must be generated that is *only* a function of the overlap of the laser and build-up cavity fringes and is not a function of the output power of the laser. Additionally, the error signal must be built in such a way that the value of the error voltage indicates specifically how the electronics must act to correct the error signal back to the desired value. Accomplishing all of these mandatory criteria is challenging, but was accomplished in the following way.

First, we manipulate an AOM with a Voltage Controlled Oscillator (VCO) in order to dither the laser frequency as it impinges upon the buildup cavity. We modulate the laser frequency at 1MHz, which is to say we move the laser in frequency space ~ 50 kHz in one microsecond. This Frequency Modulated (FM) light is then fed into the build-up cavity. This scenario is depicted in Fig. 2.6.

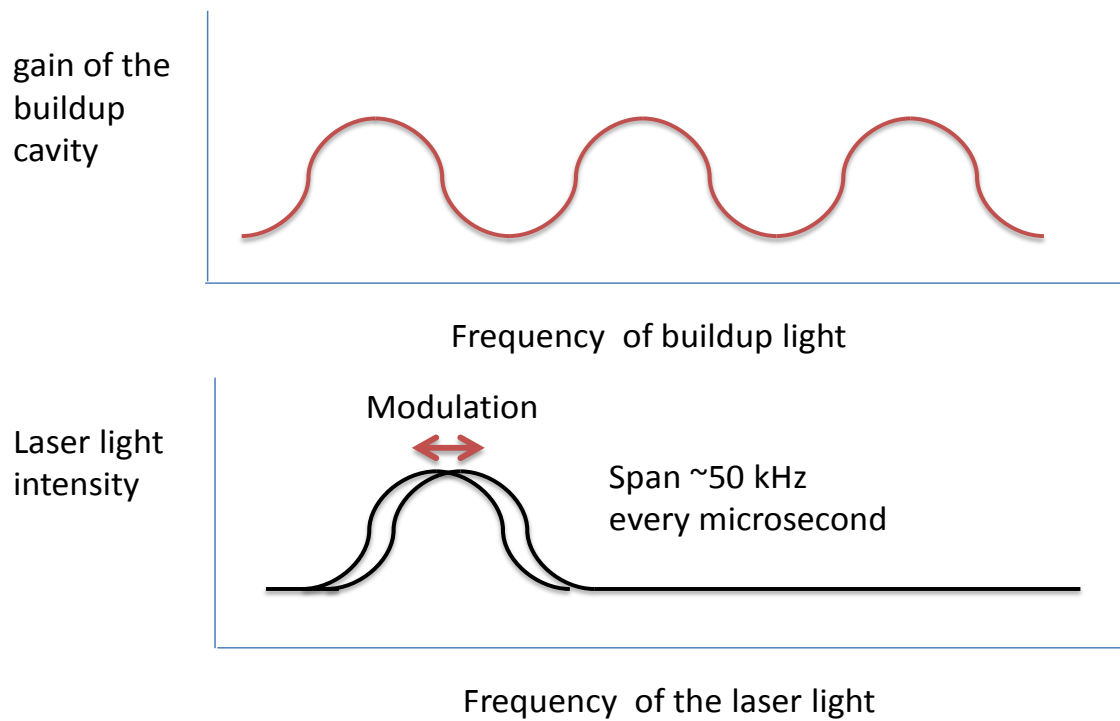


Fig. 2.6 A qualitative schematic of how the laser light is frequency modulated as it impinges upon the build-up cavity. Recall that $\Delta f_{\text{laser}} \sim 10 \text{ kHz}$ while $\Delta f_{\text{cavity}} \sim 400 \text{ kHz}$.

Acoustic noise in the lab typically shifts the laser frequency by far more than 400 kHz, the FWHM of a fringe of the build-up cavity. Recall that whenever the fringe of the laser is overlapped with a fringe of the build-up cavity, the reflected light of the front cavity mirror decreases and the light transmitted from the rear cavity mirror is increased. Thus, as noise causes a laser cavity fringe to cross over a build-up cavity fringe in frequency space, due to the 1 MHz dither on the laser, reflected light off the front cavity mirror or the transmitted light off the back cavity mirror will fluctuate in amplitude (Amplitude Modulation, AM) in time with the dither frequency and may be read by a photodiode. In other words, the cavity acts as an FM-to-AM converter. See Fig. 2.7

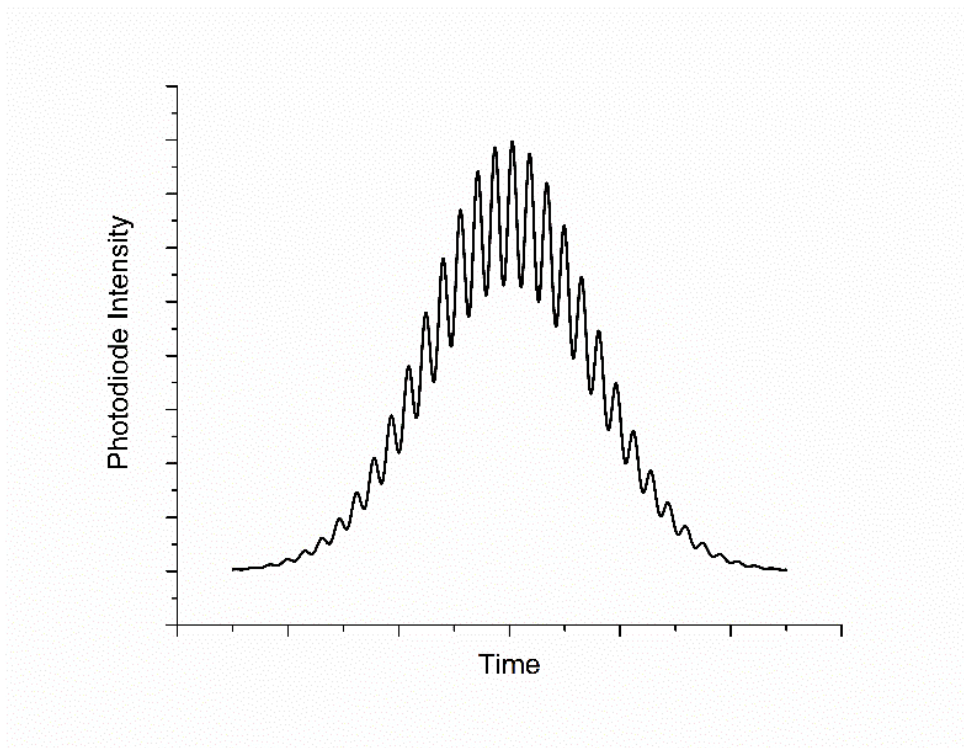


Fig. 2.7 An example of the FM-to-AM conversion when the dithered laser is scanned over the cavity fringe of the build-up cavity in frequency by monitoring the transmitted light intensity.

Thus, we feed the amplitude from either the reflected or transmitted light, read by a photodiode, from the build-up cavity and the original wavefunction that drives the AOM into a double wave mixer and this will generate the product of the two functions. Since the light from the build-up cavity will be phase shifted from the dither function, this may be modeled as:

$$\sin(\omega t) \sin(\omega t + \varphi) = \frac{1}{2} \{ \cos(\varphi) - \cos(2\omega t) \cos(\varphi) + \sin(2\omega t) \sin(\varphi) \}$$

Notice that there is a part of the left hand side of the equation that depends only on φ and another part that depends on 2ω . Critically, φ is a function of time as the value of φ will increase as the laser frequency is moving towards the peak center of the build-up cavity fringe, reach a maximum of 2ω at the maximum of the fringe, and then flip negative as the laser frequency scans over the opposite flank of the build-up cavity fringe. Thus, by monitoring the output of the double wave mixer and inserting a low pass filter that eliminates the 2ω or higher signal, we generate the desired error signal. See Fig. 2.8.

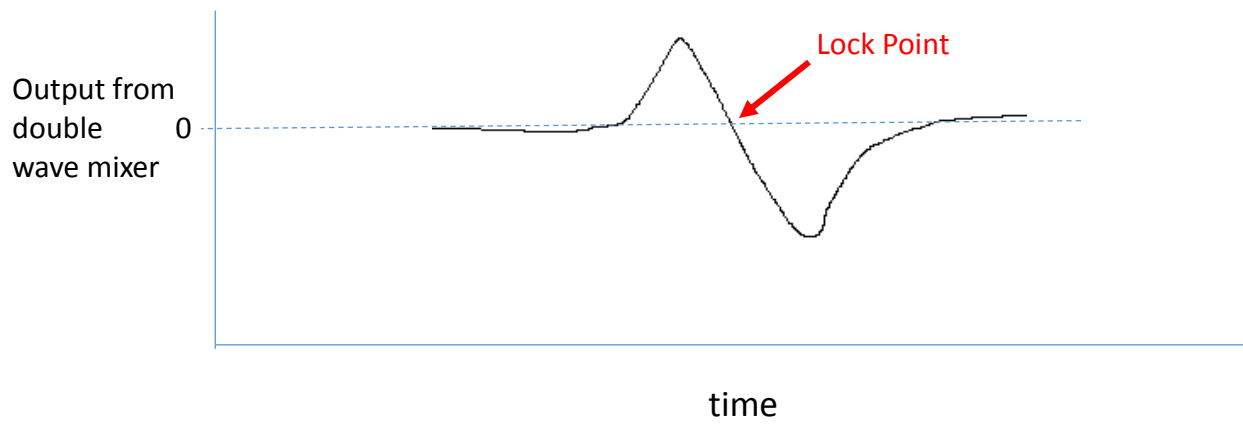


Fig. 2.8 Qualitative schematic of the form of the error signal utilized in the laser locking system as the laser fringe scans over a build-up cavity fringe. The red arrow points to the lock point of the servo loop filter system.

This is now a usable signal that can be servo-locked to, and is only sensitive to the resonance of the two cavities. By configuring the electronics to lock at the baseline voltage, then after crossing a build-up cavity fringe the servo will attempt to lock on the slope of the above curve, and the sign of the error signal informs the system whether to correct “up” or “down.” Thus, as the voltage changes and indicates that the two cavities are falling out of resonance with each other, the system will send a signal to one of three different devices which alter the frequency of the laser light or the FSR of the build-up cavity in order to bring the error voltage back to baseline.

This system relies primarily on two methods to adjust the frequency of the laser. The first is the ring piezo mounted inside the custom output coupler mount of the laser, onto which is affixed the output coupler itself (by way of Torr Seal). This necessitated a custom design and fabrication of the output coupler mount of the laser. See Fig. 2.9. The second is the AOM combined with the VCO.

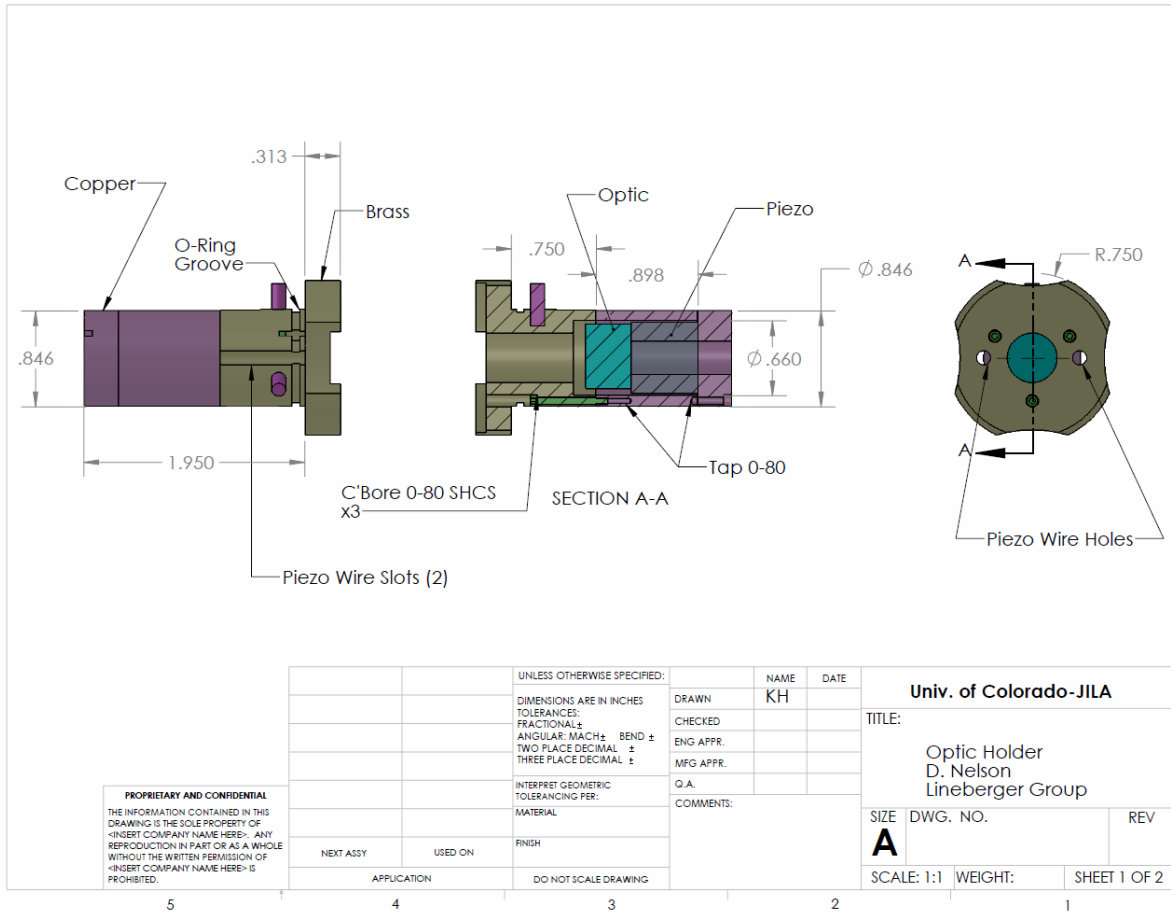
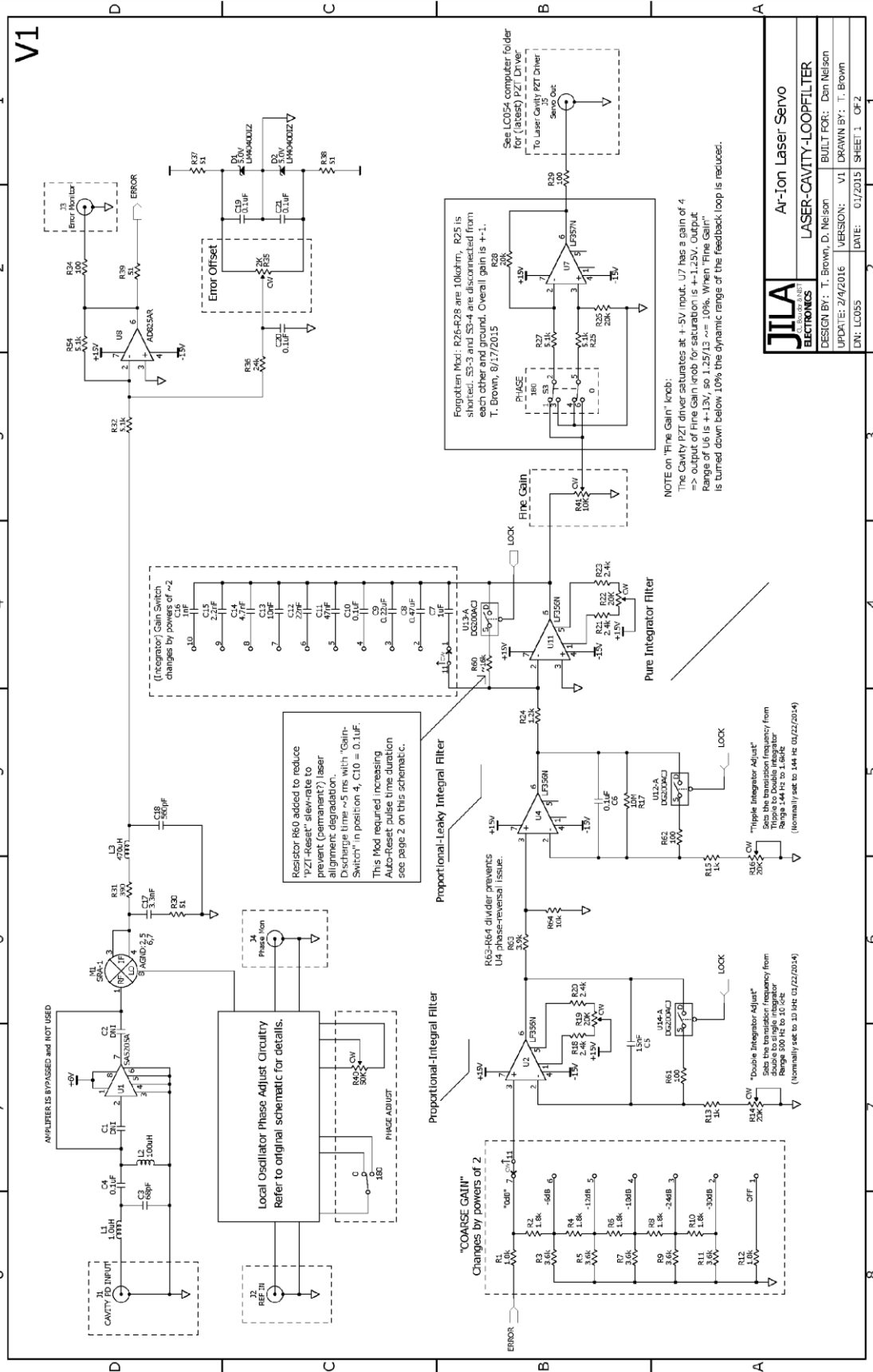


Fig. 2.9 Schematic of the custom bayonet output coupler mount fabricated to accommodate a piezoelectric actuator, onto which the output coupler optic is fused with Torr Seal adhesive.

The strategy used to achieve locking is as follows. The slew rate at which the two cavities come into and out of resonance allows for a window of opportunity of $\sim 50 \mu\text{s}$ to counteract the motion of the two cavities in frequency space. This necessitates a device that can operate at ~ 20 kHz in order to maintain the resonance. In general, this restriction rules out a piezoelectric actuator. The AOM, however, has significant gain in this region of frequency space. The AOM, then, is responsible for the initial lock, however it is limited in range in frequency space; it can only shift the input laser light by a max of 40 MHz before it runs out of range and must reset. This will extend the time over which the cavities remain resonant from $50 \mu\text{s}$ up to $500 \mu\text{s}$, but it cannot lock them permanently. To accomplish this, the piezoelectric actuator on the output coupler of the laser acts in concert with the AOM, and has far more range in altering the frequency of the laser. While the piezoelectric actuator has a very low gain response at 20 kHz, it has excellent response at 2000 Hz, corresponding to the time over which the cavities now stay resonant due to the intervention of the AOM. Once the lock is established, the AOM is responsible for countering high frequency noise that could disrupt the lock, while the piezo handles the lower frequency noise. Correctly balancing the Bode plots of the circuits which control these two devices and their associated phases such that we do not drive the circuits to oscillation is a critical factor, but will not be extensively discussed here. See Fig. 2.10 for details on these circuits.

Finally, one final set of piezoelectric actuators are affixed to the build-up cavity mirrors. Rather than have these respond to the error signal directly, these piezoelectric actuators servo off the voltage of the laser piezoelectric actuator and attempt to set that voltage to the baseline bias level. Effectively, this extends the overall range in frequency space of the laser that the piezoelectric actuator inside it is able to scan over. This final set of piezoelectric actuators are

only able to act at very low frequencies, DC–10 Hz, and so are also primarily effective at counteracting the lowest frequency noise sources, such as temperature changes.



JILA U.S. NATIONAL BUREAU OF STANDARDS	Ar-Ion Laser Servo
ELECTRONICS	LASER-CAVITY-LOOPFILTER
DESIGN BY: T. Brown, D. Nelson	BUILT FOR: Dan Nelson
UPDATE: 2/4/2016	VERSION: V1
DATE: 01/2015	SHEET 1 OF 2

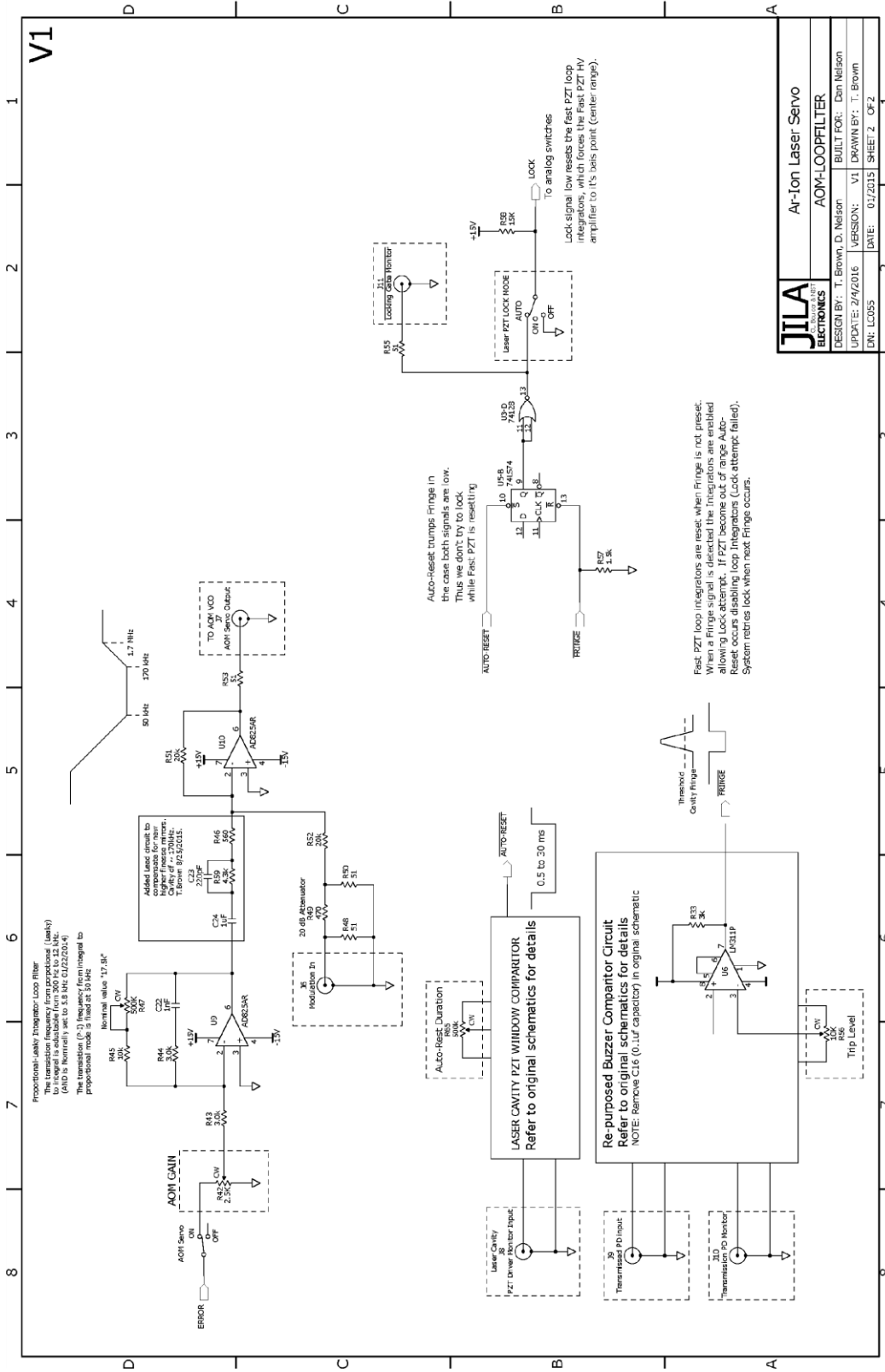


Fig. 2.10 Annotated circuit diagrams detailing the specific ways in which the laser servo works.

§ 2.6 Principles of Operation: Hemispherical Electron Energy Analyzer

Following photodetachment, a small portion of the electrons is collected and their kinetic energy is analyzed. This is done by way of a hemispherical electron energy analyzer, the specifics of which have been discussed at length previously.²⁴ A brief overview of the operational methodology is given here.

The electrons which are gathered through the collection pin hole in the molybdenum interaction region are first guided through a series of lens which are computer controlled. See Fig. 2.11. The purpose of these lenses is several fold. First, the analyzer will only transmit electrons which possess a kinetic energy within a small range of a central transmission energy, T_0 . Typically, this transmission energy is set to $T_0 \sim 1.5$ eV. Therefore, in order to scan through the full range of possible kinetic energies, the input lens stack is used to accelerate or decelerate the collected electrons so as to add or subtract precise amounts of kinetic energy before the electrons enter the annulus of the hemispheres. Thus, stepping the voltages on the lens stack and scanning through the added or subtracted kinetic energies, one is able to effectively measure a complete spectrum of electron kinetic energies. This critically provides the basis for the fact that this instrument will have a constant spectral resolution, regardless of the kinetic energy of the electrons which it measures. Second, the input lens stack is used to focus the electrons at the entrance to the annulus of the hemispheres, regardless of the added or subtracted kinetic energy. This is necessary, as the electrons' deflection through the annulus will only disperse in such a way as to be proportional to their respective kinetic energies if the electrons are generated from a point-source at the entrance to the annulus, equidistant from either hemisphere.

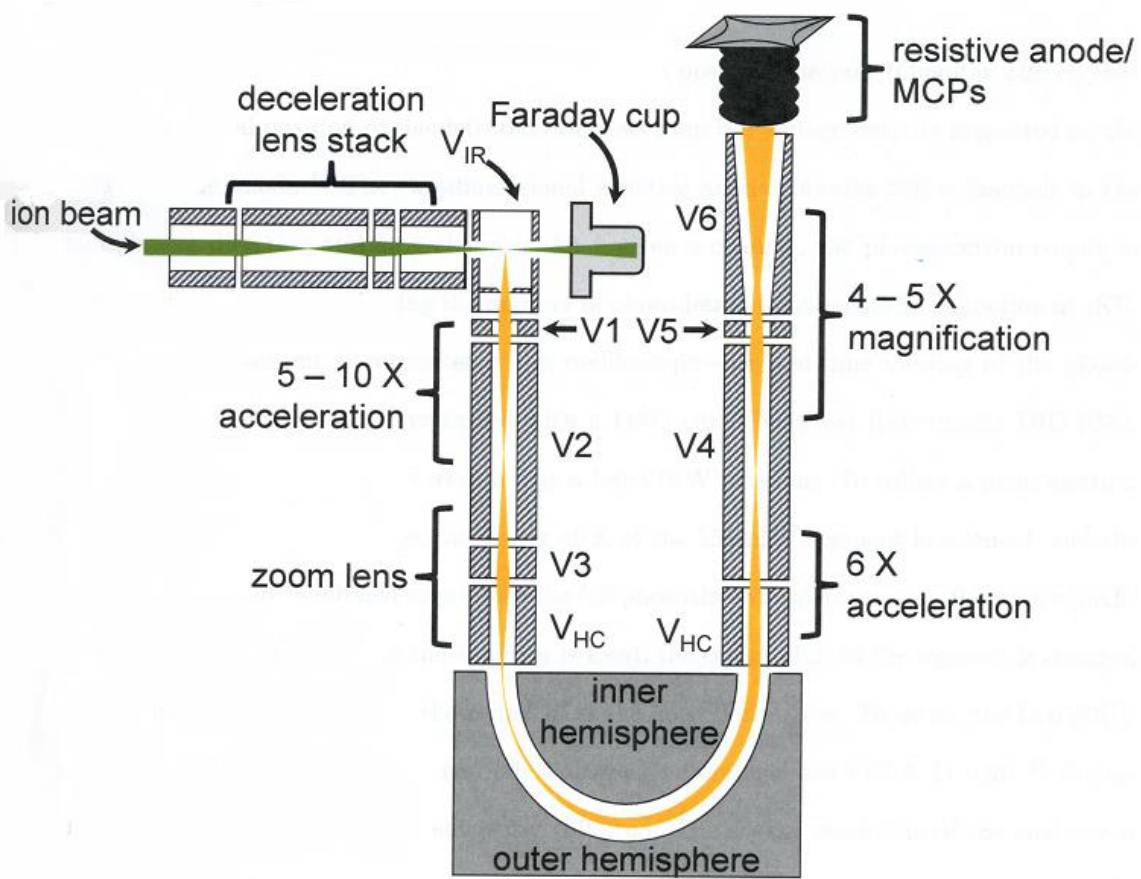


Fig. 2.11 Schematic of the electron kinetic energy analyzer system with deceleration, input, and output lens stacks included.

The theory of the motion of the electrons through the hemispherical analyzer is now discussed. As can be seen in Fig. 2.11, the analyzer is comprised of two hemispheres, one concave and one convex, the convex hemisphere partially inserted into the cavity of the other. These two pieces are then held at different voltages. This results in an electrostatic potential, in spherical coordinates, $\Phi = \frac{k}{r} + C$, where k is a constant associated with the voltage difference between the hemispheres and C is a constant of integration. This potential might be immediately recognizable as isomorphic with the famous central force field of celestial mechanics as laid out by Kepler. The equations of motion of a body in such a potential have long since been solved.²⁵

$$\frac{1}{r(\theta)} = \frac{mek}{l^2} \{1 - \varepsilon \sin(\theta + \phi)\}$$

$$\phi = \sin^{-1} \left[\frac{\left(1 - \frac{l^2}{mekr_{in}}\right)}{\varepsilon} \right]$$

$$\varepsilon = \sqrt{1 + \frac{2l^2(E + eC)}{me^2k^2}}$$

Where e is the electric charge of an electron, m is the electron mass, k is the constant determined by the voltage difference of the hemispheres, $l = vmr \cos(\phi)$, v is the velocity of the electron, ϕ is the divergence angle between the electron's velocity vector and the component of the velocity tangent to its radial position vector, ε is the eccentricity, r_{in} is the radius at which the electrons entered the electrostatic field, and E is the total energy of the electron in the central field.

Considering the annulus of the hemispheres will not permit particularly eccentric orbits to pass through, then the cases where circular orbits are formed are of interest. These orbits will occur when the minimum effective potential energy $V_{eff} = -\frac{ek}{r} - eC + \frac{l^2}{2mr^2}$ is equal to the total energy of the electrons in the central force field. The kinetic energy of an electron in such an orbit is $T = \frac{ek}{2r}$. Electrons possessing these orbits and this kinetic energy, where $r = r_0 = \frac{(r_1+r_2)}{2}$ with r_1 and r_2 being the hemispheres' respective radii, therefore define the central transmission energy, T_0 , of the analyzer. Electrons possessing kinetic energy equal to T_0 will therefore also be the electrons most efficiently transmitted through the analyzer.

Solving more specifically for the radius of electrons at the output ($\theta = \pi$) of the hemispherical analyzer in terms of the starting input radius ($\theta = 0$) gives

$$r_{out} = r_{in} \left[\frac{2T_0 r_0}{T r_{in} \cos^2(\phi)} - 1 \right]^{-1}$$

While this equation is rigorously correct, it offers little obvious physical insight. In order to extract practical information from it, one may perform a multivariate Taylor expansion evaluated about r_0 , T_0 , and $\phi = 0$ keeping only the first non-zero term past a constant. Following simplification and some rearrangement, this leads to

$$\frac{\Delta r_{out}}{r_0} \approx \frac{2\Delta T}{T_0} + \frac{3\Delta r_{in}}{r_0} - 2\phi^2$$

Where the terms with Δ refer to the difference between either the reference radius, r_0 , or the reference energy, T_0 , and the variable in question. Since the leading term in ϕ is of order ϕ^2 and this represents the divergence of the electrons at the output of the analyzer, the hemispherical analyzer is said to be perfectly focusing through first order. The critical insight, however, is that

the dispersal of the output electrons will be linear in kinetic energy. Namely, by ensuring that Δr_{in} is zero, which is to say that the electrons all enter the electrostatic field at the same radius equal to r_0 , which the input lens stack ensures, and that the divergence of the electrons is small and therefore the φ^2 term may be treated as negligible, then the dispersion of the output electrons is simply

$$D = \text{distance from } r_0 \text{ at exit} \approx \frac{2\Delta T r_0}{T_0}$$

While the Taylor expansion is useful to gain insight in the workings of the instrument, it is an approximation and fails to capture several other implications and only holds true under specific operating conditions. For example, this does not capture the linear magnification of the instrument, and assumes the electrons are generated at a point source in the entrance of the analyzer and each electron does not influence the motion of another. Nevertheless, this picture is sufficient to motivate the principles under which the hemispherical analyzer is operated.

Following the kinetic energy analysis and spatial dispersion of the electrons, an output lens stack interacts with the electrons. The purpose of this stack of lenses is to first magnify the image of the electrons, and then to accelerate this image onto a position sensitive detector without distortion. The position sensitive detector in this instrument takes the form of a stack of five Microchannel Plates (MCPs) and position detecting electronics.

The calibration of this instrument in order to affix the energy scale is achieved by measuring the $\text{O}(^3\text{P}_2) + \text{e}^- \leftarrow \text{O}^- (^2\text{P}_{3/2})$ transition in the atomic O^- photoelectron spectrum using the known EA of the O atom, 1.46112 eV.³ Additionally, a small energy scale compression factor (0.7%) is applied based on the photoelectron spectrum of O_2^- , which is determined by comparing measured peak positions to the well-known photoelectron spectrum of O_2^- .²⁶

§ 2.7 Overview: Pulsed Velocity Map Imaging Photoelectron Spectrometer

The other experiment utilized in this dissertation is now discussed. This experiment has been discussed at length previously.²⁷ The primary difference between the previous experiment and this one is that this experiment is pulsed. See Fig. 2.12. The ions are generated in a dual supersonic pulsed valve ion source. (§ 2.8) Following generation of the ions, they are extracted into a Wiley–McLaren time of flight mass spectrometer, mass separating the ions by their respective mass to charge ratios. (§ 2.9) The flight path of the ions places them into the interaction region of a velocity map imaging device. (§ 2.10) An appropriately timed nanosecond pulsed laser then interacts with only the ions of a chosen m/z , thus photodetaching electrons. The VMI repeller plate is then pulsed to operating voltage, causing the photoelectrons to be velocity mapped onto the two dimensional plane of the MCPs. Each of these components is discussed in detail in the following sections.

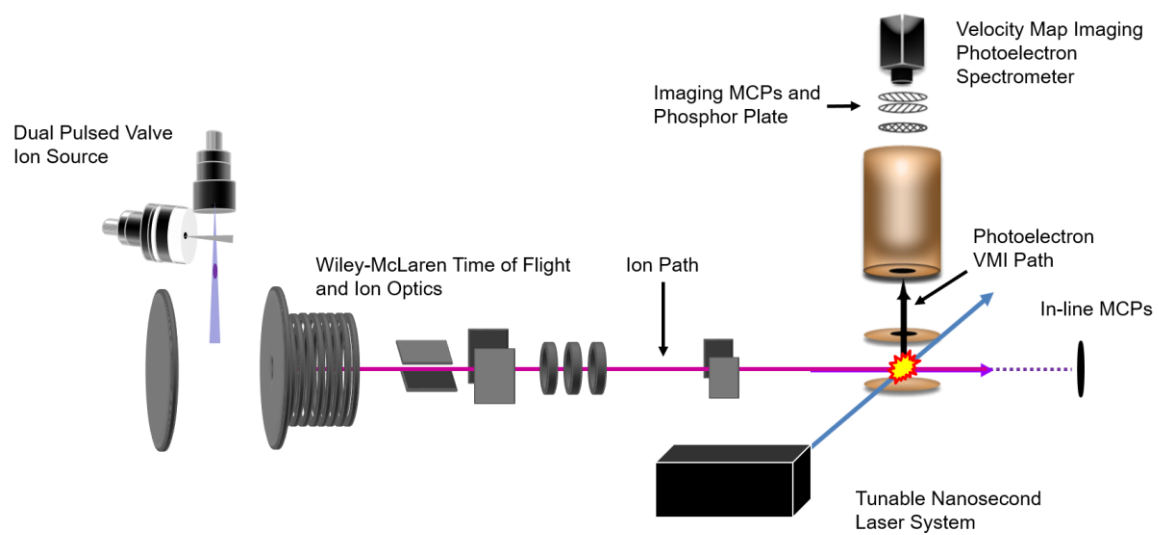


Fig. 2.12 Schematic of the pulsed VMI photoelectron spectrometer experiment.

As with the continuous instrument, this experimental setup has a series of advantages and disadvantages. Namely, as will be discussed, the dual pulsed valve ion source is capable of both rational ion synthesis, and is also capable of rapidly cooling and stabilizing even weakly bound reaction products. This allows for the generation of many novel ions and clusters. The Wiley–McClaren time of flight system presents a distinct improvement, by approximately an order of magnitude, in mass resolution over the Wien velocity filter found on the continuous apparatus. This reduces or eliminates the possibility of mass contamination in any collected photoelectron spectra. The VMI photoelectron spectrometer itself possesses 100% collection efficiency of photodetached electrons, allowing for a standard commercial pulsed Nd:YAG laser system, combined with a visible-light optical parametric oscillator (OPO) or dye laser, to be entirely sufficient. The disadvantage of the VMI photoelectron spectrometer comes in the form of the variable spectral resolution, which is a function of photoelectron kinetic energy. This will be discussed in detail in § 2.10, but in broad terms, this necessitates that several photoelectron spectra must be collected for a given anion utilizing multiple photon energies. Alternatively, this property may be used advantageously, as for very low kinetic energy electrons (< 100 meV) this spectrometer achieves a resolution of ~ 3 meV. Compared to the constant resolution of 10 meV on the continuous experiment, this allows one to obtain higher resolution photoelectron spectra. This technique is known as slow electron velocity–map imaging (SEVI) photoelectron spectroscopy.¹²

The individual components comprising this experiment will now be detailed and their principles of operation explained.

§ 2.8 Principles of Operation: Dual Pulsed Valve Ion Source

This experiment begins with ion generation which takes the form of two Parker-Hannifin Series 9 General Valves placed such that they face perpendicular to each other. One is designated the main valve, and is operated as a normal supersonic expansion. For the studies presented in this thesis, this valve will always use argon as a carrier gas seeded with trace amounts of an aromatic organic compound to be investigated. The other valve is designated the side valve and has electric discharge plates ($\Delta V \sim -1000-2000$ V) placed immediately in front of the exit aperture of the valve. The tension of the side valve is adjusted so that it accounts for $\sim 10\%$ of the base line pressure rise in the vacuum chamber upon pulsing. This valve is used to generate a plasma whose composition depends on the gas backing the valve. Typically, this is a mixture of oxygen, argon, and hydrogen. This plasma is then entrained in the primary supersonic expansion envelope, and subsequent collisions with the aromatic molecules seeded in the primary expansion effect reactions forming the anions of interest for a given experiment. See Fig. 2.13 for a schematic of this ion source reprinted from Ref. 27.

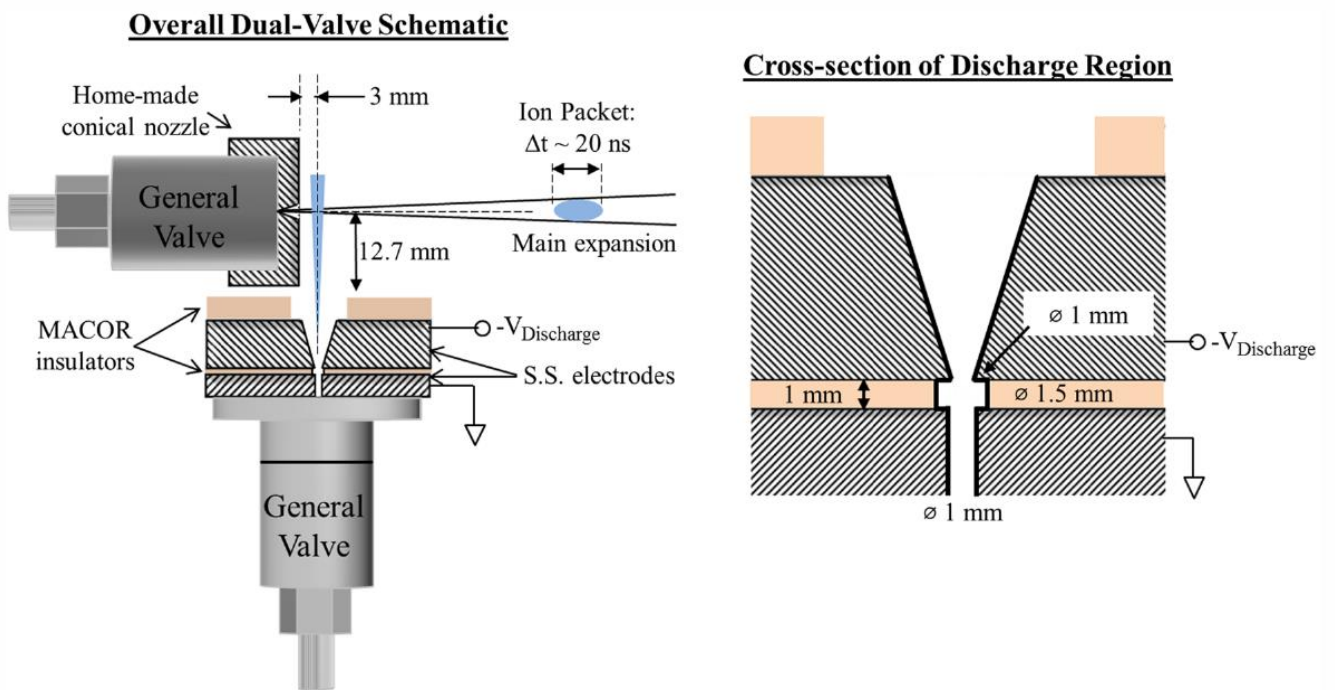


Fig. 2.13 A schematic of the ion source utilized in the experiments. Reprinted from Ref. 27.

The general theory behind the use of this experimental setup has been discussed and characterized at length previously.²⁸ For the works considered in this dissertation, this ion source was utilized in such a way as to use similar chemical reaction schemes as were found in § 2.3. As in the FA ion source, the strategy employed for all experiments presented here was to create a strong Lewis base in the side valve which is then entrained in the main supersonic expansion and will subsequently deprotonate the aromatic molecules seeded therein. The Lewis bases used in the experiments were: O^- via discharge of O_2 in Ar, OH^- via discharge of O_2 , H_2 , and Ar, and F^- via discharge of NF_3 in Ar. Following collisions and reactions with whichever base was chosen for a given experiment, the products are subsequently collisionally cooled by the argon carrier gas and extracted (utilizing an electrically pulsed metal plate) into a Wiley-McLaren Time-of-Flight (TOF) mass spectrometer to mass separate the product anions prior to performing PE spectroscopy on the anions of interest.

§ 2.9 Principles of Operation: Wiley-McLaren Time-of-Flight Mass Spectrometer

The Time-of-Flight mass spectrometer has been utilized and studied extensively, including the specific variation known as the Wiley-McLaren TOF.²⁹ In general, the principle under which a TOF mass spectrometer operates is a simple one. A charged particle which is accelerated by and toward an electrode attains a kinetic energy equal to its charge times the voltage of the electrode once it reaches the position of that electrode in space. Notice that this kinetic energy is not dependent on the mass of the particles, and recalling that $KE = \frac{1}{2}mv^2$, then particles accelerated by the same electrode and which possess the same charge but different masses will therefore possess different velocities. Thus, if one is able to generate an ensemble of ions, such as using the ion source described in §2.6, which are then simultaneously accelerated to the same kinetic energy and allowed to then travel in space unperturbed for some period, the ions will necessarily separate along the axis of motion according to their respective masses. In the case of the experiments presented here, these mass separated ions will pass into the laser interaction region of a VMI PE spectrometer, allowing for an appropriately timed nanosecond laser pulse to photodetach electrons from the ions of the appropriate mass.

Practically, several other factors must be accounted and compensated for. First we require that the ions not only be mass separated, but spatially focused into the smallest possible volume when they arrive at the VMI PE spectrometer's laser interaction region. In principle, the Wiley-McLaren TOF setup specifically allows for the ions being mass separated to also come to a single spatial focal point, solving this problem, so long as the experiment is contrived to locate this focus at the interaction volume of the VMI PE spectrometer. Realistically, more intervention is required for adequate focusing and thus several other ion optics have been added along the drift tube. Specifically, an Einzel lens³⁰ and several deflector plates are used to both focus and

steer the ions. Second, a method is required to allow for the collection of TOF mass spectra. This is accomplished by placing a double stack of MCPs immediately after the VMI PE spectrometer intersecting the ion beam, the output of which is read on an oscilloscope. This allows for real-time optimization of the TOF parameters for the best possible spatial and temporal focusing of the ions during the course of an experiment.

§ 2.10 Principles of Operation: Velocity Map Imaging Photoelectron Spectrometer

The VMI PE Spectrometer has been discussed extensively in the past²⁷ and a brief description will be given here. A VMI apparatus works on the principle that if one places an ensemble of charged particles each with a distinct velocity vector into an appropriately engineered electric field, they may be accelerated and focused onto a two dimensional plane such that the position of each particle at the detector is proportional to the 2D projection of its 3D velocity vector.¹¹ Unlike the hemispherical electron energy analyzer, the mathematics underpinning the design of the electrodes necessary to generate the appropriate electric fields are not conducive to analytical solutions which can be easily physically interpreted. Indeed, the design of first VMI apparatus was largely possible due to advances in computers and simulation software capable of calculating on-the-fly ion trajectories in the presence of electric fields.

The VMI setup used in the experiments presented here is comprised of three electrode elements: the repeller plate, the ground plate, and the extractor plate. The ground and extraction plates have a hole bored through their center to allow for the electrons to pass through. See Fig. 2.14. Prior to collecting a PE spectrum, both the repeller and ground plate are held at ground voltage, to which the ions in the Wiley-McLaren TOF have been referenced to. When the ions of interest enter the interaction region of the VMI apparatus, two actions are triggered. First, an appropriately timed nanosecond laser pulse will intercept the ions, photodetaching electrons. Second, the repeller plate is switched to the voltage necessary to form the appropriate electric fields to achieve VMI. By altering the voltage of the extraction and repeller plates one is able to change the effective range of electron kinetic energies which are observed by altering the magnification of the electron image projected onto the detector. The photodetached electrons will then be accelerated and imaged onto the detector where their positions are directly

proportional to their respective velocities. The position sensitive detector utilized here is a stack of MCPs coupled to a phosphor screen. Following an electron impacting a specific microchannel, the electron current through the impacted channel will amplify by a factor of $\sim 10^7$ and will impinge on the phosphor screen causing it to phosphoresce at the position of that microchannel, and this is then recorded by a CCD camera.

This photoelectron image is analyzed first by reconstructing the two dimensional image into a three dimensional velocity distribution using an inverse Abel transform as part of the BASEX program package. This three dimensional distribution is then converted to a one dimensional electron speed distribution, and finally an electron Kinetic Energy (eKE) distribution by a Jacobian transformation. This spectrum is converted to an electron Binding Energy (eBE) distribution by subtracting eKE from the laser photon energy, yielding the reported photoelectron spectra. This spectrum must then be calibrated; typically, this is done utilizing the known PE spectrum of an atomic anion, however the specifics of the calibrant used in a given experiment will be discussed in the chapter appropriate to that experiment.

In contrast with the hemispherical analyzer, the VMI spectrometer has a spectral resolution that is a function of eKE, namely the resolution decreases with increasing eKE. This is simply due to the conversion to kinetic energy, which goes as the square of the velocity. This resolution is determined by the eKE and the Full Width at Half Maximum (FWHM) of a peak in a photoelectron spectrum due to a single transition. Typically, a fine structure transition of an atomic anion is used to determine the resolution as a function of electron kinetic energy, as well as calibrate the energy scale. Typically, the resolution is $\sim 2-3\%$ (resolution $\sim \text{FWHM}/\text{eKE}$). However, if the photon energy is within ~ 50 meV of the binding energy of a transition, this results in low kinetic energy electrons, and the instrument attains a resolution of ~ 3 meV. This

technique is commonly referred to as Slow Electron Velocity Map Imaging (SEVI),¹² and will be used throughout the works presented in this dissertation. This will be accomplished by changing the photon energies employed in a given experiment, with details of the specifics found in the following chapters.

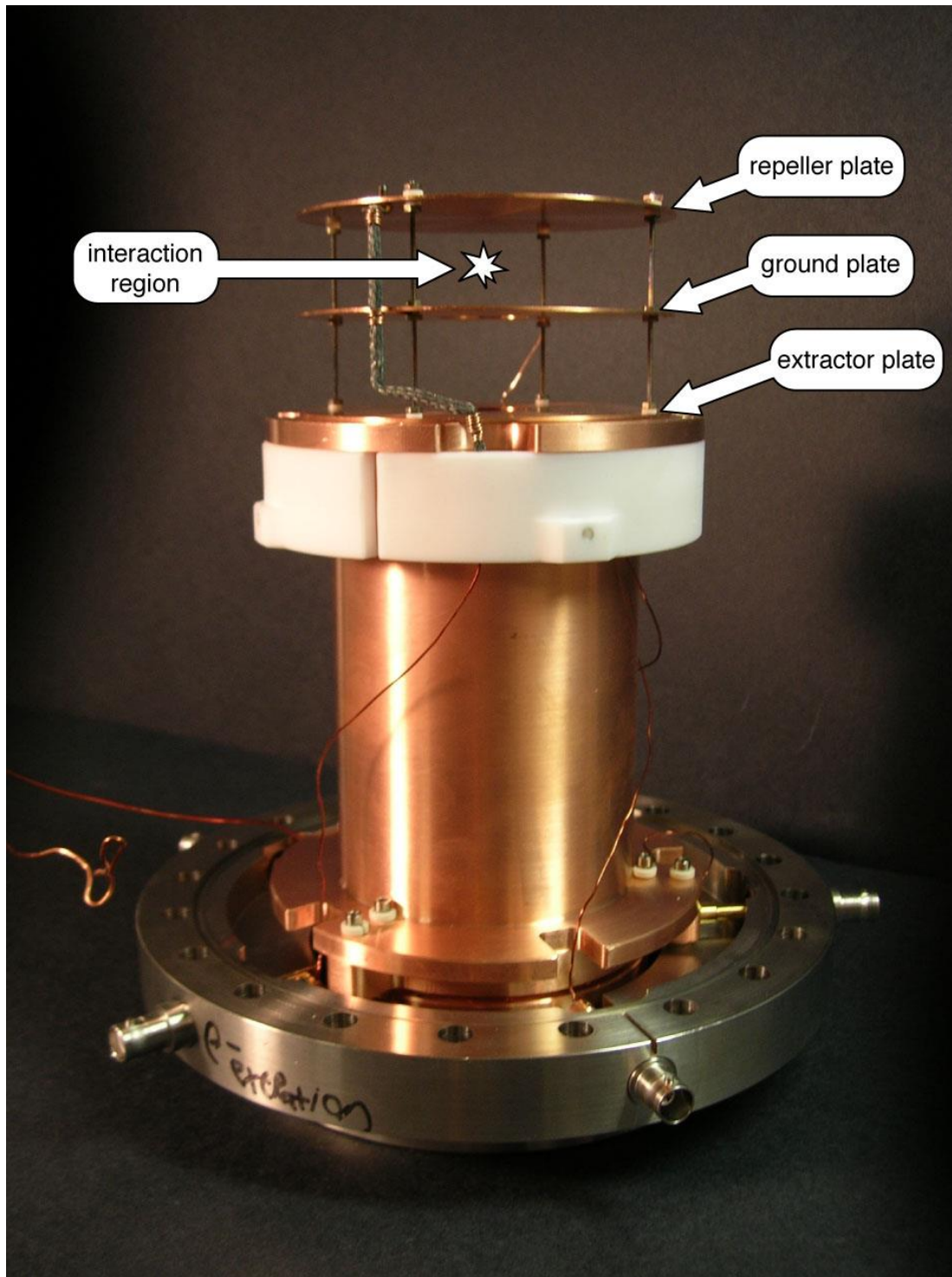


Fig. 2.14 Picture of the VMI PE spectrometer, annotated.

§ 2.11 References

- 1) L. M. Branscomb and S. J. Smith, Phys. Rev. **98**, 1127-1128 (1955).
- 2) D. T. Vier and J. E. Mayer, J. Chem. Phys. **12**, 28-34 (1944).
- 3) D. M. Neumark, K. R. Lykke, T. Andersen and W. C. Lineberger, Phys. Rev. A **32**, 1890-1892 (1985).
- 4) L. M. Branscomb, D. S. Burch, S. J. Smith and S. Geltman, Phys. Rev. **111**, 504-512 (1958).
- 5) W. C. Lineberger and B. W. Woodward, Phys. Rev. Lett. **25**, 424-427 (1970).
- 6) C. E. Kuyatt and J. A. Simpson, Rev. Sci. Instrum. **38**, 103-111 (1967).
- 7) A. Kasdan and W. C. Lineberger, Phys. Rev. A **10**, 1658-1664 (1974).
- 8) R. J. Celotta, R. A. Bennett, J. L. Hall, M. W. Siegel and J. Levine, Phys. Rev. A **6**, 631-642 (1972).
- 9) H. Handschuh, G. Ganteför and W. Eberhardt, Rev. Sci. Instrum. **66**, 3838-3843 (1995).
- 10) X. Wu, Z.-b. Qin, H. Xie, X.-h. Wu, R. Cong and Z.-c. Tang, Chin. J. Chem. Phys. **23**, 373-380 (2010).
- 11) A. T. J. B. Eppink and D. H. Parker, Rev. Sci. Instrum. **68**, 3477-3484 (1997).
- 12) D. M. Neumark, J. Phys. Chem. A **112**, 13287-13301 (2008).
- 13) D. B. Dunkin, F. C. Fehsenfeld, A. L. Schmeltekopf and E. E. Ferguson, J. Chem. Phys. **49**, 1365-1371 (1968).
- 14) C. H. DePuy and V. M. Bierbaum, Acc. Chem. Res. **14**, 146-153 (1981).
- 15) D. G. Leopold, K. K. Murray, A. E. S. Miller and W. C. Lineberger, J. Chem. Phys. **83**, 4849-4865 (1985).

- 16) D. R. Burgess and J. E. Bartmess, *Thermochemical Data in NIST Chemistry WebBook, NIST Standard Reference Database Number 69*, Eds. P.J. Linstrom and W.G. Mallard, <http://webbook.nist.gov/chemistry/>
- 17) L. Wählin, *Nucl. Instr. Meth.* **27**, 55-60 (1964).
- 18) P. H. Dawson, *International Journal of Mass Spectrometry and Ion Physics* **17**, 423-445 (1975).
- 19) J. M. Van Doren, S. E. Barlow, C. H. Depuy and V. M. Bierbaum, *Int. J. Mass Spectrom. Ion Processes* **81**, 85-100 (1987).
- 20) S. Penner, *Rev. Sci. Instrum.* **32**, 150-160 (1961).
- 21) S. W. Wren, (2011). *Photoelectron Spectroscopy of Organic Anions* (Doctoral Thesis).
- 22) M. W. Siegel, R. J. Celotta, J. L. Hall, J. Levine and R. A. Bennett, *Phys. Rev. A* **6**, 607-631 (1972).
- 23) E. D. Black, *Am. J. Phys.* **69**, 79-87 (2001).
- 24) C. S. Feigerle, (1983). *Laser Photoelectron Spectroscopy of Transition Metal Negative Ions* (Doctoral Thesis).
- 25) L. D. Landau and E. M. Lifshitz, *Mechanics* (Elsevier Ltd., 2010), 3rd edn., Vol. 1, Course of Theoretical Physics.
- 26) K. M. Ervin, I. Anusiewicz, P. Skurski, J. Simons and W. C. Lineberger, *J. Phys. Chem. A* **107**, 8521-8529 (2003).
- 27) L. Sheps, E. M. Miller and W. C. Lineberger, *J. Chem. Phys.* **131**, 064304 (2009).
- 28) Y.-J. Lu, J. H. Lehman and W. C. Lineberger, *J. Chem. Phys.* **142**, 044201 (2015).
- 29) W. C. Wiley and I. H. McLaren, *Rev. Sci. Instrum.* **26**, 1150-1157 (1955).
- 30) G. H. N. Riddle, *J. Vac. Sci. Tech.* **15**, 857-860 (1978).

CHAPTER III

ANION PHOTOELECTRON SPECTROSCOPY OF DEPROTONATED *ORTHO*-, *META*-, AND *PARA*-METHYLPHENOL

Sections of this chapter have been published in the peer-reviewed Journal of Chemical Physics under the same title, by, Daniel J. Nelson, Wilson K. Gichuhi, Elisa M. Miller, Julia H. Lehman, and W. Carl Lineberger

§ 3.1 Introduction and Background

As was discussed in § 1.3 the methylphenoxyls and methylphenoxides are of interest to a variety of fields within chemistry. These reasons have motivated the photoelectron (PE) spectroscopy study which was conducted and is presented here. The strategy to study the methylphenoxides and their corresponding neutrals, the methylphenoxyls, was as follows. Both experimental setups described in Chapter II were employed. The continuous experiment generated the anions of interest in the Flowing Afterglow ion source (§ 2.2) utilizing OH^- or NH_2^- as a Lewis base to deprotonate either *ortho*, *meta*, or *para*-methylphenol. The products of this reaction were then mass selected and the photoelectron spectra of these molecules obtained. While this experimental setup is advantageous due to the constant spectral resolution (~ 10 meV) of the hemispherical electron energy analyzer, it suffers from an inability to change wavelengths in order to observe any wavelength dependence of the spectra, or obtain high resolution (~ 3 meV) spectra. Thus the pulsed instrument is also employed. This experiment utilized the same synthesis pathway in the dual pulsed valve plasma entrainment source, *i.e.* the reaction of the neutral methylphenol isomer of interest with the Lewis base OH^- . Taking advantage of both the increased mass resolution, compared to the continuous instrument, and the increased spectral

resolution, due to a tunable laser light source, as discussed in § 2.8, additional high resolution and SEVI spectra were collected and additional physical insights were able to be drawn.

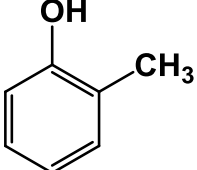
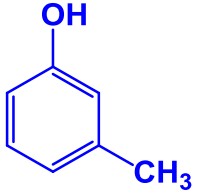
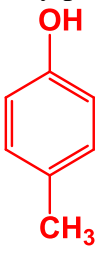
§ 3.2 Experimental Specifics

The experimental setups used to conduct these studies have already been discussed in general in Chapter II of this dissertation. However, specific details of how these instruments were employed for this experiment will now be explained.

In both instruments, methylphenol samples were obtained from Sigma Aldrich ($\geq 98\%$ purity) and used without further purification. Their chemical structure and chemical purity were verified with ^1H NMR.

In the continuous experiment, the methylphenoxide anions are prepared in a flowing afterglow ion source by proton abstraction from the parent methylphenol molecules using the hydroxide anion, OH^- , or the amide anion, NH_2^- , in approximately 0.5 Torr of helium buffer gas. The flow tube is cryogenically cooled to ~ 200 K. This collisional environment allows the reactants and products to evolve toward chemical equilibrium, so the detected anion products need not be the nascent deprotonated products. The dominant anion product observed corresponds to deprotonation of the most acidic site, with trace amounts of other products. Both OH^- and NH_2^- are energetically capable^{1,2} of deprotonating either the hydroxyl or the methyl sites for all three isomers, although the hydroxyl site is the most acidic site by over 30 kcal/mol, according to calculations at the B3LYP/aug-cc-pVQZ level. See Table 3.1. The NH_2^- anion is also energetically capable of deprotonating directly from the benzene ring, but this anion product channel is not observed.

Table 3.1 The enthalpies for the reactions removing a proton from either the OH or CH₃ groups on the methylphenols were computed and are presented here. The electron affinity for the corresponding radical of the deprotonated methylphenol is also reported. These were all calculated at the B3LYP/aug-cc-pVQZ level. In all cases the OH site is the most acidic site on the molecule by ~30 kcal/mol, with *m*-methylphenol showing the least acidic OH as compared to the CH₃. Note that the acidities of H₂O and NH₃ are 390 and 403 kcal/mol.³

Methylphenol Isomer	Deprotonation Site	Calculated $\Delta_{acid}H_{298K}^{\circ}$ (kcal/mol)	Calculated EA (eV)
<i>o</i> -methylphenol 	OH	347.6	2.135
	CH ₃	372.3	1.279
<i>m</i> -methylphenol 	OH	348.9	2.167
	CH ₃	378.8	1.013
<i>p</i> -methylphenol 	OH	349.6	2.065
	CH ₃	385.2	0.710

Following ion formation, the ions are extracted into a differentially pumped chamber ($\sim 10^{-6}$ Torr). In this chamber, the ions are focused, steered, and accelerated to 735 eV, mass selected with a Wien velocity filter (§ 2.3), and then decelerated to 35 eV before entering the laser-anion interaction region. In the interaction region, the mass-selected anions are intersected by single frequency radiation (363.806 nm, 3.40814 eV) obtained from an Ar-ion laser (§ 2.4). A small solid angle of the photodetached electrons is collected in a direction perpendicular to the laser and ion beams. The kinetic energies of these electrons are then measured by a hemispherical electron energy analyzer (§ 2.5) with a constant electron energy resolution of 10 meV. The photoelectron spectra reported here from this machine were obtained with the laser polarization oriented at the magic angle of 54.7° with respect to the photoelectron collection plane. This orientation yields photoelectron intensities that are proportional to the total photodetachment cross-section.⁴ The laser polarization was scanned to measure the anisotropy in the photoelectron angular distribution, specifically for the peak corresponding to the origin transition in the methylphenoxide anion photoelectron spectra. For the methyl deprotonated product for the *meta* isomer, the reported anisotropy parameter was averaged across the spectrum.

The pulsed experimental apparatus is now discussed. The anions of interest are produced in a dual pulsed valve plasma entrainment source (§ 2.6), again from the deprotonation of methylphenol by reaction with OH^- .⁵ The primary supersonic expansion is operated with a backing pressure of 10 psig, $\sim 1\%$ methylphenol in Ar, while the side valve is operated with a backing pressure of 35 psig, 1% O_2 , 30% H_2 and the balance Ar. The OH^- generated in the plasma source undergoes reactions with the methylphenol isomer of interest contained in the main expansion, generating products which are collisionally cooled with Ar. While not necessary

to be the case, the most thermodynamically favorable products (methylphenoxide anions, Table 3.1) were found to be by far the dominant deprotonated methylphenol produced.

Following the initial expansion, the anions are directed into a Wiley-McLaren TOF mass spectrometer by a pulsed extraction plate, where the ions are separated by their mass-to-charge ratio (m/z) and spatially focused in the center of a VMI interaction region (§ 2.8).⁶ An appropriately timed nanosecond laser pulse (discussed below) intersects the anion packet, photodetaching electrons. All of the photodetached electrons are velocity mapped onto a position sensitive phosphor screen-coupled microchannel plate detector, and subsequently imaged by a CCD camera. This photoelectron image is analyzed first by reconstructing the two dimensional image into a three dimensional velocity distribution using an inverse Abel transform as part of the BASEX program package. This three dimensional distribution is then converted to a one dimensional electron speed distribution, and finally an electron Kinetic Energy (eKE) distribution by a Jacobian transformation. This spectrum is converted to an electron Binding Energy (eBE) distribution by subtracting eKE from the laser photon energy, yielding the reported photoelectron spectra. For these experiments, the energy scale is calibrated by the S^- photoelectron spectrum.^{7, 8}

In contrast with the hemispherical analyzer, the VMI spectrometer has a spectral resolution that is a function of eKE, namely the resolution decreases with increasing eKE. This resolution is determined by the eKE and the Full Width at Half Maximum (FWHM) of a peak in a photoelectron spectrum due to a single transition. In this case, an atomic anion (S^-) was used to determine the resolution as a function of electron kinetic energy, as well as calibrate the energy scale. Typically, the resolution is ~2–3% (resolution ~ FWHM/eKE). However, if the photon energy is within ~50 meV of the binding energy of a transition, this results in low kinetic energy

electrons, and the instrument attains a resolution of ~ 3 meV. This technique is commonly referred to as Slow Electron Velocity Map Imaging (SEVI).⁹ To take advantage of the varying energy resolution of this spectrometer, a variety of photon energies are used in this experiment. The 3rd harmonic of a nanosecond Nd:YAG laser is used directly (355 nm, 3.494 eV). In addition, a visible light OPO is pumped by the 3rd harmonic of the Nd:YAG laser, supplying tunable light between 400 and 600 nm. Finally, the second harmonic of the Nd:YAG laser (532 nm, 2.330 eV) is used to pump a dye laser using DCM dye and producing 647 nm light, which is then frequency doubled to produce 323 nm (3.832 eV) light.

§ 3.3 Theoretical Methods and Simulations

Electronic and vibrational quantum calculations were carried out using the Gaussian 09 program package.¹⁰ All ground electronic state calculations were at the B3LYP/aug-cc-pVQZ level, which has been shown to be an effective compromise between accuracy and computational cost for large molecules, such as the substituted aromatic compounds studied here.¹¹ For excited electronic state calculations, Time Dependent Density Functional Theory (TD-DFT) was used with the B3LYP functional and Dunning's correlation consistent basis set, aug-cc-pVTZ. The energies and geometries of the anion ground electronic states, neutral ground electronic states, and neutral first excited electronic states were optimized for all isomers. In the case of each isomer, the ground and excited electronic state vibrational information was calculated separately for every anionic and neutral state used to simulate the PE spectra. In addition, the electron affinities (EAs) and electronic term energies for the *o*-, *m*-, and *p*-methylphenoxy radicals were calculated. The calculated geometries, normal mode vectors, and the harmonic vibrational frequencies of the anion and the corresponding neutral are used to calculate the Franck-Condon (FC) factors for the simulated photoelectron spectra using the PESCAL program.¹² In addition, a Boltzmann distribution of anion internal energy is applied (150 K or 200 K for the pulsed and continuous experiments, respectively). In the simulation, the FC factors are calculated using the harmonic oscillator approximation, which includes Duschinsky rotations and employs the Sharp-Rosenstock-Chen method.¹³⁻¹⁵ The calculated FC factors are shown as purple sticks where appropriate in the figures displayed in this chapter. These sticks are then convolved with Gaussian functions, whose integral is normalized to be equal to the calculated transition intensity, and whose FWHM is consistent with instrumental resolution, which is a function of eKE for the VMI spectrometer and is a constant 10 meV for the hemispherical analyzer. The sum

of these Gaussian functions results in the simulated spectra shown as green traces, which have been scaled in each case to match the experimental peak amplitude of the origin transition. Each simulated spectrum has also been shifted by $\sim 40\text{--}50$ meV to match the experimental electronic band origin.

§ 3.4 Expectations and Error Analysis

Before scrutinizing the photoelectron spectra of the product anions generated from reacting OH^- (or NH_2^- in the FA source) with the methylphenol isomers, it is useful to consider how the resulting photoelectron spectra from different deprotonated products might qualitatively vary. For example, the EA of the corresponding neutral is a good indication of the site of deprotonation of methylphenol. If the product anion is the result of deprotonating the alcohol group, the electron affinity of the neutral should be similar to that of the phenoxy radical (EA = $2.2538 \pm 0.0008 \text{ eV}^{16}$). If the product anion is instead the result of CH_3 deprotonation, it is reasonable to expect an EA of the corresponding neutral to be near that of the benzyl radical (EA = $0.912 \pm 0.006 \text{ eV}^{17}$). In either case, the electron is likely to localize on the deprotonated group; this should result in both a lengthening of the bond between the deprotonated group and the aromatic ring, as well as an elongation of the ring away from the negative charge when compared to the equilibrium geometry of the corresponding neutral radical. Thus, upon photodetachment, it might be expected that there will be vibrational transitions involving excitation in the neutral ring distortion modes with vibrational frequencies of $\sim 500 \text{ cm}^{-1}$. In addition, it is reasonable to predict excitation of vibrational modes in the neutral that incorporate a stretching motion along the bond between the ring and the deprotonated group, which would have fundamental vibrational frequencies of $\sim 1000 - 1500 \text{ cm}^{-1}$.

For each photoelectron spectrum, a vibrational analysis is performed by comparing the observed spectrum with the calculated photoelectron spectrum simulation. Throughout this work, the errors in the reported peak positions are related to the statistical error in finding the peak center, the error in the absolute energy scale, and the number of independent measurements of particular peaks. When reporting the position of a particular transition, such as the neutral

vibrational frequencies or the EA, this error is combined with the error associated with the offset of the actual transition from the peak center. This uncertainty can be near zero if a single transition is the major contributor to the peak shape, or, if there are multiple transitions under the peak envelope, it could be as much as the Half-Width-at-Half-Maximum (HWHM) of the peak. Note that the peaks presented in the reported spectra are broader than the instrument resolution and always arise from multiple transitions, so this latter error dominates the reported uncertainty. In the error analysis for each isomer, rotational contours were also considered. In every case, the analysis of Engelking was used¹⁸ and in all cases the shifts between peak centers of a particular transition and the true origin were estimated to be less than 0.1 meV. Thus this effect was accounted for in the uncertainty of the measurements contained in this work, but was determined to have a small impact on the reported error, even in the case of the EA measurements.

§ 3.5 Electron Affinities and Term Energies

In order to gain an overview of the full photoelectron spectra, data were collected on the VMI PE spectrometer with a photon energy of 3.494 eV (Fig. 3.1). Following deprotonation from all three reactant isomers (*o*-, *m*-, and *p*-methylphenol), there are two progressions observed. The first progression begins at approximately 2 eV eBE, with a second progression appearing at ~ 3 eV eBE. Considering the prior arguments, this would suggest that the anionic product formed is indeed methylphenoxide for all three reactant isomers. Further, considering the photoelectron spectroscopy spin selection rule $\Delta S \pm \frac{1}{2}$, and the fact that the methylphenoxide anion electronic ground state has singlet spin multiplicity, these two observed progressions must both be of doublet multiplicity. The progression starting near 2 eV in binding energy for each isomer arises from electron detachment from the anion singlet ground electronic state to form the neutral doublet ground electronic state (labeled \tilde{X}). Each progression starting near 3 eV in binding energy corresponds to a vibrational progression arising from transitions from the anion singlet ground electronic state to the first excited doublet electronic state of the neutral (labeled \tilde{A}) of methylphenoxyl. These assignments will be justified in the following paragraphs. While all three isomers of methylphenol show evidence of methylphenoxide products, another progression starting near 1 eV is observed for only the *meta* isomer. This will be shown to be the photoelectron spectrum of the anion product arising from the deprotonation of the methyl group (see Section E), forming the methylenephenol radical. It is not expected, based on TD-DFT calculations, that excited states of methylenephenol would be energetically accessible in this study.

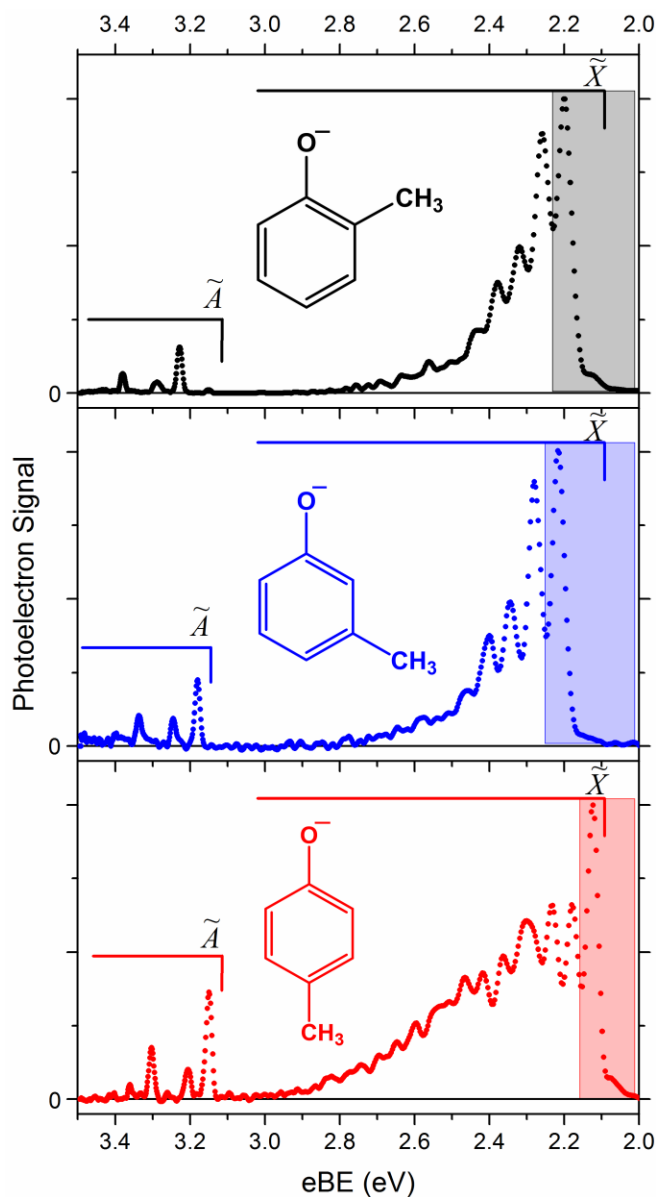


Fig. 3.1 The 355 nm photoelectron spectra of the three methylphenoxide anion isomers. These data were taken using the VMI photoelectron spectrometer. The \tilde{X} refers to the ground doublet electronic state, while the \tilde{A} refers to the first excited doublet electronic state of the corresponding neutral methylphenoxyl radicals. The data are reported as dots, with a line marking the baseline at zero. The shaded boxes indicate the energy range covered in Fig. 3.2.

In addition to the photoelectron spectra presented in Fig. 3.1, several additional spectra were collected on the continuous experiment and displayed in Fig. 3.2. Fig. 3.2 displays survey photoelectron spectra of all four products of the reaction of methylphenol with hydroxide made in the Flowing Afterglow (FA) ion source and collected with the hemispherical electron energy analyzer, utilizing 3.40814 eV photons. Note that due to the method by which hydroxide is generated in the FA source (reaction of O^- with methane gas), there is still some O^- present in the ion source region. This excess O^- is capable of both dehydrogenating (removal of H_2^+) and deprotonating the methylphenols, and a trace signal from this product channel is seen in the bottom panel of Fig. 3.2.

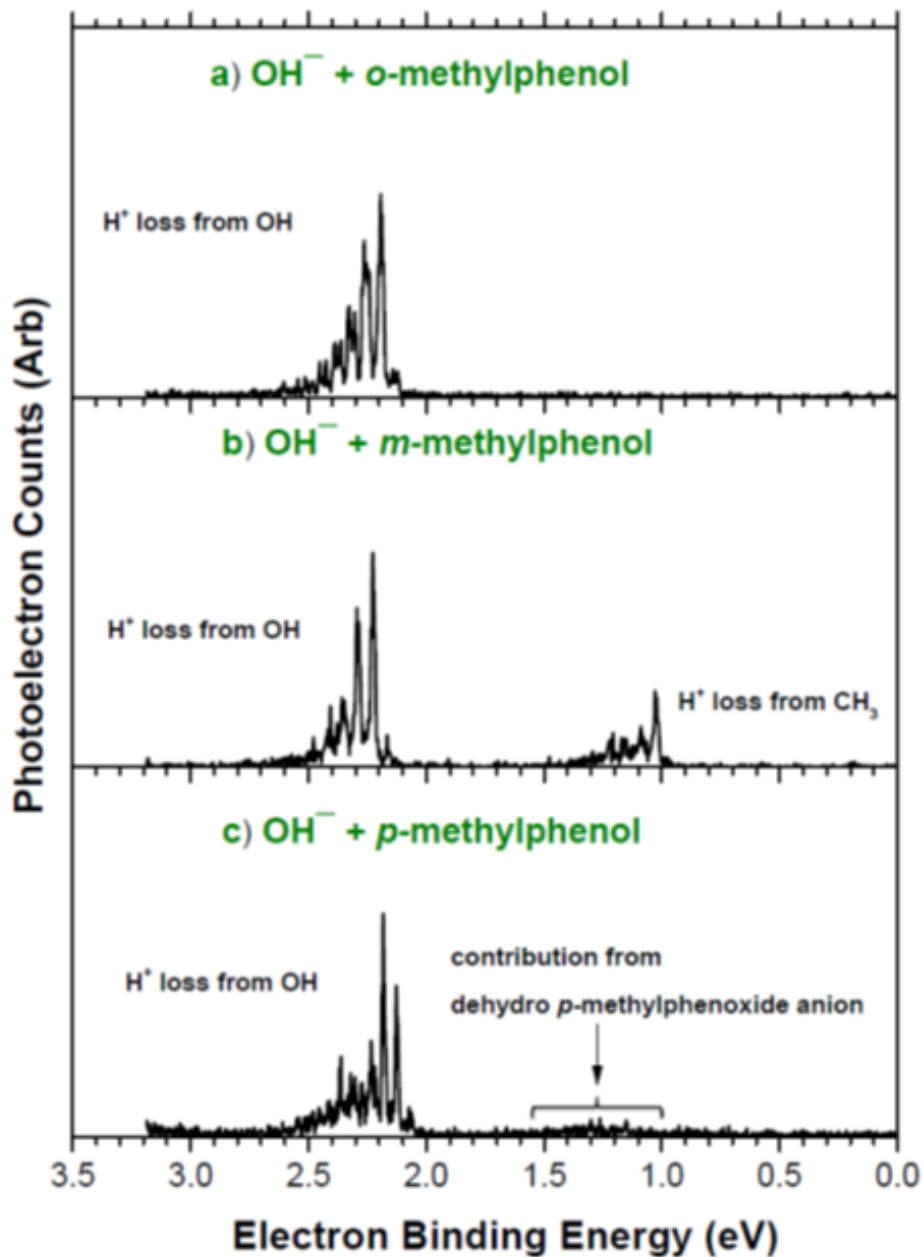


Fig 3.2 Photoelectron spectra of the products of methylphenol reacted with hydroxide in the flowing afterglow ion source obtained with a photon energy of 3.40814 eV and collected in a hemispherical energy analyzer. Note that there is a trace of O⁻ in this source which leads to a small signal from methylenephenoxide in the *para* case.

High resolution photoelectron spectra of the origin peaks for the transition to the neutral \tilde{X} state for each of the three methylphenoxide isomers were obtained using the SEVI technique (Fig. 3.3). In addition to measuring these portions of the spectra with increased resolution, the photoelectron spectra were also simulated and overlaid with experimental data. Considering the excellent agreement between the experiment and simulation, we report the EA of *o*-, *m*-, and *p*-methylphenoxyl as 2.1991 ± 0.0014 , 2.2177 ± 0.0014 , and 2.1199 ± 0.0014 eV, respectively (summarized in Table 3.2).

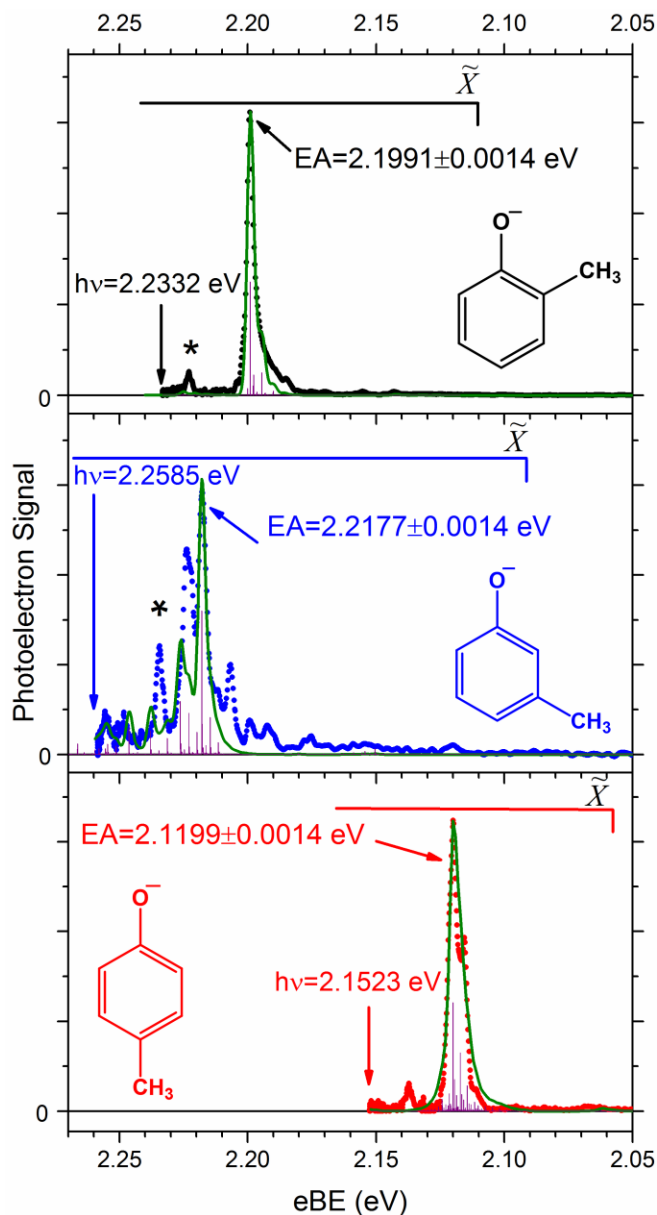


Fig. 3.3 The Slow Photoelectron Velocity-Map Imaging (SEVI) spectra of *o*-, *m*-, and *p*-methylphenoxide, allowing for the determination of the EAs of the corresponding methylphenoxyls. Experimental data are reported as dots, with a line marking the baseline at zero. Peaks labeled with an asterisk possibly represent the methyl hindered rotor vibrational transitions discussed in the text. Simulated Franck-Condon factors ($T = 150$ K) are shown as purple sticks and their convolution with the experimental resolution is shown in green. Note the x-axis only spans 220 meV, while Fig. 3.1 spanned 1.5 eV.

The transition to the neutral \tilde{A} state was investigated for all three isomers making use of 3.494 eV photons with the VMI spectrometer and shown in Fig. 3.4. The photoelectron spectra for this transition were simulated and overlaid with the experimental data, and again, these agree very well. Therefore, we can identify the electronic band origin of these progressions at 3.228 ± 0.009 , 3.180 ± 0.002 , and 3.149 ± 0.009 eV electron binding energy for *o*-, *m*-, and *p*-methylphenoxyl, respectively. Thus the term energy between the ground and first excited doublet electronic states of the neutral radicals are determined: 1.029 ± 0.009 , 0.962 ± 0.002 , and 1.029 ± 0.009 eV for *o*-, *m*-, and *p*-methylphenoxyl, respectively (summarized in Table 3.2). This energy is very similar to that in phenoxyl (1.06(5) eV),¹⁷ although the excited neutral state was not explored in detail in that study. Note that for the *ortho* and *para* isomers, a conservative error bar of 9 meV is used. This is based on the HWHM of the origin peak. However, the simulation suggests that for the *meta* isomer, less significant transitions are symmetrically distributed about the origin transition in peak A, suggesting that a smaller error bar of ± 0.002 eV is warranted.

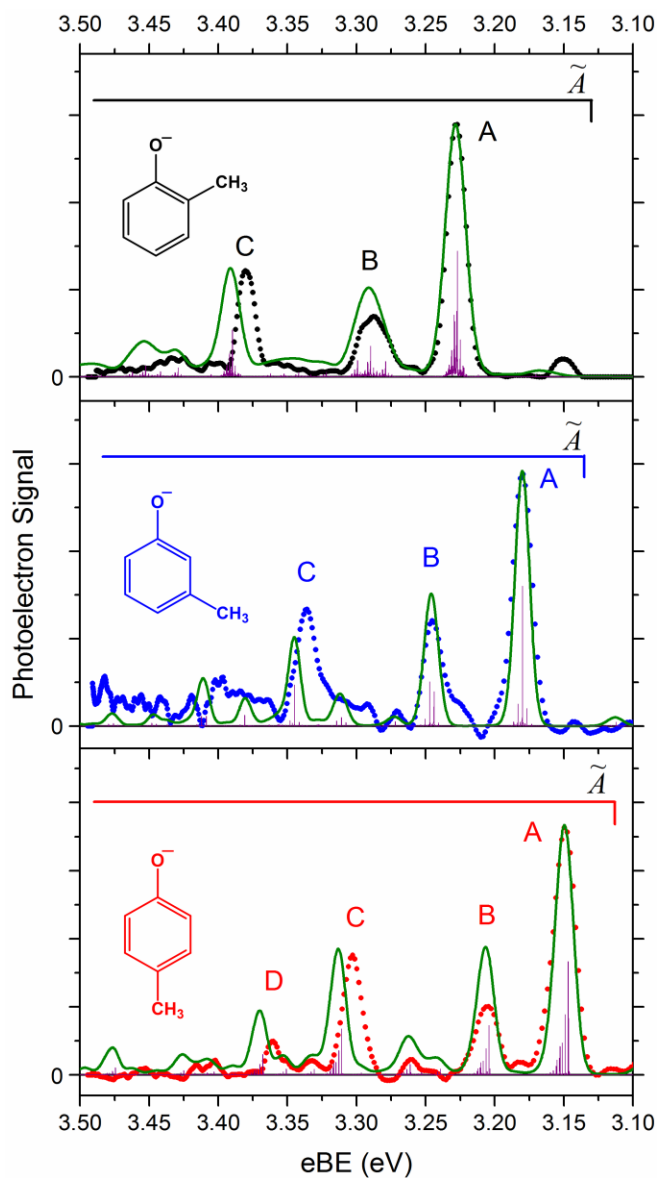
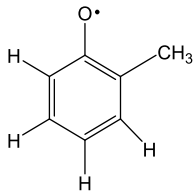
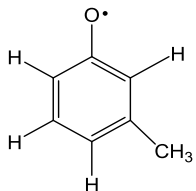
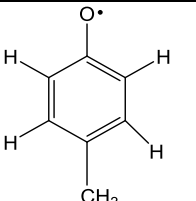


Fig. 3.4 The 355 nm anion photoelectron spectra of *o*-, *m*-, and *p*-methylphenoxide, examining the first excited doublet electronic states (\tilde{A}) of the methylphenoxyl radicals. Experimental data are shown as dots. Simulated Franck-Condon factors are shown as purple sticks and their convolution with the experimental resolution is shown in green.

Table 3.2. Summary of results. The SEVI technique was used to obtain the EAs of the three methylphenoxyl isomers. Combining these with the results from King *et al.*¹⁹ and Karsili *et al.*²⁰ allows for the determination of the gas phase acidities shown. The term energies determined in the current study for the methylphenoxyl radical $\tilde{A} \leftarrow \tilde{X}$ electronic transitions are also listed.

Deprotonated Methylphenol Isomer	EA (eV)	$D_{0,0K}$ (CH ₃ -PhO-H) (kcal/mol) ^a	$\Delta_{acid}H_{0K}^o$ (CH ₃ -PhO-H) (kcal/mol)	$\Delta_{acid}H_{298K}^o$ (CH ₃ -PhO-H) (kcal/mol) ^b	$T_0(\tilde{A} \leftarrow \tilde{X})$ (CH ₃ -PhO•) (eV)
	2.1991 ± 0.0014	<i>cis</i>	<i>cis</i>	<i>cis</i>	1.029 ±
		84.43 ± 0.14	347.31 ± 0.14	348.39 ± 0.25	0.009
	2.2177 ± 0.0014	<i>trans</i>	<i>trans</i>	<i>trans</i>	0.962 ±
		86.53 ± 0.14	348.98 ± 0.14	350.08 ± 0.25	0.002
	2.1199 ± 0.0014	83.83 ± 0.14	348.53 ± 0.14	349.60 ± 0.25	1.029 ± 0.009

^a Results from King *et al.*¹⁹ and Karsili *et al.*²⁰

^b Obtained from the 0 K experimental results and calculated C_p values at the B3LYP/aug-cc-pVQZ level. The increased error from the 0 K results is due to uncertainty in the calculated heat capacities.

In addition to the electron affinities, photoelectron angular distributions with respect to the laser polarization, characterized by the anisotropy parameter (β), were measured for these photoelectron spectra.⁴ Since the electron is being detached from what can be described as an oxygen p-like orbital, it is expected that we should observe a negative β . Photodetachment forming the neutral \tilde{X} state shows the same photoelectron anisotropy for the three isomers, $\beta \sim -0.3$, using 3.494 or 3.408 eV photons. This was also measured for the methylenephenol anion, and is approximately the same as for the methylphenoxides, $\beta \sim -0.3$. The photoelectron angular distributions resulting from photodetachment to form the neutral \tilde{A} state for all three isomers were isotropic ($\beta \sim 0$). However, these transitions are all close in binding energy (< 400 meV) to the photon energy used to examine them, and so an isotropic angular distribution is expected.²¹

§ 3.6 Vibrational Analysis: *ortho*-Methylphenoxy

The vibrational progression in the *o*-methylphenoxide photoelectron spectrum resulting from the transition to the *o*-methylphenoxy radical \tilde{X} state was studied in the hemispherical analyzer and is shown in Fig. 3.5 and with the VMI PE spectrometer with lower resolution in Fig. 3.6. Focusing on Fig. 3.5, it is evident that there is a progression resulting from exciting ring distortion vibrational modes, as the dominant peaks observed are spaced by approximately 500 cm^{-1} , as expected. All of the observed peaks are broader than the instrument resolution, implying that each peak is comprised of multiple overlapping transitions. Nonetheless, the partially resolved peak doublet labeled B and C may be fit to two Gaussian functions, and their positions relative to the band origin are 434 ± 8 and $542 \pm 8 \text{ cm}^{-1}$, respectively. While all of the peaks with larger binding energy than C are predicted to be due to multiple transitions and are beyond the ability of either instrument to resolve, peaks B and C are predicted to be primarily due to only a few transitions. Peak B is predicted to be due to a transition from the ground vibrational state of the anion to one quanta in a ring distortion vibrational mode in the neutral ($33_0^1 = 430 \pm 80 \text{ cm}^{-1}$), which has a calculated harmonic frequency of 453 cm^{-1} . Peak C is due to two transitions, each starting in the ground vibrational state of the anion and going to one quanta in two different ring distortion vibrational modes of the neutral molecule ($30_0^1, 31_0^1 = 540 \pm 80 \text{ cm}^{-1}$). These two modes are calculated to have harmonic frequencies of 540 and 577 cm^{-1} . The hindered methyl rotor vibrational mode was possibly resolved for *o*-methylphenoxy, seen in Fig. 3.3, indicated with an asterisk, and located $196 \pm 8 \text{ cm}^{-1}$ relative to the origin. This peak is likely due to a transition from the ground vibrational state in the anion to two quanta in the hindered methyl rotor vibration in the neutral state, $39_0^2 = 196 \pm 16 \text{ cm}^{-1}$. Neglecting anharmonicity, $39_0^1 = 98 \pm 8 \text{ cm}^{-1}$ is derived, which compares well with the calculated harmonic frequency of 106 cm^{-1} .

However, due to the inherent complexity of hindered rotor vibrations, a harmonic approximation is likely not valid, and so this assignment, while plausible, is only suggested.

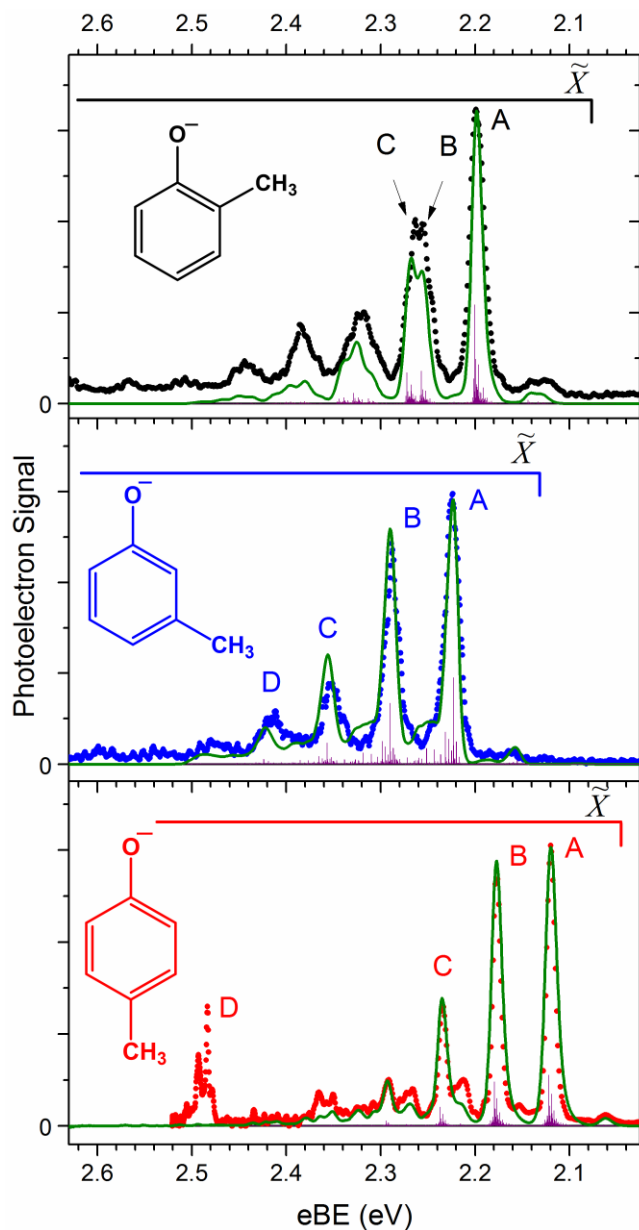


Fig. 3.5. The anion photoelectron spectra of *o*-, *m*-, and *p*-methylphenoxide, examining the ground doublet electronic states of the methylphenoxyls. Experimental data are displayed as dots. The top two panels were obtained with a photon energy of 3.40814 eV using a hemispherical energy analyzer, while the bottom panel was collected using a VMI spectrometer with a photon energy of 2.520 eV. Simulated Franck-Condon factors are shown as purple sticks and their convolution with the experimental resolution is shown in green.

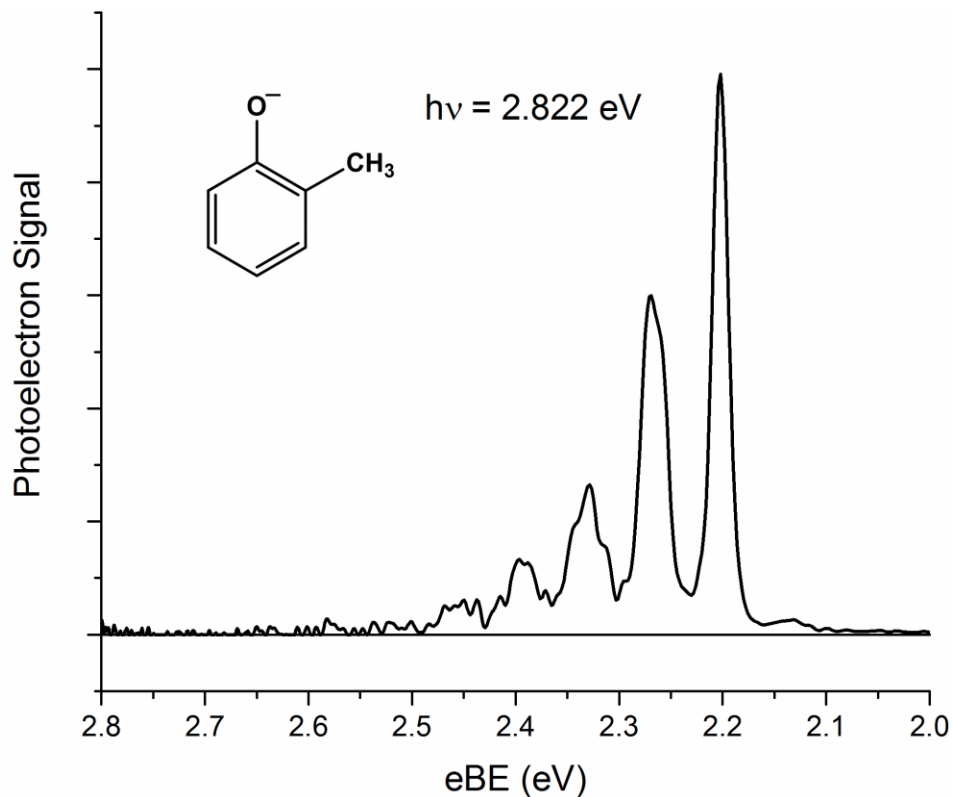


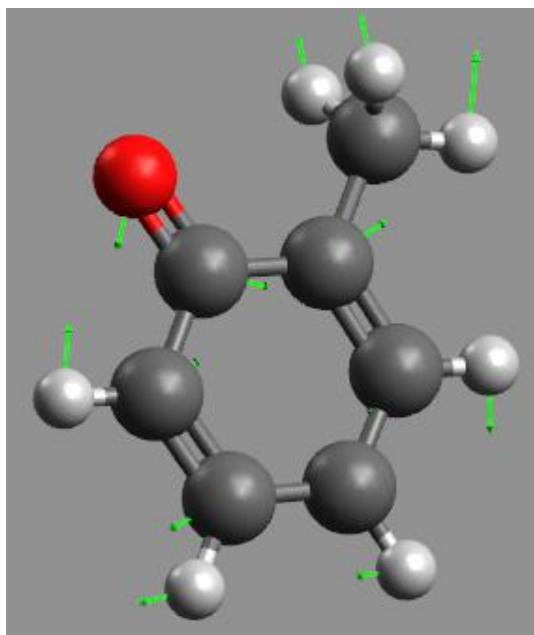
Fig. 3.6 Photoelectron spectrum of *ortho*-methylphenoxide taken with a photon energy of 2.822 eV, utilizing the VMI photoelectron spectrometer. Only experimental data are shown. The peak intensities in this spectrum are consistent with those shown in the top panel of Fig. 3.4 which were taken using the hemispherical analyzer.

The vibrational progression resulting from the transition to the excited electronic \tilde{A} state of the *o*-methylphenoxyl radical can be seen in Fig. 3.4. None of the peaks observed in the spectrum are resolution limited, which again indicates that there are multiple transitions contributing to each peak. The photoelectron spectrum was simulated and reproduces the experiment with excellent agreement. Peak A is assigned as the band origin, with peaks B and C being located $483 \pm 16 \text{ cm}^{-1}$ and $1225 \pm 16 \text{ cm}^{-1}$ higher in binding energy, respectively. While there are several predicted transitions with significant FC factors attributed to peak B, the peak intensity and position is primarily due to a transition from the anion vibrational ground state to one quanta in a ring distortion vibrational mode in the neutral \tilde{A} state, $32_0^1 = 480 \pm 190 \text{ cm}^{-1}$, predicted to have a harmonic frequency of 506 cm^{-1} . Peak C is similarly broadened past the instrument resolution, but its dominant contributor (based on FC factor intensity) is predicted to be due to a transition from the anion vibrational ground state to a single quanta in a quasi C–O stretching mode in the neutral \tilde{A} state, $15_0^1 = 1220 \pm 130 \text{ cm}^{-1}$, predicted to have a harmonic frequency of 1312 cm^{-1} .

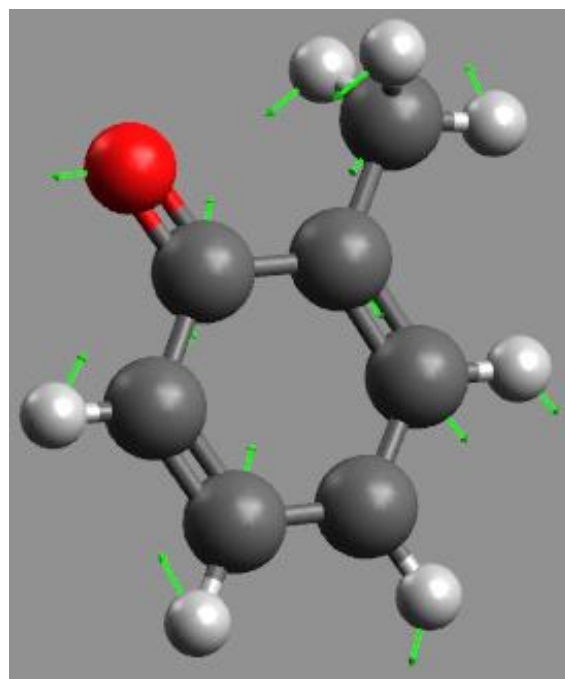
The normal mode eigenvectors of the vibrational states which are activated upon photodetachment of *o*-methylphenoxide are depicted in Table 3.3.

Table 3.3 The following diagrams show the primary Franck-Condon active normal modes of *o*-methylphenoxide. Each eigenvector shown here is that of the neutral radical, and was calculated at the B3LYP/aug-cc-pVQZ level of theory. The listed frequencies are theoretical and harmonic.

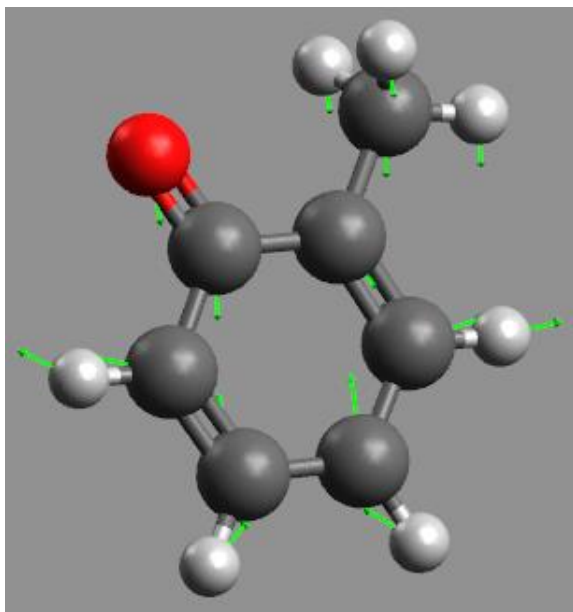
Ortho-methylphenoxy radical (\tilde{X} state)



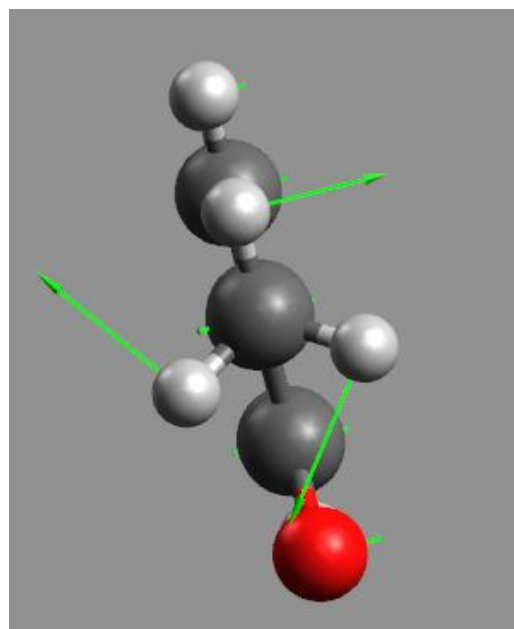
ν_{33} (453 cm^{-1})



ν_{31} (540 cm^{-1})

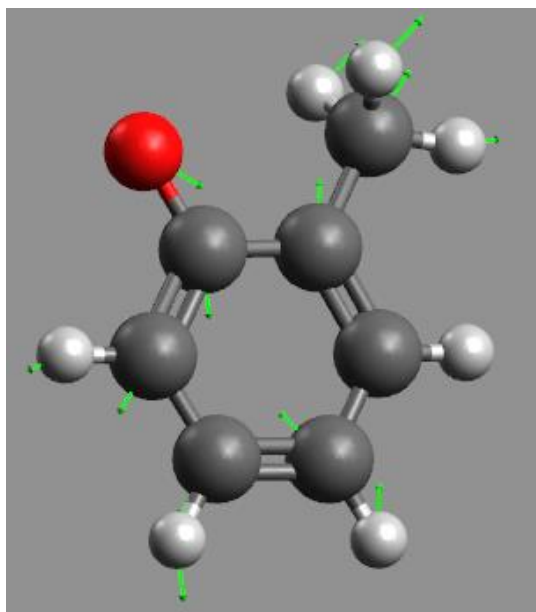


ν_{30} (577 cm^{-1})

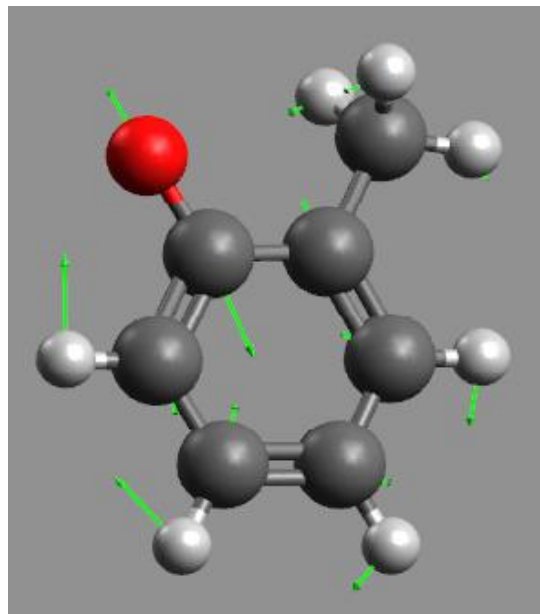


ν_{39} (106 cm^{-1})

Ortho-methylphenoxy radical (\tilde{A} state)



ν_{32} (506 cm^{-1})



ν_{15} (1312 cm^{-1})

§ 3.7 Vibrational Analysis: *meta*-Methylphenoxyl

The vibrational progression in the *m*-methylphenoxide photoelectron spectrum resulting from detachment to the *m*-methylphenoxyl radical \tilde{X} state was studied in the continuous experiment (see Fig. 3.5) and in the pulsed experiment (Fig. 3.7). As with the *ortho* isomer, a progression spaced by approximately 500 cm^{-1} is observed for the *meta* isomer, once again suggesting that ring distortion modes are excited upon photodetachment of the anion. Assuming that peaks B–D in Fig. 3.5 are due to only one mode, these peaks are due to transitions from the ground anionic state to 1, 2, or 3 quanta of a single vibrational mode in the neutral state, with peak locations (relative to the EA) of $564 \pm 8\text{ cm}^{-1}$, $1079 \pm 8\text{ cm}^{-1}$, and $1587 \pm 8\text{ cm}^{-1}$ for peaks B, C, and D, respectively. These correspond to the following transitions: $31_0^1 = 560 \pm 50\text{ cm}^{-1}$, $31_0^2 = 1080 \pm 64\text{ cm}^{-1}$, $31_0^3 = 1590 \pm 90\text{ cm}^{-1}$. The simulated spectrum (overlaid) agrees well with the experiment and confirms that this vibrational progression is primarily due to transitions from the ground anionic state to excitation in a ring distortion vibrational mode in the neutral state with a calculated harmonic frequency of 540 cm^{-1} , agreeing with the experimentally measured $31_0^1 = 560 \pm 50\text{ cm}^{-1}$ transition. The hindered methyl rotor vibrational mode was also likely measured for *m*-methylphenoxyl (Fig. 3.3, designated with an asterisk, located at $134 \pm 8\text{ cm}^{-1}$ relative to the origin). This peak is possibly due to a transition from the ground vibrational state in the anion to two quanta in the hindered methyl rotor, $39_0^2 = 135 \pm 16\text{ cm}^{-1}$. This allows for a determination of the methyl hindered rotation vibrational frequency, assuming no anharmonicity, $39_0^1 = 67 \pm 8\text{ cm}^{-1}$, compared with the calculated harmonic frequency of 81 cm^{-1} . Again, this assignment is only suggested, due to the anharmonicity of hindered rotor vibrations.

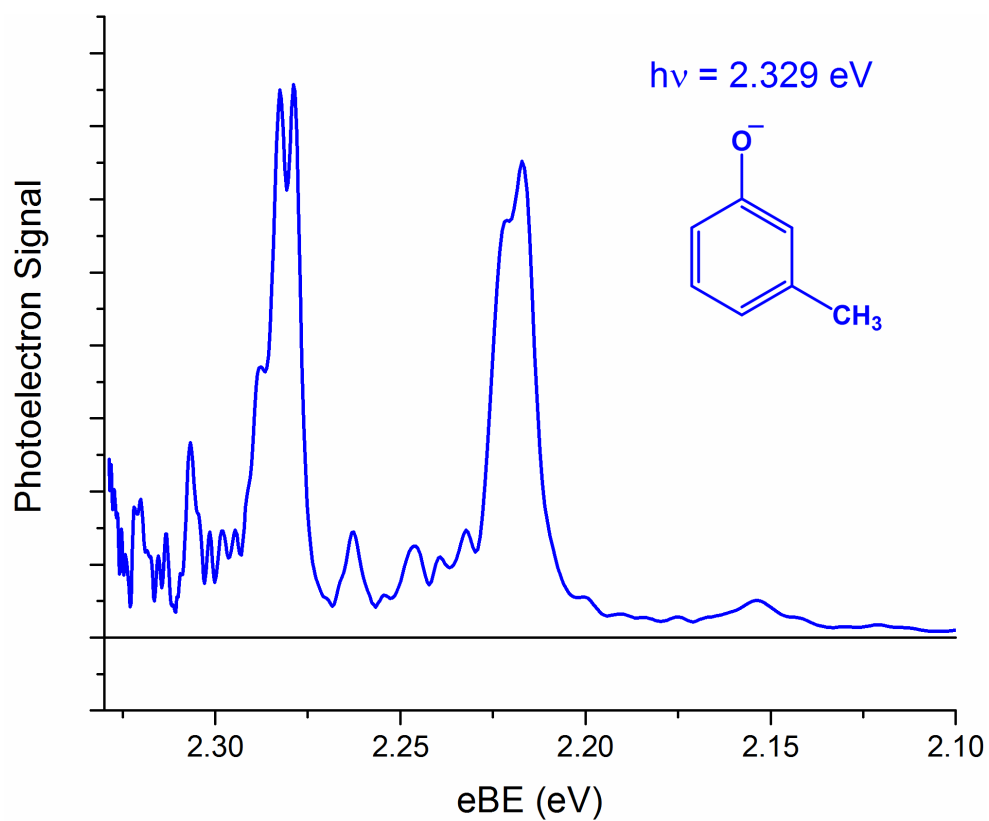


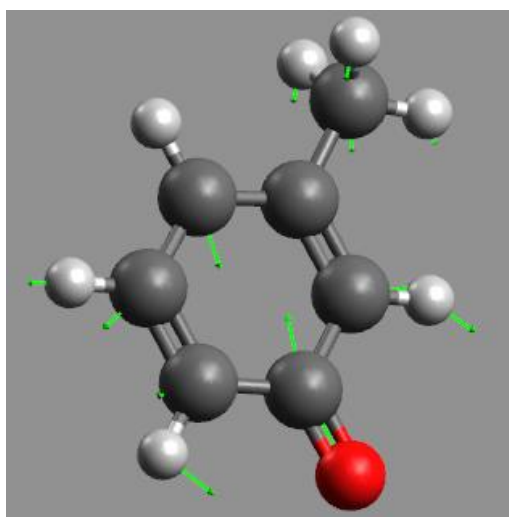
Fig. 3.7 The photoelectron spectrum of *meta*-methylphenoxide taken on the VMI spectrometer with a photon energy of 2.329 eV.

The photoelectron spectrum vibrational progression observed for the transition to the excited \tilde{A} state of the *m*-methylphenoxyl radical can be seen in Fig. 3.4, overlaid with the simulated spectrum. Peak A is assigned as the band origin, with peaks B and C located 523 ± 8 cm^{-1} and 1260 ± 8 cm^{-1} higher in binding energy, relative to peak A. According to the simulation, peak B has many contributing transitions, broadening it past instrument resolution, but it is primarily due to two transitions from the anionic ground vibronic state to one quanta in either of two ring distortion vibrational modes in the neutral \tilde{A} state, 31_0^1 , $32_0^1 = 520 \pm 96$ cm^{-1} , predicted to have harmonic frequencies of 516 and 542 cm^{-1} . These peaks cannot be resolved due to our instrument resolution. Peak C is similarly broadened past instrument resolution and is predicted to be primarily due to a transition from the anionic ground state to a single quanta in a quasi O–C stretching mode in the neutral \tilde{A} state, $15_0^1 = 1260 \pm 90$ cm^{-1} , which has a calculated harmonic frequency of 1330 cm^{-1} .

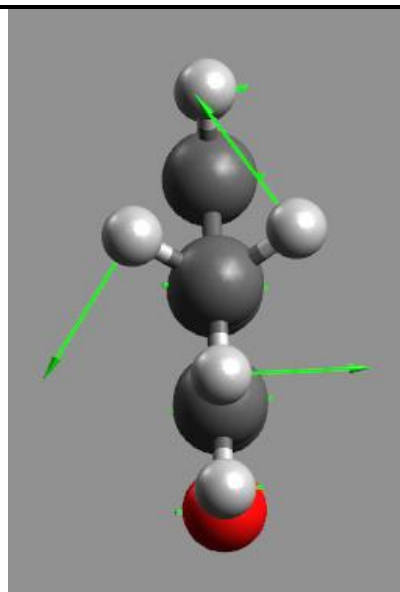
The normal mode eigenvectors of the vibrational states which are activated upon photodetachment of *m*-methylphenoxide are depicted in Table 3.4.

Table 3.4 The following diagrams show the primary Franck-Condon active normal modes of *m*-methylphenoxide. Each eigenvector shown here is that of the neutral radical, and was calculated at the B3LYP/aug-cc-pVQZ level of theory. The listed frequencies are theoretical and harmonic.

Meta-methylphenoxyl radical (\tilde{X} state)

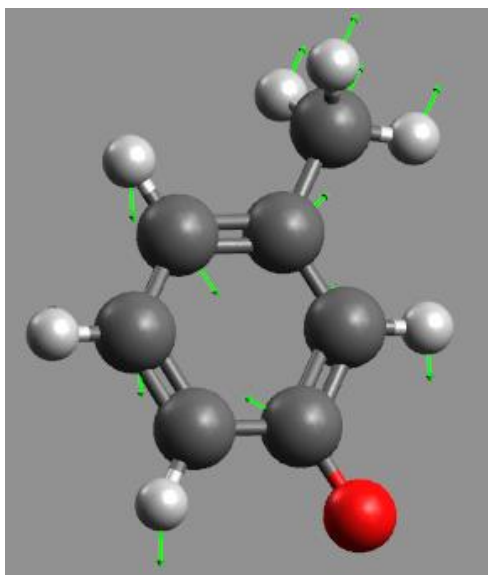


ν_{31} (540 cm^{-1})

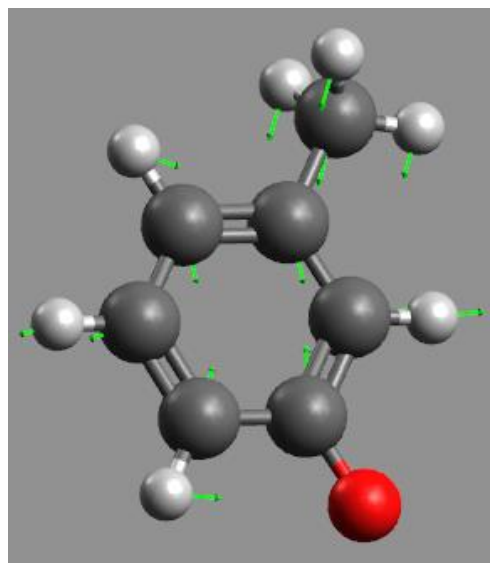


ν_{39} (81 cm^{-1})

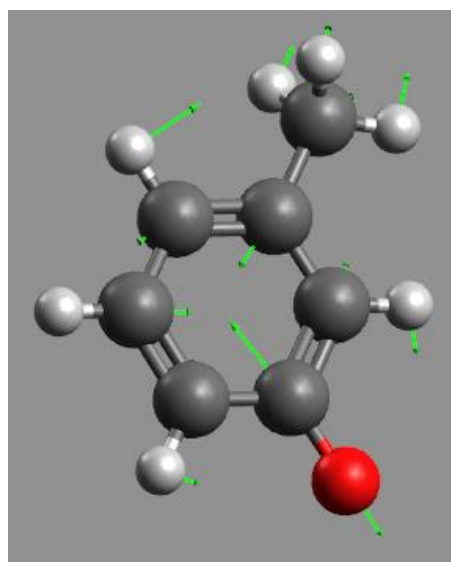
Meta-methylphenoxy radical (\tilde{A} state)



ν_{32} (516 cm^{-1})



ν_{31} (542 cm^{-1})



ν_{15} (1330 cm^{-1})

§ 3.8 Vibrational Analysis: *para*-Methylphenoxyl

The photoelectron spectrum of *p*-methylphenoxide, accessing the neutral \tilde{X} state, was studied in the VMI spectrometer with a photon energy of 2.520 eV, Fig. 3.5. Peak A is assigned as the band origin. Peaks B and C, located at $460 \pm 8 \text{ cm}^{-1}$ and $921 \pm 8 \text{ cm}^{-1}$ relative to the origin, suggest a vibrational progression arising from transitions from the ground state of the anion to the *p*-methylphenoxyl ground state with one or two quanta (for peaks B and C) in a ring distortion vibrational mode in the neutral radical, $32_0^1 = 460 \pm 40 \text{ cm}^{-1}$ and $32_0^2 = 920 \pm 40 \text{ cm}^{-1}$. The simulated spectrum agrees with the measured transition, and predicts this ring distortion harmonic frequency to be 463 cm^{-1} . There is one notable disagreement with theory that may be seen in this spectrum, located at $\sim 2.5 \text{ eV}$ binding energy and labeled D. Peak D contains 3 separate peaks at 2893 ± 8 , 2931 ± 8 , and $3006 \pm 8 \text{ cm}^{-1}$, relative to peak A. These are reasonable frequencies for C-H stretching modes in the radical, but their intensities are not recovered in the simulation. It should be noted that due to the nature of the variable resolution of the VMI and the location of the peaks being close to the photon energy, the peak amplitudes exaggerate the perceived importance of these transitions. In fact, the integrated intensity of these peaks are approximately equal to half the intensity of peak C.

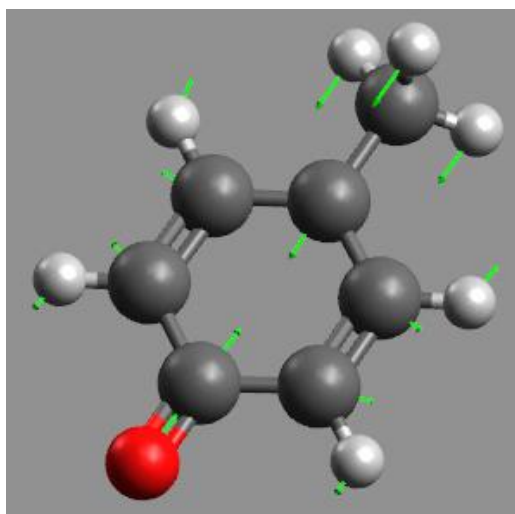
The *p*-methylphenoxide photoelectron spectrum accessing the neutral excited \tilde{A} state is shown in Fig. 3.4, and overlaid with the simulated spectrum. Peak A is the band origin. Peak B, located $459 \pm 8 \text{ cm}^{-1}$ from the origin, corresponds to the transition from the anionic vibrational ground state to one quanta in a ring distortion vibrational mode in the neutral \tilde{A} state, $32_0^1 = 460 \pm 80 \text{ cm}^{-1}$, with a predicted harmonic vibrational frequency of 461 cm^{-1} . Peak C, located at $1239 \pm 8 \text{ cm}^{-1}$ relative to the origin, is assigned to a transition from the anionic ground vibrational state to one quanta in a quasi C–O stretch vibrational mode, $15_0^1 = 1240 \pm 90 \text{ cm}^{-1}$, in the neutral \tilde{A}

state with a calculated fundamental vibrational frequency of 1320 cm^{-1} . Finally peak D, located at $1703 \pm 80\text{ cm}^{-1}$, relative to peak A, is assigned to a combination band, $15_0^1 32_0^1 = 1700 \pm 90\text{ cm}^{-1}$.

The normal mode eigenvectors of the vibrational states which are activated upon photodetachment of *p*-methylphenoxide are depicted in Table 3.5.

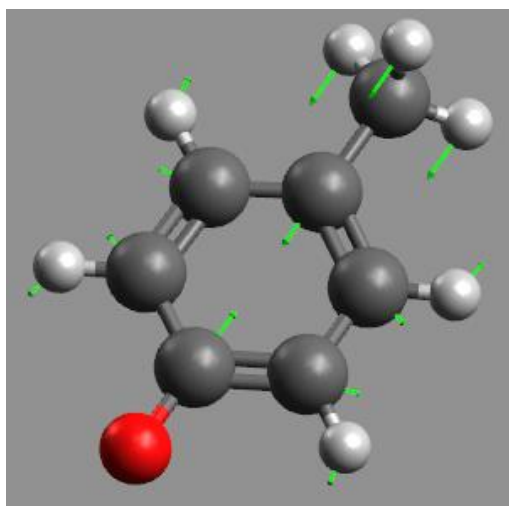
Table 3.5 The following diagrams show the primary Franck-Condon active normal modes of *p*-methylphenoxide. Each eigenvector shown here is that of the neutral molecule, and was calculated at the B3LYP/aug-cc-pVQZ level of theory. The listed frequencies are theoretical and harmonic.

Para-methylphenoxyl radical (\tilde{X} state)

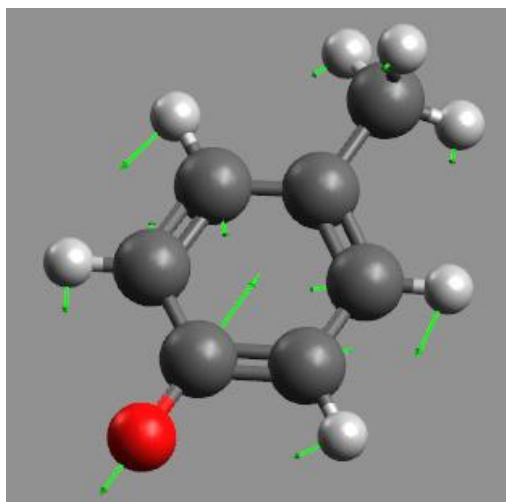


ν_{32} (463 cm^{-1})

Para-methylphenoxyl radical (\tilde{A} state)



ν_{32} (461 cm^{-1})



ν_{15} (1320 cm^{-1})

§ 3.9 CH₃ Deprotonated *meta*-Methylphenol

The *meta* isomer of methylphenol behaves differently from the other isomers in its chemical reactivity. While the other isomers only show evidence of deprotonation at the alcohol group, the *meta* isomer displays deprotonation at the methyl group as well. The photoelectron spectrum of methyl deprotonated *m*-methylphenol is shown in Fig. 3.8, with the simulated spectrum overlaid. While the agreement between the experiment and the simulation is clear, there is more broadening than predicted. The dominant peaks in the spectrum are spaced by ~ 500 cm⁻¹, again indicating that there is significant vibrational activity in ring distortion vibrational modes in the neutral radical. Peak A, the band origin, arises from the transition from the ground vibronic state of the anion to the ground vibronic state of the neutral. As such, the EA of *m*-methylenephenol is 1.024 ± 0.008 eV. Peak B is located 513 ± 8 cm⁻¹ higher in binding energy relative to peak A. The simulation predicts that peak B is mainly due to vibrational transitions from the anionic ground state to one quanta in either of two modes, 31_0^1 , $30_0^1 = 510 \pm 110$ cm⁻¹, with predicted harmonic frequencies of 525 and 547 cm⁻¹. However, due to our resolution, we could not resolve these. Our calculations show that the CH₂ and OH groups lie in the plane of the ring for both anion and neutral states, and thus excitations of CH₂ umbrella modes or OH internal rotations are neither expected nor observed.

The normal mode eigenvectors of the vibrational states which are activated upon photodetachment of the *m*-methylenephenol anion are depicted in Table 3.6.

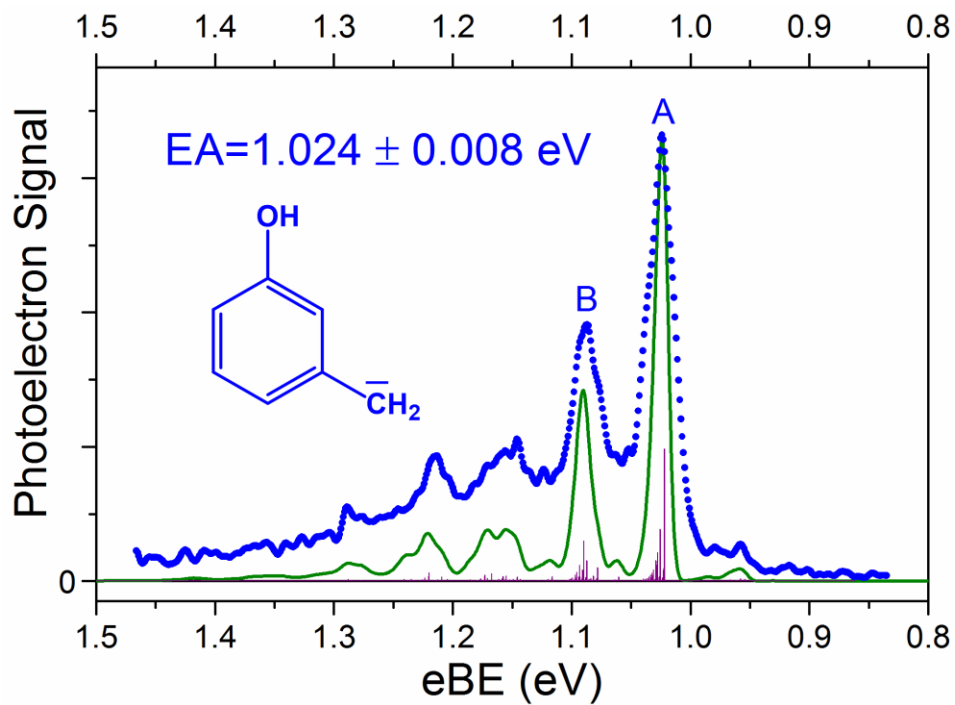
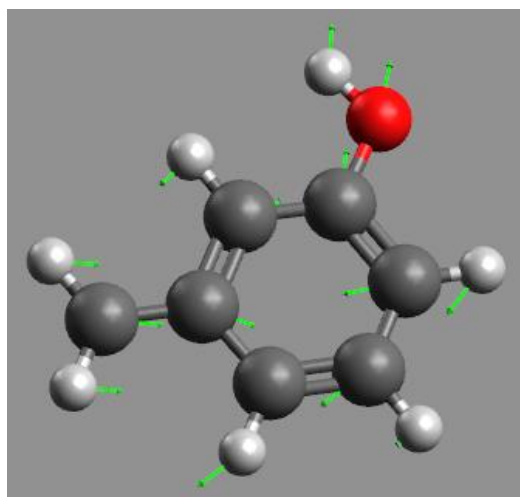


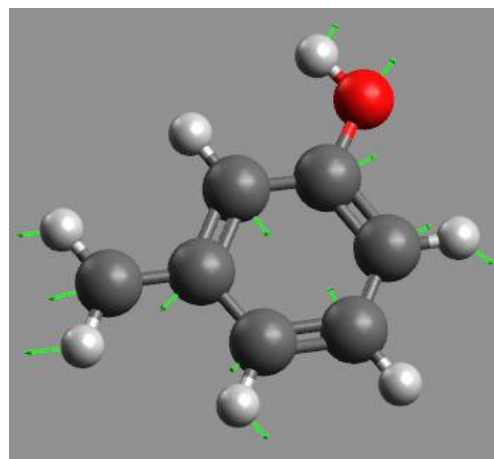
Fig. 3.8. Photoelectron spectrum of methyl deprotonated *meta*-methylphenol, taken with a photon energy of 3.408 eV and collected with a hemispherical energy analyzer. Experimental data are plotted with dots, the calculated Franck-Condon factors are shown as purple sticks, and the stick spectra convoluted with the experimental resolution is shown in green.

Table 3.6 The following diagrams show the primary Franck-Condon active normal modes of *m*-methylenephenol. Each eigenvector shown here is that of the neutral molecule, and was calculated at the B3LYP/aug-cc-pVQZ level of theory. The listed frequencies are theoretical and harmonic.

Meta-methylenephenol (\tilde{X} state)



ν_{31} (525 cm^{-1})



ν_{30} (547 cm^{-1})

A summary of all the vibrational analysis results may be found in Table 3.7.

Table 3.7 The experimentally measured frequencies of the Franck-Condon active normal modes for the doublet ground (\tilde{X}) and first excited (\tilde{A}) states of the three methylphenoxyl radicals. The calculated (B3LYP/aug-cc-pVQZ) harmonic frequencies are listed in parentheses below the measured frequency. All values are in cm^{-1} .

<i>o</i> -Methylphenoxyl Radical	<i>m</i> -Methylphenoxyl Radical	<i>p</i> -Methylphenoxyl Radical
\tilde{X} state	\tilde{X} state	\tilde{X} state
$\nu_{30} = 540 \pm 80$ (577)	$\nu_{31} = 560 \pm 50$ (540)	$\nu_{32} = 460 \pm 40$ (461)
$\nu_{31} = 540 \pm 80$ (540)	$\nu_{39} = 66 \pm 8$ (81)	
$\nu_{33} = 430 \pm 80$ (453)		
$\nu_{39} = 98 \pm 8$ (106)		
\tilde{A} state	\tilde{A} state	\tilde{A} state
$\nu_{15} = 1220 \pm 130$ (1312)	$\nu_{15} = 1260 \pm 90$ (1330)	$\nu_{15} = 1240 \pm 90$ (1320)
$\nu_{32} = 480 \pm 190$ (506)	$\nu_{31} = 520 \pm 96$ (542)	$\nu_{32} = 460 \pm 80$ (461)
	$\nu_{32} = 520 \pm 96$ (516)	

§ 3.10 Photon Energy Dependence of the *para*-Methylphenoxide Photoelectron Spectra

The photoelectron spectrum of *p*-methylphenoxide was first obtained using the fixed frequency (364 nm, 3.408 eV) spectrometer. The simulated spectrum did not reproduce the relative intensity of the first three peaks in the experimental photoelectron spectrum as well as we would normally expect; additionally, empirically adjusting bond lengths and angles did not improve the comparison. Consequently, the VMI instrument, which utilizes a tunable light source, was employed to reinvestigate the photoelectron spectrum of *p*-methylphenoxide at a number of photon energies above and below 3.408 eV, and these spectra are shown in Fig. 3.9. The photon energies employed spanned from 3.494 eV (panel **A**) to 2.520 eV (panel **D**). The experimental photoelectron spectra show substantial variations over this range of photon energies. An additional two photon energies were used during this investigation and are reported in Fig. 3.10.

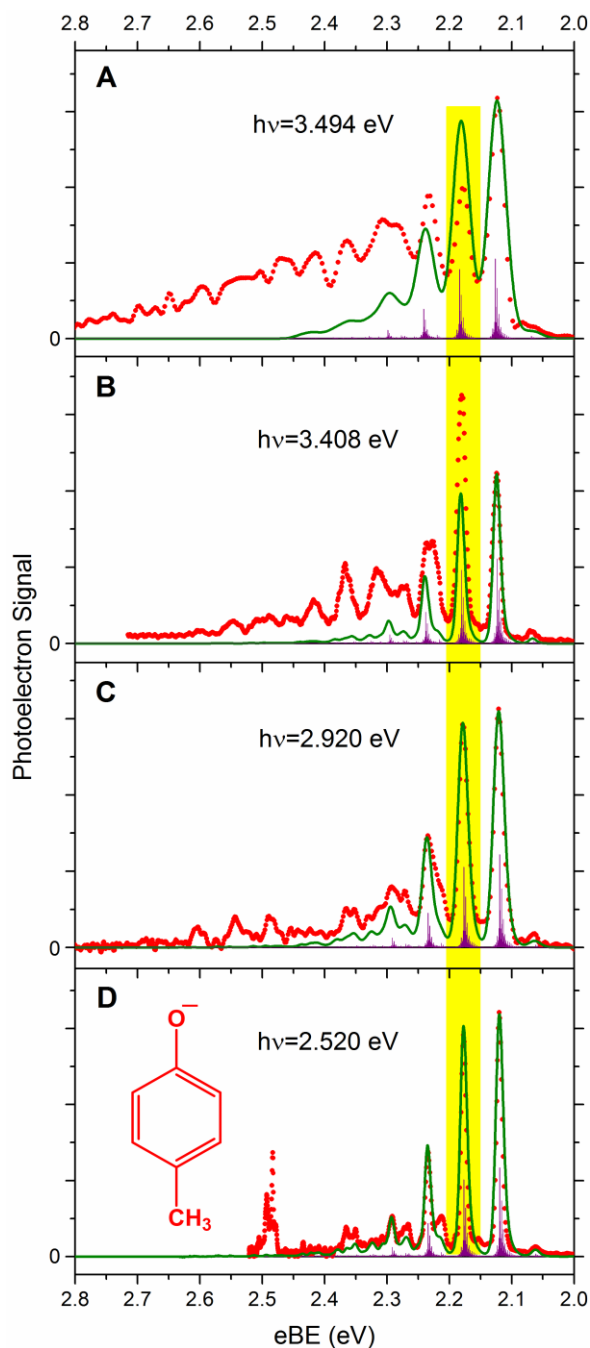


Fig. 3.9 Photoelectron spectra of *p*-methylphenoxide taken at a variety of photon energies, displaying a photon energy dependence as discussed further in the text. Data in panels **A**, **C**, and **D** ($h\nu = 3.494$ eV, 2.920 eV, and 2.520 eV) are obtained with a VMI spectrometer, while panel **B** ($h\nu = 3.408$ eV) was collected with a hemispherical energy analyzer. Experimental data are shown as dots, while calculated Franck-Condon factors are shown as purple sticks and their convolution with experimental resolution shown in green. The highlighted peaks emphasize the intensity dependence on photon energy and are attributed to autodetachment, which is discussed further in the text.

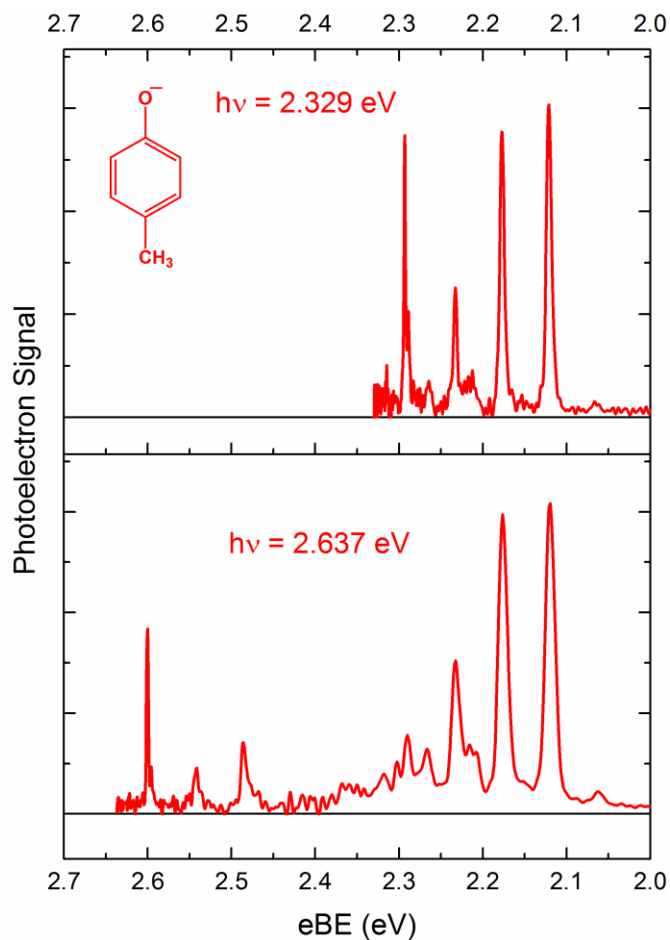


Fig. 3.10 Photoelectron spectra of *para*-methylphenoxide obtained with the VMI spectrometer with photon energies of 2.329 eV and 2.637 eV for the top and bottom panels respectively. Note how the changing resolution can cause peaks close to the photon energy to appear more dominant due to their narrowing FWHM and corresponding increase in amplitude to conserve the transition integrated intensity.

An important assumption for all of the calculated photoelectron spectra simulations reported here is that the electronic contribution to the overall photodetachment cross section is essentially constant over the photon energy range corresponding to the width of the vibronic envelope; in this limit, the relative intensities of the vibronic transitions are well-represented by the calculated Franck-Condon factors (§ 1.1). This assumption means that the simulated photoelectron spectrum should not depend on photon energy. Thus the photoelectron spectra simulations (solid green lines) plotted in all four panels of Fig. 3.9 differ only in the convolution of the Franck-Condon factors to reflect the changing experimental resolution with photoelectron kinetic energy. The experimental data in Fig. 3.9, however, show a significant photon energy dependence of the *p*-methylphenoxide photoelectron spectrum, which cannot be justified by the changing experimental resolution. While there is good agreement between the experiment and the photoelectron simulation at the lowest photon energy (panel **D**), theory and experiment fall further out of agreement as the photon energy increases. As the photon energy is increased, there are several peaks which change intensity relative to the origin peak, and there is an appearance of a broad continuum under the spectrum in the top panel. For example, the highlighted peak in Fig. 3.9 changes intensity relative to its neighboring peaks with different photon energies. This behavior arises from electron autodetachment, a multistep process whereby the anion absorbs a photon to an excited *anionic* state which lies above the electron detachment threshold, and subsequently transfers to the *neutral* ground electronic state, ejecting an electron in the process. TD-DFT calculations predict eight optically accessible anion excited electronic states between 1.9 and 3.3 eV above the ground anion state, and thus it is outside the scope of this work to further pursue a theoretical modeling of these spectra. In the current study, *m*-methylphenoxide also displayed evidence of autodetachment, but at a greater photon energy (3.832 eV obtained

via doubling the output of a dye laser utilizing DCM dye) than *p*-methylphenoxide. See Fig. 3.11. Observing autodetachment from *o*-methylphenoxide was not pursued in this work, but likely exists as well. This will be discussed in greater detail in the following section.

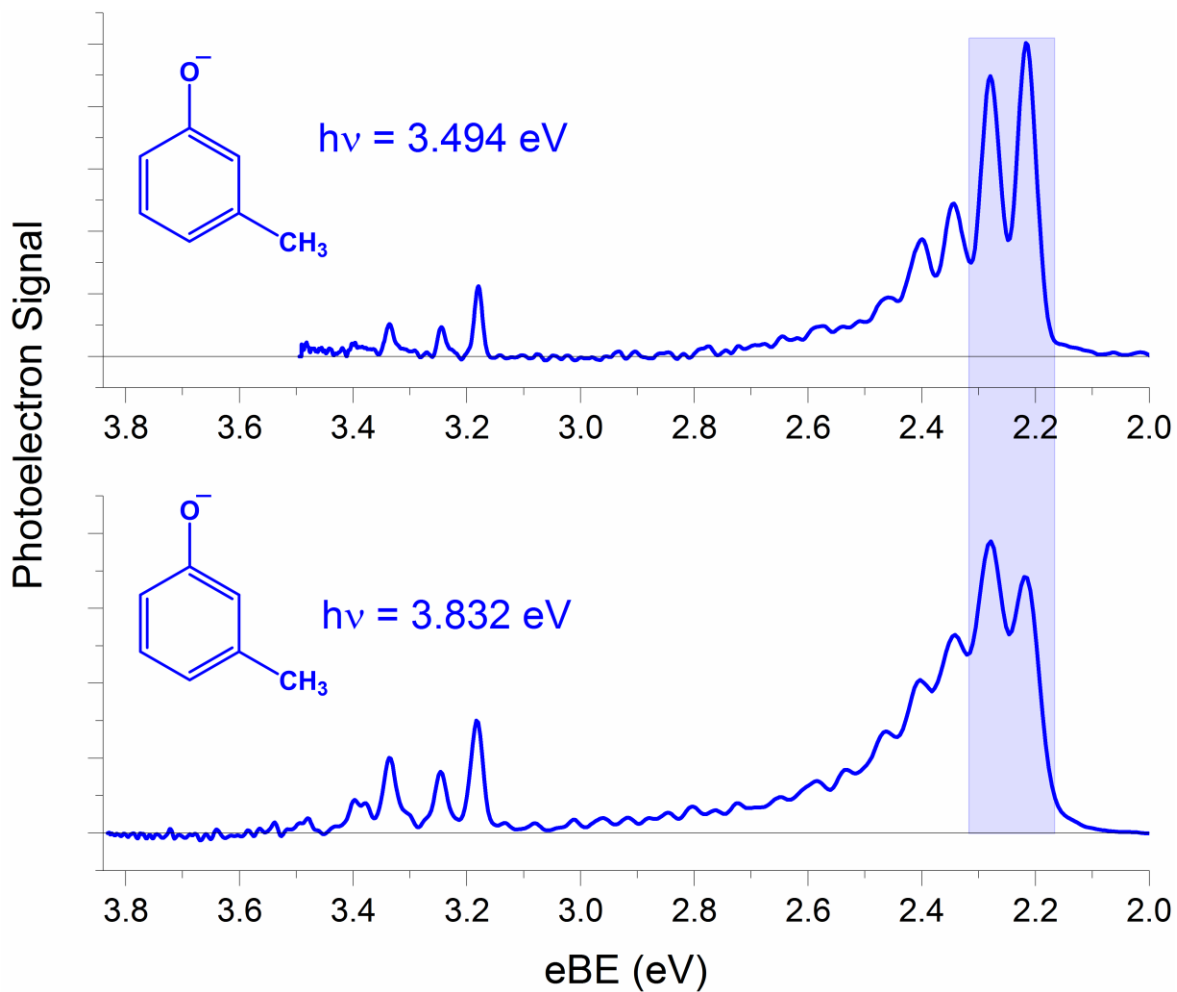


Fig. 3.11 The photoelectron spectrum of *meta*-methylphenoxide taken on the VMI spectrometer with photon energies of 3.494 eV and 3.832 eV. Only experimental data are shown. The highlighted region demonstrates the photon energy dependence of the peak intensities characteristic of autodetachment.

§ 3.11 Discussion

The photoelectron spectra of methyl deprotonated *m*-methylphenol and *o*-, *m*-, and *p*-methylphenoxide have been presented. In the following discussion, the electron affinities and active vibrational modes of the corresponding neutral radicals will be compared with other substituted aromatic radicals, *e.g.* halobenzyl, phenoxy, and benzyl radicals. In addition, the autodetachment behavior of the methylphenoxides studied in this work will be discussed and compared with previous work on phenoxide. Finally, we combine the experimental EAs with the methylphenol O–H bond dissociation energies^{19, 20} to derive the gas phase acidity of the three methylphenols.

The electron affinities of the three methylphenoxy isomers are all close to 2.2 eV, while the *meta* isomer has the largest EA, and the *para* has the smallest (see Table 3.2). This ordering can be readily rationalized using resonance stabilization and aromaticity concepts: the *meta* isomer does not benefit from resonance stabilization of the neutral radical, whereas the *ortho* and *para* isomers do. In the neutral *meta* form, the electron donating group (CH₃) cannot donate charge to the strongly electron withdrawing O radical group, hence raising its energy relative to that of the other neutral isomers. For all three isomers, the anionic form is closed shell and would be minimally perturbed by resonance stabilization since there is a formal negative charge on O. Thus, it is the neutral resonance stabilization (or lack thereof in the *meta* isomer) that dictates the relative EA of the *meta* isomer compared to the *ortho* and *para* isomers. The relative EAs of the *ortho* and *para* isomers are more difficult to predict and explain the observed trend. Both benefit from resonance, and the *ortho* isomer has the additional complication of the O...CH₃ interaction. Regardless, it is experimentally determined that the *para* isomer has the lowest EA, while *meta* has the highest. This same trend is seen in the halobenzylys, which are also doubly substituted

benzenes, but with an electron withdrawing group (CH₂) and another very weak electron withdrawing group (the halogens, by induction).²²

There is only one prior experimental measurement of the EA of any of the methylphenoxyls in the literature. McMahon and Kebarle²³ used gas phase proton transfer equilibria to determine an EA for *p*-methylphenoxyl of ~2.17 eV. This result is consistent with our more accurate measurement of 2.1199±0.0014 eV. In addition to the previous experimental work, there was also a theoretical study by Angel and Ervin²⁴ which used CBS-QB3 calculations to obtain the EA of *m*-methylphenoxyl to be 2.19 eV. This calculation also agrees well with our experimental measurement of 2.2177±0.0014 eV.

The vibrational progressions seen in the photoelectron spectra for all of these molecules show the clear signature of both active ring distortion normal modes (for transitions to the neutral \tilde{X} and \tilde{A} states) and active quasi C–O stretching normal modes (for transitions to the neutral \tilde{A} state). A summary of the measured (and calculated) vibrational frequencies for all three methylphenoxyl radicals is found in Table 3.7. While many transitions comprise the spectra presented in this work, the transitions shown in this table account for all significant vibrational modes which compose the observed progressions for each isomer. As mentioned previously, this behavior can be explained with a simple physical picture. For the methylphenoxide anions, adding the extra electron elongates the bond between the oxygen and the aromatic ring, as well as elongating the bonds within the ring away from the localized negative charge on the oxygen, compared to the equilibrium structure of the neutral radical. Upon photodetachment, one would therefore expect the excitation of ring distortion vibrations, which are observed, and C–O stretches. However, there is little evidence for any significant activity in C–O stretching modes for the transition to the neutral \tilde{X} state, and B3LYP calculations also predict little change in the

C–O bond lengths. A similar physical picture can be obtained for the methyl deprotonated *m*-methylphenol photoelectron spectrum. For the photoelectron spectra of methylphenoxide accessing the neutral \tilde{A} state, both ring distortion and C-O stretching modes are excited. The neutral \tilde{A} state is formed by removing an electron from the aromatic π system in the anion, resulting in the π^* neutral excited \tilde{A} state. The antibonding π system in the benzene ring elongates the C-O bond in the \tilde{A} neutral state relative to the anion. Thus, upon photodetachment from the anion to form the neutral excited \tilde{A} state, one would expect this C-O stretching vibration to be active.

Beyond the direct comparison with previous studies of the methylphenoxyl radicals, similar substituted aromatic compounds should be considered. Perhaps the most obvious of this group would be phenoxyl and benzyl. The phenoxyl radical has an EA of 2.2538 ± 0.0008 eV.¹⁶ There is a relatively small decrease (< 130 meV) in the EA of phenoxyl upon the addition of a methyl group, forming the methylphenoxyl radicals studies here. Methyl is a very weak electron donating group and so it is expected to have only a minor effect on the EA. It was observed that phenoxide had the same ring distortion vibrational modes excited upon photodetachment as are seen here for all three of the methylphenoxides.

In the case of deprotonation from the methyl group, a comparison with benzyl is appropriate. The EA of benzyl is 0.912 ± 0.006 eV.¹⁷ Benzyl shows a minor increase (~ 0.1 eV) in its EA upon attaching a *meta* hydroxyl group, forming methylenephenol radical. This is perhaps surprising considering OH is a strongly electron donating group in aromatic systems, and therefore might lead one to conclude that it should largely disrupt the electronic structure of the system and thus the EA. However, there are two reasons why this is actually not the case. First, the only isomer of methyl deprotonated methylphenol observed in this work is the *meta*

isomer. *Meta* isomers in aromatic systems are unique for their lack of resonance structures compared to that of *ortho* and *para* isomers. Hence, the impact of the electron donating effect of the OH in the *meta* isomer is diminished. Second, the primary effect of adding an electron donating group to the aromatic ring would be to localize the negative charge in the CH₂ carbanion. However, the charge is already localized on the CH₂ group, hence the change in overall behavior would be minimal. Both *m*-methylenephenol and benzyl show similar ring distortion vibrational progressions in their photoelectron spectra, further confirming the low level of perturbation.

In addition to comparing the EAs and vibronic structure of methylphenoxyl radicals, the methylphenoxide anion autodetachment behavior can be compared and discussed. Gunion *et al.*¹⁷ and more recently Liu *et al.*²⁵ found autodetachment in the photoelectron spectroscopy of phenoxide. Specifically, Liu *et al.* identified a dipole bound anion electronic excited state as the state responsible for facilitating autodetachment. Hydroxyphenoxide, a close analog of methylphenoxide, has also been recently studied.^{26, 27} Autodetachment was observed in the photoelectron spectrum of *o*-hydroxyphenoxide, again attributed to a dipole bound anion electronic excited state.²⁶ In the current study, the *m*- and *p*-methylphenoxide anions both display signatures of electron autodetachment. Considering the many similarities between the methylphenoxides, one might also expect to observe autodetachment in the *ortho* isomer, but this was not pursued experimentally in this work. For *m*-methylphenoxide (see Supplementary Material for more information), there is a higher onset energy ($3.494 \text{ eV} < h\nu_{\text{onset}} \leq 3.832 \text{ eV}$) for observing autodetachment as compared to the *para* isomer ($2.520 \text{ eV} < h\nu_{\text{onset}} \leq 2.637 \text{ eV}$). These onsets and the anion state(s) involved could not be confirmed by our TD-DFT anion excited state calculations, primarily due to the abundance of available predicted excited electronic states that

could be responsible for this phenomenon. The TD-DFT calculations suggest a similar number of optically accessible excited states for all three anionic isomers. However, theoretically investigating this further is beyond the scope of this work.

Having measured the electron affinities of the methylphenoxyl radicals, these results are combined with the measured bond dissociation energies^{19, 20} (Table 3.2) to determine the gas phase acidities using a thermodynamic cycle.³ This cycle provides a direct experimental measure of the 0 K enthalpy with a small (± 0.14 kcal/mol) uncertainty for the deprotonation reaction: $\text{HA} \rightarrow \text{H}^+ + \text{A}^-$. The dominant source of uncertainty arises from the error associated with the H–A bond strength, as seen in Table 3.2. We may further combine this 0 K result with the calculated constant pressure heat capacities of the species involved in the acid reaction in order to obtain the enthalpy at 298 K:³

$$\begin{aligned} \Delta_{acid}H_{298\text{K}}^0(\text{CH}_3\text{PhOH}) \\ = \Delta_{acid}H_{0\text{K}}^0(\text{CH}_3\text{PhOH}) + \int_0^{298} [C_p(\text{CH}_3\text{PhO}^-) + C_p(\text{H}^+) - C_p(\text{CH}_3\text{PhOH})] dT \end{aligned}$$

This results in $\Delta_{acid}H_{298\text{K}}^0 = 348.39 \pm 0.25$, 348.82 ± 0.25 , 350.08 ± 0.25 , and 349.60 ± 0.25 kcal/mol for *cis-ortho*-, *trans-ortho*-, *m*-, and *p*-methylphenol, using a conservative estimate of the error associated with calculating the C_p of these various molecules.³ These results are also found in Table 3.2. Note that King *et al.*¹⁹ were able to differentiate between *cis-ortho* and *trans-ortho* isomers of methylphenol, where *cis* and *trans* refer to the direction of the hydrogen of the OH group with respect to the CH₃ group.

The acidities of the three methylphenol isomers (four isomers, if the *cis*-, and *trans*-conformers of the *ortho* isomer are considered) have been studied several times in the past. In general, the reported error bars have been in the range of 1-3 kcal/mol. McMahon and Kebarle²³

initially measured the acidity at 298 K of *o*-methylphenol as 346.2 kcal/mol. Two other studies (McMahon *et al.*²³ and Angel *et al.*²⁴) examined *m*-methylphenol and determined the gas phase acidity at 298 K to be 347.3 and 348.2 ± 1.2 kcal/mol, respectively. Finally, *p*-methylphenol was studied by McMahon²³ and determined the gas phase acidity at 298 K to be 347.7 kcal/mol. The current study presented here agrees well with the previous studies, and has greatly improved on these measurements with an error of ± 0.25 kcal/mol. In addition to a direct comparison, one could also compare the acidity of phenol at 298 K (348.0 ± 1.0 kcal/mol, reported by Angel and Ervin,²⁴ or the 0 K acidity derived from the works of Kim *et al.*¹⁶ and King *et al.*²⁸: 347.43 ± 0.12 kcal/mol) to that of the methylphenols. The addition of a methyl group to a phenol minimally affects the acidity by increasing the room temperature reaction enthalpy by only ~ 1 kcal/mol. It is interesting, though, that because of the increased accuracy in the current study, one is able to observe that the trend in acidity increases going from *ortho* to *para* isomers. This order is due to the combination of the D_0 and the EA measured for each isomer; the trend is not mirrored in the D_0 and EA energetic ordering, where increasing D_0 and EA goes as *para*, *ortho*, *meta* instead. This order is also different than that observed for the aqueous acidity, which places the trend *ortho*, *para*, *meta* for increasing acidity,²⁹ likely due to solvation effects.

§ 3.12 Conclusions

The EAs of *o*-, *m*-, and *p*-methylphenoxide were measured: 2.1991 ± 0.0014 , 2.2177 ± 0.0014 , and 2.1199 ± 0.0014 eV, respectively. The EA of *m*-methylenephenol was also measured: 1.024 ± 0.008 eV. Using the methylphenol (O-H) bond strengths reported by King *et al.*¹⁹ and revised by Karsili *et al.*²⁰ a thermodynamic cycle was constructed and the acidities of the three methylphenols were obtained to a substantially degree of accuracy than previously reported, with $\Delta_{acid}H_{298K}^0 = 348.39 \pm 0.25$, 348.82 ± 0.25 , 350.08 ± 0.25 , and 349.60 ± 0.25 kcal/mol for *cis-ortho*-, *trans-ortho*-, *m*-, and *p*-methylphenol. The term energies for the neutral $\tilde{A} \leftarrow \tilde{X}$ doublet π to doublet π^* transition in the three isomers of methylphenoxyl were measured: 1.029 ± 0.009 , 0.962 ± 0.002 , and 1.029 ± 0.009 eV, for *ortho*, *meta*, and *para* isomers, respectively. In all reported photoelectron spectra, ring distortion vibrational normal modes were activated upon photodetachment, leading to vibrational progressions spaced by ~ 500 cm^{-1} . For the photoelectron detachment to the neutral \tilde{A} states, C–O stretching modes were also excited, leading to additional vibrational transitions with associated frequencies of ~ 1300 cm^{-1} . Electron autodetachment was observed in both *m*- and *p*-methylphenoxide photoelectron spectra, although the *para* isomer had an earlier onset photon energy for observing autodetachment, despite having similar calculated anion excited electronic states.

§ 3.13 References

- 1) B. Ruscic, A. F. Wagner, L. B. Harding, R. L. Asher, D. Feller, D. A. Dixon, K. A. Peterson, Y. Song, X. Qian, C.-Y. Ng, J. Liu, W. Chen and D. W. Schwenke, *J. Phys. Chem. A* **106**, 2727-2747 (2002).
- 2) C. T. Wickham- Jones, K. M. Ervin, G. B. Ellison and W. C. Lineberger, *J. Chem. Phys.* **91**, 2762-2763 (1989).
- 3) K. M. Ervin and V. F. DeTuri, *J. Phys. Chem. A* **106**, 9947-9956 (2002).
- 4) J. Cooper and R. N. Zare, *J. Chem. Phys.* **48**, 942-943 (1968).
- 5) Y.-J. Lu, J. H. Lehman and W. C. Lineberger, *J. Chem. Phys.* **142**, 044201 (2015).
- 6) A. T. J. B. Eppink and D. H. Parker, *Rev. Sci. Instrum.* **68**, 3477-3484 (1997).
- 7) H. Hotop and W. C. Lineberger, *J. Phys. Chem. Ref. Data* **14**, 731-750 (1985).
- 8) C. Blondel, W. Chaibi, C. Delsart, C. Drag, F. Goldfarb and S. Kröger, *Eur. Phys. J. D* **33**, 335-342 (2005).
- 9) D. M. Neumark, *J. Phys. Chem. A* **112**, 13287-13301 (2008).
- 10) M. J. Frisch, G. W. Trucks, H. B. Schlegel, G. E. Scuseria, M. A. Robb, J. R. Cheeseman, G. Scalmani, V. Barone, B. Mennucci, G. A. Petersson, H. Nakatsuji, M. Caricato, X. Li, H. P. Hratchian, A. F. Izmaylov, J. Bloino, G. Zheng, J. L. Sonnenberg, M. Hada, M. Ehara, K. Toyota, R. Fukuda, J. Hasegawa, M. Ishida, T. Nakajima, Y. Honda, O. Kitao, H. Nakai, T. Vreven, J. A. Montgomery Jr., J. E. Peralta, F. Ogliaro, M. J. Bearpark, J. Heyd, E. N. Brothers, K. N. Kudin, V. N. Staroverov, R. Kobayashi, J. Normand, K. Raghavachari, A. P. Rendell, J. C. Burant, S. S. Iyengar, J. Tomasi, M. Cossi, N. Rega, N. J. Millam, M. Klene, J. E. Knox, J. B. Cross, V. Bakken, C. Adamo, J. Jaramillo, R. Gomperts, R. E. Stratmann, O. Yazyev, A. J. Austin, R. Cammi, C. Pomelli, J. W. Ochterski, R. L. Martin, K. Morokuma, V. G. Zakrzewski, G. A. Voth, P. Salvador, J. J. Dannenberg, S. Dapprich, A. D. Daniels, Ö. Farkas, J. B. Foresman, J. V. Ortiz, J. Cioslowski and D. J. Fox, *Gaussian 09 Rev. B01*, 2009, see www.gaussian.com
- 11) A. D. Becke, *J. Chem. Phys.* **98**, 5648-5652 (1993).

- 12) K. M. Ervin, PESCAL, Fortran Program for Franck-Condon Analysis of Molecular Photoelectron Spectra, 2010, see <http://wolfweb.unr.edu/~ervin/pes/>
- 13) T. E. Sharp and H. M. Rosenstock, *J. Chem. Phys.* **41**, 3453-3463 (1964).
- 14) E. B. Wilson, Jr., *Phys. Rev.* **45**, 706-714 (1934).
- 15) P. Chen, *Unimolecular and Bimolecular Reactions Dynamics* (John Wiley & Sons, Chichester, 1994) 371.
- 16) J. B. Kim, T. I. Yacovitch, C. Hock and D. M. Neumark, *Phys. Chem. Chem. Phys.* **13**, 17378-17383 (2011).
- 17) R. F. Gunion, M. K. Gilles, M. L. Polak and W. C. Lineberger, *Int. J. Mass Spectrom. Ion Processes* **117**, 601-620 (1992).
- 18) M. J. Travers, D. C. Cowles, E. P. Clifford, G. B. Ellison and P. C. Engelking, *J. Chem. Phys.* **111**, 5349-5360 (1999).
- 19) G. A. King, A. L. Devine, M. G. D. Nix, D. E. Kelly and M. N. R. Ashfold, *Phys. Chem. Chem. Phys.* **10**, 6417-6429 (2008).
- 20) T. N. V. Karsili, A. M. Wenge, B. Marchetti and M. N. R. Ashfold, *Phys. Chem. Chem. Phys.* **16**, 588-598 (2014).
- 21) A. Sanov, *Annu. Rev. Phys. Chem.* **65**, 341-363 (2014).
- 22) J. B. Kim, P. G. Wenthold and W. C. Lineberger, *J. Phys. Chem. A* **103**, 10833-10841 (1999).
- 23) T. B. McMahon and P. Kebarle, *J. Amer. Chem. Soc.* **99**, 2222-2230 (1977).
- 24) L. A. Angel and K. M. Ervin, *J. Phys. Chem. A* **110**, 10392-10403 (2006).
- 25) H.-T. Liu, C.-G. Ning, D.-L. Huang, P. D. Dau and L.-S. Wang, *Angew. Chem. Int. Ed.* **52**, 8976-8979 (2013).
- 26) D.-L. Huang, H.-T. Liu, C.-G. Ning and L.-S. Wang, *J. Chem. Phys.* **142**, 124309 (2015).

27) M. L. Weichman, J. B. Kim and D. M. Neumark, *J. Phys. Chem. A* **119**, 6140-6147 (2015).

28) M. G. D. Nix, A. L. Devine, B. Cronin, R. N. Dixon and M. N. R. Ashfold, *J. Chem. Phys.* **125**, 133318 (2006).

29) W. M. Haynes, *CRC Handbook of Chemistry and Physics* (CRC Press, New York, 2016-2017).

CHAPTER IV

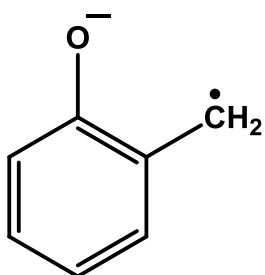
PHOTOELECTRON SPECTROSCOPY AND THERMOCHEMISTRY OF *o*-, *m*-, AND *p*-METHYLENEPHENOXIDE ANIONS

Portions of this chapter will be submitted for publication in The Journal of Chemical Physics under the same title, by Daniel J. Nelson, Wilson K. Gichuhi, Charles M. Nichols, Julia H. Lehman, Veronica M. Bierbaum, and W. Carl Lineberger

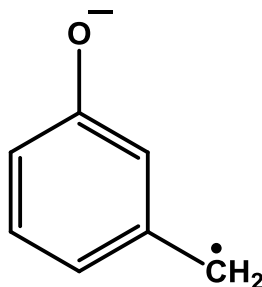
§ 4.1 Introduction and Background

As was discussed in § 1.2 and § 1.4, distonic radical ions and diradicals are of interest to many fields of chemistry, affecting such varied fields from pharmacology¹ to combustion chemistry.² This chapter will focus on three distonic radical anions and the diradicals which result upon electron photodetachment:

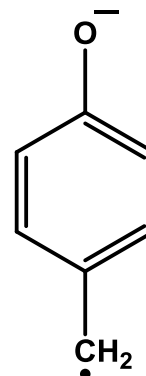
o-methylene phenoxide



m-methylene phenoxide



p-methylene phenoxide



Due to their frequently unstable and short lived nature, as well as their complicated electronic structure,³⁻¹² they are challenging to investigate both experimentally and theoretically. Collecting Photoelectron (PE) spectra of these distonic anions will prove to be no exception. While the *ortho* and *para* isomers will be shown to display some signal that is interpretable as

direct photodetachment, the *meta* isomer shows no conclusive evidence of the same. All three isomers display photoelectron signal that cannot be easily interpreted, and the implications of this will be discussed.

In addition to anion PE spectroscopy, the thermodynamic properties of the methylenephenoxide isomers are studied using a Flowing Afterglow – Selected Ion Flow Tube (FA-SIFT) mass spectrometer in conjunction with the acid bracketing procedure,¹³ thus providing information on the acidities of the methylenephenol radicals. Together with the Electron Affinities (EAs) provided by PE spectroscopy, acidities from the FA-SIFT machine, and a thermodynamic cycle, bond dissociation energies are also measured.

A note to future readers of this document: Unlike the other chapters in this dissertation, the analysis and interpretation of the data presented here is not yet fully complete. As such, any reader who seeks the final analysis is directed to the paper that will be published under the same title as this chapter in The Journal of Chemical Physics.

§ 4.2 Experimental Specifics

Samples of *o*-, *m*-, and *p*-methylphenol were obtained from Sigma-Aldrich Inc. ($\geq 98\%$ pure) and used without further purification. Selectively deuterated samples of two methylphenol isomers, 3,4,5,6-d₄,OD-*o*-methylphenol and methyl-d₃-*m*-methylphenol, were purchased from CDN Isotopes, Inc. ($\geq 98\%$ pure) and used without further purification. Selectively deuterated *p*-methylphenol, 2,3,5,6-d₄,OD-*p*-methylphenol, was purchased from Sigma-Aldrich Inc. ($\geq 98\%$ pure) and used as received. Acids for the acid bracketing experiments (Instrument C, see below) were all purchased from Sigma-Aldrich Inc. with the exception of phenol which was purchased through Mallinckrodt Pharmaceuticals Inc. The acids and their given purities are as follows: *p*-trifluoromethylphenol ($\geq 97\%$), 3-mercaptopropionic acid ($\geq 99\%$), *o*-chlorophenol ($\geq 99\%$), *p*-fluorophenol ($\geq 99\%$), propionic acid ($\geq 99.5\%$), acetic acid ($\geq 99\%$), phenol ($\geq 99\%$), 2,2,3,3,3-pentafluoro-1-propanol ($\geq 97\%$), 2,2,2-trifluoroethanol ($\geq 99.5\%$). All of these acids were used without further purification. The low vapor pressure of many of these compounds necessitated that they had to be gently heated ($\sim 40^\circ\text{C}$).

Three distinct experimental setups are used. Instrument A is a continuous photoelectron spectrometer (§ 2.2). Instrument B is the pulsed photoelectron spectrometer discussed in § 2.7. Instrument C is a Flowing Afterglow-Selected Ion Flow Tube (FA-SIFT) mass spectrometer.¹⁴ All three of these instruments have been discussed in detail previously, so only a brief description follows.¹⁴⁻¹⁹

In Instrument A, the ions of interest are generated in a flowing-afterglow He (~ 0.5 Torr) plasma. Molecular oxygen is added to this plasma, which generates O⁻. This radical anion is a strong base ($\Delta_{acid}H_{298\text{K}}^o(\text{HO})=382.60 \pm 0.07$ kcal/mol²⁰), and is capable of abstracting either H⁺ from a hydrocarbon reactant, resulting in an anion and hydroxyl radical, or it may remove both a

hydrogen atom and a proton, resulting in an anion and a water molecule. In the present experiment, the hydrocarbons in question are the three methylphenol isomers. Each methylphenol isomer is added through a gas inlet immediately after the $O^{\bullet -}$ radical anions are generated. The products from this reaction remain in ~ 0.5 Torr of He for several milliseconds, thermally equilibrating with the walls of the chamber, 300 K, before being extracted through a 1 mm orifice into a differentially pumped region, $\sim 10^{-6}$ Torr.

The reactants and products undergo more than a single collision, and hence the *nascent* product distributions arising from the reaction of $O^{\bullet -}$ and the methylphenols (*i.e.* the products of a single collision between an $O^{\bullet -}$ and methylphenol molecule) are not necessarily the products observed in the PE spectra. This is due to the long time (several milliseconds, on average) the reactants and products are in a collisional environment before entering a collision free environment. The $O^{\bullet -}$ anion can in general react at many sites on any given hydrocarbon, giving rise to many possible products. These products stay in a ~ 0.5 Torr atmosphere of He after their creation, allowing for subsequent collisions with other products or reactants allowing for the system to proceed toward chemical equilibrium. In the extreme case that the system is allowed to come fully to equilibrium, then one should expect to primarily observe the most thermodynamically favorable products (methylenephenoxide + water) with only trace amounts of other possibilities. While this experiment is likely not at chemical equilibrium, it is also likely that the nascent product distribution is not preserved.

After being produced and extracted into the differentially pumped region, the anionic products are accelerated to 735 eV, mass selected with a Wien velocity filter ($m/\Delta m \sim 60$), before being slowed to 35 eV and intersected with a fixed frequency argon ion laser ($h\nu = 3.40814$ eV), thereby photodetaching electrons from the mass-selected ions of interest. A

small solid angle of these electrons is gathered in a direction perpendicular to both the ion and laser beams, and their kinetic energy is measured using a hemispherical electron energy analyzer.

The laser radiation is linearly polarized at the magic angle (54.7°) with respect to the plane in which the photoelectrons are detected. Using this particular angle ensures that the gathered photoelectrons will be directly proportional to the anion's PE cross-section.²¹ The laser has an output power of ~ 1 Watt at 364 nm, which is coupled into the chamber via a build-up cavity locked to the laser cavity, increasing the circulated in-cavity power to ~ 100 Watts.

The collected PE spectra are calibrated to the PE spectra of O^- and O_2^- .^{22, 23} This provides an absolute linear energy scale and corrects for nonlinear distortion with a minor (0.7%) compression factor. The calibration spectrum of O^- also allows for a measurement of the instrument's resolution, 10 meV. This is obtained by measuring the full-width-half-maximum (FWHM) of the $O(^3P_2) + e^- \leftarrow O^- (^2P_{3/2})$ transition. As this peak results from a single atomic transition, its FWHM is a good approximation of the instrument's resolution.

In Instrument B,¹⁹ the anions of interest are synthesized in a dual pulsed valve plasma entrainment source utilizing the same reaction of methylphenol with O^- . This source uses two General Valves placed perpendicular to each other. The first is the primary supersonic expansion (10 psig, $\sim 1\%$ methylphenol in Ar), while the other valve is designated as the side valve (35 psig, 30% O_2 in Ar). During daily operation, the side valve tension is adjusted such that it is responsible for $\sim 10\%$ of the total pressure rise in the source vacuum chamber. The side valve has a pulsed parallel plate discharge at the valve exit ($\Delta V \sim -2000$ V).¹⁷ This generates a plasma which is entrained in the primary supersonic expansion. The dominant anion generated therein, O^- , then undergoes reactions with the methylphenol isomer of interest contained in the main expansion, generating products which are collisionally cooled with Ar. While not necessary to be

the case, the most thermodynamically favorable products from the reaction of O^- with methylphenol were found to be the dominant product in the *ortho* and *para* cases.

Following their initial formation, the anions are steered into a Wiley-McLaren TOF mass spectrometer by a pulsed extraction plate, where the ions are temporally separated by their mass-to-charge ratio (m/z) and spatially focused into the center of a Velocity Map Imaging (VMI) interaction region.¹⁸ A nanosecond laser pulse is timed to intercept the anion m/z of interest, photodetaching electrons. The light sources used to obtain the spectra reported here are the second and third harmonic of a Nd:YAG laser, with photon energies of 2.330 and 3.494 eV, respectively. The three dimensional distribution of photodetached electrons are velocity mapped onto a two dimensional position sensitive phosphor screen-coupled microchannel plate detector, and then imaged by a CCD camera. This photoelectron image is reconstructed into the original three dimensional velocity distribution utilizing an inverse Abel transform. This is then converted to a one dimensional electron speed distribution. Both steps are performed using the BASEX program.²⁴ Finally an electron Kinetic Energy (eKE) distribution is generated by means of a Jacobian transformation. This spectrum is converted to an electron Binding Energy (eBE) distribution by subtracting the eKE from the laser photon energy ($eBE = h\nu - eKE$), yielding the reported photoelectron spectra. For these experiments, the energy scale is calibrated by the S^- photoelectron spectrum.^{25, 26}

The VMI spectrometer has a spectral resolution that is a function of eKE; the resolution decreases with increasing eKE. This resolution is determined by the eKE and the FWHM of a peak in a photoelectron spectrum due to a single transition. In all cases shown in this work, the photoelectron spectrum of S^- was used to determine the resolution as a function of eKE, as well as calibrate the energy scale. Typically, the resolution is ~2–3% (resolution \sim FWHM/eKE).^{25, 26}

Instrument C produces ions in a similar fashion to Instrument A.¹⁴ The ions are created in a Flowing Afterglow He plasma, though for this instrument the plasma is made by electron emission via a heated filament. The O⁻ is generated via N₂O in the presence of the flowing afterglow plasma. The methylphenol sample is added downstream of O⁻ formation, and the same reaction discussed with Instrument A takes place. The products and reactants similarly remain in a ~ 0.5 Torr atmosphere of He for several milliseconds before being extracted through a 1 mm orifice into a differentially pumped region, ~10⁻⁶ Torr. The anionic products are then mass selected with a quadrupole mass filter and subsequently entrained in a reaction flow tube with a laminar flow of He (~ 0.5 Torr). There are gas inlets at regular intervals along this flow tube where neutral gas reagents may be added so as to study the thermochemistry and kinetics of gas phase ion-neutral reactions; however in this study, only the thermochemistry is examined. Specifically, neutral acids with known gas phase acidities are reacted with the anions of interest in order to perform acid bracketing. All anions are then extracted into a differentially pumped chamber, ~10⁻⁷ Torr, mass analyzed with a triple quadrupole mass analyzer and detected with a Channeltron.

Acid bracketing is a procedure that can be summarized as follows.¹³ The mass selected methylenephenoxides are reacted with neutral acids of known deprotonation enthalpy (reference acids) in the laminar flowing helium. As the anions are Lewis bases, a collision with a neutral acid will likely result in a proton transfer from the acid to the base if the proton affinity of the base is larger than the deprotonation enthalpy of the acid. This yields a decrease in the anion abundance, which is monitored for a variety of reference acids. A rapid proton transfer reaction with a reference acid indicates an exothermic reaction and is indicated by a “+” in Table 4.3. The deprotonation enthalpy of the conjugate acid of the methylenephenoxides (*i.e.* the

methylenephenols) must therefore be between the values of the two reference acids wherein the proton transfer reaction changed from endothermic to exothermic.

While performing experiments with Instrument C, it became necessary to inject CO₂ clustered with the ions of interest into the flow tube region, as this produced greater signal. This procedure should not interrupt the chemistry observed since the clusters are injected at 30-70 V which is more than sufficient to break the cluster into the parent ion and CO₂, whereupon the parent ion is free to react unencumbered in the flow tube.

Throughout this work, errors in reported peak positions in the photoelectron spectra, typically on the order of 1 meV or less, are due to several factors: the statistical error in fitting the peaks to Gaussian functions to obtain the peak center, the uncertainty in the absolute energy scale, and the number of independent measurements. When reporting the energy difference between peaks as a particular transition, the previous errors are taken into account and are combined with the uncertainty associated with the offset of the actual transition compared to the peak center. This uncertainty can be smaller or comparable to the aforementioned errors if only a single vibronic transition is the major contributor to the peak. However, if there are multiple transitions under the peak envelope, which can sometimes manifest itself as a non-Gaussian peak or a peak possessing a FWHM wider than would be predicted by the experimental resolution at that eKE, it could be as much as the Half-Width-at-Half-Maximum (HWHM) of the peak. The peaks presented in all reported spectra are broader than the instrument resolution and always arise from multiple transitions with significant transition intensity. Hence, this latter error dominates the reported uncertainty.

§ 4.3 Theoretical Methods and Simulations

The ROCBS-QB3 composite quantum chemistry method has been used to calculate the adiabatic EAs of all the diradicals studied here. This method has been shown to work well with heavily spin-contaminated systems, as well as for open shell species.¹² The B3LYP/aug-cc-pVTZ density functional theory model chemistry²⁷ was used to calculate the normal modes of all the anions and neutrals studied here, which are subsequently used to compute Franck–Condon (FC) factors. This level of theory was also used to determine $\Delta_{acid}H_{298 K}^{\circ}$ of the protonated form of all the anions of interest. All of these electronic structure, normal mode, and thermochemical calculations were carried out using the Gaussian 09 program package,²⁸ the FC factors were calculated using the PESCAL program,²⁹ and the FC factors were converted into simulations of the spectra with home–built code.

To simulate the experimental spectra, PESCAL calculates the positions of all the possible vibrational transitions and the Franck-Condon factor associated with each transition. This information, combined with a 200 K Maxwell-Boltzmann distribution of energy (for Instrument B, 300 K for Instrument A) in the initial anionic states, provides a stick spectrum. These sticks are then convolved with Gaussian functions whose integral area is equal to the calculated transition intensity (FC factor) and whose FWHM is commensurate with the instrument resolution to yield the final simulated spectra. PESCAL utilizes Duschinsky rotation matrices and displacement vectors to match the initial state normal mode coordinates to the final state normal mode coordinates such that the FC integrals may be evaluated via the Sharp-Rosenstock-Chen method.³⁰⁻³³ These Franck-Condon based simulated photoelectron spectra make use of the harmonic oscillator approximation, with no anharmonic corrections or cross-mode couplings.

§ 4.4 Results: Overview

The reaction of O^- with methylphenol could produce a number of different anionic products in theory. Deuteration studies were employed to verify which products were dominant and would be further studied using photoelectron spectroscopy. Fig. 4.1 displays mass spectra collected with Instrument C, showing the products from the reaction of selectively deuterated methylphenols with O^- . In each case, the primary product is shown to be deprotonation from the hydroxyl group, generating methylphenoxide. This product has been previously studied and its PE spectrum collected.³⁴ Photodetachment from methylphenoxide produces signal that spans from approximately 2.1 to 2.7 eV. The next most abundant product evident in the mass spectra is a loss of both H and D from the starting methylphenol. The acidities associated with the hydrogens attached to the aromatic ring in the methylphenols has been previously calculated,³⁴ and abstraction from these sites is either thermo-neutral or endothermic. This is in contrast to the acidity of the hydrogens found on the methyl groups of the methylphenols, for which it is exothermic to abstract those hydrogens with either O^- , OH, or OH^- . Therefore, the anionic product from the loss of both H and D is expected to be an isomer of methylenephenoxide.

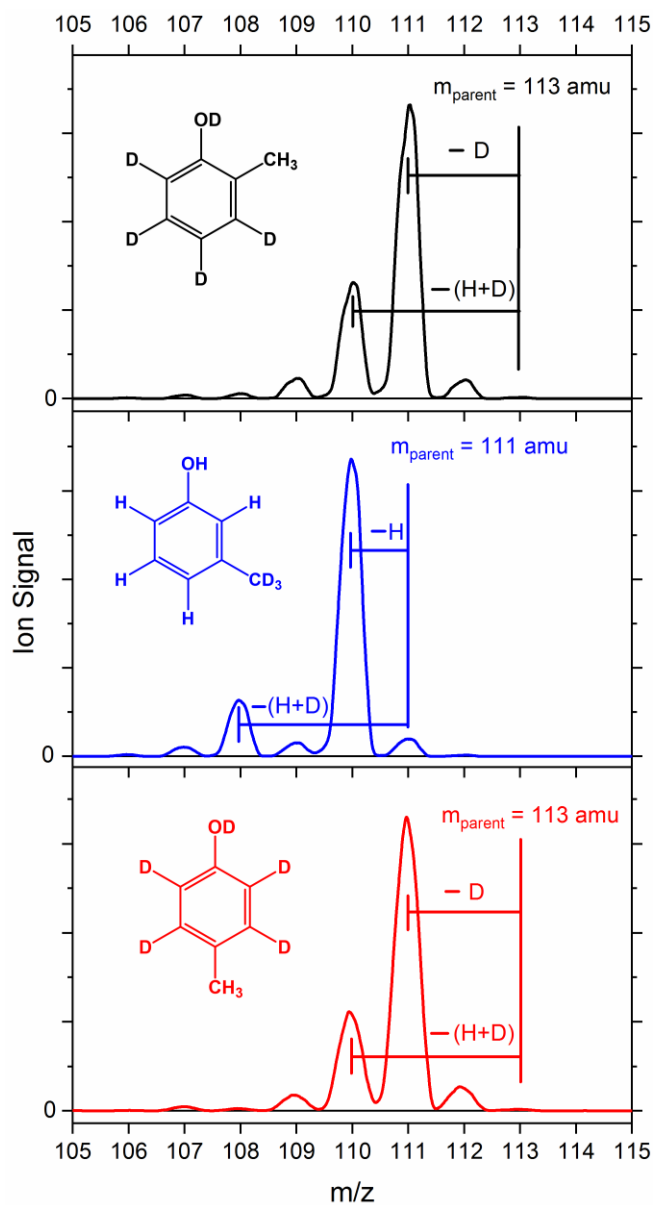


Fig. 4.1 Mass spectra collected on the FA-SIFT instrument of selectively deuterated cresols reacted with O^- . In each panel, the parent cresol structure is shown and a vertical line indicates the parent mass. In each case, deprotonation from the O site is the largest observed product channel, while the next largest channel is H + D loss from the hydroxyl and methyl groups. More details may be found in the text.

Electronic structure calculations as well as FC simulations were carried out for other possible structural isomers with the same mass as methylenephenoxide ($m/z = 106$), and were compared to the experimental PE spectra. This was in an effort to rule out possible proton transfer, ring opening, ring rearrangement, or other reactions giving rise to any of the features seen in the spectra. No photoelectron signatures belonging to isomers other than methylenephenoxide were positively identified in the spectra. However, even in combination with the deuteration study (Fig. 4.1), this cannot definitively rule out the existence of such anions in the experiment.

Prior to examining the spectra, it is useful to consider what one might expect from the photoelectron spectra of the methylenephenoxide anions. There are three observations we might expect to make: the EAs of the neutral isomers, the normal mode vibrations excited upon photodetachment, and the possibility of observing excited electronic states. The PE spectra of the methylphenoxide anions have previously been studied³⁴ and it was found that the EAs of the methylphenoxyl isomers are approximately 2 eV. This was primarily due to the fact that the negative charge in the anion was localized on the oxygen. In the case of the methylenephenoxide anions, the functional groups on the aromatic ring are O and CH₂, as opposed to O and CH₃ for methylphenoxide. CH₂ is electron withdrawing and can be expected to attract charge density away from the O and onto the aromatic ring in the anion. In the extreme case that the charge density is totally localized on the aromatic carbon ring, as in benzyne,³⁵ then the EA will be ~1 eV. Thus, an electron withdrawing group such as CH₂ is expected to reduce the EA of methylenephenoxyl as compared to methylphenoxyl. In addition, the isomers of the methylphenoxides all had ring distortion vibrational progressions in the ground electronic ground state which were excited upon photodetachment, spaced by ~ 500 cm⁻¹. This is also expected to

be observed in photodetachment from methylenephenoxides, with the caveat that due to the more delocalized nature of the negative charge in the anion, a more diverse selection of vibrational modes may become excited upon photodetachment. Finally, with a sufficiently high photon energy, we might expect to access both the ground and the lowest lying excited electronic states of the neutrals. Considering the PE spin selection rule $\Delta S = \pm \frac{1}{2}$, detachment from the doublet ground state of the anion would result in either singlet or triplet multiplicity for the electronic states of the neutral. The singlet-triplet splitting for the methylenephenoxyls is calculated to be on the order of 1.5–2.0 eV. With an EA estimated to be between approximately 1 and 2 eV, a photon energy of 3.494 eV might be sufficient to observe the origin of the triplet excited state of the neutral.

Fig. 4.2 shows the photoelectron spectra of the three methylenephenoxide anions, obtained utilizing Instrument B with a photon energy of 3.494 eV. For each isomer, a considerable amount of activity may be seen spanning the spectra from ~1 eV through to the photon energy, 3.494 eV. The activity can largely be split into three regions, based on eBE: A) 1 – 2 eV; B) 2 – 2.7 eV; C) 2.7 – 3.494 eV, as denoted by the shaded regions in Fig. 4.2. The intensity of these spectra have been scaled for the reader's convenience, however, the overall signal of the *meta* isomer was approximately 10x lower than for the other two isomers. This was due to a decrease in ion signal in the mass spectrum, when compared to the remaining two isomers, and not from a difference in the integrated photoelectron cross section. For *ortho* and *para* isomers, the largest integrated intensity belongs to the lowest eBE peaks, spanning approximately 1 – 2 eV, or region A. The onset of these peaks being near 1 eV is consistent with the predicted EA of the methylenephenoxyl diradical. These progressions are labeled S_0 on their respective spectra. While there is signal above the noise level in region A of the middle panel

(*meta*) of Fig. 4.2, the integrated intensity is far lower than for the other spectra presented.

Assigning this region was not possible and will be explained in the discussion section. The transition from the anionic electronic ground state to the first electronically excited triplet state of the neutral is also identified for the *ortho* and *para* isomers. These transitions are labeled T₁ in Fig. 4.2 and comprise region C of the spectral region considered.

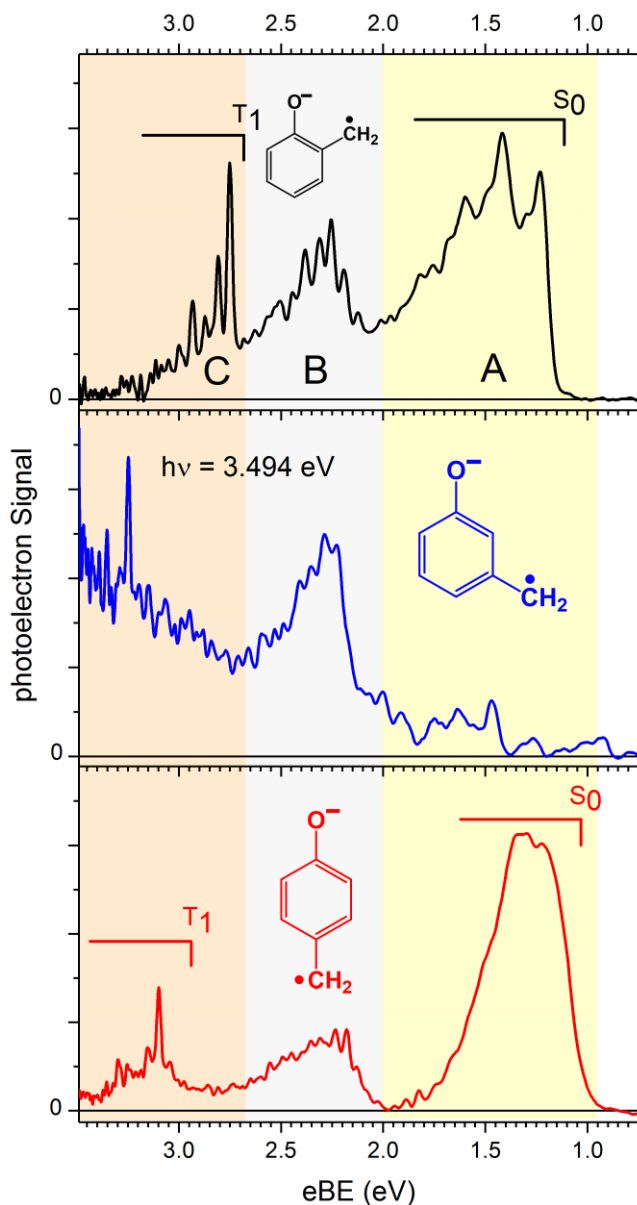


Fig. 4.2 Photoelectron spectra taken on the VMI photoelectron spectrometer with a photon energy of 3.494 eV of the three isomers of methylenephenoxide. The spectra are highlighted into three separate regions, A, B, and C, to make discussion easier. The PE spectra of the *ortho* and *para* isomers accessing the ground singlet and first excited triplet electronic states of the neutral are labeled. The *meta* isomer and the other unlabeled portions of PE spectra are explained in the main text, while the vibrational structure of the labeled electronic states are further investigated in the following figures. Note that the *meta* photoelectron signal is approximately 10x smaller than that from *ortho* and *para* isomers, but is shown on the same scale for ease of viewing.

This leaves region B of the three spectra presented in Fig. 4.2 initially unassigned, and the reasons for this will be examined both in § 4.7 and in § 4.9.

Photoelectron angular distributions with respect to laser polarization were measured for the photoelectron spectra shown in Fig. 4.2. The angular distributions are characterized by the anisotropy parameter (β). The electron in each case must be detached from what may accurately be described as a hybrid oxygen p-like molecular orbital and a conjugated aromatic π system; it is therefore expected that we should observe a negative β when observing detachment to the neutral singlet ground state utilizing a photon energy of 3.494 eV.^{21, 36} Photodetachment forming the neutral S_0 state displays the same photoelectron anisotropy for the *ortho* and *para* isomers, $\beta \sim -0.15$, using a photon energy of 3.494 eV. This anisotropy parameter stayed approximately constant at ~ -0.15 for the progression also seen beginning at ~ 2 eV binding energy in all three isomers as well. The photoelectron angular distribution for electrons with binding energies greater than 3 eV for all three isomers were isotropic ($\beta \sim 0$). However, these transitions are all close in binding energy ($< \sim 500$ meV) to the photon energy used to examine them, thus the photoelectrons have low kinetic energies, and so an isotropic angular distribution is expected.³⁶

§ 4.5 Results: Photodetachment to the ground S_0 State of *o*-, and *p*-Methylenephenoxyl

In order to obtain accurate EAs for the *ortho* and *para* isomers, higher resolution spectra of region A in Fig. 4.2 are necessary. Recall that the resolution of the VMI spectrometer improves as the eKE is decreased. While the transition to S_0 might appear broad in Fig. 4.2, higher resolution can be achieved by either changing the photon energy used in Instrument B, or utilizing the constant energy resolution inherent to Instrument A. This latter option was chosen and the results are shown in Fig. 4.3, where the experimental data are shown as black and red traces, while the theoretical results are shown as the purple sticks (FCFs) and the green curves (convolution). The higher resolution data reveal structured spectra, including clearly defined peaks that can be attributed to transitions from the anion to the neutral S_0 state. The origin peak is approximately 1 eV, as expected for the EA of methylenephenoxyl radicals. The PE spectra for both the *ortho* and *para* isomers displayed in Fig. 4.3 show a series of peaks spaced by intervals of approximately 500 cm^{-1} , indicating the expected excitation of ring distortion vibrational modes.

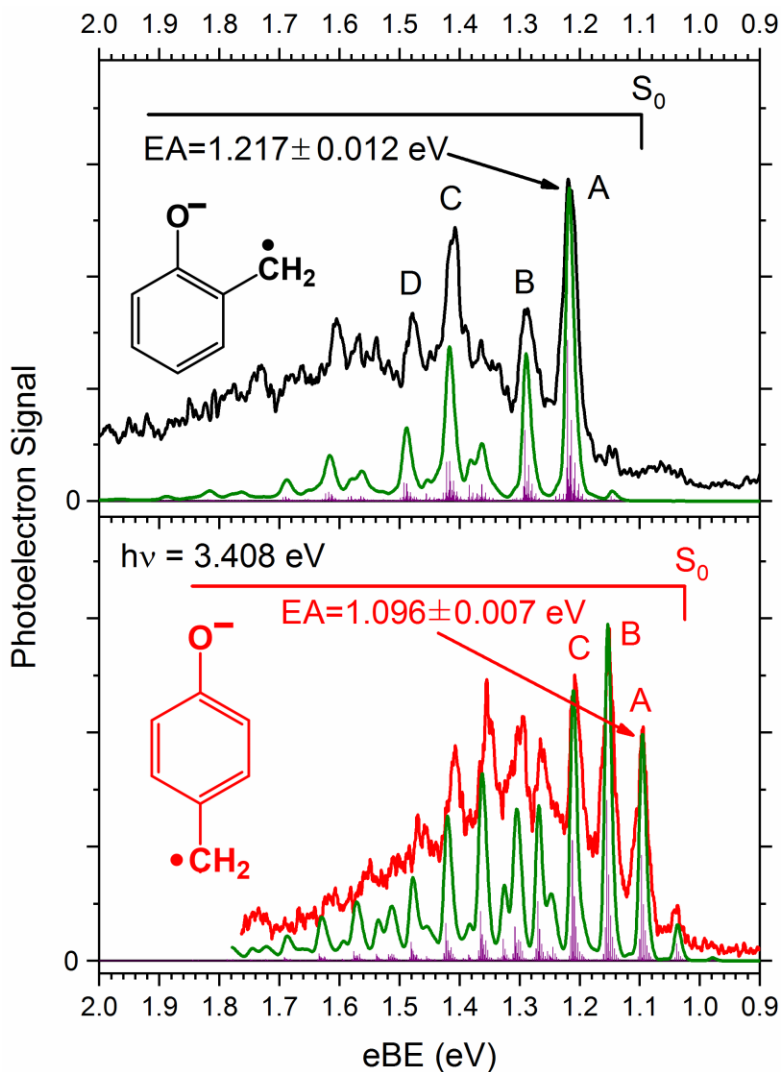


Fig. 4.3 Photoelectron spectra of the *o*- and *p*-methylenephenoxy anions obtained using Instrument A utilizing a photon energy of 3.408 eV are shown in the black and red traces, respectively. Instrument A has a constant spectral resolution of 10 meV. The calculated transitions and their corresponding Franck–Condon intensities are represented by purple sticks, while their convolution with experimental resolution are shown in green.

In order to aid in further analyzing the spectra in Fig. 4.3, a comparison between theory and experiment is instructive. For both isomers, there is very good agreement between the experimental results and the theoretical predictions, further confirming the assignment of these photoelectron spectra as detachment from *o*- and *p*-methylenephenoxide to form the S_0 state of the corresponding neutral diradical. For *o*-methylenephenoxide (top panel), peak A is predicted to be due primarily to the transition from the anion vibronic ground state to the neutral vibronic ground state, *i.e.* the EA. Note that while the origin transition possesses the largest predicted transition intensity to contribute to the peak, many other transitions also contribute. These are primarily transitions from the anion ground electronic state with one quanta populating a FC active vibrational mode to the neutral ground electronic state with one quanta populating the analogous vibrational mode which was populated in the anion, commonly known as sequence bands. The center of peak A is measured to be 1.217 ± 0.001 eV, leading to a measurement of the EA = 1.217 ± 0.012 . Similarly, peak A for the *para* isomer (lower panel, Fig. 4.3) is predicted to be dominated by the origin transition (EA), with its peak center located at 1.096 ± 0.001 eV, and thus the EA is measured to be 1.096 ± 0.007 eV. For both *ortho* and *para* isomers, the width of peak A is significantly broader than the experimental resolution and the transitions that make up peak A are distributed non-symmetrically about the peak center, giving rise to the non-Gaussian shape. Thus, the peak HWHM is used in the error analysis and is the dominant contributor to the error on the EA.

For the *o*-methylenephenoxide isomer photoelectron spectrum (top panel, Fig. 4.3), Peaks B, C, and D are located 571 ± 10 , 1571 ± 10 , and 2105 ± 10 cm^{-1} relative the center of peak A. Peak B is predicted to have arisen primarily from a transition to an excited ring distortion vibrational mode, as was expected. The peak spacing relative to the EA yields an experimental

measure of the neutral *o*-methylenephenoxyl radical $28_0^1 = 570 \pm 180 \text{ cm}^{-1}$, as compared with the predicted value of 576 cm^{-1} . Peak C is predicted to arise from the transition from the ground vibronic state of the anion to one quanta of either of two vibrational modes of the neutral, which have approximately equal FCFs. Both of these neutral vibrational modes combine ring distortion motion with C–O stretch motion, and have calculated harmonic frequencies of $\nu_8 = 1625$ and $\nu_9 = 1586$. Due to experimental resolution and congestion, they were not experimentally separated, leading to a measurement of both $9_0^1, 8_0^1 = 1570 \pm 270 \text{ cm}^{-1}$. Peak D is a combination band arising from transitions from the ground vibronic state of the anion to combinations of ν_9 and ν_8 with ν_{28} , thus allowing for the measurement, $8_0^1 28_0^1, 9_0^1 28_0^1 = 2100 \pm 140 \text{ cm}^{-1}$. These results are summarized in Table 4.1, while the eigenvectors for these modes may be found in Table 4.2.

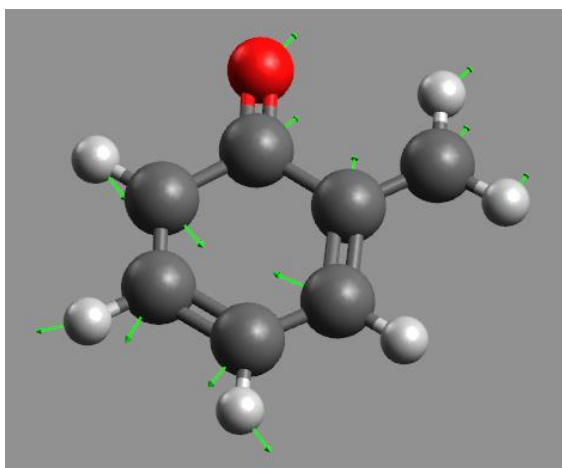
The vibrational excitations found within the electronic transition from the ground doublet state of the *p*-methylenephenoxide anion to the electronic ground singlet state of the corresponding neutral (bottom panel of Fig. 4.3) is now examined. Peaks B and C have peak centers 452 ± 10 and $899 \pm 10 \text{ cm}^{-1}$ higher in binding energy relative to peak A. The intensities of peaks B and C are primarily attributed to excitations of one ring distortional vibrational mode with a predicted harmonic frequency of 464 cm^{-1} and assigned ν_{30} . Thus, the transitions involving this mode may be measured: $30_0^1 = 450 \pm 80 \text{ cm}^{-1}$ and $30_0^2 = 900 \pm 140 \text{ cm}^{-1}$. Peaks higher in binding energy than peak C are due to many transitions, including combination bands of a variety of ring distortion vibrational modes ($\sim 500 \text{ cm}^{-1}$) as well as modes which incorporate ring distortion motion with C–O stretch motion ($\sim 1500 \text{ cm}^{-1}$). Since these peaks are not clearly dominated by only one or two transitions, further assignments are not straightforward.

Table 4.1 The experimentally measured frequencies of the Franck-Condon active normal modes for the singlet ground (S_0) and first triplet excited (T_1) states of *o*- and *p*-methylenephenoxyl diradicals. The calculated (B3LYP/aug-cc-pVTZ) harmonic frequencies are listed in parentheses below the measured frequency. All values are in cm^{-1} . Details describing the motion of these normal modes are described in the text.

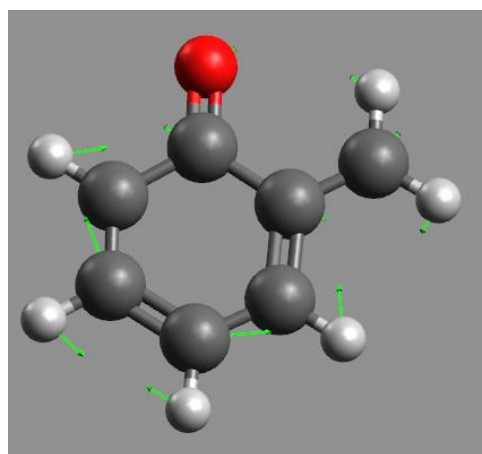
<i>o</i>-Methylenephenoxyl	<i>p</i>-Methylenephenoxyl
S_0 state	S_0 state
$\nu_{28} = 570 \pm 180 \text{ cm}^{-1}$ (577 cm^{-1})	$\nu_{30} = 450 \pm 80 \text{ cm}^{-1}$ (464 cm^{-1})
$\nu_9 = 1570 \pm 270 \text{ cm}^{-1}$ (1586 cm^{-1})	
$\nu_8 = 1570 \pm 270 \text{ cm}^{-1}$ (1625 cm^{-1})	
T_1 state	T_1 state
$\nu_{31} = 450 \pm 160 \text{ cm}^{-1}$ (456 cm^{-1})	N/A
$\nu_{28} = 450 \pm 160 \text{ cm}^{-1}$ (529 cm^{-1})	
$\nu_7 = 1470 \pm 170 \text{ cm}^{-1}$ (1530 cm^{-1})	

Table 4.2 The following diagrams display the primary Franck-Condon active normal modes discussed in the text for each product studied. Each eigenvector shown here is that of the neutral radical, and calculations were carried out at the B3LYP/aug-cc-pVTZ level of theory/basis set.

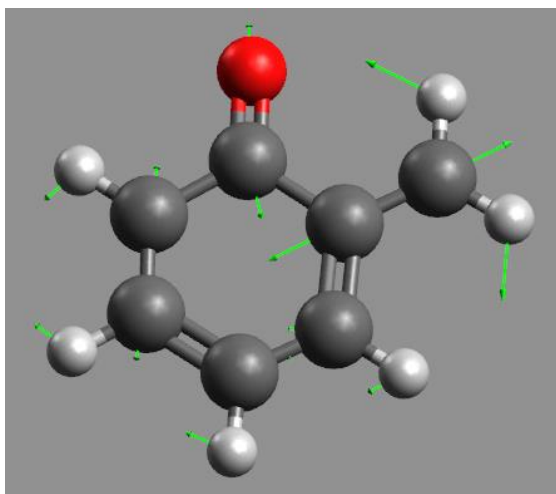
Ortho-Methylenephenoxyl radical (S_0 state)



ν_{28} (577 cm^{-1})

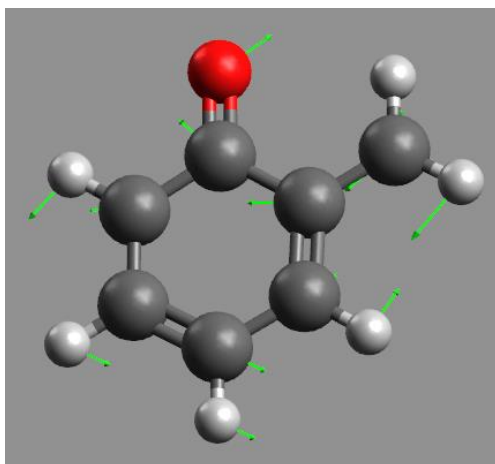


ν_9 (1586 cm^{-1})

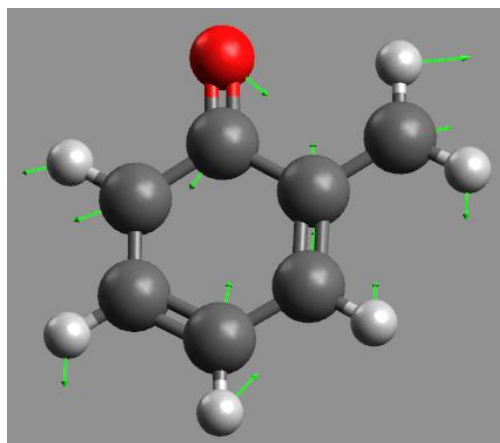


ν_8 (1625 cm^{-1})

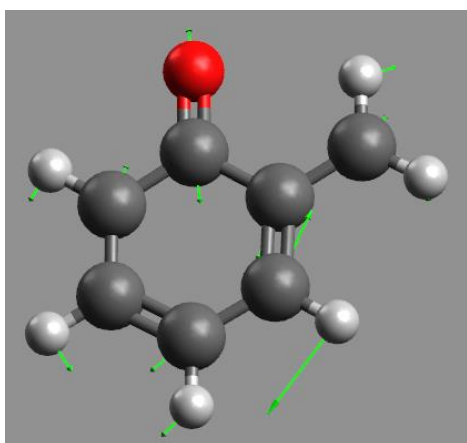
Ortho-Methylenephenoxyl radical (T_1 state)



ν_{31} (456 cm^{-1})

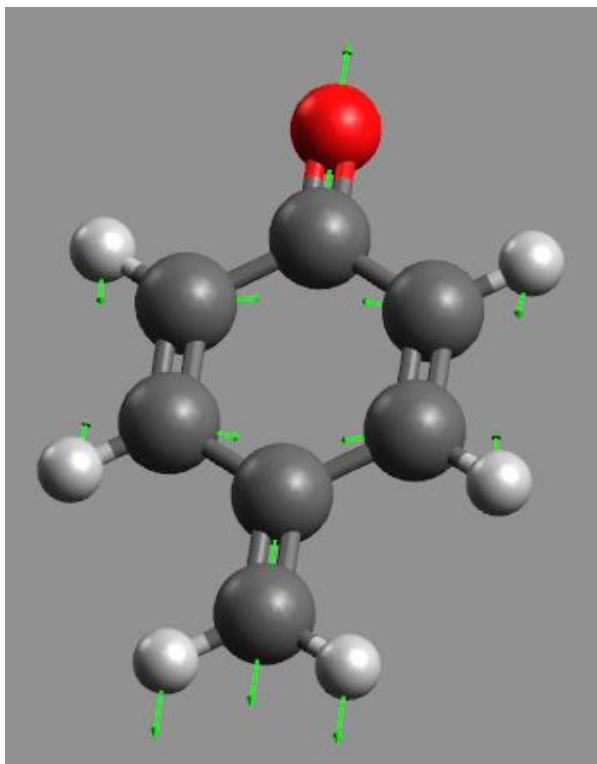


ν_{28} (529 cm^{-1})



ν_7 (1530 cm^{-1})

Para-Methylenephenoxyl radical (S_0 state)



ν_{30} (464 cm^{-1})

§ 4.6 Results: Photodetachment to the T₁ State of *o*-, and *p*-Methylenephenoxyl

The singlet – triplet splittings for the *ortho* and *para* isomers are also measured. Fig. 4.4 displays region C of the PE spectra accessing the excited neutral states of the *ortho* and *para* isomers, collected utilizing Instrument B with a photon energy of 3.494 eV. The experimental data are colored black and red, while theoretical modeling is shown in green and purple. Peak A in the *ortho* spectrum is located at 2.752 ± 0.001 eV. This is approximately 1.5 eV above the EA. Theoretical calculations (ROCBS–QB3) predict the first electronically excited triplet state to be 1.498 eV above the ground state, while the first electronically excited singlet state is over 3 eV higher in energy than the ground state. Given the experimental location of this peak in the spectrum, it is assigned to arise from the transition from the anion vibronic ground state to the vibrational ground state of the neutral first electronically excited triplet state. This leads to a measurement of the T₁ electronic band origin, 2.752 ± 0.015 eV electron binding energy. Combining this value with the EA allows for a measurement of $\Delta E_{ST}(o\text{-methylenephenoxyl}) = 1.535 \pm 0.019$ eV, agreeing very well with the theoretically predicted energy difference (1.495 eV). As for the *para* isomer, due to the fact that there is a predicted $\pi/2$ radian angle change in the CH₂ group, a similar simulation is not possible to aid our analysis. Since all of the peaks in this spectrum for the *para* isomer are far wider than the experimental resolution (by a factor of 2 or even 3) and considering the presence of a broad underlying continuum, without a simulated spectrum to provide more guidance, only a lower bound may be placed on the origin transition for this progression: ≥ 2.9 eV. This provides an experimental bound on the $\Delta E_{ST} \geq 1.8$ eV, compared to the theoretical prediction of $\Delta E_{ST} = 1.962$ eV.

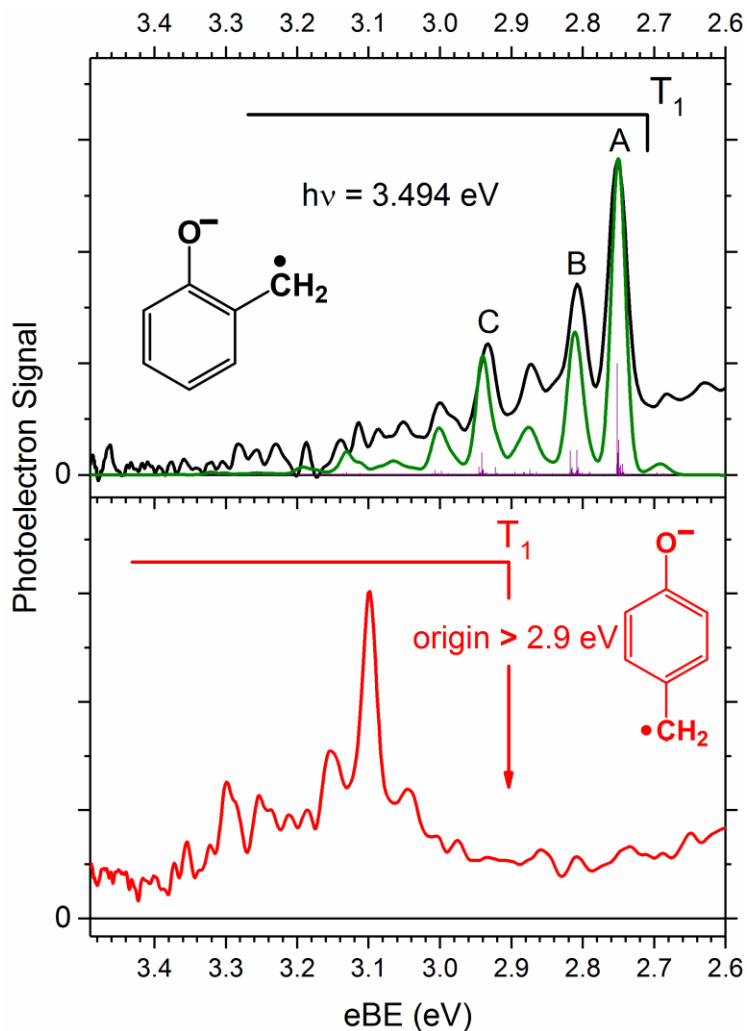


Fig. 4.4 Photoelectron spectra accessing the first triplet electronic excited states of the *o*- and *p*-methylenephenoxyl diradicals are shown in black and red traces, respectively. These spectra were collected on the VMI PE spectrometer utilizing a photon energy of 3.494 eV. The spectrum of the *ortho* isomer was successfully simulated and shown as the convolution (green trace) of the predicted transition positions and their respective Franck–Condon factors (purple sticks). The *para* isomer simulation proved to be unsuitable at the same level of theory due to a $\pi/2$ radian angle change between the anion and the neutral of the CH_2 group.

The vibrational transitions found within the electronic transition from the ground doublet state of the *o*-methylenephenoxide anion to the first electronic excited triplet state of the corresponding neutral (top panel of Fig. 4.4) may also be analyzed. Fig. 4.4 displays the photoelectron spectrum of the *o*-methylenephenoxide anion accessing the neutral triplet state. These data were obtained with Instrument B and a photon energy of 3.494 eV. Experimental data are presented as red or black curves while the simulated spectrum is represented by a green trace. Peaks B and C are located 455 ± 10 and $1471 \pm 10 \text{ cm}^{-1}$ higher in binding energy relative to peak A which is dominated by the origin transition. Theory predicts peak B to be dominated by excitation of two ring distortion vibrational modes with harmonic frequencies calculated to be 456 and 529 cm^{-1} , ν_{31} and ν_{28} , respectively. Due to their proximity in frequency to each other, these two modes cannot be independently measured, and therefore we assign both transitions $31_0^1, 28_0^1 = 450 \pm 160 \text{ cm}^{-1}$. Peak C is predicted to be due to one vibrational excitation of a combination ring distortion, C–O stretch mode with a harmonic frequency predicted to be 1530 cm^{-1} and is determined to arise from excitation of ν_7 . This allows for an experimental measurement of the transition $7_0^1 = 1470 \pm 170 \text{ cm}^{-1}$.

The *para* isomer also shows evidence of an excited electronic state vibrational progression, however no modeling of this progression is shown. There is a predicted large geometry change in the CH₂ group between the neutral electronic ground state and the first electronic excited state; the CH₂ rotates $\pi/2$ radians with respect the ring plane. Several attempts to simulate the photoelectron spectrum and compensate for this effect were made, but none qualitatively reproduced the experimental data and displayed non-physical behavior. These efforts included excluding vibrational transitions in the simulations which involved CH₂ motion,

however, as all modes include this motion to varying degrees, this approach failed to produce meaningful results.

§ 4.7 Results: Unassigned Features

There is little that can be concluded from region A in the PE spectrum of *m*-methylenephenoxide, found in Fig. 4.2. There are large disparities between the experimental results and the numerous calculations attempted, unlike the results for *o*- and *p*-methylenephenoxide. In addition, each considered isomer was calculated at several levels of theory, and these displayed large differences in the predicted EAs of the same molecule. For example, calculating the EA of *m*-methylenephenoxyl using ROCBS-QB3 yields an EA of 0.777 eV, however that same structure calculated with B3LYP/aug-cc-pVTZ returned a value of 2.170 eV. Other possible isomers were considered, from ring-opened structures to seven membered ring structures, but were discounted due to the lack of agreement at both a qualitative and quantitative level between the experimental and calculated EA and overall photoelectron spectrum. The methods and basis sets were also varied; CBS-APNO, wB97XD/aug-cc-pVTZ, and CCSD/aug-cc-pVDZ were all computed, but this did not reveal any insight into the problem. The only constant throughout these calculations was their agreement that the ground state of the *m*-methylenephenoxyl diradical was the triplet state, contrary to the other two isomers. The reasons for these theoretical failings are explored in § 4.9.

In order to further attempt to understand the PE spectrum of *m*-methylenephenoxide, an additional spectrum was collected at a higher photon energy than 3.494 eV. Fig. 4.5 displays the photoelectron spectrum of *m*-methylenephenoxide obtained with two photon energies, 3.494 and 3.832 eV (generated via doubling the output of a 532 nm pumped DCM dye laser), collected on instrument B. As can be seen, there is a dramatic difference between the two spectra which is attributed to electron autodetachment, and cannot be explained by changing instrument resolution nor threshold effects.

Region B in Fig. 4.2 is now examined in greater detail and with higher resolution. Fig. 4.6 displays the PE spectra of all three methylenephenoxide isomers recorded with the VMI PE spectrometer utilizing a photon energy of 2.330 eV. These spectra provide a higher resolution examination of the progressions beginning at ~ 2 eV binding energy for each isomer. As can be seen, no theoretical modelling of these spectra is shown. This omission was the result of a failure of theory to accurately simulate or predict these progressions. When attempting to simulate these spectra excited electronic states of the neutral diradicals were considered. Additionally, sequential photon absorption processes were also simulated, *e.g.* the anion absorbs a photon and transitions to a repulsive electronic state, ejecting a hydrogen or methylene group and then the resulting anion subsequently absorbs a second photon which undergoes photodetachment as normal. These processes were discounted as no bond simulated had a predicted dissociation energy below 3.8 eV, and thus, with even the highest energy photon used in this work, 3.494 eV, we would not have been able to access such a process. Peak A in the PE spectra for the *ortho*, *meta*, and *para* isomers is located at 2.118 ± 0.001 , 2.227 ± 0.001 , and 2.177 ± 0.001 eV binding energy. Assuming these peaks represent the origin transitions, they do not match any known EA value of any likely organic molecule of the appropriate mass.^{34, 37-40} This was further confirmed by also obtaining the PE spectra of methylphenoxide with a photon energy of 2.330 eV and overlaying these data upon the spectra found in Fig. 4.6. See Fig. 4.7. Additionally, examining the energetic spacing between peak A in Fig. 4.6 and peaks at higher binding energy in each isomer reveals energy differences of ~ 500 cm⁻¹, suggesting ring distortion vibrational excitation. This is examined further in § 4.9.

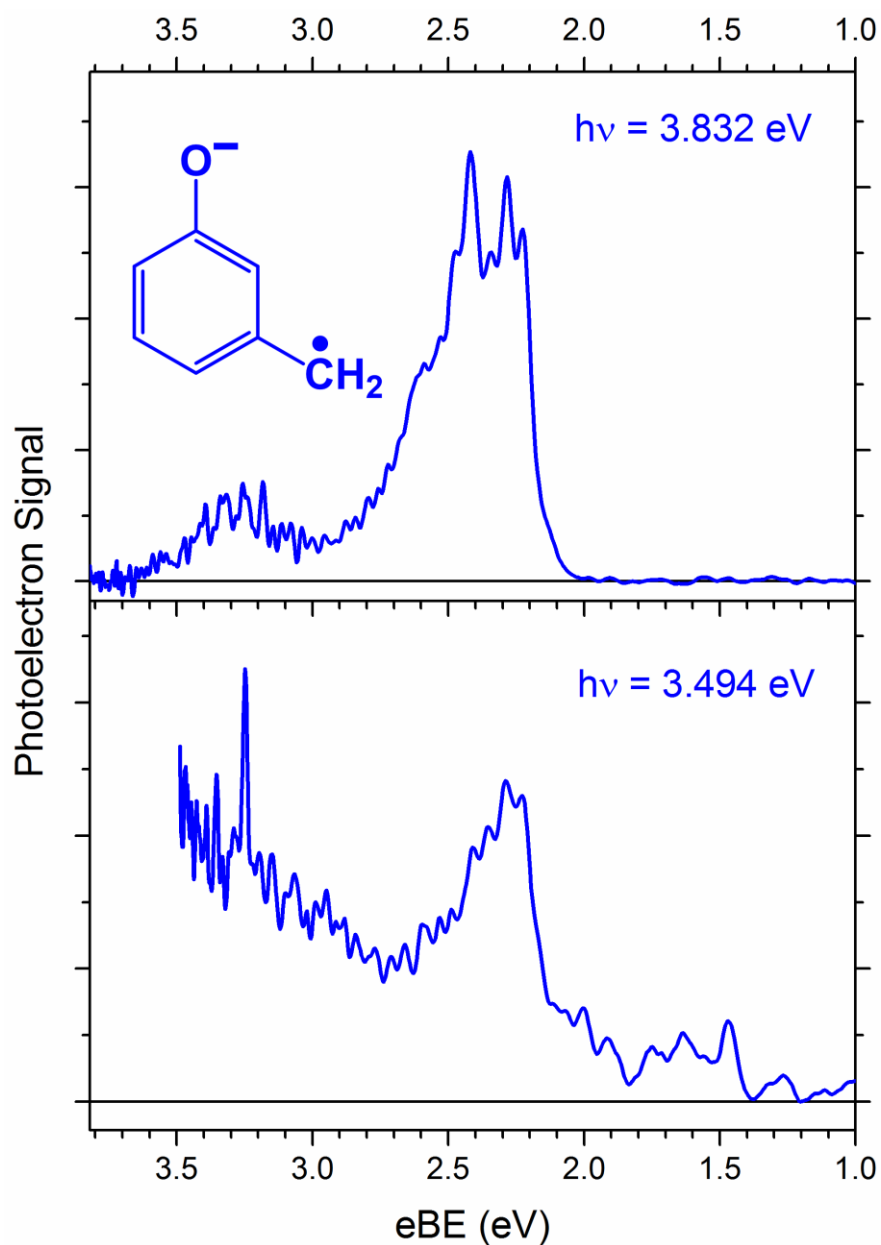


Fig. 4.5 Photoelectron spectra of *m*-methylenephenoxide anions obtained on instrument B with two different photon energies, 3.494 and 3.832 eV. As can be observed, there is a photon energy dependence displayed between the two spectra. This again arises from autodetachment. More details in the text.

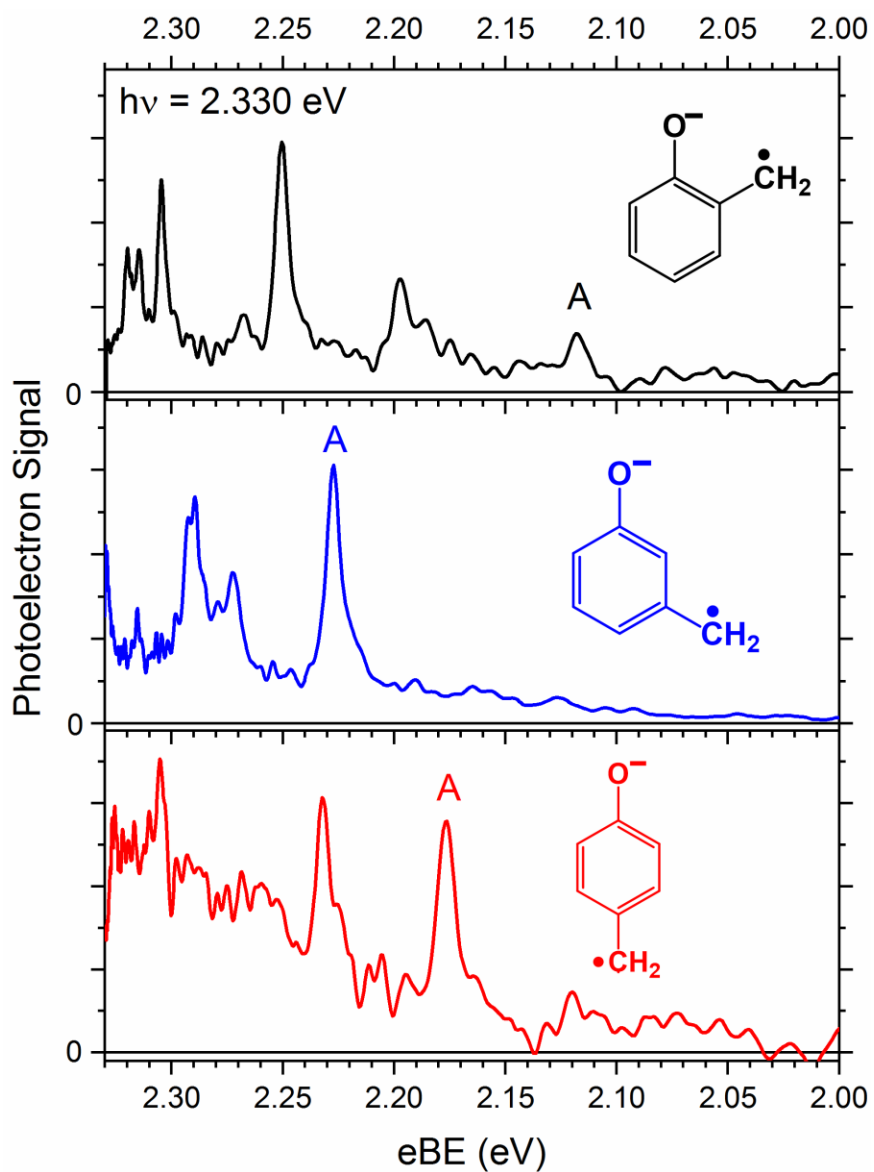


Fig. 4.6 Photoelectron Spectra of the three isomers of the methylenephenoxy anion, collected on the VMI PE spectrometer with a photon energy of 2.330 eV. No simulated spectra are shown as none succeeded in reproducing these data. These spectra were compared to the known PE spectra of methylphenoxide, phenoxide, and benzyl anion, and quantitatively disagree. See Fig. 4.7 for a comparison to methylphenoxide at the same photon energy.

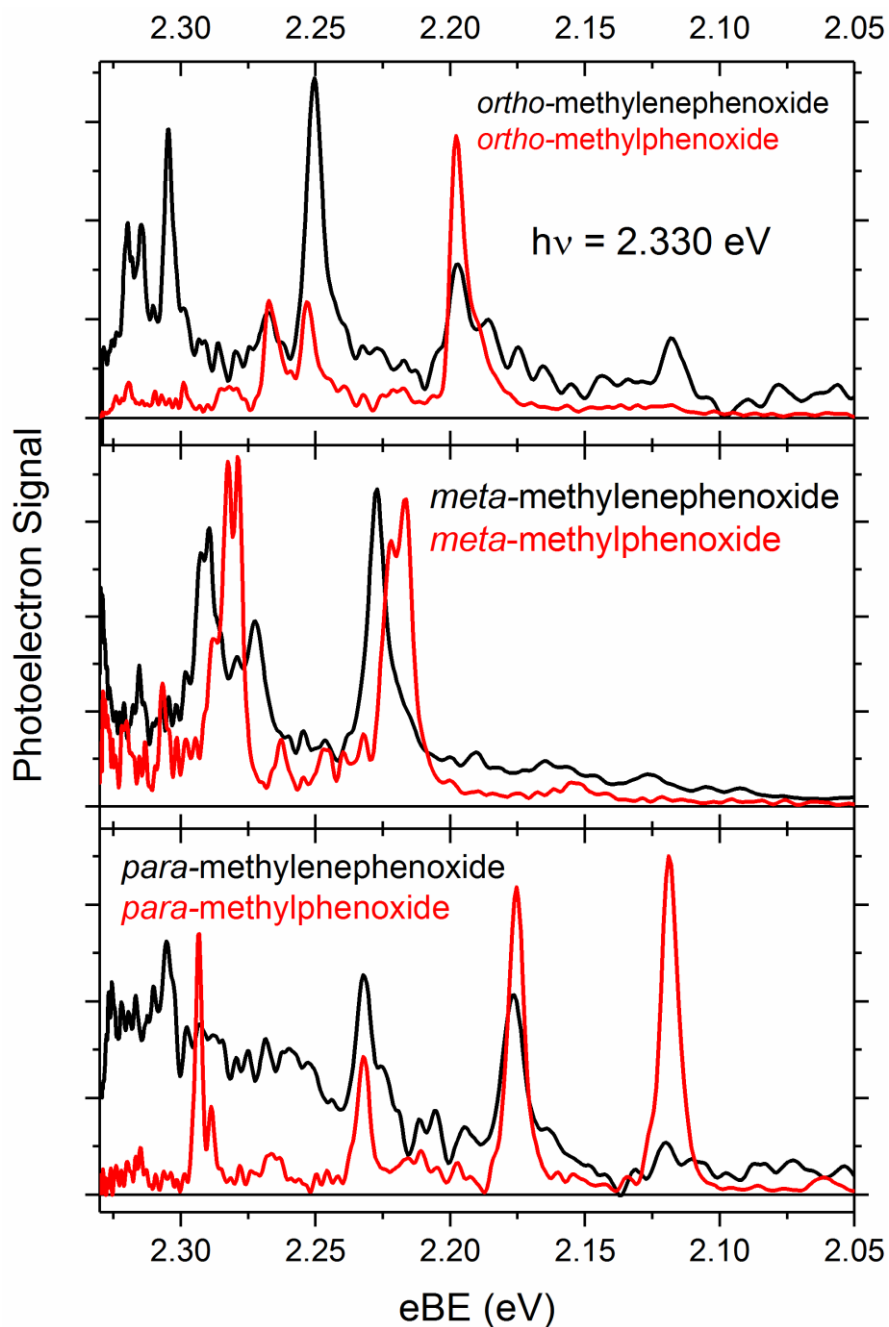


Fig. 4.7 Photoelectron spectra obtained with a photon energy of 2.330 eV on instrument B. These spectra were obtained by simply alternating the laser timing to either intersect $m/z = 106$ (methylenephenoxy, black curves) or 107 (methylphenoxy, red curves). For any given isomer, the red and black spectra may share several similarities, however, they quantitatively are not the same.

§ 4.8 Results: Thermochemistry

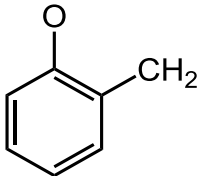

The acid bracketing technique was used to identify the acidity of the protonated forms of the three anions of interest in this paper, namely *o*-, *m*-, and *p*-methylenephenol. See Table 4.3. These results were gathered with Instrument C and are combined with the other thermodynamic results in Table 4.4. Using these data, experimental values for the acidity ($\Delta_{acid}H_{298K}^{\circ}$) of the *o*-, *m*-, and *p*-methylenephenol radicals were found to be 341.4 ± 4.3 , 349.1 ± 3.0 , and 341.4 ± 4.3 kcal/mol respectively. These were theoretically (B3LYP/aug-cc-pVTZ) predicted to be 341.3, 347.0, and 340.4 kcal/mol, respectively. This modelling was performed assuming that the protonation site of the distonic radical anions in the experiment is at O, and the close agreement with the experimental results corroborate this assumption. Protonation on the CH₂ site was also modeled, but those predictions fell outside the experimental error bars by >10 kcal/mol, and were so discounted.

The experimental determination of both the acidities, as well as the EAs of *o*- and *p*-methylenephenoxyl enables a determination of the O-H bond strength in the methylenephenol radical isomers in the gas phase, via a thermochemical cycle.⁴¹ The experimental values for the acidities had to be adjusted to their 0 K values using the calculated heat capacities at constant pressure, C_p.³⁴ The dissociation energies were derived to be 48 ± 5 and 45 ± 5 kcal/mol for *o*- and *p*-methylenephenol, respectively.

Table 4.3 Summary of acid bracketing results. A “+” denotes an exothermic proton transfer occurred, while a “-” denotes its absence. All acidities taken from the NIST Chemistry Reference Database.⁴²

Reference Acid	$\Delta_{acid}G_{298 K}^{\circ}$ /kcal mol ⁻¹	$\Delta_{acid}H_{298 K}^{\circ}$ /kcal mol ⁻¹	<i>o</i> - methylene- phenoxide	<i>m</i> - methylene- phenoxide	<i>p</i> - methylene- phenoxide
<i>p</i> -Trifluoromethylphenol	330.1 ± 1.9	337.0 ± 2.2	+	+	+
3-Mercapto-propionic acid	332.4 ± 1.9	339.4 ± 2.2	+	+	+
<i>o</i> -Chlorophenol	337.1 ± 1.9	343.4 ± 2.4	-	+	-
<i>p</i> -Fluorophenol	339.9 ± 1.9	346.8 ± 2.2	-	+	-
Propionic acid	340.4 ± 2.0	347.4 ± 2.2	-	+	-
Acetic acid	341.1 ± 2.0	348.1 ± 2.2	-	+	-
Phenol	342.3 ± 2.0	350.0 ± 2.0	-	-	-
2,2,3,3,3-Pentafluoro-1- propanol	348.8 ± 6.0	355.4 ± 6.1	-	-	-

Table 4.4 Summary of Results. Measured values are displayed in plain text while calculated values are in italics.

	EA / eV	Singlet-Triplet splitting / eV	$\Delta_{acid}H_{298K}^{\circ} /$ <i>kcal mol⁻¹</i>	BDE ^a / <i>kcal mol⁻¹</i>
	1.217 ± 0.012 <i>1.296^b</i>	1.535 ± 0.019 <i>1.498^b</i>	341.4 ± 4.3 <i>341.3^b</i>	48 ± 5 <i>58^b</i>
	1.096 ± 0.007 <i>1.178^b</i>	≥ 1.8 <i>1.962^b</i>	341.4 ± 4.3 <i>340.4^b</i>	45 ± 5 <i>56^b</i>

^aRefers to O-H bond of the corresponding methylenephenol radical
^bCalculated value: ROCBS-QB3 for all but the acidities, which used B3LYP/aug-cc-pVTZ

§ 4.9 Discussion

In general, the *ortho* and *para* isomers display good agreement with theory in regions A and C of Fig. 4.2, and may be mostly understood with simple physical pictures, such as resonance and molecular orbital theory. On the contrary, the data obtained on the *meta* case has proven highly resistant to the calculations that were attempted. Region B (Fig. 4.2) is similar among the three isomers but is unexplained thus far. Regardless, several observations may be made. First, all three isomers display a progression starting at ~ 2 eV binding energy, which suggests that the observed electrons were strongly associated with an oxygen prior to photodetachment. Second, each of these progressions display regularly placed peaks with a spacing of ~ 500 cm^{-1} . This is indicative of ring distortion vibrational mode excitations upon photodetachment. Third, in each case the highest intensity peak is not at the start of the progression, see Fig. 4.2, suggesting a large geometry change between the anion and neutral species. These spectra were also compared with PE spectra of other likely aromatic compounds, such as phenoxide³⁷ or the methylphenoxides.³⁴ While the spectra are not in quantitative agreement, both in peak positions and relative peak intensities, there are striking similarities to the overall spectra. See Fig. 4.7. The similarities among these spectra, along with the general observations listed above, suggest that the anion responsible for region B contains a ring structure and that the negative charge is localized on the oxygen.

Given the above experimental observations, a range of structural isomers with $m/z = 106$ were tested with the aid of calculations. Single reference electronic structure calculations failed to predict the origin of the progressions in region B, and thus we conclude that these progressions do not arise from single photon detachment (or direct detachment) from

methylenephenoxide. It is possible for multi-photon events to occur in this spectrometer, although this was not tested directly using power dependence measurements.

The electron affinities of the two methylenephenoxyl diradicals measured in this work can be compared to the deprotonated methylphenols, studied previously, in order to gain some physical insight.³⁴ The EAs for the *o*-, *m*-, and *p*-methylphenoxyl radicals are 2.1991 ± 0.0014 , 2.2177 ± 0.0014 , and 2.1199 ± 0.0014 eV, respectively. Qualitatively, the two measured methylenephenoxyl diradicals have an EA of ~ 1 eV, while the methylphenoxyl radicals all have EAs of ~ 2 eV. The main difference between these two groups of molecules is that the methylphenoxyls have a CH₃ functional group, which is slightly electron donating, whereas the methylenephenoxyl diradicals have a \bullet CH₂ group, which is electron withdrawing. Using this as a starting point, one can think of the CH₃ group repelling the excess charge in the anion onto the O, while the \bullet CH₂ group attracts the excess charge away from the O, and into the ring. Removing an electron strongly localized on a functionalized oxygen on a ring generally takes ~ 1.5 - 2 eV to accomplish, whereas removing an electron delocalized about an aromatic ring requires ~ 1 eV.³⁵ ³⁷ This model accounts for the ~ 1 eV difference in EAs between the methylenephenoxyls and methylphenoxyls. This physical picture would also lead one to expect more ring distortion upon photodetachment for the methylenephenoxide anions compared to the methylphenoxides, and indeed, the longer, more congested vibronic progressions found within the PE spectra of the methylenephenoxide anions support this expectation.

The singlet-triplet splittings in the *o*- and *p*- methylenephenoxyl diradicals are now considered. The ground state has been identified as an open shell singlet electronic state for both isomers. An experimental determination of the singlet-triplet splittings for each has been identified and found to be 1.535 ± 0.019 and ≥ 1.8 eV, in agreement with the calculated values of

1.498 and 1.962 eV, respectively. This was an initially surprising result. One might consider the case of the benzyne diradical, studied previously,³⁵ to be an appropriate analog of methylenephenoxide and use this to guide their intuition. In that system, as the two radical sites were brought closer together, i.e. starting with *para*-, then *meta*-, and finally *ortho*-benzyne, the singlet-triplet energy difference monotonically increased from 0.167 ± 0.016 to 1.628 ± 0.013 eV. This makes intuitive sense. One would expect the coupling between the two radical electrons would increase as they come into closer spatial proximity with one another, thus translating the singlet and triplet states further apart in energy. In the methylenephenoxyl diradicals, this does not appear to be the case. Indeed, the opposite trend is observed; the *para* isomer displays the largest observed splitting, ≥ 1.8 eV. However, it is important to consider the influence of resonance on this analysis. In the neutral singlet state of methylenephenoxyl, the radical electron on the $\cdot\text{CH}_2$ functional group can interact with the conjugated π system of the aromatic ring, and likewise for the radical electron localized about the O. This has a stabilizing effect in the neutral ground state, as the $\cdot\text{CH}_2$ group may form a quasi-double bond with the ring, drawing charge density from it. However, in the triplet state the radical electrons are forced into orbitals in the plane of the benzene ring, and are so unable to conjugate with the aromatic π system. Thus the system has lost the stabilizing effects it benefitted from in the neutral ground electronic singlet state, putting the triplet state higher in energy than what might have otherwise been expected. While this does explain why the *para* isomer has a much larger ΔE_{ST} as compared to *p*-benzyne by an order of magnitude, it does not necessarily explain why *p*-methylenephenoxyl has a larger singlet-triplet splitting than *o*-methylenephenoxyl, since they should both benefit from approximately the same resonance effects. Likely, the added complication of the O...CH₂ interaction in the *ortho* isomer and/or the increased symmetry of the *para* case is significant. As

to the *meta* isomer, the spectrum remains unassigned for the reasons previously given, and thus no measurement of the singlet – triplet splitting can be performed. Since calculations have proven unreliable for this isomer, a calculation of ground and excited states, though performed, will not be presented here. Whether the ground state is a singlet or triplet state must remain an open question for the moment.

Utilizing these same resonance ideas discussed above, the vibrational structures observed can also be explained. As opposed to the methylphenoxide anions, which showed primarily only ring distortion modes ($\sim 500\text{ cm}^{-1}$) being activated upon photodetachment, the methylenephenoxy anions display both ring distortion, and C–O, C–C stretching/ring distortion modes ($\sim 1600\text{ cm}^{-1}$) becoming excited upon photodetachment. This is again due to the fact that CH_2 is an electron withdrawing group, attracting the excess charge away from the O and onto the ring in the anion, as well as onto the CH_2 itself. In the anionic form, these ions will distort the ring away from a benzene-like structure. For example, in the *p*-methylenephenoxy anion the CCC angle about the α -carbon to the O is 115° while the CCC angle about the α -carbon to the CH_2 group is 114° , according to calculations. If this structure were an ideal benzene ring, these angles would be 120° . Upon photodetachment to form the neutral diradical however, these angles have equilibrium values of 117° and 116° , respectively. Thus upon photodetachment, the ring becomes less strained and approaches a more benzene-like equilibrium structure. This is qualitatively true for the ortho isomer as well. In addition, the C–O and C–CH₂ bonds each constrict by $\sim 0.05\text{ \AA}$ upon photodetachment giving rise to C–O, and C–C stretching-like modes which were not as prevalent at all in the PE spectra of the methylphenoxides accessing the ground neutral state. This makes intuitive sense; in the deprotonated case, an electron donating methyl group attached to the ring would not cause the

electron to be localized as much about the α -carbon of the O, and so less distortion of the C-O bond is expected. In the case of the methylenephenoxides the opposite is true, as the electron would be drawn more towards the ring and to the CH_2 group.

For those spectra wherein we claim good agreement between experimental data and theoretical simulations (see Figs. 4.3 and 4.4), there remain several disparities which should be addressed. First, in all cases, there is more broadening than can be explained by experimental resolution or predicted spectral congestion. One might consider if rotational broadening could explain this, but the predicted changes in the rotational constants for all the isomers considered here are $< 0.01 \text{ cm}^{-1}$, making this an unlikely contribution to the observed broadening.⁴³ Such an extensive broadening in larger aromatic, and/or frequently diradical, compounds have been frequently observed previously.^{3, 8, 44} Second, at higher binding energies, the predicted peak positions tend to trend higher in energy compared to the experiment, but this is an expected feature of anharmonicity. Third, in the course of studying these species, several more spectra than shown in the main text here were taken with other photon energies, and a photon energy dependence of the *meta* PE spectra were observed and are found in Fig. 4.5. This phenomenon is attributed to electron autodetachment, which has been a hallmark in similar aromatic species.^{34, 37-39} This hypothesis is corroborated by time-dependent density functional theory (TD-DFT) excited state calculations which predict many (>10) optically accessible anionic excited electronic states within 3 eV of the ground electronic state. The broadening observed in these spectra varies with photon energy, and autodetachment is the likely cause of the majority of the disagreement with our simulations, which do not take such phenomena into account.

The thermochemistry of these molecules is now considered. The relatively weak bond strengths of the methylenephenol radical isomers may be found in Table 4.4. This property may

also be explained with similar resonance ideas as were introduced earlier. The electron withdrawing nature of the $\cdot\text{CH}_2$ group removes electron density, and therefore bond strength, from the O-H bond, explaining these weak BDEs. Additionally, the methylenephenoxide distonic radical anions are relatively non-reactive, as evidenced by the low proton affinities. As a general rule, one might expect such species to be reactive and quite basic.⁴⁵ Indeed, distonic radical anions and cations are often found to be reactive intermediates in organic mechanisms.^{46, 47} However, these data suggest that this group would be long lived, and reasonably stable. In this case, this is likely due to the electron withdrawing nature of the $\cdot\text{CH}_2$ group as well, strongly drawing the negative charge onto the aromatic ring, and onto the $\cdot\text{CH}_2$ itself, thus stabilizing the anion. Relatively nonreactive distonic radical anions are not without precedent, but could prove to be interesting to some in the scientific community.^{48, 49}

§ 4.10 Conclusions

Anion photoelectron (PE) spectroscopy was performed and the photoelectron spectra of the distonic radical *o*-, *m*-, and *p*-methylenephenoxide anions have been reported. The EAs of the *o*-, and *p*- methylenephenoxyl diradicals were measured to be 1.217 ± 0.012 and 1.096 ± 0.007 eV, respectively. Upon photodetachment, these distonic radical anions were shown to have Franck Condon active vibrational ring distortion modes with measured frequencies of 570 ± 180 and 450 ± 80 cm^{-1} in the *ortho* and *para* isomers accessing the neutral diradical singlet ground electronic states. C-O/ring distortion vibrational modes were also activated in the *para* isomer accessing the same electronic state of the neutral diradical. These transitions could not be separately measured and therefore the only value for the frequency of these modes is 1570 ± 270 cm^{-1} . Photodetachment to the first electronically excited triplet state was also investigated and similar vibrational modes were found to be Franck–Condon active for the *ortho* isomer, while the *para* isomer proved more difficult to interpret. The *ortho* isomer showed excitation of ring distortion vibrational modes with a measured frequency of 450 ± 160 cm^{-1} and excitation of a C-O/ring distortion vibrational mode with a frequency of 1470 ± 170 cm^{-1} . The thermochemistry of these molecules were also investigated using Flowing Afterglow-Selected Ion Flow Tube mass spectrometry with the acid bracketing technique, and thus the proton affinity of the *o*-, *m*-, and *p*-methylenephenol radicals were determined to be 341.4 ± 4.3 , 349.1 ± 3.0 , and 341.4 ± 4.3 kcal/mol respectively. Construction of a thermodynamic cycle allowed for an experimental determination of the weak bond dissociation energy of the O-H bond for the *ortho* and *para* isomers, 49 ± 5 , and 47 ± 5 kcal/mol respectively. Most of the trends and behaviors observed here can be explained by resonance and the effects of electron withdrawing groups in aromatic chemistry.

§ 4.11 References

- 1) B. Breiner, K. Kaya, S. Roy, W.-Y. Yang and I. V. Alabugin, *Org. Biomolec. Chem.* **10**, 3974-3987 (2012).
- 2) K. M. Stirk, L. K. M. Kiminkinen and H. I. Kenttamaa, *Chem. Rev.* **92**, 1649-1665 (1992).
- 3) G. E. Davico, R. L. Schwartz, T. M. Ramond and W. C. Lineberger, *J. Amer. Chem. Soc.* **121**, 6047-6054 (1999).
- 4) E. Goldstein, B. Beno and K. N. Houk, *J. Amer. Chem. Soc.* **118**, 6036-6043 (1996).
- 5) J. Gräfenstein, A. M. Hjerpe, E. Kraka and D. Cremer, *J. Phys. Chem. A* **104**, 1748-1761 (2000).
- 6) L. Koziol, V. A. Mozhayskiy, B. J. Braams, J. M. Bowman and A. I. Krylov, *J. Phys. Chem. A* **113**, 7802-7809 (2009).
- 7) R. Lindh, T. J. Lee, A. Bernhardsson, B. J. Persson and G. Karlstroem, *J. Amer. Chem. Soc.* **117**, 7186-7194 (1995).
- 8) W. C. Lineberger and W. T. Borden, *Phys. Chem. Chem. Phys.* **13**, 11792-11813 (2011).
- 9) A. Rajca, *Chem. Rev.* **94**, 871-893 (1994).
- 10) E. Ramos-Cordoba and P. Salvador, *Phys. Chem. Chem. Phys.* **16**, 9565-9571 (2014).
- 11) V. Vanovschi, A. Krylov and P. Wenthold, *Theoretical Chemistry Accounts* **120**, 45-58 (2008).
- 12) G. P. F. Wood, L. Radom, G. A. Petersson, E. C. Barnes, M. J. Frisch and J. A. Montgomery, *J. Chem. Phys.* **125**, 094106 (2006).
- 13) M. A. Kurinovich and J. K. Lee, *J. Am. Soc. Mass Spectrom.* **13**, 985-995 (2002).
- 14) J. M. Van Doren, S. E. Barlow, C. H. DePuy and V. M. Bierbaum, *Int. J. Mass Spectrom. Ion Processes* **81**, 85-100 (1987).

- 15) D. G. Leopold, K. K. Murray, A. E. S. Miller and W. C. Lineberger, *J. Chem. Phys.* **83**, 4849-4865 (1985).
- 16) K. M. Ervin, J. Ho and W. C. Lineberger, *J. Phys. Chem.* **92**, 5405-5412 (1988).
- 17) Y.-J. Lu, J. H. Lehman and W. C. Lineberger, *J. Chem. Phys.* **142**, 044201 (2015).
- 18) A. T. J. B. Eppink and D. H. Parker, *Rev. Sci. Instrum.* **68**, 3477-3484 (1997).
- 19) L. Sheps, E. M. Miller and W. C. Lineberger, *J. Chem. Phys.* **131**, 064304 (2009).
- 20) B. Ruscic, A. F. Wagner, L. B. Harding, R. L. Asher, D. Feller, D. A. Dixon, K. A. Peterson, Y. Song, X. Qian, C.-Y. Ng, J. Liu, W. Chen and D. W. Schwenke, *J. Phys. Chem. A* **106**, 2727-2747 (2002).
- 21) J. Cooper and R. N. Zare, *J. Chem. Phys.* **48**, 942-943 (1968).
- 22) K. M. Ervin, I. Anusiewicz, P. Skurski, J. Simons and W. C. Lineberger, *J. Phys. Chem. A* **107**, 8521-8529 (2003).
- 23) D. M. Neumark, K. R. Lykke, T. Andersen and W. C. Lineberger, *Phys. Rev. A* **32**, 1890-1892 (1985).
- 24) V. Dribinski, A. Ossadtchi, V. A. Mandelshtam and H. Reisler, *Rev. Sci. Instrum.* **73**, 2634-2642 (2002).
- 25) H. Hotop and W. C. Lineberger, *J. Phys. Chem. Ref. Data* **14**, 731-750 (1985).
- 26) C. Blondel, W. Chaibi, C. Delsart, C. Drag, F. Goldfarb and S. Kröger, *Euro. Phys. J. D* **33**, 335-342 (2005).
- 27) A. D. Becke, *J. Chem. Phys.* **98**, 5648-5652 (1993).
- 28) M. J. Frisch, G. W. Trucks, H. B. Schlegel, G. E. Scuseria, M. A. Robb, J. R. Cheeseman, G. Scalmani, V. Barone, B. Mennucci, G. A. Petersson, H. Nakatsuji, M. Caricato, X. Li, H. P. Hratchian, A. F. Izmaylov, J. Bloino, G. Zheng, J. L. Sonnenberg, M. Hada, M. Ehara, K. Toyota, R. Fukuda, J. Hasegawa, M. Ishida, T. Nakajima, Y. Honda, O. Kitao, H. Nakai, T. Vreven, J. A. Montgomery Jr., J. E. Peralta, F. Ogliaro, M. J. Bearpark, J. Heyd, E. N. Brothers, K. N. Kudin, V. N. Staroverov, R. Kobayashi, J. Normand, K. Raghavachari, A. P. Rendell, J. C.

Burant, S. S. Iyengar, J. Tomasi, M. Cossi, N. Rega, N. J. Millam, M. Klene, J. E. Knox, J. B. Cross, V. Bakken, C. Adamo, J. Jaramillo, R. Gomperts, R. E. Stratmann, O. Yazyev, A. J. Austin, R. Cammi, C. Pomelli, J. W. Ochterski, R. L. Martin, K. Morokuma, V. G. Zakrzewski, G. A. Voth, P. Salvador, J. J. Dannenberg, S. Dapprich, A. D. Daniels, Ö. Farkas, J. B. Foresman, J. V. Ortiz, J. Cioslowski and D. J. Fox, REV. B, Gaussian 09, 2009, see www.gaussian.com

29) K. M. Ervin, PESCAL, 2010, see www.wolfweb.unr.edu/~ervin/pes/

30) K. M. Ervin, T. M. Ramond, G. E. Davico, R. L. Schwartz, S. M. Casey and W. C. Lineberger, J. Phys. Chem. A **105**, 10822-10831 (2001).

31) T. E. Sharp and H. M. Rosenstock, J. Chem. Phys. **41**, 3453-3463 (1964).

32) P. Chen, *Unimolecular and Bimolecular Reactions Dynamics* (John Wiley & Sons, Chichester, 1994) 371.

33) E. B. Wilson, Jr., Phys. Rev. **45**, 706-714 (1934).

34) D. J. Nelson, W. K. Gichuhi, E. M. Miller, J. H. Lehman and W. C. Lineberger, J. Chem. Phys. **146**, 074302 (2017).

35) P. G. Wenthold, R. R. Squires and W. C. Lineberger, J. Amer. Chem. Soc. **120**, 5279-5290 (1998).

36) A. Sanov, Annu. Rev. Phys. Chem. **65**, 341-363 (2014).

37) R. F. Gunion, M. K. Gilles, M. L. Polak and W. C. Lineberger, Int. J. Mass Spectrom. Ion Processes **117**, 601-620 (1992).

38) D.-L. Huang, H.-T. Liu, C.-G. Ning and L.-S. Wang, J. Chem. Phys. **142**, 124309 (2015).

39) H.-T. Liu, C.-G. Ning, D.-L. Huang, P. D. Dau and L.-S. Wang, Angew. Chem. Int. Ed. **52**, 8976-8979 (2013).

40) K. K. Morishetti, P. Sripadi, V. Mariappanadar and J. Ren, Int. J. Mass spectrom. **299**, 169-177 (2011).

41) K. M. Ervin and V. F. DeTuri, J. Phys. Chem. A **106**, 9947-9956 (2002).

- 42) J. E. B. D. R. Burgess, *Thermochemical Data in NIST Chemistry WebBook, NIST Standard Reference Database Number 69*, Eds. P.J. Linstrom and W.G. Mallard, <http://webbook.nist.gov/chemistry/>
- 43) M. J. Travers, D. C. Cowles, E. P. Clifford, G. B. Ellison and P. C. Engelking, *J. Chem. Phys.* **111**, 5349-5360 (1999).
- 44) T. Ichino, S. M. Villano, A. J. Gianola, D. J. Goebbert, L. Velarde, A. Sanov, S. J. Blanksby, X. Zhou, D. A. Hrovat, W. T. Borden and W. C. Lineberger, *J. Phys. Chem. A* **115**, 1634-1649 (2011).
- 45) S. Gronert, *Chem. Rev.* **101**, 329-360 (2001).
- 46) M. Born, S. Ingemann and N. M. M. Nibbering, *Mass Spectrom. Rev.* **16**, 181-200 (1997).
- 47) V. N. Staroverov and E. R. Davidson, *J. Amer. Chem. Soc.* **122**, 186-187 (2000).
- 48) G. Gryn'ova and M. L. Coote, *J. Amer. Chem. Soc.* **135**, 15392-15403 (2013).
- 49) K. Pius and J. Chandrasekhar, *J. Chem. Soc. [Perkin 2]* 1291-1295 (1988).

CHAPTER V

ANION PHOTOELECTRON SPECTROSCOPY OF DEPROTONATED INDOLE AND INDOLINE

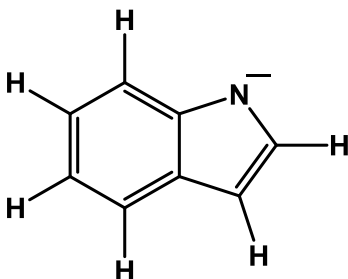
Portions of this chapter have been submitted for publication to The Journal of Chemical Physics under the same title, by, Daniel J. Nelson, Allan M. Oliveira, and W. Carl Lineberger

§ 5.1 Introduction and Background

As was discussed in § 1.5, the biologically relevant bicyclic aromatic molecules indole and indoline are of consequence to the fields of biochemistry and biophysics due to their role as chromophores in biological systems.

The anion photoelectron spectra of indolide is presented in this study. These data provide the electron affinity of the associated neutral, indolyl, and those vibrational modes which are excited upon electron photodetachment of indolide, aided by quantum chemical calculations. Combining the newly measured EA of indolyl with the past measured acidity allows for the determination of the bond dissociation energy.¹

Structure of Indolide



The PE spectroscopy of deprotonated indoline was also collected, however the anion photoelectron spectrum of deprotonated indoline consisted of a featureless broad band extending

from ~1.3 eV to 1.7 eV electron Binding Energy (eBE). The congested nature of the spectrum is likely due to the presence of multiple isomers of deprotonated indoline, including ring opened structures. As such, the results and discussion of the deprotonated indoline data are held separate from the indolide data and examined last, for the sake of clarity.

§ 5.2 Experimental Specifics

The experimental apparatus has been discussed in detail previously^{2,3} (§ 2.7) and will only be explained briefly here, with special attention as to the generation of the anions of interest.

Indole (99% pure) was purchased from Sigma Aldrich Inc. and used without further purification. Crystalline indole has a relatively low vapor pressure and was heated to ~70 °C to obtain adequate indolide production.

The anion of interest is formed in a dual pulsed valve ion source.³ (§ 2.8) These valves (Parker-Hannifin General Valve, Series 9) are oriented such that the gas expansions are perpendicular to each other. One of the valves is the primary supersonic expansion (10 psig, ~1% indole or indoline, in Ar). The other valve, designated the side valve (35 psig, 1% O₂, 30% H₂, in Ar), produces about 5 % of the total gas load. The side valve has discharge plates placed immediately in front of the valve exit, producing a plasma containing hydroxide. The plasma is subsequently entrained into the supersonic expansion of the primary valve. This allows for deprotonation of indole by OH⁻.⁴ The hydroxide anion will be shown to only generate indolide upon reaction with indole in this experimental setup. The resultant product and byproducts are collisionally cooled by the Ar atoms in the main supersonic expansion.

The entrained anions are then extracted into a Time-Of-Flight (TOF) Wiley-McLaren mass spectrometer. (§ 2.9) The anions are separated by their mass-to-charge ratio (m/z) and spatially focused at the interaction region of a Velocity Map Imaging (VMI) photoelectron spectrometer. (§ 2.10) An appropriately timed nanosecond pulse from the photodetachment laser then intersects the anions of a chosen mass. The VMI first stage is pulsed to the operating voltage, velocity mapping the photoelectrons onto the plane of a Micro-Channel Plate (MCP) coupled to a phosphor screen and subsequently imaged with a CCD camera. The resulting image gives direct

measurement of the two-dimensional velocity distribution. The MEVELER (Maximum Entropy Velocity Legendre Reconstruction) program⁵ was used to reconstruct the full three-dimensional velocity distribution of the photoelectrons. This three dimensional distribution is transformed into the one dimensional speed distribution, and then into the electron Kinetic Energy (eKE) distribution, by means of a Jacobian transform. Finally, the eKE is transformed into the electron Binding Energy (eBE) by subtracting the eKE distribution from the photon energy.

The VMI has an energy resolution that depends upon eKE, with the best resolution obtained for the lowest photoelectron kinetic energy. For the experiments reported here, the energy resolution was determined to follow the relation

$$\text{Resolution(eKE)} \cong (0.003 + 0.03 \text{ eKE}) \text{ eV} \quad (1)$$

The constant term is the limiting resolution of the apparatus, in this case 3 meV. The energy scale in the overview spectrum shown in Fig. 5.1 was calibrated with the known photoelectron spectrum of S⁻.⁶⁻⁸ By employing multiple laser wavelengths, we can obtain composite photoelectron spectra spanning several eV, with resolution near the instrumental limit throughout the full range. This procedure is known as Slow Electron Velocity-Map Imaging (SEVI) photoelectron spectroscopy, pioneered by Neumark.⁹ The data in Figs. 5.2-4 were obtained at a number of laser wavelengths, chosen so as to take advantage of this higher resolution approach. The photon energies used to obtain these spectra were calibrated with an ATOS λ -meter (LRL-005).

All of the spectra shown here are obtained making use of a seeded Nd:YAG pulsed nanosecond laser. The data found in Fig. 5.1 were obtained utilizing the 3rd harmonic of the Nd:YAG lasing transition (3.494 eV). The spectra shown in Figs. 5.2 and 5.3 were collected

utilizing photon energies generated by a visible light optical parametric oscillator (OPO) pumped by the 3rd harmonic of the aforementioned Nd:YAG laser.

Throughout this work, uncertainty in the reported peak positions are functions of the statistical error in finding the peak center, the error in the absolute energy scale, and the number of independent measurements of particular peaks. When reporting the energy associated with a particular transition associated with a peak, the uncertainty in that peak position is combined with the error associated with the offset of the actual transition from the peak center. This aggregated additional uncertainty can be near zero if only a single vibronic transition is the major contributor to the peak shape. If, however, multiple unresolved vibronic transitions contribute significantly to the overall envelope, the uncertainty in location of any individual transition could be as large as the Half-Width-at-Half-Maximum (HWHM) of the peak. Shifts caused by asymmetry in the rotational envelope about each vibrational transition are taken into account. using the peak shape analysis of Engelking and coworkers.¹⁰ This rotational correction did not have a significant effect for transitions reported here. In general, the peaks presented in these spectra are comprised of multiple transitions, and the uncertainty associated with these contributions is the dominant component of the reported uncertainties of transition energies.

§ 5.3 Theoretical Methods and Simulations

Optimized geometries, electronic structure, and harmonic vibrational normal mode analyses were carried out utilizing the Gaussian 09 program suite.¹¹ These calculations were performed at the B3LYP/aug-cc-pVTZ level of theory/basis set. This combination has been found to be an effective compromise between accuracy and computational cost.¹² Several excited state calculations were also carried out and made use of Time Dependent Density Functional Theory (TD-DFT) employing the same hybrid functional, B3LYP, and Dunning basis set, aug-cc-pVTZ. All reported EAs are calculated from the Zero-Point Energy (ZPE) corrected energy difference between the optimized electronic ground neutral state and the optimized electronic ground anionic state.

The optimized geometries and harmonic normal mode analyses were utilized to simulate the photoelectron spectra collected in this experiment and aid in their interpretation. These spectra were simulated assuming that only the Franck-Condon Factors (FCFs, § 1.1) influence a given photodetachment transition intensity; *i.e.* the electronic component of the photodetachment cross-section is constant across a given spectrum. Thus, the simulated spectra do not capture behavior such as electron autodetachment. The FCFs were computed via the Sharp-Rosenstock-Chen method, making use of Duschinsky rotations.¹³⁻¹⁵ These factors, associated with specific vibrational transitions, along with an assumed 200 K Boltzmann distribution of internal energy in the anions, were computed with the PESCAL program.¹⁶ While these simulations assume full thermal equilibration among the vibrational degrees of freedom of indolide, such is not necessarily the case. These intensities associated with specific transitions are represented as red sticks in Figs. 5.1–5.4, where the length of any stick is equal to the calculated intensity of that transition, and it is located at the calculated transition electron binding energy. These transition

intensities are converted into simulations of the experimental spectra by convolving each transition with Gaussian functions whose FWHM is commensurate with the instrument resolution, which is a function of eKE , and whose integrated area is equal to that of the calculated transition intensity via home-built programs. The simulations presented are shifted such that the calculated EA matched the observed value. They are also scaled in intensity such that the origin transition of the simulated spectra is in agreement with the peak attributed to the origin transition in the experimental data. This procedure results in the green curves shown in Figs. 5.1–5.4.

It is important to underscore several subtleties involved in a Sharp–Rosenstock–Chen Franck–Condon analysis of polyatomic photoelectron spectra of species that are as large as indole. This analysis first requires identifying and matching the *molecular motion* of particular vibrations in the anion (in the ground electronic state, for any case shown here) to the molecular motion of vibrations of the neutral in some electronic state. The eigenvectors representing these motions may be found in § 5.6, Table 5.3. Hence, a vibrational normal mode designated ν_{35} in the anion might be associated, for instance, with ν_{39} in the neutral molecule. While the molecular motion of a particular vibration will be relatively invariant to the level of theory used to compute it, the frequency associated with that eigenvector may shift by $\sim 50\text{ cm}^{-1}$. This shift might change what is labeled as ν_{30} at one level of theory to be labeled, for example, ν_{33} in a different level of theory, but the molecular motions will remain largely unchanged and therefore would be matched to the same mode in the anion. This relabeling of normal modes depending on the level of theory utilized is not unique to the neutral and will also affect the anion. The simulations shown here rely only on the molecular motions to calculate the FCFs; thus while the ordering scheme used here to label the vibrational modes might be sensitive to the level of theory one might use, the simulations of the PE spectra are not.

Assigning any given peak to a specific transition or transitions is a challenging task for a large molecule, such as indole, and one must rely heavily upon theoretical simulations. Considering the low symmetry of indolyl (C_s), the ordering convention employed here for the calculated vibrational normal modes are simply organized first by the allowed symmetries of the vibrational modes (A' or A'') and then by frequency as seen in Table 5.1. Table 5.1 also provides each Franck–Condon factor associated with the transition from the ground vibrational state in the anion to one quanta of the appropriate mode (and zero quanta in all other normal modes) in the neutral radical. The FCFs have been normalized such that the FCF for the origin transition from the anionic ground vibronic state to the neutral ground vibronic state is unity. This table provides the basis for the vibrational analysis found within this work. Considering the density of vibrational states of both the anion and neutral molecules studied here, computing a given vibrational transition energy and comparing this against the position of the peaks comprising the collected PE spectra cannot result in any firm assignments. Consequently, the computed Franck–Condon factors must be utilized in order to narrow the field of potential vibrational transition assignments to only one or two transitions for a given peak. Even this can only be done if one or two calculated FCFs dominate the predicted intensity of the peak in question. These assignments are further governed by the inherent limitations of relying on the appropriateness of the harmonic oscillator approximation. As such, several assignments made in this work must only be suggested, rather than concretely stated. It is within the limits of these constraints that vibrational transitions are assigned to peaks.

Table 5.1 Calculated Vibrational Analysis of Indolyl

<i>A'</i> Calc. Indolyl Harmonic Transition Energies (cm ⁻¹)		FCF	<i>A''</i> Calc. Indolyl Harmonic Transition Energies (cm ⁻¹)		FCF
1 ₀ ¹	3221	<0.01	28 ₀ ¹	997	<0.01
2 ₀ ¹	3196	<0.01	29 ₀ ¹	963	<0.01
3 ₀ ¹	3193	<0.01	30 ₀ ¹	922	<0.01
4 ₀ ¹	3189	<0.01	31 ₀ ¹	886	<0.01
5 ₀ ¹	3175	<0.01	32 ₀ ¹	783	<0.01
6 ₀ ¹	3167	<0.01	33 ₀ ¹	774	<0.01
7 ₀ ¹	1629	<0.01	34 ₀ ¹	744	<0.01
8 ₀ ¹	1602	0.10	35 ₀ ¹	575	<0.01
9 ₀ ¹	1495	<0.01	36 ₀ ¹	543	<0.01
10 ₀ ¹	1466	0.24	37 ₀ ¹	412	<0.01
11 ₀ ¹	1460	0.07	38 ₀ ¹	241	<0.01
12 ₀ ¹	1373	0.08	39 ₀ ¹	202	<0.01
13 ₀ ¹	1346	0.03			
14 ₀ ¹	1303	<0.01			
15 ₀ ¹	1233	0.03			
16 ₀ ¹	1202	0.07			
17 ₀ ¹	1169	<0.01			
18 ₀ ¹	1162	0.06			
19 ₀ ¹	1096	0.02			
20 ₀ ¹	1026	<0.01			
21 ₀ ¹	966	0.06			
22 ₀ ¹	899	0.11			
23 ₀ ¹	854	<0.01			
24 ₀ ¹	770	0.02			
25 ₀ ¹	587	0.08			
26 ₀ ¹	545	<0.01			
27 ₀ ¹	408	<0.01			

Calculated photoelectron harmonic transition energies and their associated FCFs. Note that the notation of X_0^1 implies that all vibrational modes other than vibrational mode X received no quanta of vibrational excitation. The Franck–Condon factors have been normalized such that the vibronic origin transition FCF is unity. Those vibrations which have been positively identified in this work are shown in bold red font. Note that while the difference in frequency for many modes may be small (~ 10 cm⁻¹), the FCF can vary by a factor of up to 1,000.

§ 5.4 Results: Overview

Prior to examining the data, it is useful to hypothesize the likely behaviors one might expect to observe upon photodetachment of deprotonated indole. In the case of indole, it is likely that deprotonation will occur at the N–H site as this likely has a much greater acidity than any other site on the molecule. This would result in the formation of an anion which might be expected to have a similar PE spectrum to that of pyrrolide, based on the structural similarity of the molecules. The pyrrolyl radical was shown to have an EA of 2.145 ± 0.010 eV and the PE spectrum of pyrrolide displayed excitation of ring distortion vibrational modes upon photodetachment.¹⁷ Assuming that the EA of indolyl would be close to the EA of pyrrolyl is consistent with our calculation of the EA of indolyl, 2.357 eV. If, however, a ring carbon site is deprotonated, a photoelectron spectrum similar to cyclopentadienide might be expected.¹⁸ Although vibrational structure similar to pyrrolyl was observed upon photodetachment of cyclopentadienide (ring distortion vibrational modes), the EA of cyclopentadienyl radical was measured as 1.808 ± 0.006 eV,¹⁸ a value which is significantly lower than that of the pyrrolyl radical. This analysis implies that if the product of deprotonation from a C–H site on indole was present, we would observe a photoelectron spectrum with an origin ~ 0.5 eV eBE below the calculated indolyl electron affinity.

In order to examine the above hypotheses, an overview photoelectron spectrum of indolide obtained with a photon energy of 3.494 eV was collected and is shown in Fig. 5.1. The experimental data are shown as black dots, the calculated Franck Condon factors appear as red sticks, and the full theoretical simulation of the photoelectron spectrum of the indolyl ground state is shown as a green curve. The agreement between theory and experiment is qualitatively correct, but the ground state simulation does not appear to account for the weak, broad feature around

3.2 eV binding energy. As can be seen, the origin of this band is comprised of an intense peak, with a center near 2.4 eV eBE. This result is consistent with the calculation of the EA of indolyl, 2.357 eV, and confirms the formation of the indolide anion. The shaded region was obtained in high resolution (SEVI) and is shown in Fig. 5.2. No photoelectron signals were observed at lower binding energies, which indicates that indole anions arising from carbon site deprotonation are not present in detectable quantities. Thus we conclude that the only observed isomer of deprotonated indole is indolide.

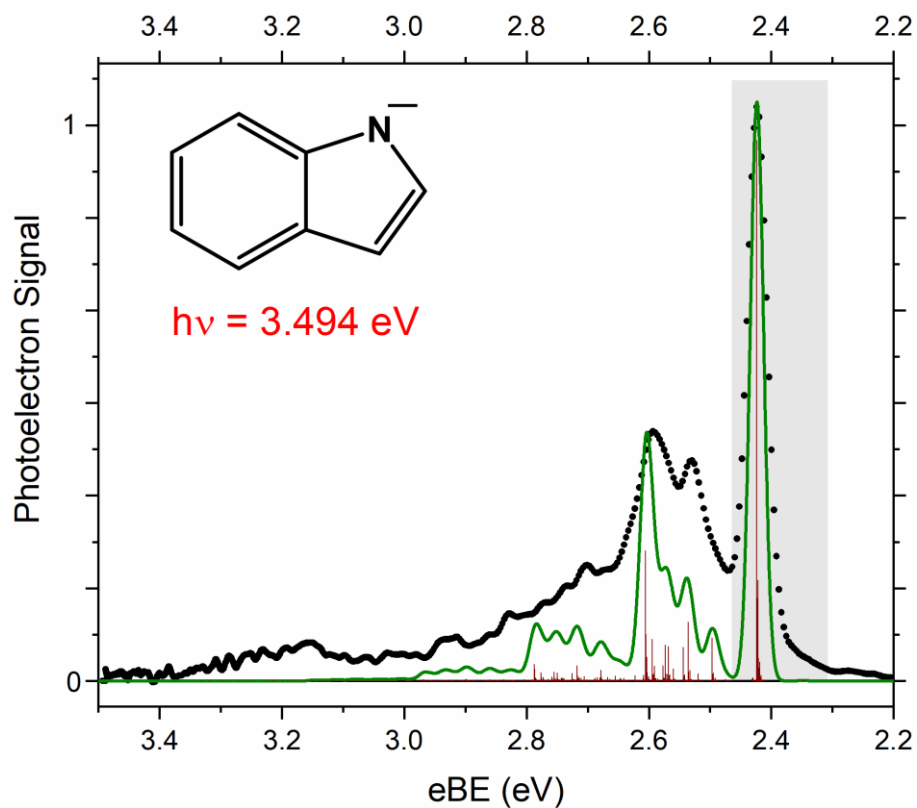


Fig. 5.1 The photoelectron spectrum of indolide obtained with a photon energy of 3.494 eV. The calculated transitions and their associated intensities are represented by red sticks, while the convolution of these sticks with Gaussian functions whose FWHM is commensurate with the instrument resolution is shown in green. This simulation assumed a temperature of 200 K. The shaded region was obtained in high resolution and shown in Fig. 5.2.

The photoelectron spectra presented in this work showed no definitive evidence of the presence of an excited electronic state of indolyl. This result is consistent with the calculated term energy of the first excited electronic state of indolyl being ~ 1.5 eV, and thus would not be accessible with the 3.494 eV photon energy available.

§ 5.5 Results: Electron Affinity of Indolyl and Photoelectron Angular Distributions of Indolide

In order to obtain the EA of indolyl with a greater degree of accuracy and precision, the SEVI technique was employed. Fig. 5.2 displays the SEVI PE spectrum of the origin peak of the progression shown in Fig. 5.1 (grey shaded area). Again, the experimental data are shown as black dots, while the green trace and the red sticks represent the simulation and individual calculated harmonic vibrational transitions and their respective intensities. The calculated origin transition, *i.e.* the transition from the ground electronic and vibrational anionic state to the ground electronic and vibrational state of the neutral radical (0_0^0), has been made bold in the figure. The experimental peak is asymmetric indicating that while the peak primarily arises from the origin transition, other vibrational transitions also contribute. The simulation supports this; while the origin transition dominates the simulated spectrum, there are a number of less significant red-shifted transitions from the origin transition. These additional transitions in the 200 K simulation are the result of sequence-band transitions involving vibrationally excited anions. While observable in the simulations, they do not have a significant effect on the determination of the location of the origin peak, when the fit is limited to an energy range corresponding to roughly the upper 60% of the origin peak, as seen in Fig. 5.2. This procedure allows for a direct measurement of the position of the intense peak, and hence the EA of indolyl, 2.4315 ± 0.0017 eV.

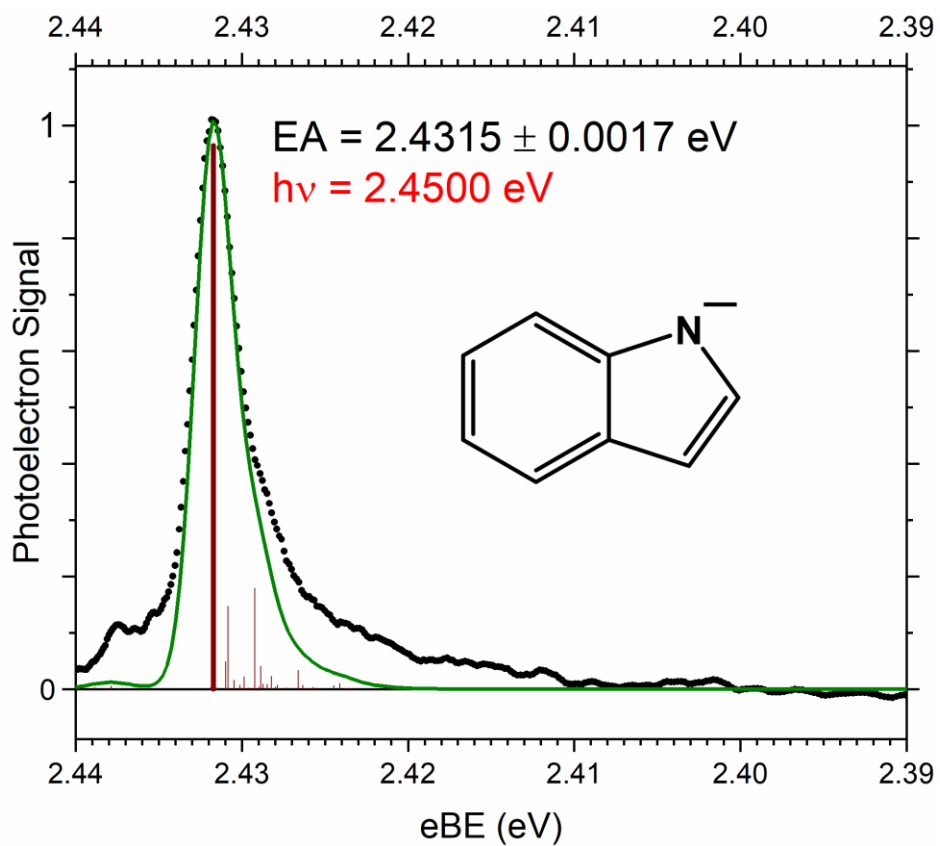


Fig. 5.2 The Slow Electron Velocity–Map Imaging (SEVI) PE spectrum of the origin transition of indolide acquired with a photon energy of 2.4500 eV. The simulated spectrum is shown in green, with the individual transitions and their respective intensities shown as red sticks. The 0_0^0 transition stick is shown in bold. This simulation assumed a temperature of 200 K.

In addition to the electron affinities, photoelectron angular distributions with respect to the laser polarization, characterized by the anisotropy parameter (β), were measured for these photoelectron spectra. Since the electron detached from indolide to form the ground electronic state of indolyl can be described as populating a nitrogen p-like orbital, it is expected that we should observe an isotropic angular distribution ($\beta \sim 0$) for low kinetic energy photoelectrons which shifts to an anisotropic distribution characterized by negative values of β at higher kinetic energies.^{19, 20} This is, in fact, what is observed. In the case of low kinetic energy photoelectrons, such as those found in Figs. 5.2 and 5.3, an isotropic angular distribution of the origin transition is observed. When utilizing a photon energy of 3.494 eV (Fig. 5.1), giving rise to photoelectron kinetic energies higher than in the PE spectra found in Figs. 5.2 and 5.3, an anisotropic angular distribution of the origin transition was observed, characterized by $\beta \sim -0.25$.

§ 5.6 Results: Vibrational Analysis of Indolyl

Considering the large number of vibrational modes predicted to be activated upon photodetachment of indolide, several spectra were obtained at three different photon energies in an attempt to obtain higher resolution spectra of these vibrational transitions. See Fig. 5.3. Experimental data are shown in black, while theoretical modeling is shown as red sticks and green curves. Several observations are immediately apparent. First, in all three spectra there appears to be large photoelectron signal at near zero eKE (the highest reported eBE in each case). This arises from the high resolution of the instrument at very low eKE (high eBE) combined with many transitions accessible near the photodetachment threshold for all three photon energies employed. Second, the intensity ratios of all peaks relative to the origin transition appear to be qualitatively different from the same ratios in Fig. 5.1, where the photon energy utilized was higher, 3.494 eV. This is evidence of a photon energy dependence in the PE spectrum of indolide. This is discussed in section 5.7. In addition to these phenomena, there are several sharp peaks identified in the figure, and a vibrational analysis may be performed as follows.

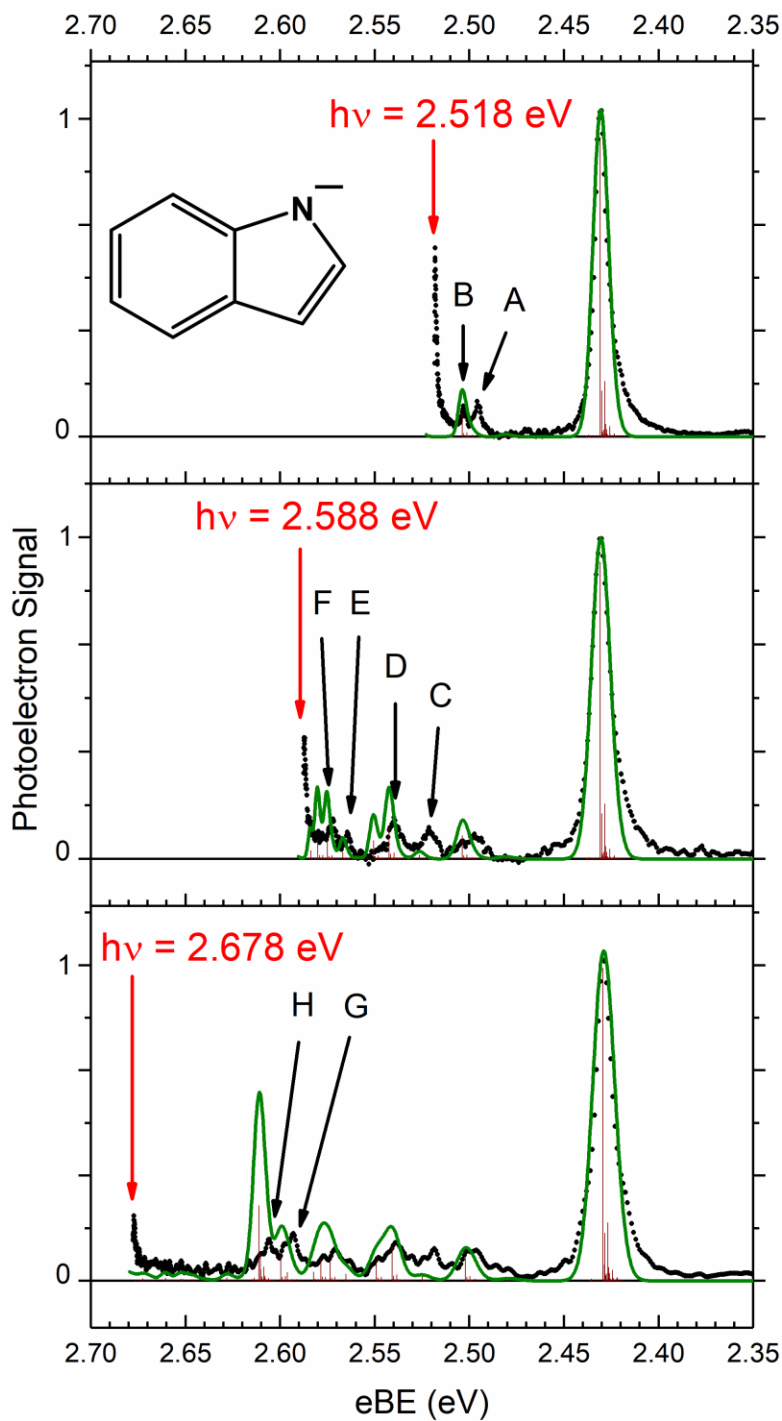


Fig. 5.3 Photoelectron spectra of indolide obtained with three separate photon energies, 2.518 eV (upper panel), 2.588 eV (middle panel), and 2.678 eV (lower panel). This demonstrates the high resolution of the VMI spectrometer at low electron kinetic energies, and takes advantage of this fact. Using this feature, several peaks may be identified and assigned to specific transitions. The sharp rise at near-zero kinetic energy (the highest reported eBE in each panel) is due to the highest resolution of the instrument being within 30 meV of the photon energy. See the text, and Table 5.2 for more information.

The vibrational analysis begins with the spectrum on the top panel of Fig. 5.3 with two peaks labelled A and B. The peak centers are located energetically at 521 ± 15 and $577 \pm 15 \text{ cm}^{-1}$, respectively, above the origin peak center. The simulation shown in green overlaid on the data shows one transition with significant intensity in this region, the 25_0^1 transition, with a transition energy calculated as 587 cm^{-1} relative to the origin transition. Hence, peak B may be assigned to the 25_0^1 transition, with a measured transition energy of $577 \pm 15 \text{ cm}^{-1}$. Peak A remains unassigned, though it is possible to suggest either 26_0^1 or 27_0^1 , based on symmetry and the predicted harmonic frequencies of these vibrational modes. The middle panel of Fig. 5.3 shows four additional peaks labelled C–F, with peak centers located at 722 ± 15 , 870 ± 15 , 1071 ± 15 , $1139 \pm 15 \text{ cm}^{-1}$, respectively, relative to the origin transition. Several transitions overlap the spectral region containing peak C, however, only one has the proper symmetry and an appreciable FCF, 24_0^1 . Hence this is the transition assigned to give rise to peak C with a measured transition energy, relative to the origin transition, of $24_0^1 = 720 \pm 50 \text{ cm}^{-1}$. Peak D is predicted to primarily arise from two separate transitions, 22_0^1 and 21_0^1 . Considering the proximity of the predicted harmonic vibrational frequencies of these normal modes, the transitions cannot be individually measured. In addition, we cannot verify the presence of both transitions independently, and so either one or both may be contributing to this peak. Hence the transitions are measured to be 22_0^1 and/or $21_0^1 = 870 \pm 80 \text{ cm}^{-1}$. Similarly, peaks E and F, located respectively at 1071 ± 15 and $1139 \pm 15 \text{ cm}^{-1}$ relative to the origin transition peak arise from at least two of the three different transitions with significant predicted FCFs in this region of the photoelectron spectrum, 16_0^1 , 18_0^1 , and 19_0^1 . The bottom panel of Fig. 5.3 identifies peaks G and H, located 1314 ± 15 and $1407 \pm 15 \text{ cm}^{-1}$ higher in binding energy than the origin peak. Peak G arises primarily from the 12_0^1 transition, and thus a transition energy may be determined, $1310 \pm 35 \text{ cm}^{-1}$. Peak H is

predicted to be dominated by two separate transitions with calculated harmonic frequencies inseparably close to each other, 11_0^1 and 10_0^1 . Similar to the situation for peak D, there is no experimental way to prove the contribution of either transition to the peak H line shape, though the 11_0^1 transition is theoretically predicted to have a FCF ~ 3.4 times larger than the 10_0^1 transition. Thus the transitions associated with Peak H are assigned as 11_0^1 *and/or* $10_0^1 = 1400 \pm 70 \text{ cm}^{-1}$. These results are summarized in Table 5.2.

All of the above assigned vibrational transitions are associated with vibrational normal modes which are of A' symmetry and can be described as ring distortion motions. The eigenvectors associated with these normal modes may be found in Table 5.3.

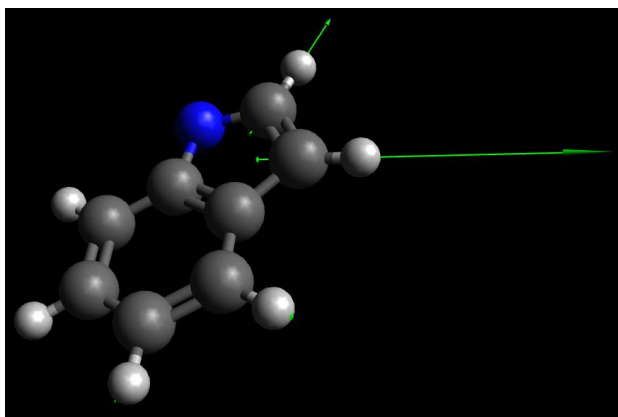
Table 5.2 Summary of Experimental Vibrational Assignments

Peak	Position Relative to 0_0^0 (cm^{-1})	Assignment (cm^{-1})
A	521 ± 15	
B	577 ± 15	$25_0^1 = 580 \pm 25$
C	722 ± 15	$24_0^1 = 720 \pm 50$
D	870 ± 15	22_0^1 and/or $21_0^1 = 870 \pm 80$
E	1071 ± 15	
F	1139 ± 15	
G	1314 ± 15	$12_0^1 = 1310 \pm 35$
H	1407 ± 15	11_0^1 and/or $10_0^1 = 1400 \pm 70$

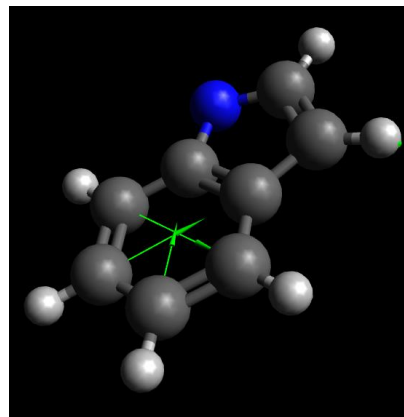
Vibrational analysis of the indolide photoelectron spectrum found in Fig. 5.3. Some assignments could not be made to a satisfactory level of confidence. Several suggested assignments are presented in the main text for these unassigned peaks.

Table 5.3 The following diagrams show the vibrational normal modes with associated mode labels and calculated frequencies discussed in the main text for indolyl in the ground electronic state. Each eigenvector shown here is that of the neutral radical, and was calculated at the B3LYP/aug-cc-pVTZ level of theory.

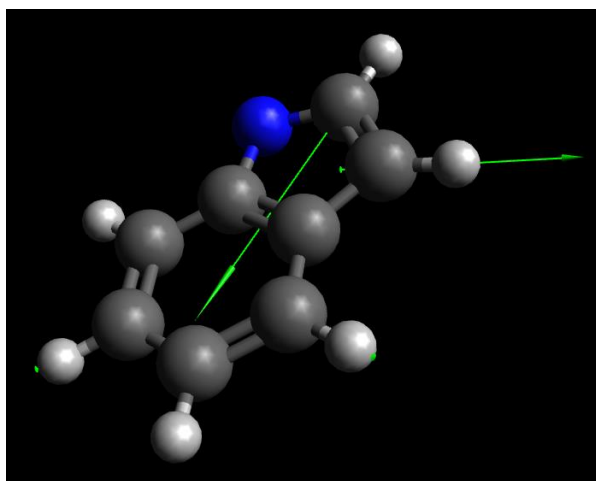
Indolyl Radical (modes of A' symmetry)



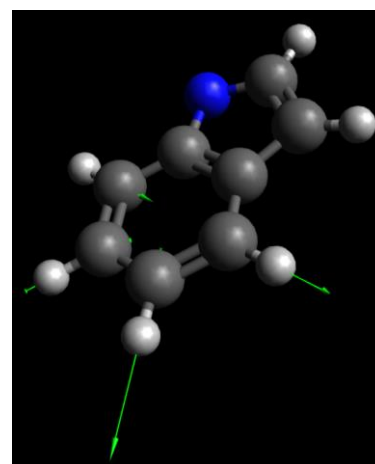
ν_1 (3221 cm^{-1})



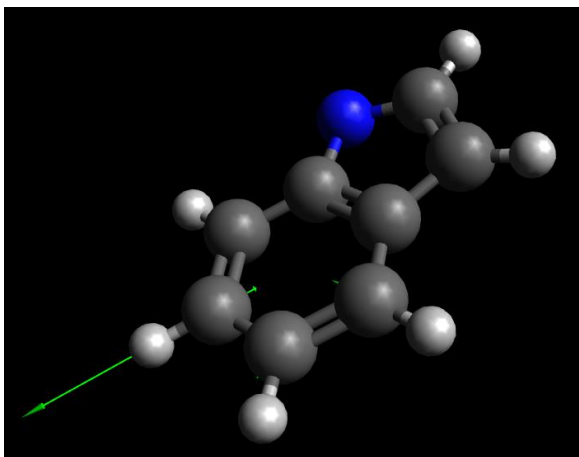
ν_2 (3196 cm^{-1})



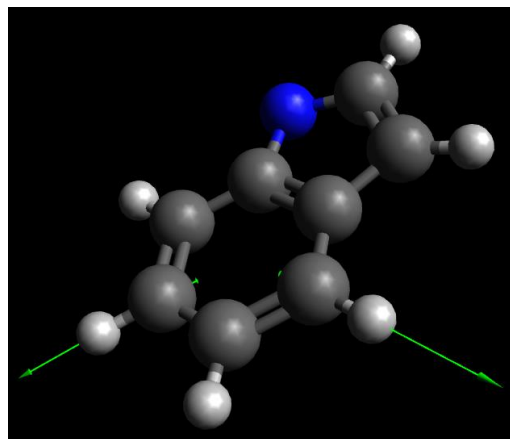
ν_3 (3193 cm^{-1})



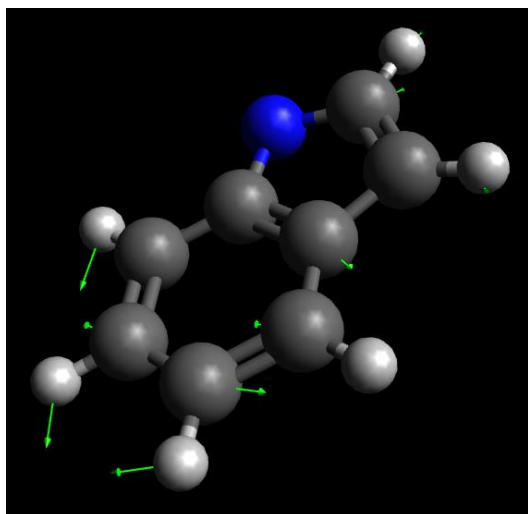
ν_4 (3189 cm^{-1})



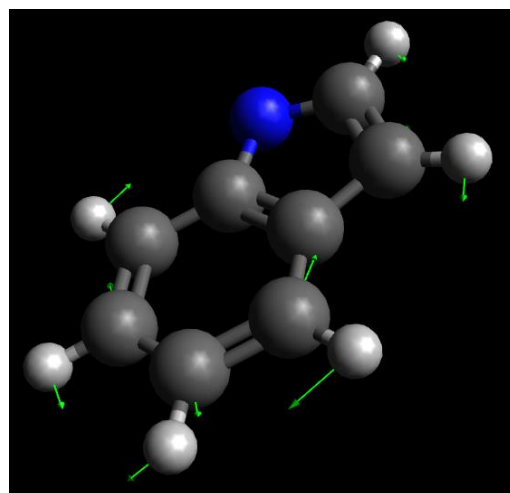
ν_5 (3175 cm^{-1})



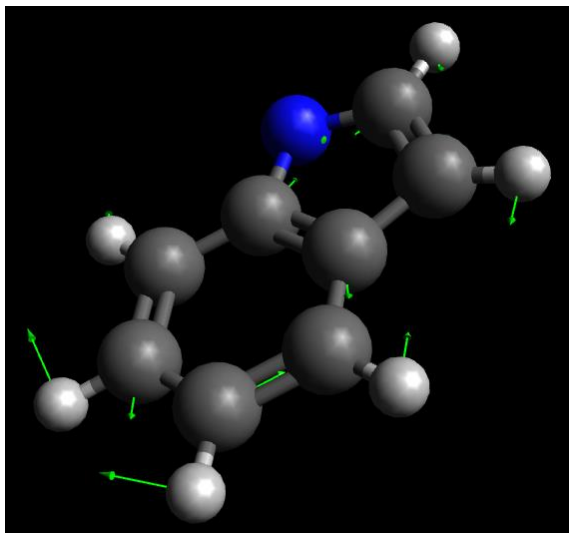
ν_6 (3167 cm^{-1})



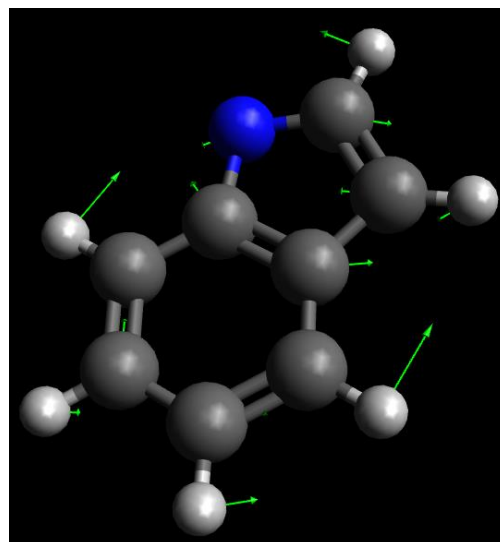
ν_7 (1629 cm^{-1})



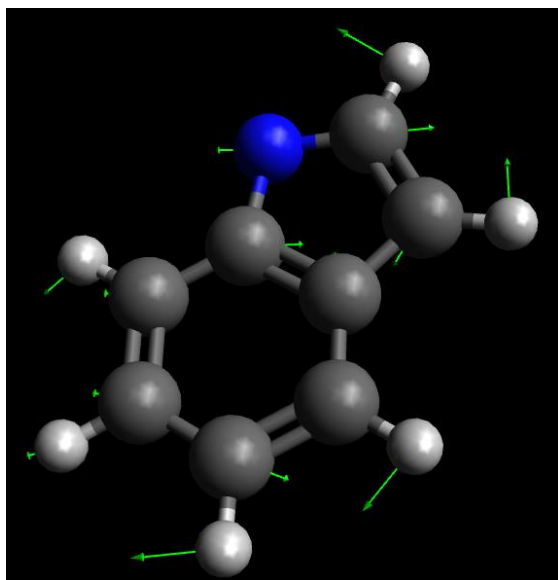
ν_8 (1602 cm^{-1})



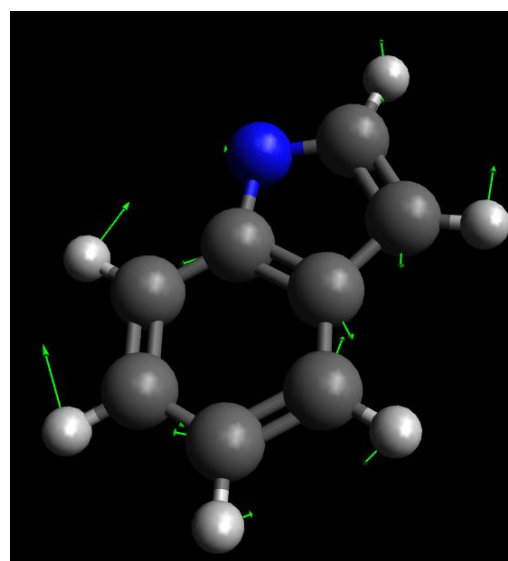
ν_9 (1495 cm^{-1})



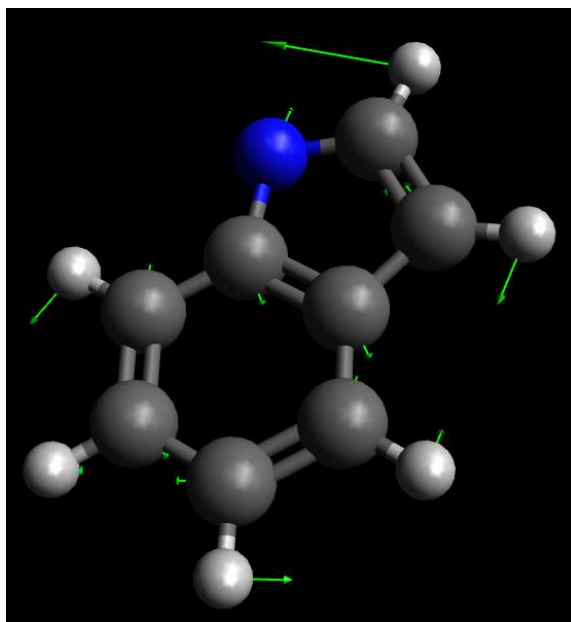
ν_{10} (1466 cm^{-1})



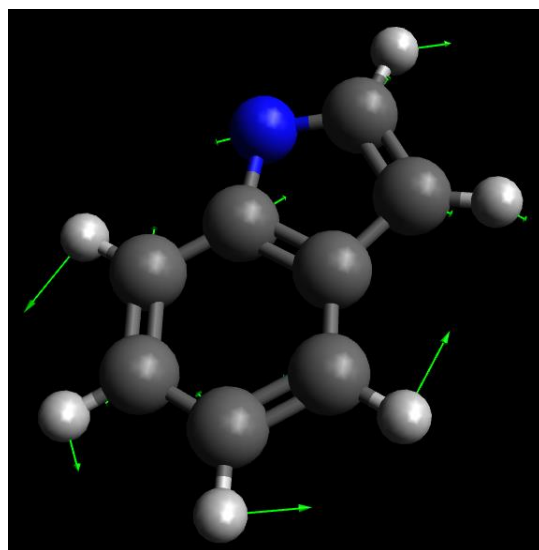
ν_{11} (1460 cm^{-1})



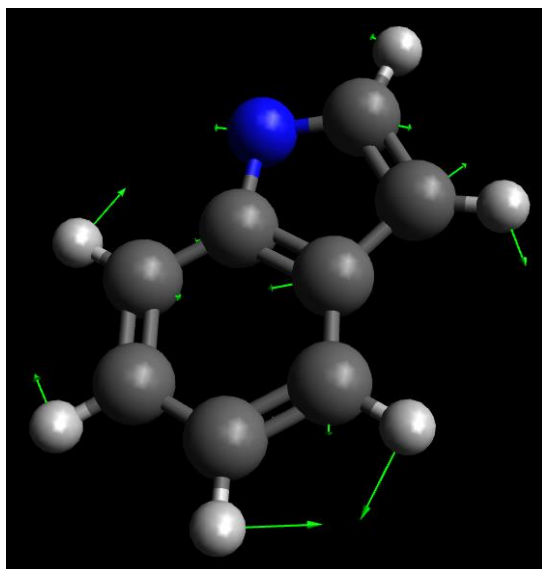
ν_{12} (1373 cm^{-1})



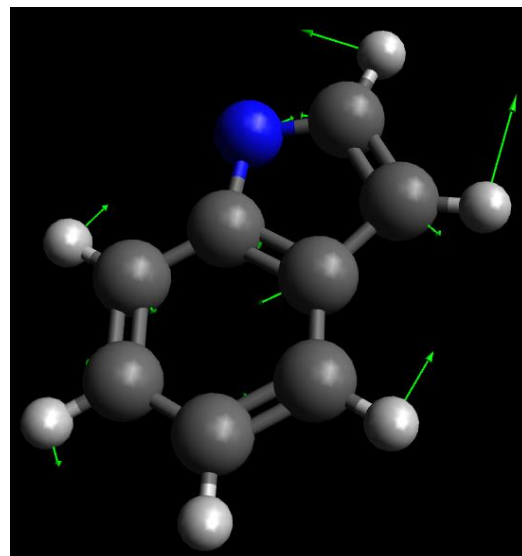
ν_{13} (1346 cm^{-1})



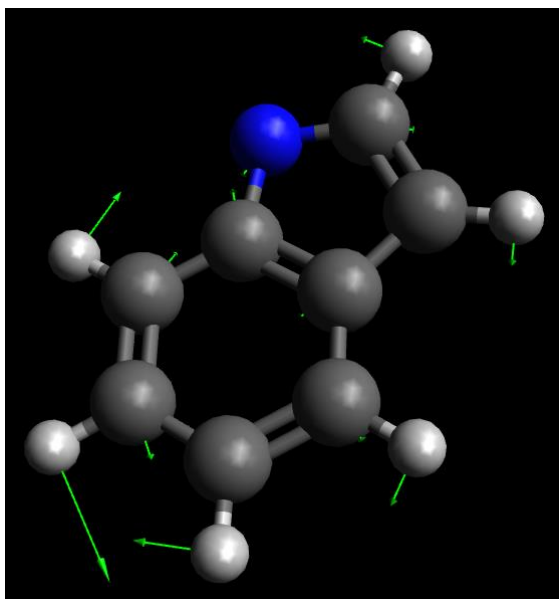
ν_{14} (1303 cm^{-1})



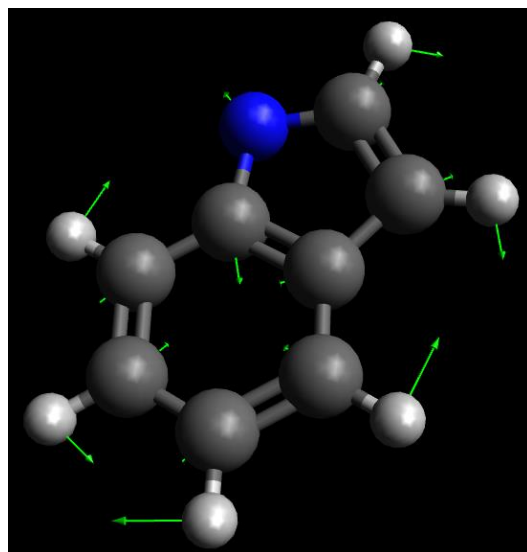
ν_{15} (1233 cm^{-1})



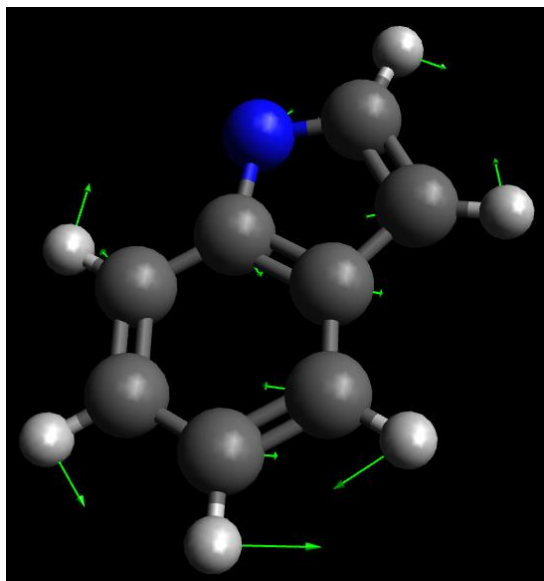
ν_{16} (1202 cm^{-1})



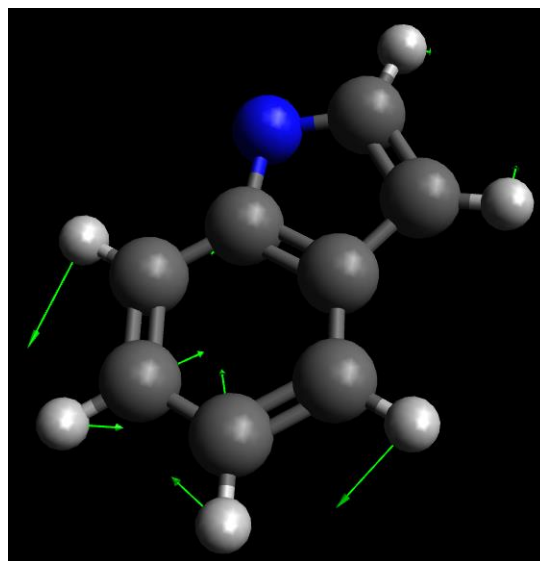
ν_{17} (1169 cm^{-1})



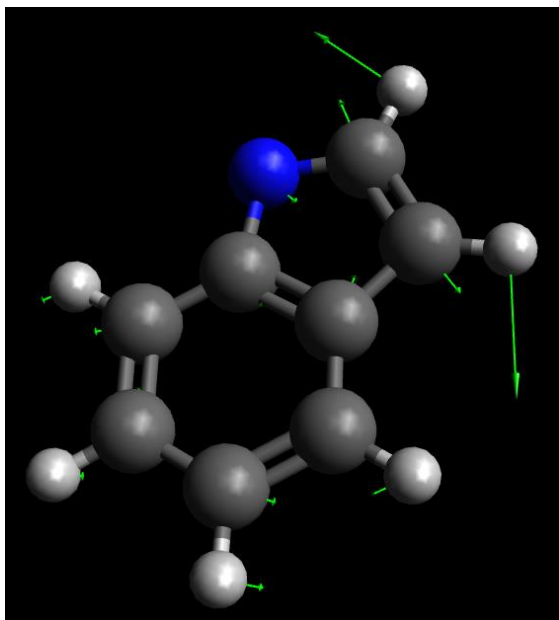
ν_{18} (1162 cm^{-1})



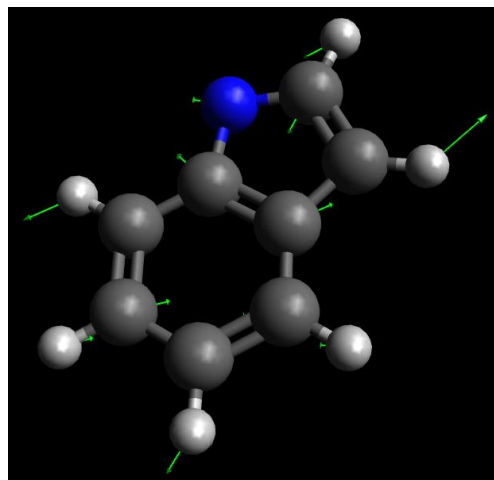
ν_{19} (1096 cm^{-1})



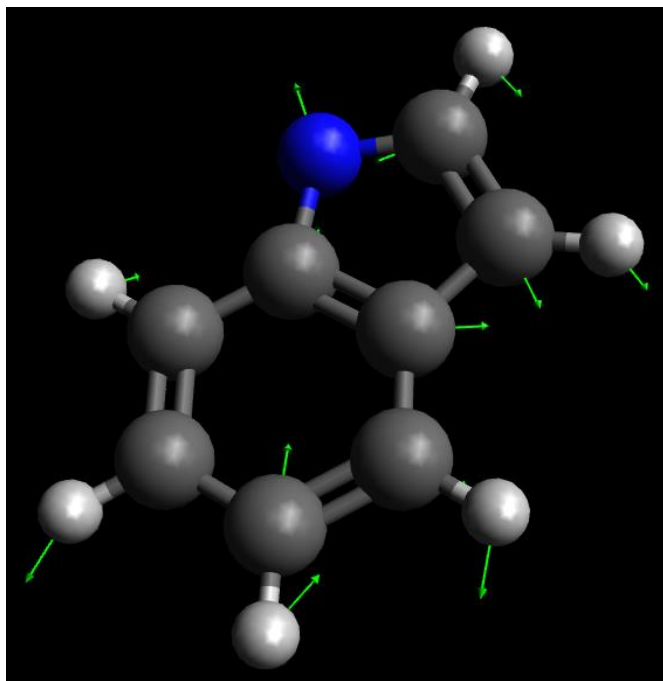
ν_{20} (1026 cm^{-1})



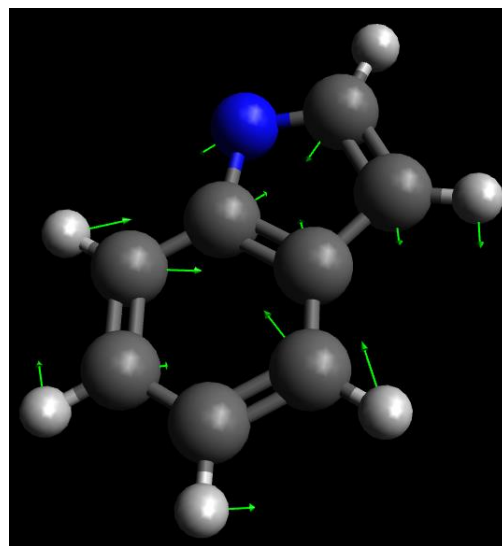
ν_{21} (966 cm^{-1})



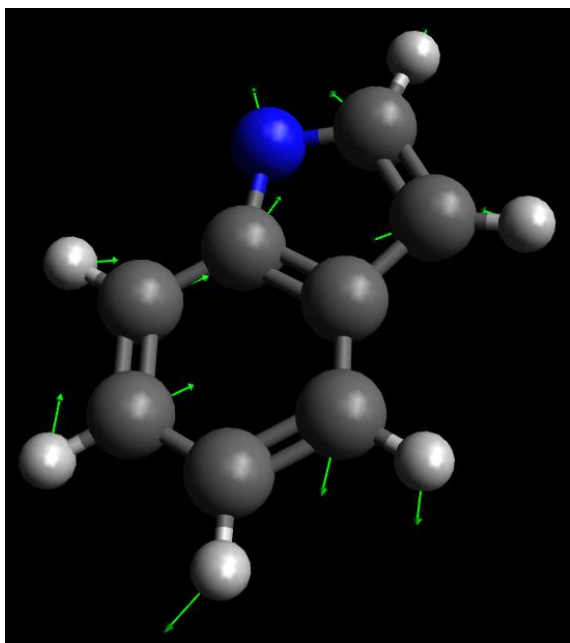
ν_{22} (899 cm^{-1})



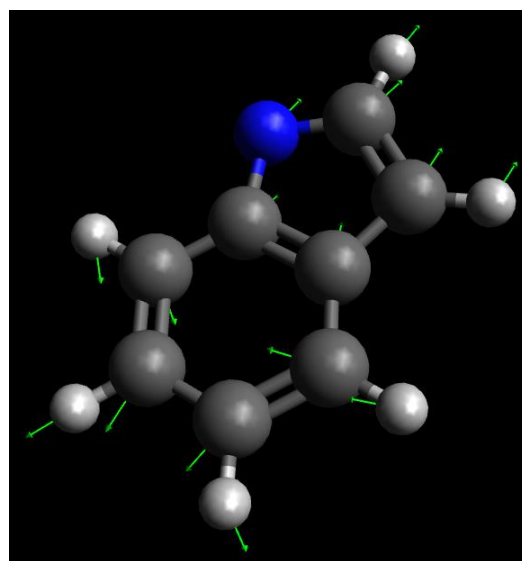
ν_{23} (854 cm^{-1})



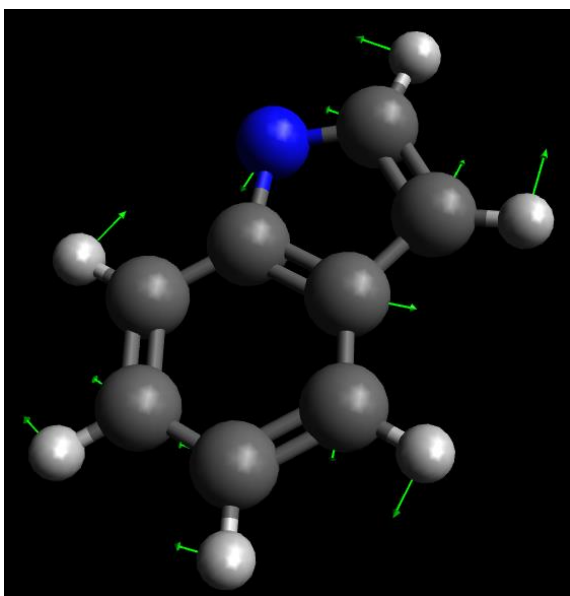
ν_{24} (770 cm^{-1})



ν_{25} (587 cm^{-1})

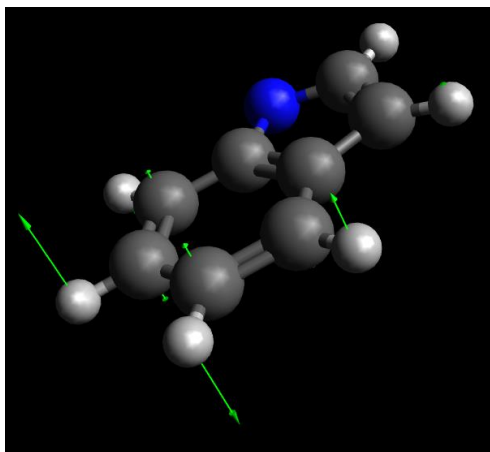


ν_{26} (545 cm^{-1})

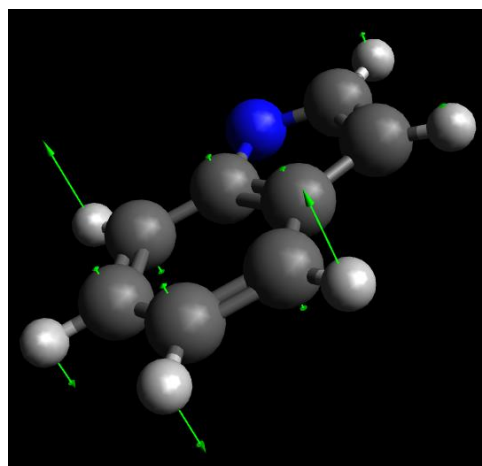


ν_{27} (408 cm^{-1})

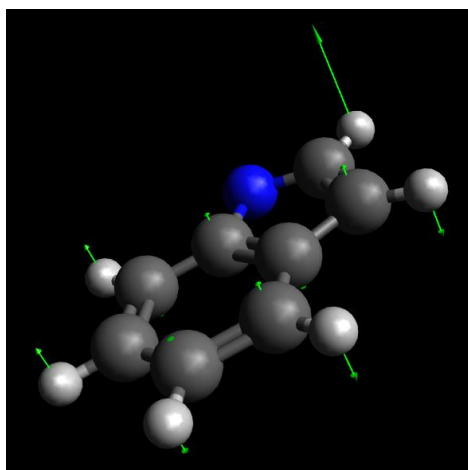
Indolyl Radical (modes of A'' symmetry)



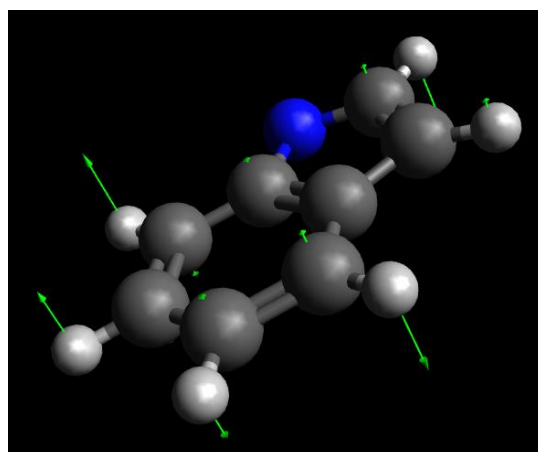
ν_{28} (997 cm^{-1})



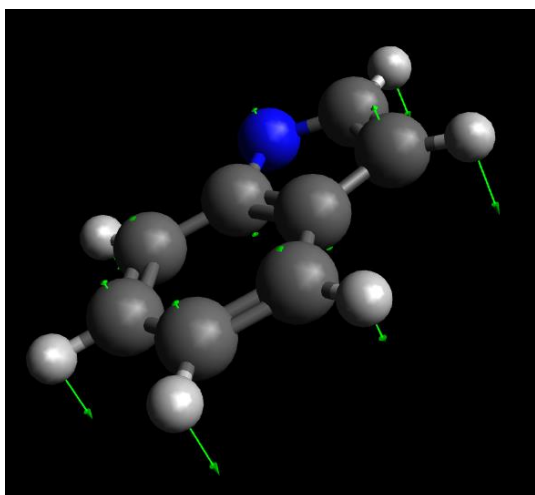
ν_{29} (963 cm^{-1})



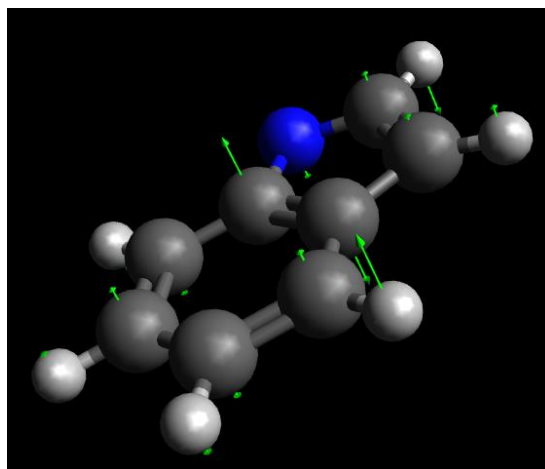
ν_{30} (922 cm^{-1})



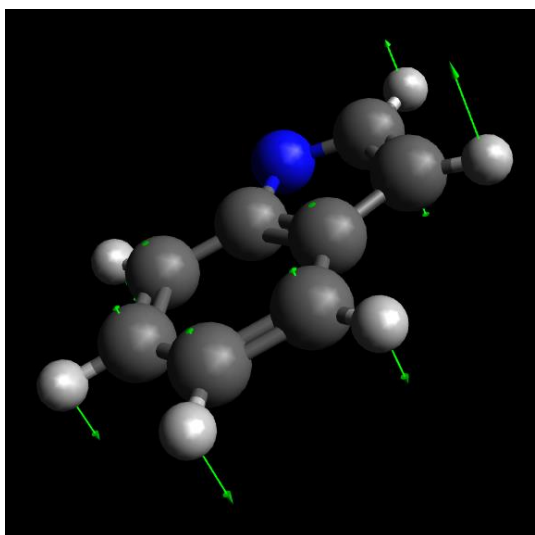
ν_{31} (886 cm^{-1})



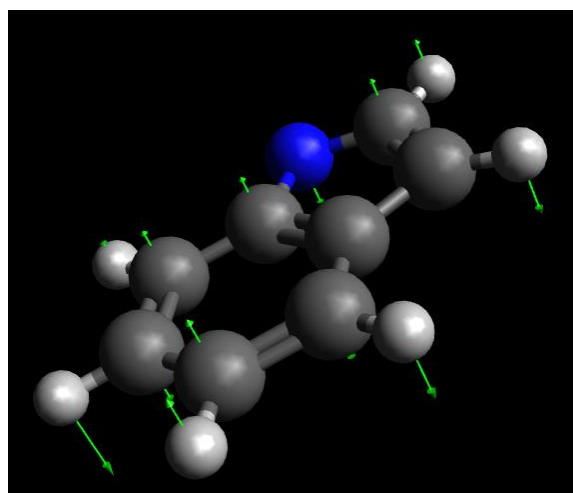
ν_{32} (783 cm^{-1})



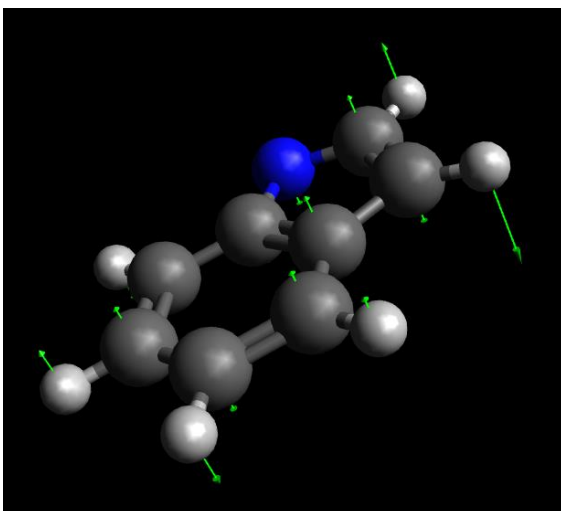
ν_{33} (774 cm^{-1})



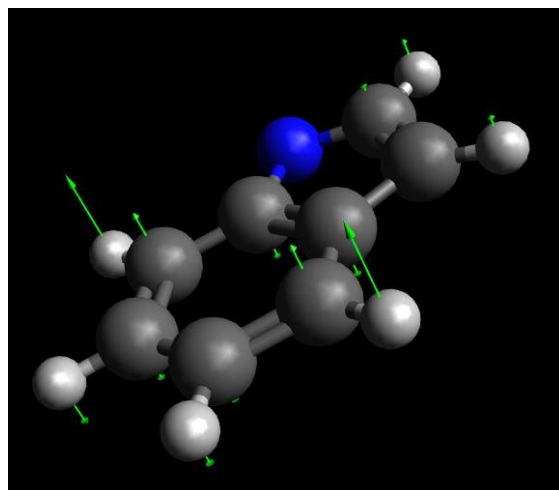
ν_{34} (744 cm^{-1})



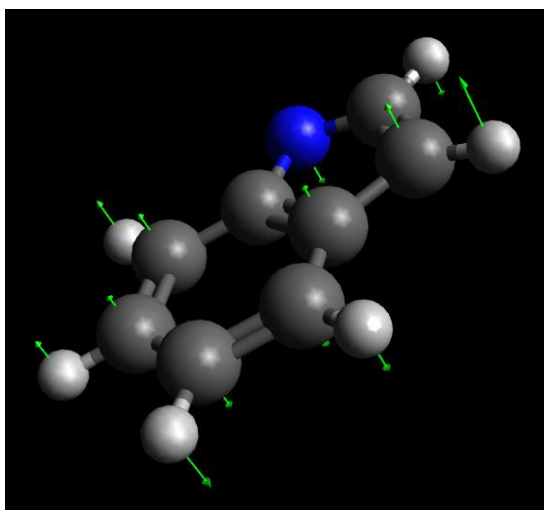
ν_{35} (575 cm^{-1})



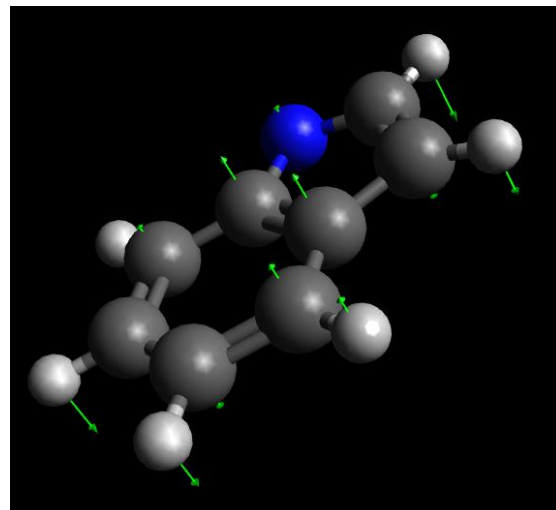
ν_{36} (543 cm^{-1})



ν_{37} (412 cm^{-1})



ν_{38} (241 cm^{-1})



ν_{36} (202 cm^{-1})

§ 5.7 Discussion

The EA of indolyl was measured to be 2.4315 ± 0.0017 eV. This value may be compared to previous studies of indolyl in the literature. The EA of the indolyl radical has been measured twice previously.^{21, 22} In the case of Taft *et al.*²¹ this is accomplished by means of applying a thermochemical cycle to their proton transfer equilibria data, and thus the EA was determined to be 2.52 ± 0.20 eV. This value was later updated in 2010 by McKay *et al.*²², utilizing anion photoelectron spectroscopy to find an EA of 2.31 ± 0.15 eV via photoelectron spectroscopy. This present work is in agreement with these two past studies and greatly improves the accuracy of the measurement of the EA of the indolyl radical.

Several structural analogs of indolyl may also be examined and compared to the measured EA of indolyl: pyrrolyl, phenyl, cyclopentadienyl, and cyclopentyl radical.^{17, 23, 24} One may think of pyrrolide as an analog of indolide, while phenide or cyclopentadienide may represent indole deprotonated at a carbon site on the molecule. The pyrrolyl radical was shown to have an EA of 2.145 ± 0.010 eV, while the EAs of phenyl and cyclopentadienyl are 1.096 ± 0.006 eV and 1.808 ± 0.006 eV, respectively.^{17, 23, 24} Both analogs of carbon site deprotonation display a lower EA than pyrrolyl radical, wherein the excess charge on the anion is concentrated about the nitrogen atom. This is consistent with the EA of indolide, 2.4315 ± 0.0017 eV and demonstrates that the EA of pyrrolyl radical is not greatly perturbed by the addition of a fused aromatic ring to the structure, resulting in indolyl. This is expected; the pyrrolyl ring is aromatic and the addition of another aromatic ring, which is neither strongly electron donating or withdrawing, to the conjugated π system will not significantly disrupt the qualitative aspects of the aromatic electronic structure.

Upon electron photodetachment from indolide, several vibrational modes are excited; the eigenvectors associated with these vibrational modes may be found in the supplementary material. All of the modes that are activated upon photodetachment share two characteristics. First they are all of A' symmetry, and so preserve the only plane of symmetry of the molecular point group, C_s , which is also the plane of the molecule itself. Second, all of the observed vibrational modes describe molecular motion that can be characterized as ring distortions. This behavior has been observed in aromatic anion PE spectroscopy previously.^{17, 18, 23, 25} Both of these observations are intuitively understandable. Indolide will have the excess charge density primarily localized about the nitrogen group. This increased charge density will cause the bonds along the fused aromatic ring structure to lengthen from an idealized pyrrole-like structure, while preserving the C_s symmetry. Upon photodetachment, the new equilibrium geometry will be closer to that of pyrrole, causing vibrational motion to be activated which incorporates displacements along the bonds which make up the fused aromatic ring, resulting in both vibrations which do not break the symmetry of the molecule and which might be described as ring distortion motion.

The intensities of peaks seen in the photoelectron spectrum of indolide change as a function of photon energy, as can be observed by comparison of the PE spectrum displayed in Fig. 5.1, obtained with a photon energy of 3.494 eV, with the PE spectra displayed in Fig. 5.3, that were obtained with several photon energies ~ 1 eV lower than 3.494 eV. For example, in the bottom panel of Fig. 5.3 one may note that the ratio of the intensity of peak H to the origin transition peak is different from the same ratio in Fig. 5.1. This ratio in Fig. 5.3 is far lower than what is found in Fig. 5.1. This variability in peak intensity ratios cannot be explained by threshold effects. This variation must be due to electron autodetachment in competition with direct photodetachment, a behavior that has been observed in other aromatic systems.^{23, 25, 26} This

conclusion is borne out in excited state quantum chemical calculations (TD-DFT) of the indolide anion which predict 9 optically accessible electronic states with term energies ranging from 2.5 – 3.6 eV above the ground vibronic state energy. Due to the density of the available states and the inherent complexity of autodetachment, it is beyond the scope of this work to further investigate this phenomenon theoretically.

The thermodynamic implications of the improved measurement of the EA of indolyl measured in this work are now considered. By means of a thermochemical cycle,¹ we may combine the measured EA value found in this work with the previous measurement of the acidity ($\Delta_{acid}H_{298\text{ K}}^0$) of indole. Meot-Ner *et al.*²⁷ previously reported the acidity as $\Delta_{acid}H_{600\text{ K}}^0$ (N-H) = 352 ± 2 kcal/mol. This enthalpy may be converted to the more conventional enthalpy at 298 K by means of the calculated constant-pressure heat capacities of the species involved in the standard acid reaction: $\text{HA}_{(g)} \rightarrow \text{H}^+_{(g)} + \text{A}^-_{(g)}$.

$$\Delta_{acid}H_{T_f}^0(\text{HA}) = \Delta_{acid}H_{T_i}^0(\text{HA}) + \int_{T_i}^{T_f} [C_p(\text{A}^-) + C_p(\text{H}^+) - C_p(\text{HA})] dT \quad (2)$$

Where T_i and T_f are the initial and final temperatures. Utilizing eqn. 2 allows for the determination of the temperature adjusted previous measurement of the acidity, $\Delta_{acid}H_{298\text{ K}}^0$ (N-H) = 351 ± 2.25 kcal/mol. Thus, one may combine the EA of indolyl, measured in this work, with the temperature corrected gas phase acidity of indole (Meot-Ner *et al.*) to derive the bond dissociation energy of indole, $D_0(\text{N-H}) = 93.3 \pm 2.5$ kcal/mol. The value of $D_0(\text{N-H})$ was investigated recently by Nix *et al.*²⁸ who reported an upper bound of 91.2 kcal/mol for this bond strength. This value, coupled with the present measurement of the bond dissociation energy, shows that $D_0(\text{N-H})$ lies within the narrow range $90.8 \leq D_0(\text{N-H}) \leq 91.2$ kcal/mol.

§ 5.8 Deprotonated Indoline

As was stated in § 5.1, the case of deprotonated indoline proved less than revealing and as such shall be discussed separately here.

Deprotonated indoline was generated in the same ion source detailed in § 5.2, changing the main valve to expand a mixture of ~1% indoline in Ar with a backing pressure of 10 psig, while the side valve was changed to discharge a gas mixture at 35 psig backing pressure with 2% NF_3 in Ar. This generates fluoride ions²⁹ which are entrained in the main expansion, which can then react with the neutral indoline.

The photoelectron spectrum presented in Fig. 5.4 is obtained with the laser radiation from a dye laser making use of the LDS 698 dye, pumped by the 2nd harmonic (2.330 eV) of the Nd:YAG laser.

Prior to examining the data, it is useful to hypothesize the likely behaviors one might expect to observe upon photodetachment of deprotonated indoline. In the case of N–H deprotonated indoline, there is little guidance from previously studied anions. It is possible to make several predictions based on the electronic structure calculations performed here. Assuming the deprotonation occurs at the N–H site, the EA of the corresponding radical was calculated to be 1.291 eV. Alternatively, if deprotonation occurs at one of the sp^3 hybridized carbon centers, then the EA of the corresponding radical was calculated to be considerably lower, < 0.5 eV. For comparison, the EA of the cyclopentyl radical was measured through a thermochemical cycle and shown to be a negative value.²⁴

There are fewer conclusions that may be drawn from the photoelectron spectrum of deprotonated indoline shown in Fig. 5.4. The experimental data are shown in black, while the

simulation of the molecule shown in the figure is represented by both the green curve and the red sticks. This PE spectrum is qualitatively different from the simulation of the molecule displayed in the figure. Regardless, several observations and conclusions may be made. First, the calculated EA for the N–H deprotonated indoline is 1.291 eV and is in reasonable agreement with the data which displays the PE spectrum commencing at ~1.3 eV. Second, deprotonated indoline has a mass of 118 amu, and the ratio of the ion intensity of $m/z = 119$ to $m/z = 118$ in the mass spectrum was 8%. Considering the abundance of ^{13}C (~1%), this confirms that the PE spectrum obtained from the $m/z = 118$ products contain 8 carbon atoms, and thus is a product of indoline. Third, the PE angular distribution of deprotonated indoline was determined to be characterized by a slightly positive value of $\beta \sim 0.1$. However, considering the fact that we suspect multiple isomers to be contributing to the PE spectrum shown in Fig. 5.4, the physical meaning of this anisotropy is not interpretable. Finally, several ring-opened structures were calculated and were shown to have plausible values of electron affinities, 1.2 – 1.45 eV, while deprotonation from the sp^3 hybridized carbon atoms resulted in EA values < 0.5 eV and can thus be ruled out as contributing to this spectrum. It is important to note that, although it is likely that N–H deprotonated indoline is formed in the experiment, it is possible that the observed photoelectron spectrum derives solely from ring-opened structures and/or isomers of $\text{C}_8\text{H}_8\text{N}^-$. This is due to our inability to resolve individual transitions in the spectrum.

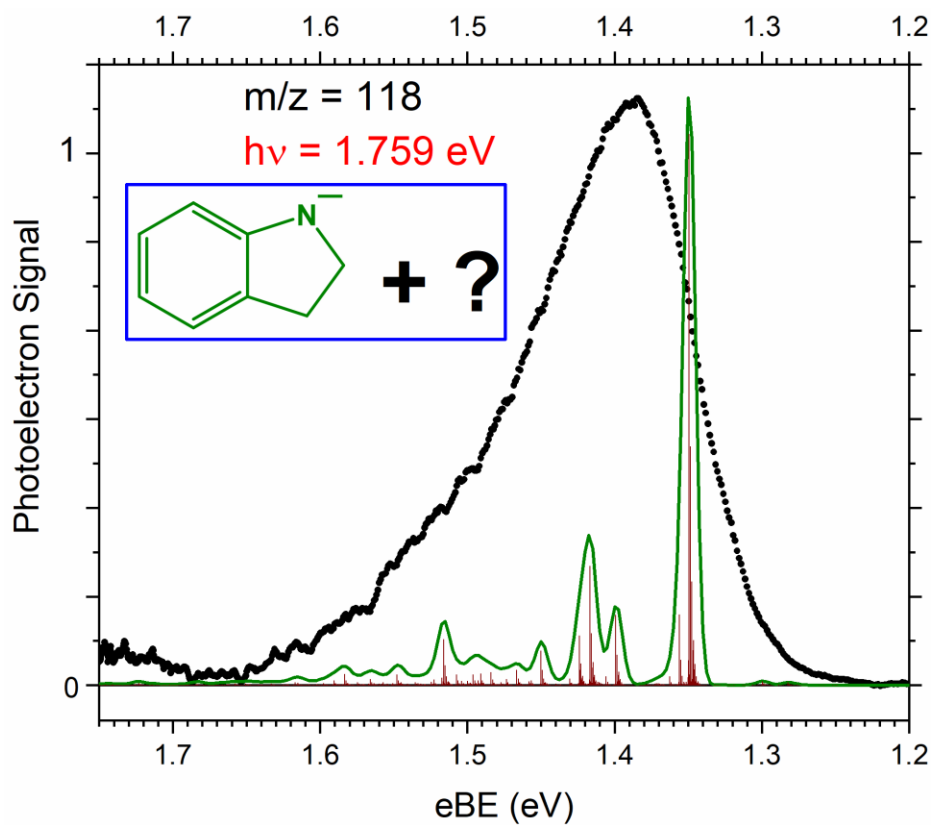


Fig. 5.4 The photoelectron spectrum of the anionic product(s) of $F^- + \text{indoline}$ with a mass to charge ratio of 118. This spectrum was obtained with a photon energy of 1.759 eV. Note that at a binding energy of 1.4 eV, with this photon energy, the VMI spectrometer has a spectral resolution of 11 meV. The simulation shown in green is that of the anion shown in the figure. More information may be found in the text.

Attempts were made to simulate the harmonic FC PE spectra of the ring-opened structures; however, this did not offer any new insights as to the interpretation of the data. Considering the available bonds within the fused rings of the molecule, a N–C bond is the most likely to be broken. The ring-opened structures all display large geometry changes upon photodetachment, and thus result in two major obstacles with respect to simulating PE spectra. First, large geometry changes imply that the PE spectrum will activate many vibrational normal modes with a high probability of populating multiple quanta in these modes. This results in a PE spectrum which is highly congested and experimentally unresolvable with a broad envelope. Second, the simulations which we are able to perform are explicitly reliant on the fact that the harmonic oscillator approximation is appropriate for the system being simulated. The harmonic oscillator approximation would not be at all appropriate for these ring-opened systems, as the resultant potential energy surfaces attributed to the alkyl chains would almost certainly be highly anharmonic. Hence, very little of actual consequence may be concluded from a harmonic simulation of the PE spectra. Performing anharmonic calculations or more sophisticated simulations would likely elucidate these data more clearly, but are beyond the scope of this work.

While no obvious analogs of N–H deprotonated indoline have been studied to date, the cyclopentyl radical may be considered an analog of indoline deprotonated at either of the sp^3 hybridized carbon sites on the molecule. The cyclopentyl radical does not bind electrons, and so one may safely hypothesize that the EA of the radical corresponding to indoline deprotonated at a sp^3 hybridized carbon site would be either quite low or negative. This is corroborated by theory which predicts the EAs of these neutral deprotonated indoline isomers to be < 0.5 eV. Therefore,

it is concluded that the PE spectrum displayed in Fig. 5.4 does not arise from indoline deprotonated at a sp^3 carbon site, considering that the spectrum shown originates at ~ 1.3 eV.

§ 5.9 Conclusions

The anion photoelectron spectra of deprotonated indole and indoline have been collected utilizing several photon energies in order to take advantage of the high resolution associated with slow electrons in this apparatus. The SEVI photoelectron spectrum of indolide show the EA of indolyl to be 2.4315 ± 0.0017 eV. Indolide photodetachment activates numerous ring distortion vibrations upon photodetachment, which have A' symmetry. Previous work studying the gas phase acidity of indole²⁷ allows for a new independent measure of $D_0(\text{N-H}) = 93.3 \pm 2.5$ kcal/mol, which compares well with the previously measured bound on the bond dissociation energy.²⁸ Combining the conclusions of this experiment with the previously reported bound on the dissociation energy implies that the value of $D_0(\text{N-H})$ falls within the range: $90.8 \leq D_0(\text{N-H}) \leq 91.2$ kcal/mol. The photoelectron spectrum of deprotonated indoline exhibited far more spectral congestion than was anticipated, apparently a result of the presence of multiple isomers of deprotonated indoline, although specific identification was not possible. The relative intensities of vibrations excited in the photoelectron spectrum of indolide displayed a strong photon energy dependence, the result of electron autodetachment.

§ 5.10 References

- 1) K. M. Ervin and V. F. DeTuri, *J. Phys. Chem. A* **106**, 9947-9956 (2002).
- 2) L. Sheps, E. M. Miller and W. C. Lineberger, *J. Chem. Phys.* **131**, 064304 (2009).
- 3) Y.-J. Lu, J. H. Lehman and W. C. Lineberger, *J. Chem. Phys.* **142**, 044201 (2015).
- 4) B. Ruscic, A. F. Wagner, L. B. Harding, R. L. Asher, D. Feller, D. A. Dixon, K. A. Peterson, Y. Song, X. Qian, C.-Y. Ng, J. Liu, W. Chen and D. W. Schwenke, *J. Phys. Chem. A* **106**, 2727-2747 (2002).
- 5) B. Dick, *Phys. Chem. Chem. Phys.* **16**, 570-580 (2014).
- 6) T. Andersen, H. K. Haugen and H. Hotop, *J. Phys. Chem. Ref. Data* **28**, 1511-1533 (1999).
- 7) H. Hotop and W. C. Lineberger, *J. Phys. Chem. Ref. Data* **4**, 539-576 (1975).
- 8) C. Blondel, W. Chaibi, C. Delsart, C. Drag, F. Goldfarb and S. Kröger, *Euro. Phys. J. D* **33**, 335-342 (2005).
- 9) D. M. Neumark, *J. Phys. Chem. A* **112**, 13287-13301 (2008).
- 10) M. J. Travers, D. C. Cowles, E. P. Clifford, G. B. Ellison and P. C. Engelking, *J. Chem. Phys.* **111**, 5349-5360 (1999).
- 11) M. J. Frisch, G. W. Trucks, H. B. Schlegel, G. E. Scuseria, M. A. Robb, J. R. Cheeseman, G. Scalmani, V. Barone, B. Mennucci, G. A. Petersson, H. Nakatsuji, M. Caricato, X. Li, H. P. Hratchian, A. F. Izmaylov, J. Bloino, G. Zheng, J. L. Sonnenberg, M. Hada, M. Ehara, K. Toyota, R. Fukuda, J. Hasegawa, M. Ishida, T. Nakajima, Y. Honda, O. Kitao, H. Nakai, T. Vreven, J. A. Montgomery, J. E. Peralta, F. Ogliaro, M. Bearpark, J. J. Heyd, E. Brothers, K. N. Kudin, V. N. Staroverov, R. Kobayashi, J. Normand, K. Raghavachari, A. Rendell, J. C. Burant, S. S. Iyengar, J. Tomasi, M. Cossi, N. Rega, J. M. Millam, M. Klene, J. E. Knox, J. B. Cross, V. Bakken, C. Adamo, J. Jaramillo, R. Gomperts, R. E. Stratmann, O. Yazyev, A. J. Austin, R. Cammi, C. Pomelli, J. W. Ochterski, R. L. Martin, K. Morokuma, V. G. Zakrzewski, G. A. Voth, P. Salvador, J. J. Dannenberg, S. Dapprich, A. D. Daniels, Farkas, J. B. Foresman, J. V. Ortiz, J. Cioslowski and D. J. Fox, *Gaussian 09*, Revision B.01, 2009, see <http://gaussian.com/>
- 12) A. D. Becke, *J. Chem. Phys.* **98**, 5648-5652 (1993).

- 13) T. E. Sharp and H. M. Rosenstock, *J. Chem. Phys.* **41**, 3453-3463 (1964).
- 14) E. B. Wilson, Jr., *Phys. Rev.* **45**, 706-714 (1934).
- 15) P. Chen, *Unimolecular and Bimolecular Reactions Dynamics* (John Wiley & Sons, Chichester, 1994) 371.
- 16) K. M. Ervin, PESCAL, Fortran Program for Franck-Condon Analysis of Molecular Photoelectron Spectra, 2010, see <http://wolfweb.unr.edu/~ervin/pes/>
- 17) A. J. Gianola, T. Ichino, R. L. Hoenigman, S. Kato, V. M. Bierbaum and W. C. Lineberger, *J. Phys. Chem. A* **108**, 10326-10335 (2004).
- 18) T. Ichino, S. W. Wren, K. M. Vogelhuber, A. J. Gianola, W. C. Lineberger and J. F. Stanton, *J. Chem. Phys.* **129**, 084310 (2008).
- 19) J. Cooper and R. N. Zare, *J. Chem. Phys.* **48**, 942-943 (1968).
- 20) A. Sanov, *Annu. Rev. Phys. Chem.* **65**, 341-363 (2014).
- 21) R. W. Taft and F. G. Bordwell, *Acc. Chem. Res.* **21**, 463-469 (1988).
- 22) A. R. McKay, M. E. Sanz, C. R. S. Mooney, R. S. Minns, E. M. Gill and H. H. Fielding, *Rev. Sci. Instrum.* **81**, 123101 (2010).
- 23) R. F. Gunion, M. K. Gilles, M. L. Polak and W. C. Lineberger, *Int. J. Mass Spectrom. Ion Processes* **117**, 601-620 (1992).
- 24) C. H. DePuy, S. Gronert, S. E. Barlow, V. M. Bierbaum and R. Damrauer, *J. Amer. Chem. Soc.* **111**, 1968-1973 (1989).
- 25) D. J. Nelson, W. K. Gichuhi, E. M. Miller, J. H. Lehman and W. C. Lineberger, *J. Chem. Phys.* **146**, 074302 (2017).
- 26) C. S. Anstöter, C. R. Dean and J. R. R. Verlet, *J. Phys. Chem. Lett.* **8**, 2268-2273 (2017).
- 27) M. Meot-Ner, J. F. Liebman and S. A. Kafafi, *J. Amer. Chem. Soc.* **110**, 5937-5941 (1988).

28) M. G. D. Nix, A. L. Devine, B. Cronin and M. N. R. Ashfold, *Phys. Chem. Chem. Phys.* **8**, 2610-2618 (2006).

29) B. Christophe, D. Christian and G. Fabienne, *Journal of Physics B: Atomic, Molecular and Optical Physics* **34**, L281 (2001).

CHAPTER VI
STATE-RESOLVED VELOCITY MAP IMAGING OF SURFACE-SCATTERED
MOLECULAR FLUX

Portions of this chapter have been published in the journal Physical Chemistry Chemical Physics (PCCP) under the same title by, J. R. Roscioli, D. J. Bell, D. J. Nelson, and D. J. Nesbitt

§ 6.1 Introduction and Background

Unlike the preceding chapters in this dissertation, this final chapter presents an entirely different study focusing on dynamical interactions of molecules with surfaces and does not utilize photoelectron spectroscopy at all. As such, more detail and background shall be given to introduce new concepts before detailing the results and conclusions of the study.

The field of surface chemistry has experienced a surge of research in recent years, with particular focus on scattering,¹⁻¹⁰ surface composition,^{11, 12} dynamics^{13, 14} and reactivity.¹⁵⁻¹⁷ The primary goal of these activities has been to develop, with ever increasing clarity, a coherent picture of the inelastic and reactive events which govern much of the heterogeneous chemistry that we observe in nature. These processes are ubiquitous, finding relevance in ice crystal formation and dust grain chemistry in deep space,¹⁸⁻²⁰ gas-aerosol^{21, 22} and gas-liquid^{6, 7} interactions of atmospheric interest, as well as metal-surface chemistry such as oxidation/reduction and energy transfer at gold, silver, and other metal interfaces.^{4, 23} In light of this importance, a variety of techniques have been employed to explore the physical nature of reactions at interfaces. Reflected-angle infrared spectroscopy (RAIRS),²⁴ sum frequency generation (SFG),^{11, 25} and surface photoelectron spectroscopy,²⁶ for example, have served as highly selective probes of local interfacial structure and surface interactions. Time-of-flight mass spectrometry,^{5, 13} quantum-state resolved spectroscopic methods,^{1-4, 9, 17, 27} and pressure-

based sticking coefficient measurements,⁸ have been successful at measuring the dynamics and interactions that dominate gas-surface collisions.

These combined classes of experimental methods have yielded important insight into the collision dynamics exhibited by a wide variety of atomic, non-polar (*e.g.* N₂, CO₂, etc.), and polar (*e.g.* HCl, NO, etc.) projectiles, scattering from both insulating and metallic solids and liquids. From a broad perspective, experiments and simulations over the past 30 years have revealed that there are at least two components to molecular flux following non-reactive scattering – one which has come into thermal equilibrium with the surface before desorbing (trapping or thermal-desorption, TD), and one which has inelastically scattered from the surface in one or a few collisions (impulsive scattering, IS).^{1, 5, 27} The IS component is especially interesting, as it retains a “memory” of the projectile’s incident energy content, impact geometry, and velocity distribution.²⁸ These parameters map via the collision event into a set of final quantum state and velocity distributions, with a transformation function that depends sensitively upon a variety of surface properties, such as roughness, local surface mass, temperature, electronic structure, and gas-surface interaction potentials. The experimental ability to control a projectile’s incident parameters via supersonic molecular beams and chopped effusive sources, along with the ability to precisely measure much of the final energy and velocity distribution of the scattered flux, has shed light upon the nature of the transformation function and the dominant factors that govern it.

Experiments have built upon the TD/IS model framework to elucidate details about particularly chemically relevant surface interactions. For example, Kay and coworkers used King and Wells-based trapping probability measurements combined with incident angle variations to uncover information on novel binding mechanisms at the water-vapor/water-ice

interface.⁸ Likewise, two-laser pump-probe methods have been combined with state-resolved resonance-enhanced multiphoton ionization (REMPI) measurements by Huang *et. al.*, to reveal highly non-adiabatic energy transfer events by which vibrationally excited NO relaxes when scattering from a metal surface (Au(111)), but not from an insulating surface (LiF).⁴ Molecular beam chopping schemes have been used in combination with mass spectrometry in the work of Nathanson *et. al.* and Saecker *et. al.* to explore gas-liquid scattering dynamics that reveal possible binding and proton exchange mechanisms at the interface.^{5, 6}

While these studies and many others have provided a strong methodological foundation for future experimental research as well as established directions for theoretical exploration, much work still lies ahead in the surface-scattering field. For example, the correlation between internal quantum states and translational degrees of freedom in the scattered flux is challenging to obtain and generally not well understood, although recent state-resolved Dopplerimetry studies of gas-liquid collisions have made crucial first steps toward this goal.²⁹ Additional key insights should in principle be available from experiments which combine the sensitivity of mass-resolved time-of-flight methods with the detailed dynamical information from quantum-state resolved techniques. In this context, velocity map imaging (VMI) represents a recent and powerful advancement in measurement of 2D and 3D velocity distributions, which has helped establish new paradigms in a wide arena of chemical processes including photoionization, photolysis, and photodetachment.^{30, 31} A critical feature of the VMI technique is the use of electrostatic lenses that both accelerate and focus a spatially extended group of ions to create a high resolution velocity map. Most importantly, each pixel in this map corresponds to a particular velocity vector projected onto the image plane, independent of spatial origin for the ionization process. Consequently, velocity map imaging methods offer access to a powerful new

tool in surface scattering experiments, based on a full accounting of translational and internal quantum state energy content before and after a collision event.

The central focus of this study is to introduce such an experimental tool, which combines i) supersonic molecular beams, ii) state-resolved resonance enhanced multiphoton ionization, and iii) velocity-map imaging, and in the process offers a powerful new glimpse into the quantum state resolved dynamics of surface scattering events. As an initial test system, we apply these methods to quantum state resolved HCl scattering from Au(111) supported on atomically flat mica. In particular, these VMI methods reveal that the incident hyperthermal HCl clearly exhibits branching between trapping-desorption (TD) and impulsive scattering (IS) trajectories, which are now easily resolved and cleanly identified in the velocity maps. This resolution in velocity space allows for unambiguous analysis of the IS component without a model-dependent deconvolution from a TD fraction. Coupled with the quantum-state resolution inherent to REMPI-based ionization,^{9, 32, 33} analysis of the images probes correlations between rotational and translational distributions of surface-scattered molecules, and thereby yielding fundamentally new dynamical insights into the scattering of this prototypical HCl/Au(111) system.

§ 6.2 Experimental Setup and Apparatus

The apparatus used in this study is a modified velocity-map imager, as shown in Fig. 6.1, with important changes in both the repeller plate electrode as well as the molecular beam orientation. The important issues in achieving such a capability are a) placing a surface within the imager, b) probing the scattered molecules such that we observe the full velocity distribution, c) incorporating temperature control of the surface and d) designing the imager to minimize electrostatic charging of its insulating components.

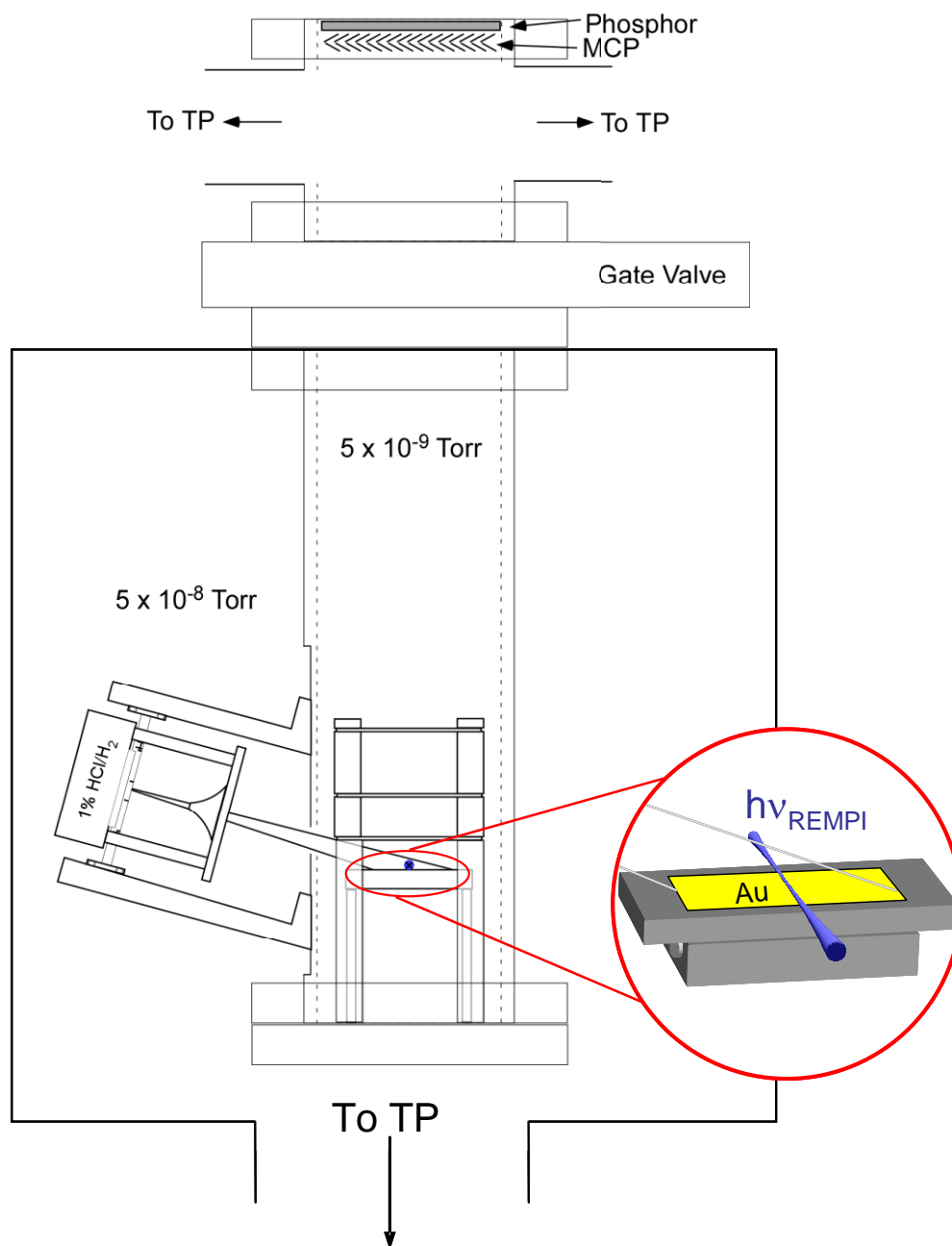


Fig. 6.1 Experimental setup of the velocity-map imager (VMI) adapted to probe surface scattering dynamics. A pulsed supersonic jet of 1% HCl in 150 Torr of H₂ impinges upon an Au(111) surface at an incident angle of 75° (relative to the surface normal) after skimming. The surface is embedded in a 75 x 25 x 6 mm copper heater mount which also serves as a repeller plate as shown in the right inset. The VMI is mounted within a grounded flight tube at 5×10^{-9} Torr (maintained by two 250 L/s turbomolecular pumps, TP). Ions impact a double-layer MCP coupled to a phosphor screen that is monitored by a 690 kpixel CCD and a photomultiplier tube. The flight tube resides in an outer chamber (base pressure 5×10^{-8} Torr) pumped by a 1400 L/s turbomolecular pump. The UV REMPI laser is introduced perpendicular to the molecular beam within < 0.5 mm of the gold surface (right inset).

Many possible layouts could allow one to introduce a molecular beam to a surface within a VMI, but of utmost importance is that the electric fields which define the focusing potential between the repeller plate and first lens are unaffected by the presence of the surface. This restriction precludes the possibility of placing the interface at some angle between the electrodes, as this would lead to distorted velocity maps. Instead, the surface is embedded in a heater mount which also serves as the repeller plate (as shown in Fig. 6.1) of the imager. The typical repeller plate of the VMI is therefore replaced with a free-standing, gold-plated copper structure containing a groove in which the sample rests. The mount is heated by an embedded cylindrical cartridge heater, capable of heating the surface to 600 K. The aluminum electrostatic lenses of the VMI are 1.5 mm thick and 70 mm in diameter. The distance between the repeller plate (i.e., the heater mount) and the first lens is 15 mm. Typical voltages applied to the repeller and first lens are +2000 V and +1600 V, respectively.

The surface used in this experiment is a 100 nm thick layer of Au vapor-deposited on an atomically-flat 20 x 20 mm mica substrate (Phasis, Inc.), with typical Au(111) domain sizes of 0.5 - 1 μm^2 in area, verified with Atomic Force Microscopy (AFM). The sample is held in place using two copper clamps at the ends of the surface. These scattering experiments are all performed with the Au sample heated to 500 ± 5 K, where the temperature is measured using a type K thermocouple mounted on the copper heating block. In conjunction with the base pressure of $\sim 5 \times 10^{-9}$ Torr within the VMI flight tube and the heated substrate conditions, the gold remains clean over the course of a typical 6-hour data run, as confirmed by water contact angle measurements taken before and after an experiment. Over the course of the 4 datasets that comprise the data presented here, 3 separate Au(111)/mica surfaces were used.

In order to create undistorted velocity maps, the repeller plate (i.e. the heater mount) cannot be tilted to allow access to a molecular beam. Instead, the molecular beam must be introduced at an angle relative to the VMI axis. In this study, the HCl molecules impinge at a near-grazing 75° angle relative to the surface normal, thereby largely confining the incident velocity vector component within the surface plane. The VMI is mounted on the bottom flange of an 89 mm ID stainless steel flight tube, which is pumped using two 250 L/s turbomolecular pumps to yield a base pressure of $< 5 \times 10^{-9}$ Torr. The flight tube has 3 small apertures in it, one (12 mm dia.) for the entrance of the pulsed molecular beam, and two (9.5 mm dia.) for the laser entrance and exit. Two aluminum struts on the outside of the flight tube are used to mount the pulsed valve. A 2 mm diameter skimmer is displaced 40 mm from the orifice using four aluminum posts attached to the pulsed valve face. The valve itself is a PZT design based upon that of Proch and Trickle,³⁴ with a typical pulse width of 250 μ s and orifice diameter of 0.5 mm. The supersonic jet is formed from 150 Torr of a 1% mixture of HCl in H₂. These conditions produce beam kinetic energies of 21 ± 5 kcal/mol. The ionization laser fires within the first 90 μ s of the gas pulse, in order to eliminate contributions from thermalized background species due to collisions in the chamber.

The detection scheme is based upon state-resolved $2 + 1$ resonantly enhanced multiphoton ionization (REMPI) of HCl.^{32,33} To ensure a complete picture of the velocity distribution, the REMPI ionization region must be intersected by all (or nearly all) possible velocity vectors in the scattered flux. Two possible scenarios afford this condition: One is a small gas-surface collision area probed by a much larger ionization region located directly over the impact point. Alternatively, a large impact area can be probed by a very small ionization region located close to the surface. Because the REMPI scheme is two-photon based (where the

third photon is a saturating ionization pulse), large electric fields and a tight laser focus are critical to efficient ionization. The first scenario of a spatially extended ionization region would reduce the ion yield too severely, thus rendering this configuration unfeasible. The second scenario, however, is quite feasible, and in particular can be attained using a skimmed molecular beam traveling 12.5 cm from the orifice before forming a ~ 17 (width, w) \times 66 (length, l) mm elliptical collision area on the gold surface. The UV REMPI laser passes within $d = 370 \mu\text{m}$ of the Au, where the suitable choice of $\frac{d}{w} \leq 0.03$ ensures that the ionization pulse probes a nearly complete velocity distribution of the scattered molecular flux.

In this experimental layout, the ionization region is defined by the extent of the laser focus rather than the spatial extent of the gas pulse. The importance of this is illustrated by considering what possible range of ionization loci within a VMI apparatus map onto points in the imaging plane reflective of the true velocity distribution. Only those ions created within an area approximately $1/3$ of the diameter of the first electrostatic lens aperture focus correctly at the imaging plane. Those ions generated outside of this area are mapped incorrectly to points on the imaging plane that are not representative of their velocity vectors. In the case of the VMI dimensions used here, the region in the apparatus that produces a well-focused image is ~ 3 mm in diameter. As a consequence, the ionization region must be restricted to < 3 mm in length, which is achieved by expanding the beam width from 2 mm to 19 mm in a Galilean telescope, followed by tight focusing with a $f = 40$ cm lens. Spherical aberration at the focus is minimized using plano-convex lenses with their convex sides facing the collimated part of the laser beam. In the limit of Gaussian beam focusing without aberration or astigmatism, this setup produces a focal region that is $\sim 350 \mu\text{m}$ in length and $\sim 7 \mu\text{m}$ in radius. By moving the focus toward and away from the center of the VMI and monitoring the velocity map of a room temperature

distribution of HCl molecules, we find that the ionization region is ~1 mm in length. This is roughly three times larger than the expected value of 350 μm , likely due to the non-Gaussian transverse profile of the frequency-tripled dye laser beam.

For all rotational levels from $J = 0$ through 12, the tripled output of a Nd:YAG-pumped pulsed dye laser operating at 10 Hz is used to probe the Q-branch of the $V \ ^1\Sigma^+ \leftarrow X \ ^1\Sigma^+$ REMPI transition, accessing the $v' = 12$ level in the $V \ ^1\Sigma^+$ state near 237 nm.³³ The list of line positions is presented in Table 6.1. Initial attempts at observing vibrationally-excited HCl in the scattered flux yielded no appreciable population within the signal-to-background limit of this experimental setup. The laser power is varied using a set of reflective neutral density filters (Thorlabs, Inc.) to establish that the ionization efficiency is indeed quadratic with respect to laser power. To minimize space-charge effects as well as facilitate operation under single-ion counting conditions, we adjust the laser intensity to yield on-resonant signals of < 30 ions/laser shot. Typical laser powers used are thus dependent upon the rotational state being probed, i.e. ≤ 10 $\mu\text{J}/\text{pulse}$ for low J states (i.e. $J = 0 - 3$) with larger number densities, and up to ≥ 100 $\mu\text{J}/\text{pulse}$ for the highest J states significantly populated ($J = 10 - 12$) and much lower densities. To average over small but measurable Doppler shifts in the image, the laser is scanned by 0.009 nm (~ 1.6 cm^{-1}) over the REMPI transition during image acquisition.

Table 6.1 Line positions and state assignments of (2+1) REMPI transitions. All transitions are V $^1\Sigma^+ \leftarrow X^1\Sigma^+$ Q-branch transitions, accessing the $v' = 12$ vibronic level in the V $^1\Sigma^+$ state.

J''	λ (nm)
0	235.997
1	236.033
2	236.104
3	236.213
4	236.356
5	236.533
6	236.751
7	237.000
8	237.290
9	237.599
10	237.935
11	238.287
12	238.641

In order to reliably measure the rotational state populations of scattered HCl, the ions produced by the REMPI laser are counted using centroiding software, with the resulting ion count divided by the square of the laser power and the stagnation pressure behind the pulsed valve orifice (~150 Torr). A weakly power- and J-dependent effective linestrength, $S(J)$, must also be taken into account. This is determined from velocity maps of a distribution of room temperature HCl molecules for $J = 0 - 12$, which are obtained by delaying the laser pulse relative to the gas pulse such that the ionization step occurs ~1 ms after the pulse valve fires. This ensures that the distribution of HCl molecules which originated from a supersonic jet have had time to thermally equilibrate with the VMI drift tube walls at 300 K. The resulting HCl rotational state populations can be least-squares fit to a room temperature Boltzmann distribution, where the modest residual deviations are used to extract small but finite correction factors due to multiple detection pathways. These factors are primarily a consequence of an $H^+/Cl^+/HCl^+$ photofragmentation branching ratio:

$$BR(36) = \frac{I(36)}{I(1) + I(35) + I(36)}$$

where $BR(m)$ and $I(m)$ refer to the branching ratio and the intensity measured in the mass spectrum at mass m , respectively. Room-temperature data which takes into account the measured $BR(36)$ branching ratio (rather than using the empirical linestrength factor) exhibits the same rotational state distribution, only with slightly more point-to-point scatter.

The velocity calibration is determined from a velocity map of the H^+ (i.e. $m/z = 1$) branch produced during the HCl REMPI process. The energetics of this process are well established,³⁵ and produces several sharp rings in the velocity map. The calibration is confirmed by similarly obtaining the velocity map of O_2 photolysis at 224.999 nm,³⁰ and found to be within 1% of that obtained based upon the map of proton formation from HCl.

Ions produced by the REMPI step are detected on a double-microchannel plate (MCP, chevron) coupled to a fast phosphor screen (41 ± 1 ns decay constant), which is in turn monitored by a 690 kpixel CCD and a photomultiplier tube. Because the VMI also acts as a mass spectrometer for any ion produced during the REMPI step, the MCP is gated over 100 ns from 1300 V to 1700 V using a high-voltage pulse generator (DEI) to detect only $m/z = 36$ ions. The ion impacts are counted on-the-fly using centroiding software (DaVis), and then analyzed with home-built computer programs.

For each rotational state, a scattering distribution is obtained consisting of 1800 laser shots. Because there is a small non-resonant ionization signal from HCl, off-resonant background images are also acquired and subtracted from the on-resonant images. The typical acquisition time to obtain each image is ~ 3 minutes. The velocity map for every J-state probed in this study reflects the sum of 4 images taken on separate days. Due to the broad range in energies sampled by the scattered flux result in a relatively sparse velocity map, which can then be improved by smoothing with a rolling Gaussian average described by a standard deviation of $\sigma = 4$ pixels.

As one particularly useful experimental detail, we have used acetal copolymer static dissipative posts and spacers (Pomalux SD-A) within the VMI to reduce electrostatic charging and stray field generation. This material resembles Teflon in strength and durability, but exhibits moderate surface and bulk resistivities of $10^9 - 10^{11}$ Ω /square and $10^9 - 10^{11}$ Ω -cm, respectively. This results in an effective resistance between accelerating plates of ~ 8 G Ω .

§ 6.3 Collected Velocity Maps

Sample final J-state dependent velocity maps produced by a high kinetic energy, 21 ± 5 kcal/mol, beam (1% HCl balance H₂) scattering from a clean Au(111)/mica supported surface are presented in the right side of Fig. 6.2. The coordinate system used in analysis of these maps is shown schematically in Fig. 6.2(a) and is defined as follows. The scattering plane is represented by the trajectory of a molecule traveling along the cylindrical axis of the incident molecular beam and undergoing perfect specular reflection at the surface. The velocity component parallel to both the scattering plane and the surface is designated $v_{\text{in-plane}}$, while $v_{\text{out-of-plane}}$ is the component perpendicular to the scattering plane and also parallel to the surface. The remaining velocity vector, v_z , is directed along the surface normal. The incident (non-scattered) molecular beam is present in all of the raw data as a very sharp, narrow feature near $v_{\text{in-plane}} \sim 2100$ m/s and $v_{\text{out-of-plane}} \sim 0$ m/s. Because this feature carries no information about the scattering event, we fit it to a sum of 2D Gaussian functions and subtract from the raw data to produce images without incident beam contamination. We note that this beam subtraction protocol is quite generally applicable to a wide range of scattering energies, but in the present case is substantially aided by complete resolution of the incident beam feature in the velocity map. The 2-D Gaussian functions used to describe the incident beam are fit simultaneously with the scattered data to the complete set of $J = 2 - 12$ velocity maps, with overall amplitude and shifts in the central location allowed to vary from state to state. Incident beam contamination in the $J = 0$ and 1 maps are also fit and removed with a similar sum of 2D Gaussians. However, due to complications as a result of much higher incident beam intensities in these J states, this is performed independently from the $J = 2 - 12$ data set.

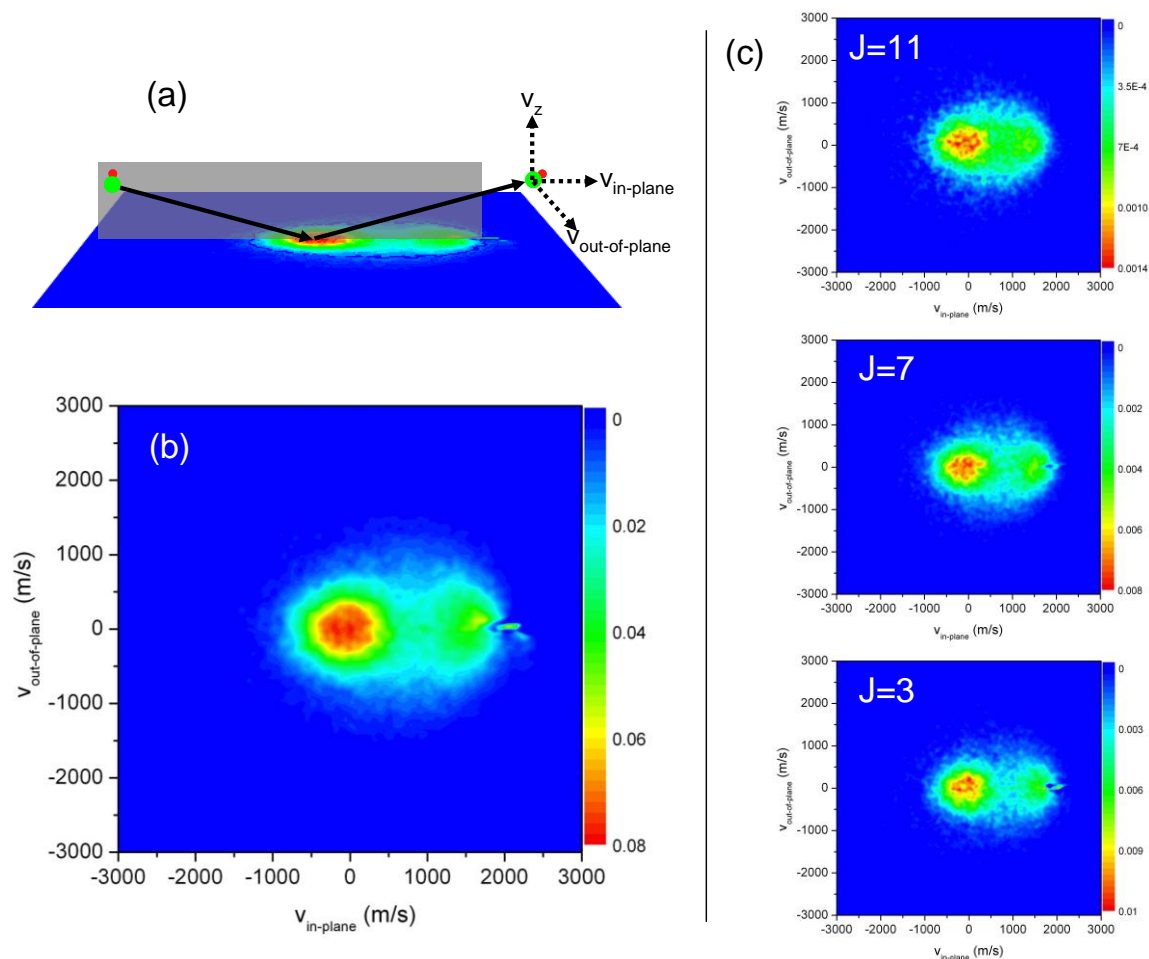


Fig. 6.2 Velocity map images of scattered HCl from a 1% HCl/H₂ incident supersonic jet with $E_{inc} = 21(5)$ kcal/mol. The coordinate system used for analysis is shown in panel (a), where the scattering plane contains the incident and specular-scattering velocity vectors. (b) Velocity map of HCl integrated over all rotational states, revealing i) a thermal desorption feature near $v_{in-plane} = v_{out-of-plane} = 0$ m/s, and ii) an impulsive scattering component near $v_{in-plane} \sim 1500$ m/s. (c) State-resolved velocity maps for HCl molecules in $J = 3, 7,$ and 11 reveal both TD and IS components, with the position of the IS component changing systematically with J .

Such an analysis permits a variety of different visual representations of the velocity map data. For example, an *integrated* velocity map, which simply reflects the sum over all quantum states if the HCl ionization step were not rotationally resolved, is shown in Fig. 6.2(b). This velocity map clearly reveals a bimodal distribution, with one component peaking around the velocity origin ($v_{\text{in-plane}} \approx v_{\text{out-of-plane}} \approx 0$) and an additional strongly forward scattering feature near $v_{\text{in-plane}} \approx 1500$ m/s. Exploration of the quantum state-resolved velocity maps, a few samples of which are shown in Fig. 6.2(c), reveal that the low-energy feature remains relatively unchanged between J-states, while the higher velocity component is strongly dependent upon rotational energy content. One interpretation of these sets of velocity maps would be in support of microscopic branching, with the low energy peak centered around the velocity origin due to trapping desorption (TD) and the forward-scattered peak due to impulsive scattering (IS) events. Such dependence highlights a major advantage of the REMPI/VMI technique, i.e. providing first glimpses of *correlated* quantum state and final velocity distributions in the scattering dynamics.

§ 6.4 Velocity Map Analysis

Projections of the velocity map images onto the $v_{\text{in-plane}}$ - and $v_{\text{out-of-plane}}$ - axes permit a much more detailed view of the velocity distributions parallel and perpendicular to the scattering plane. The profile along the $v_{\text{in-plane}}$ direction for molecules in $J = 2 - 11$, shown in Fig. 6.3(a), is obtained by integrating over $v_{\text{out-of-plane}}$ at each value of $v_{\text{in-plane}}$. The profiles have been normalized in order to facilitate a qualitative comparison. Immediately apparent is an asymmetry which favors the forward-scattering ($v_{\text{in-plane}} > 0$) direction, signifying the presence of a non-thermal, impulsive scattering component in the flux. Interestingly, some of the forward-scattered molecules access in-plane velocities up to +2000 m/s, implying that they retain most of their initial momentum vector. In addition, flux in the backward-scattering region of the profile extends to -1400 m/s, i.e., well outside of the thermal regime. For comparison, a Gaussian function associated with a 500 K Boltzmann distribution is shown as a dashed red line in Fig. 6.3(a). Specifically, 2.5σ for a 500 K distribution corresponds to ± 850 m/s, which from Gaussian statistics represent the velocity boundaries containing 98.8% of thermally-desorbing flux. This indicates the important presence of impulsive backscattering trajectories, in spite of the near-grazing incident angle of 75° . Together, these results suggest that impulsively scattered molecules span the remarkably broad in-plane velocity range of $-1400 < v_{\text{in-plane}} < +2000$ m/s, despite scattering from wide regions of a nominally atomically-flat Au(111) surface.

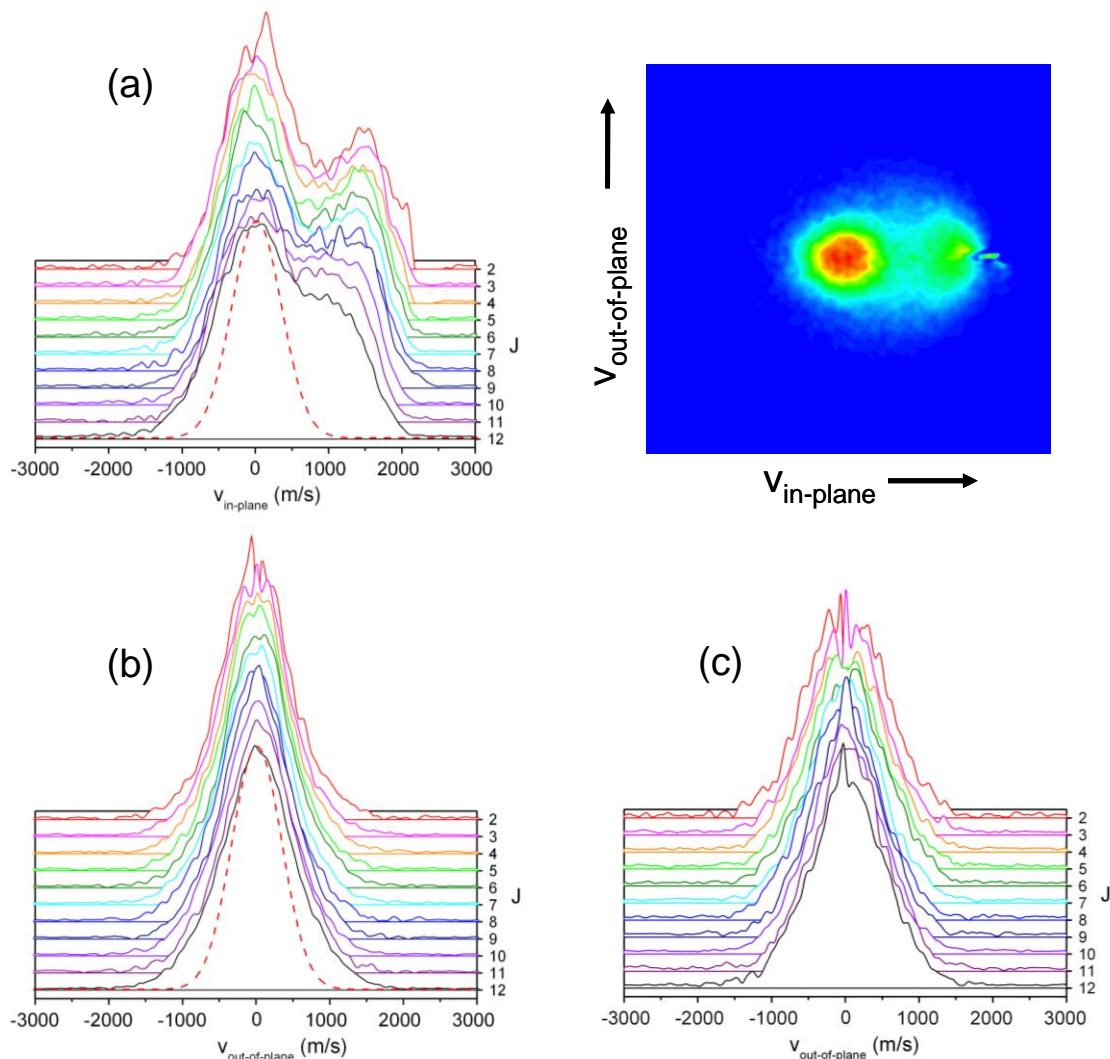


Fig. 6.3 (a) Integrated velocity distributions parallel to the scattering plane (along $v_{\text{in-plane}}$) for scattered HCl molecules in $J = 2 - 12$ originating from a 21 ± 5 kcal/mol incident beam. The distribution is clearly forward scattered, with a J -state dependence in the high- $v_{\text{in-plane}}$ region. (b) The perpendicular component of scattered flux in $J = 2 - 12$ is symmetric about $v_{\text{out-of-plane}} = 0$, but has a hyperthermal component. Fits to the out-of-plane velocity profile of only those molecules with $v_{\text{in-plane}} > 850$ m/s, shown in (c) for $J = 2 - 12$, yields a temperature of 1128 ± 34 K, illustrating that these impulsively-scattered molecules contribute to the hyperthermal component of the profiles in (b). Red curves in (a) and (b) correspond to a $T_{\text{surf}} = 500$ K distribution for comparison. Top right inset illustrates the $v_{\text{in-plane}}$ and $v_{\text{out-of-plane}}$ coordinates.

The velocity distribution perpendicular to the scattering plane for molecules in $J = 2 - 12$ is obtained by integrating over all $v_{\text{in-plane}}$ for each value of $v_{\text{out-of-plane}}$, and presented in Fig. 6.3(b). The profile in this dimension is symmetric about $v_{\text{out-of-plane}} = 0$ m/s, as expected given the symmetry axis of the experiment. This projection is nearly Gaussian, but its full-width at half-maximum (FWHM) of over 1000 m/s for all J states reflects the presence of significantly hyperthermal contributions (a 500 K Gaussian distribution is shown as a red dashed line). As a simple first model, we performed a two-temperature fit (sum of two Gaussian functions) to the data, with one temperature fixed at 500 K, and found the second component to be 1582 ± 34 K. Spatial isolation in a velocity map again provides a powerful means for probing the internal and translational energy content of the hyperthermal fraction, without deconvolution from a thermal component. This capability is explicitly illustrated in Fig. 6.3(c), where the $v_{\text{out-of-plane}}$ distribution is now obtained by integrating only over the forward-scattering region from $v_{\text{in-plane}} = 850 - 3000$ m/s (i.e. outside 99% of the 500 K thermal regime) for $J = 2 - 12$. The profiles are well fit to a Gaussian lineshape, yielding an effective temperature of $T_{\text{out-of-plane}} = 1128 \pm 34$ K.

Of particular interest in the data series of Fig. 6.3(a) is a reduction in the highest translational energy component of the scattered HCl with increasing J state. Such a trend may be the result of conservation of energy, where increased rotational excitation when scattering comes at the cost of translational motion. We can quantify this possibility further by fitting the impulsively-scattered component of the dataset using a 3-dimensional model that, in spherical coordinates, is described by:

$$P(s, \theta, \phi) = A \times \left(e^{-\frac{(s-s_0)^2}{\sigma_s^2}} \right) \times \text{Cos}^p(\theta - \theta_0) \times \text{Cos}^q(\phi)$$

where, s is the speed of the impulsively-scattered HCl, whose most probable value is s_0 and has a standard deviation of σ_s . The angular components of the flux are described by cosine

distributions in θ and ϕ that are raised to a power, with the distribution in θ centered on a final scattering angle θ_0 . This three-dimensional model is then integrated in Cartesian coordinates over the v_z direction to create a 2-D velocity map. As a result of parameter correlation, θ_0 is held fixed at the specular 75° angle, a constraint which has been shown to be justified in the case of HCl scattering from MgO(100) and Au(111), though for less steep range of incidence angles ($\sim 0^\circ - 45^\circ$).^{36, 37} The corresponding advantage of such a specular assumption is that it permits a 3D velocity map to be characterized from 2D velocity data, and therefore a full accounting of energy transfer in the HCl/Au(111) impulsive scattering dynamics. Based on this model, the kinetic energy associated with the extracted speed is plotted as a function of J-state in Fig. 6.4(a) (red circles), along with the rotational energy content ($E_{\text{rot}} = B_{\text{HCl}} J(J+1)$, blue circles), and the sum of the two energy components (black squares). This plot reveals that the sum of the two components is constant across $J = 2 - 12$, implying that the *reduction* in final translational energy content is balanced by a corresponding *increase* in rotational energy content. Such a trend is consistent with a dynamical constraint such as conservation of energy, and predicts that the anticorrelated rotational excitation of the scattered HCl comes at the “cost” of translational energy during the scattering event. This result is consistent with previous experimental studies of NO scattering from Ag(111),^{38, 39} where, within a range of E_{rot} similar to that studied here ($0 < E_{\text{rot}} < 1600 \text{ cm}^{-1}$), the translational energy content is similarly counterbalanced with E_{rot} . Interestingly, this anticorrelation breaks down in NO/Ag(111) at even higher rotational excitation (i.e., $E_{\text{rot}} > 1600 \text{ cm}^{-1}$), ostensibly due to a roll off in efficiency of energy transfer to surface phonon modes with increasing J. However, such an energy regime is higher than that studied here.

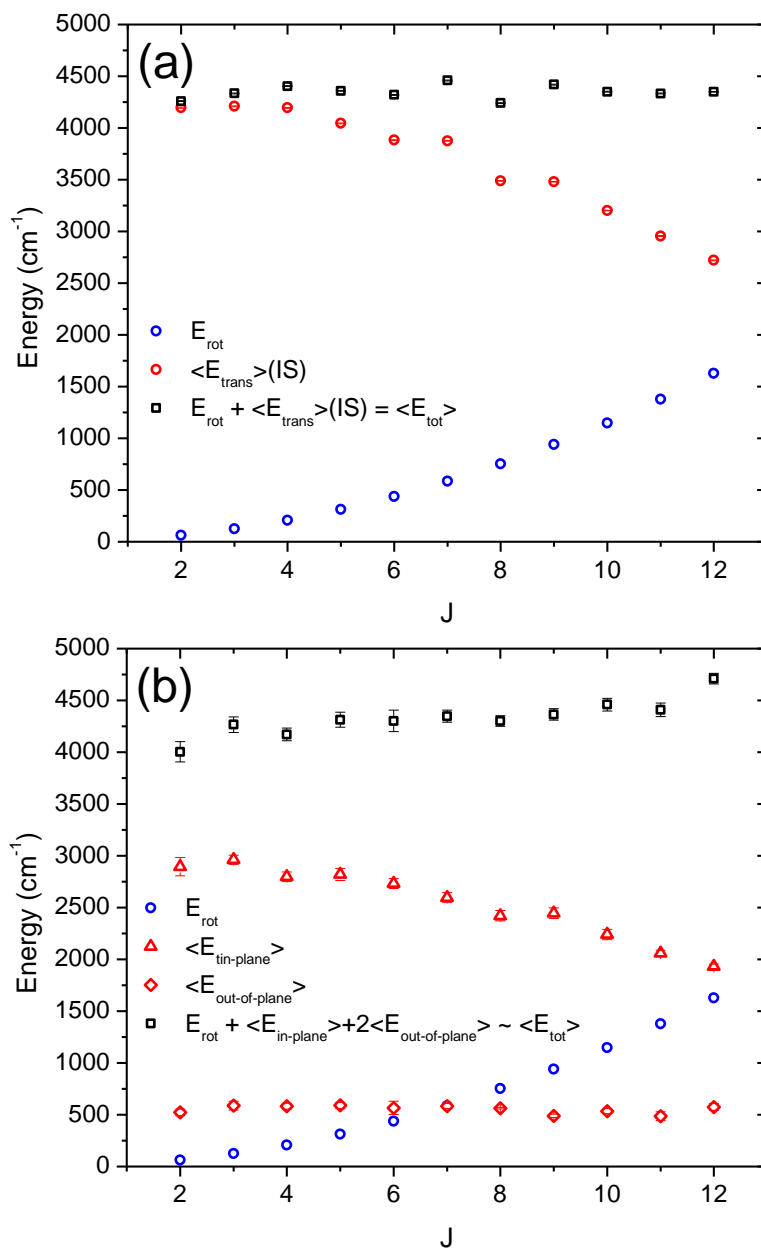


Fig. 6.4 Tracking the energy content in various degrees of freedom as a function of J-state. In (a), red circles correspond to total translational energy extracted from fits of the 2-D velocity maps to a 3-D model as described in the text. The sum of this energy with the rotational energy (blue circles), shown as black squares, indicates that rotational excitation is occurring at the cost of translational energy. In (b), deconstructing the translational energy into $\langle E_{\text{in-plane}} \rangle$ (red triangles) and $\langle E_{\text{out-of-plane}} \rangle$ (red diamonds) reveals that most of the energy content is contained in the in-plane coordinate. In the first-order picture where $\langle E_z \rangle \sim \langle E_{\text{out-of-plane}} \rangle$, the total energy content (black squares) is very similar to that obtained using the 3-D model in (a).

One point worth noting from this 3D model analysis is that the predicted total energy content of $\sim 4300 \text{ cm}^{-1}$ is roughly 40% less than the incident energy of $\sim 7300 \text{ cm}^{-1}$. This is qualitatively consistent with trends observed in scattering NO from Ag(111), where NO molecules with low E_{rot} were found to lose $\sim 30\%$ of their total energy to the surface at an incident angle of 60° (although we note the energy loss was found to decrease with θ_{inc}).³⁹ Both of these observations differ somewhat from previous HCl/Au(111) studies,⁹ where the predominant fraction of incident energy was reported to be largely *retained* (i.e., $E_{\text{trans}} + E_{\text{rot}} \sim E_{\text{inc}}$) in the scattered HCl molecules. One possible explanation could be our current lack of direct VMI information on the velocity distribution normal to the scattering plane (i.e. v_z), and a corresponding failure of our 3D model to quantitatively recapitulate this distribution. This can be remedied by incorporating “DC slicing” methods in our VMI apparatus,⁴⁰ a capability which is currently under development.

We can rigorously measure the average in- and out-of-plane kinetic energies, $\langle E_{\text{in-plane}} \rangle$ and $\langle E_{\text{out-of-plane}} \rangle$, for the impulsively-scattered HCl, and thereby gauge relative contributions of these two velocity components to the total energy content. Here, $\langle E_{\text{out-of-plane}} \rangle$ and $\langle E_{\text{in-plane}} \rangle$ are calculated according to:

$$\langle E_{out-of-plane} \rangle = \frac{\sum_{v_{out-of-plane}} P_{v_{out-of-plane}} \times E_{v_{out-of-plane}}}{\sum_{v_{out-of-plane}} P_{v_{out-of-plane}}}$$

$$\langle E_{in-plane} \rangle = \frac{\sum_{v_{in-plane}} P_{v_{in-plane}} \times E_{v_{in-plane}}}{\sum_{v_{in-plane}} P_{v_{in-plane}}}$$

To implement these calculations, $P_{v_{in-plane}}$ and $P_{v_{out-of-plane}}$ are required for the IS channel, which we obtain from Gaussian fits to the integrated velocity component distributions in Fig. 6.3(a) and (b). Specifically, the $v_{in-plane}$ traces (Fig. 6.3(a)) are already partially resolved into IS and TD components and thus are simply fit to a sum of two Gaussians, one to the TD component centered at $v_{in-plane} = 0$ and the other capturing the IS flux evident in the vicinity of $v_{in-plane} \sim 1500$ m/s. For the out-of-plane velocity distributions (Fig. 6.3(b)), the traces are also fit to a sum of two Gaussians, with both centered on $v_{out-of-plane} = 0$ m/s. One of the Gaussians represents the TD fraction at a fixed temperature of 500 K, while the other represents $P_{v_{out-of-plane}}$, which is used in the calculation of $\langle E_{out-of-plane} \rangle$.

The corresponding results are plotted in Fig. 6.4(b). $\langle E_{in-plane} \rangle$ (red triangles) is the largest energetic contributor to the IS component, containing $2500 \pm 500 \text{ cm}^{-1}$ of translational energy, while $\langle E_{out-of-plane} \rangle$ (red diamonds) is significantly smaller, $\sim 500 \text{ cm}^{-1}$. The larger energy content in the scattering plane is consistent with forward scattering at grazing angles, while its systematic decrease with J suggests that most of the rotational excitation is coming at the cost of

the in-plane velocity component. On the other hand, the much smaller and narrower out-of-plane kinetic energy content is consistent with a highly directional jet cooled incident beam scattering from an atomically-flat Au surface. Once again, the sum of $E_{\text{rot}} + \langle E_{\text{in-plane}} \rangle + \langle E_{\text{out-of-plane}} \rangle$ is remarkably flat with respect to final J state. In particular, there is an anticorrelation between E_{rot} and $\langle E_{\text{in-plane}} \rangle$, which provides evidence for an energetic dynamical constraint between these two degrees of freedom.

We can take this analysis one step further. Though $\langle E_{\text{normal}} \rangle$ is not measured directly in the present studies, one would expect for such glancing incidence angles qualitatively similar velocity distributions along the v_z and $v_{\text{out-of-plane}}$ directions and therefore similarly modest energy content. The corresponding J-dependent results for E_{tot} in this approximation of $\langle E_{\text{out-of-plane}} \rangle \sim \langle E_z \rangle$ are shown in Fig. 4(b) (black squares). Interestingly, these results are very nearly identical to those obtained from the 3-D velocity fit model, indicating that these two model treatments are at least self-consistent. However, these total energy values are still significantly short of the energy content of the incident beam, which implies substantial energy transfer (40%) to the surface. Indeed, to account for the entire incident beam energy, $\langle E_z \rangle$ would need to be 5-fold higher ($\sim 3000 \text{ cm}^{-1}$), i.e., nearly comparable to $\langle E_{\text{in-plane}} \rangle$, which seems a surprising scenario given the near-grazing incident angle. However, there is some indication of a trend in this direction. Studies by Sau *et al*⁴¹ and Brako *et al*⁴² for thermal rare gas atoms scattering from Ag(111) surfaces, for example, illustrate that the scattering can be sub-specular as the incident angle approaches grazing and as the surface temperature is increased. Specifically, for scattering Ar from Ag(111), it was found experimentally⁴¹ that the angular distributions peaked at $\sim 55^\circ$ for an incident angle of 65° , consistent with energy transfer from incident beam into the v_z coordinate. Thus, though unlikely, we cannot rule out that scattered HCl at glancing incidence is

gaining energy normal to the surface, giving rise to larger total energy content and therefore consistent with a lower efficiency of energy transfer into the surface. To resolve this issue further, DC slice experimental efforts with v_z resolution are clearly needed that will allow for a direct 3D velocity map reconstruction of the scattered HCl.⁴⁰

The systematically anticorrelated reduction in $\langle E_{\text{in-plane}} \rangle$ with increasing E_{rot} is especially interesting and implies that an energy conservation rule connects these two degrees of freedom. Previous studies of the HCl/Au(111) system at less grazing incident angles have shown that the final rotational energy content after scattering from the surface depends primarily upon incident translational energy content *normal* to the surface, (i.e. $E_{z,\text{inc}}$) rather than the total beam energy. Based upon these trends, it was concluded that rotational excitation occurred primarily by collisional exchange with the normal component of the *incident* energy. In contrast, we find here a very clear anticorrelation between the *final* values $\langle E_{\text{in-plane}} \rangle$ and $\langle E_{\text{rot}} \rangle$, with the majority of the rotational excitation arising at a cost to $v_{\text{in-plane}}$. One possible explanation is motivated by the sub-specular scattering angles in Ar/Ag(111) studies,⁴¹ where at grazing angles the Ar atoms gained energy in the v_z coordinate. If $\langle E_z \rangle$ excitation occurs by redirecting energy from the $\langle E_{\text{in-plane}} \rangle$ coordinate, and such a process also induces rotational excitation, then the trend in Fig. 6.4(b) could in principle be observed. A second possibility is that at the grazing incident angles explored in this study, the HCl may have a greater propensity to “skip along the surface” during a nominally impulsive scattering interaction. Multiple consecutive collision dynamics could yield increased probability for collisions with step edges between the Au(111) sample domains, thereby enhancing momentum exchange from $v_{\text{in-plane}}$ to v_z and rotational excitation.

§ 6.5 Rotational State Distributions and Energy Maps

The rotational populations and velocity profiles extracted from the velocity maps provide an initial assessment of how the internal energy is distributed in the scattered flux. Rotational Boltzmann analyses of these high incident energy HCl molecules scattered from the 500 K Au(111)/mica surface are presented in Fig. 6.5. The distribution extracted from the raw images (after correcting for power, stagnation pressure, degeneracy, and linestrength) is presented in light grey, while the data for which the incident beam has been removed, as described above, are shown in black. First, we note that scattering of this high-energy HCl produces a slightly rotationally hyperthermal distribution. Specifically, the data are consistent with single temperature fit of $T_{\text{rot}} = 574 \pm 12$ K, which is clearly hotter than the Au surface. This is in support of our previous conclusion from the velocity maps that the scattered flux exhibits more than simple thermal desorption (TD) dynamics, for which the temperature might be expected to match the surface temperature. Interestingly, there is little evidence in the data in support of a dual temperature TD + IS behavior, such as has been commonly observed in quantum state resolved hyperthermal scattering from insulating liquids.^{1,2} One reason for this could be that the Au(111) surface is already quite hot, making it more difficult to deconvolute from such a 2-temperature Boltzmann analysis the relatively small differences between IS and TD components. The power of the VMI method is that these TD and IS rotational distributions may nevertheless be distinguishable by probing different locations in the velocity map, which will be addressed below.

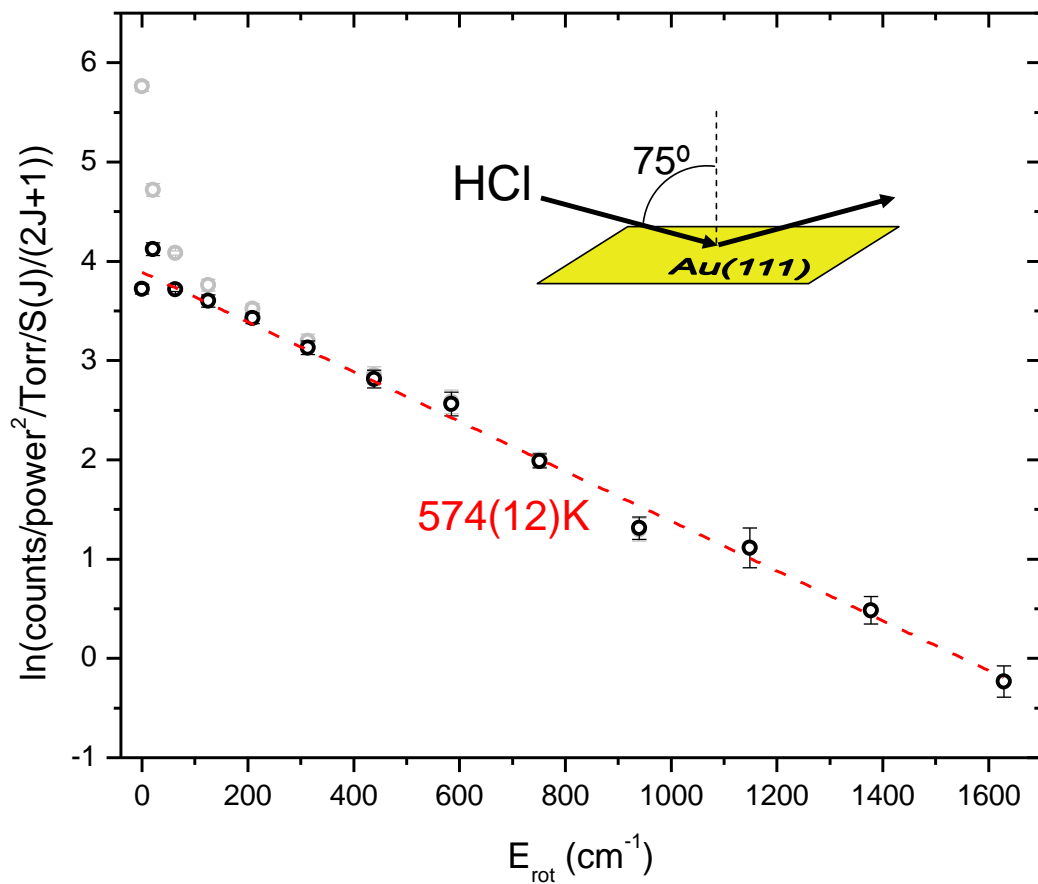


Fig. 6.5 Rotational distribution of molecules scattered from a 1% HCl/H₂ beam at 21 ± 5 kcal/mol. Raw populations are shown in grey, whereas the distribution derived from images in which the incident beam has been subtracted is shown in black. A linear fit to the data (red dashed line) reveals a hyperthermal distribution, indicating the presence of a hyperthermal component.

The complete quantum-state resolution of the REMPI process provides access to rotational state populations that can be further used to correlate rotational and translational energy content. Specifically, we can create an intensity-weighted rotational energy “map” by calculating $\langle E_{rot} \rangle$ at each $(v_{in-plane}, v_{out-of-plane})$ pixel, with $\langle E_{rot} \rangle$ determined from the expression:

$$\langle E_{rot} \rangle(v_{in-plane}, v_{out-of-plane}) = \frac{\sum_{J=0}^{12} I_{v_{in-plane}, v_{out-of-plane}, J} \times E_J}{\sum_{J=0}^{12} I_{v_{in-plane}, v_{out-of-plane}, J}}$$

and plotting it on the same axes as a normal velocity map (Fig. 6.6, center panel). Black areas in the rotational energy map correspond to pixels where there are too few events to reliably define $\langle E_{rot} \rangle$, which we take to be less than one ion count in each J-state.

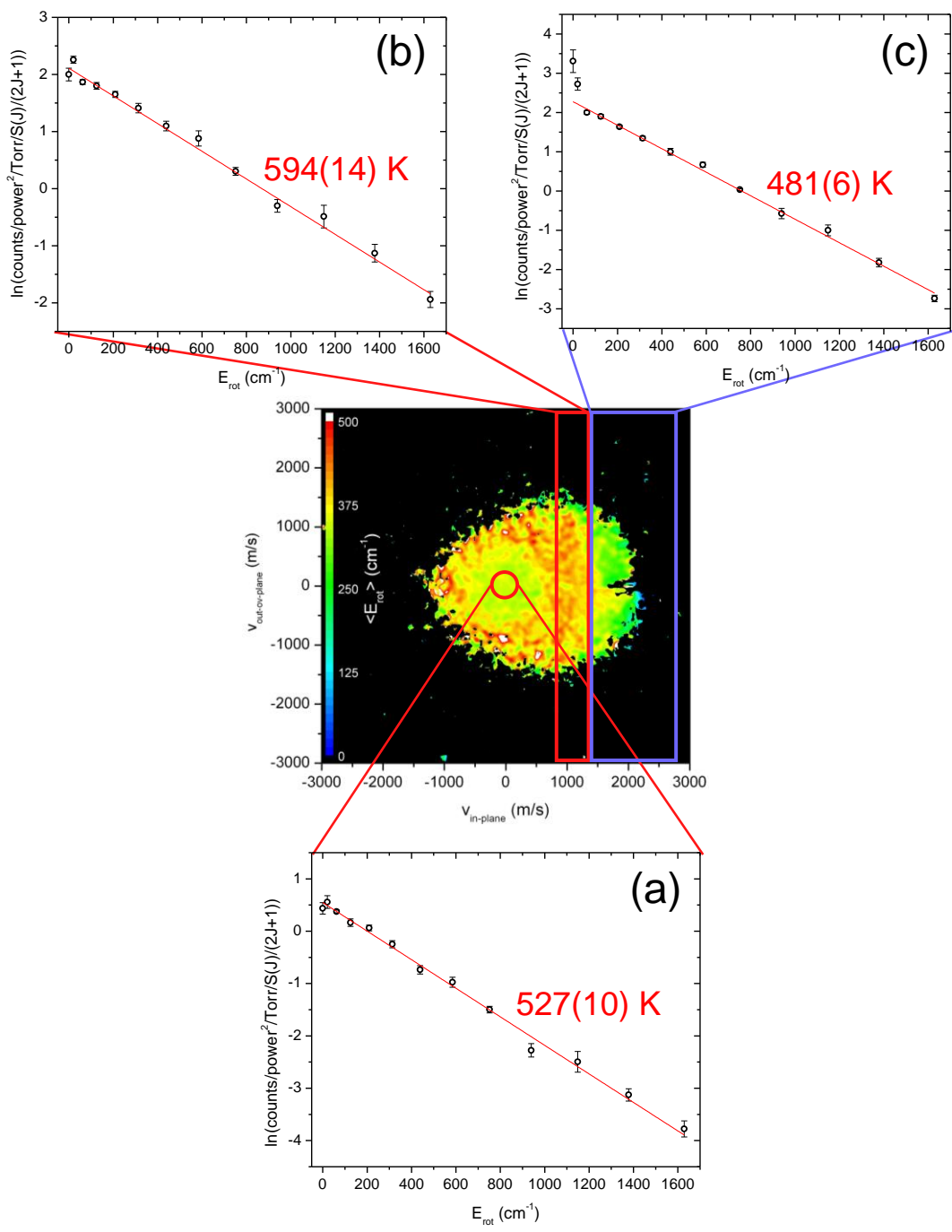


Fig. 6.6 Center: average rotational energy of a scattered HCl beam ($E_{inc} = 21 \pm 5$ kcal/mol) at every value of $v_{in-plane}$ and $v_{out-of-plane}$. Color scale is in units of cm^{-1} . Black pixels contain too few statistics to provide a reliable rotational energy (i.e., at least one ion count in each rotational state). The rotational distribution is shown in (a) for the “TD” region of the map, while (b) and (c) show the distributions in different $v_{in-plane}$ regions of the IS-scattered component, where (b) corresponds to HCl with $850 < v_{in-plane} < 1400$ m/s, and (c) to $v_{in-plane} > 1400$ m/s.

Visual inspection of the rotational energy map in Fig. 6.6 reveals qualitative differences within different velocity regions. At $v_{\text{in-plane}} = v_{\text{out-of-plane}} = 0$ m/s, the map exhibits a rotational temperature of ~ 350 cm⁻¹, which would be expected for thermally-desorbing molecules leaving the surface at a temperature of ~ 500 K. In most of the remaining area of the map, the energy content is hyperthermal, with rotational energy reaching equivalent temperatures of >720 K (>500 cm⁻¹). This area of the map is the same region that exhibits translationally hot $v_{\text{in-plane}}$ and $v_{\text{out-of-plane}}$ components, confirming that flux in this region is hyperthermal in all observed degrees of freedom. Of particular interest here is the reduction of $\langle E_{\text{rot}} \rangle$ with increasing $v_{\text{in-plane}}$, which is a consequence of the same effect that was manifested earlier in Fig. 6.4, where the highly forward-scattered flux is sacrificing rotational excitation for translational energy content. Interestingly, within the same region, this effect is not observed in the out-of-plane coordinate, for which the rotational energy appears independent of $v_{\text{out-of-plane}}$. This again supports the observation that rotational excitation is correlated with loss of incident translational energy (mostly along $v_{\text{in-plane}}$), rather than from interactions responsible for translational energy perpendicular to the scattering plane.

The central image in Fig. 6.6 represents a compilation of the entire dataset into one rotational energy map. However, the information in this map still contains the actual rotational distribution as a function of $v_{\text{in-plane}}$ and $v_{\text{out-of-plane}}$. Figs. 6.6(a), (b), and (c) illustrate the utility of the VMI/REMPI technique to provide this additional and highly correlated information. In Fig. 6.6(a), for example, the subset of rotational data extracted from the nominally “TD” region is shown to exhibit a temperature of 527 ± 10 K. This is significantly cooler than the total velocity map unresolved distribution (574 ± 12 K) and notably closer to that of the Au(111) surface (500 K). That this temperature is still slightly hyperthermal is not at all surprising, as there are IS-

type scattering events appearing in this region as well. Indeed, Fig. 6.6(b) illustrates that the section of IS-type molecules with $v_{\text{in-plane}}$ closest to the TD region (i.e., $850 < v_{\text{in-plane}} < 1400$ m/s) are now substantially hyperthermal with temperatures of 594 ± 14 K. However, it is interesting to note that impulsive collisions do not all necessarily result in a hyperthermal distribution. This is explicitly shown in Fig. 6.6(c), where the subset of the most forward-scattered molecules ($v_{\text{in-plane}} > 1400$ m/s) is well characterized by a *subthermal* temperature of 481 ± 6 K. Of course, this observation is also entirely consistent with the anticorrelation between E_{rot} and $E_{\text{in-plane}}$ evident in Fig. 6.4(b), as well as a simple physical picture for conversion from incident translation into scattered rotational energy.

As a final comment, although these velocity-map images represent initial steps toward a more complete picture of the impulsive scattering dynamics, further understanding will require knowledge of the scattering distribution in the v_z direction. This can be achieved using DC-slicing methods developed by Suits and coworkers, where the ions are slowed before impact with the MCP,^{40,43} and gated to select those within a certain range of v_z . Future experimental work will include probing both non-reactive and reactive scattering trajectories from more complicated surfaces, such as self-assembled monolayers (SAMs),¹³ thin films, and low vapor pressure liquids.⁵ Of particular interest will be the possibility of reactions at -OH/-OD and -NH₂/-ND₂ terminated SAM interfaces, where a new glimpse into proton-exchange mechanisms at interfaces may be revealed through the unique combination of full quantum state, H/D isotope, and 3D velocity map distributions in the scattered flux.⁴⁴

§ 6.6 Conclusions

We have presented the results from a new velocity-map imaging instrument which yields velocity and quantum-state distributions of molecules scattered from a surface. A cold HCl beam is created via a pulsed supersonic expansion, which impinges upon a 500 K Au(111)/mica surface embedded in the repeller plate of a VMI. The REMPI-based ionization occurs within 0.5 mm of the surface, probing >95% of the velocity distribution of the scattered flux. The resulting images clearly show forward-scattering trajectories that are both rotationally and translationally hyperthermal, as well as back-scattering trajectories with velocity components significantly outside the thermal 500 K regime. The ability of a velocity map to spatially separate the hyperthermal, impulsive scattering molecules from the thermally-desorbing component allows us to analyze the IS distribution in isolation, as well as explore detailed correlations between different degrees of freedom. In particular, we find that highly forward-scattered molecules are characterized by *lower* rotational energy content, but in a way that is balanced by a corresponding *increase* in translational energy. Such a trend is consistent with the presence of a dynamical constraint reminiscent of energy conservation in the collision process, yielding a total energy independent of the final rotational J state. However, our best estimates of the resulting total energies are 40% below that of the incident beam, which implies that simple energy conservation is not the only factor, and that there is substantial energy transfer into the surface. Indeed, the density of information provided by such a combination of i) molecular beam scattering, ii) full quantum state resolution, and iii) velocity map imaging is much higher than previously possible, and promises myriad new opportunities for exploring gas-surface, gas-liquid and gas-self assembled monolayer collision dynamics at unprecedented levels of detail.

§ 6.7 References

- 1) B. G. Perkins, T. Haber and D. J. Nesbitt, *J. Phys. Chem. B* **109**, 16396-16405 (2005).
- 2) B. G. Perkins and D. J. Nesbitt, *J. Phys. Chem. B* **110**, 17126-17137 (2006).
- 3) H. Hou, S. J. Gulding, C. T. Rettner, A. M. Wodtke and D. J. Auerbach, *Science* **277**, 5322 (1997).
- 4) Y. Huang, C. T. Rettner, D. J. Auerbach and A. M. Wodtke, *Science* **290**, 111 (2000).
- 5) G. M. Nathanson, P. Davidovits, D. R. Worsnop and C. E. Kolb, *J. Phys. Chem.* **100**, 13007-13020 (1996).
- 6) M. E. Saecker, S. T. Govoni, D. V. Kowalski, M. E. King and G. M. Nathanson, *Science* **252**, 1421-1424 (1991).
- 7) G. M. Nathanson, *Ann. Rev. Phys. Chem.* **55**, 231-255 (2004).
- 8) E. R. Batista, P. Ayotte, A. Bilic, B. D. Kay and H. Jonsson, *Phys. Rev. Lett.* **95**, (2005).
- 9) K. R. Lykke and B. D. Kay, *J. Chem. Phys.* **92**, 2614-2623 (1990).
- 10) P. U. Andersson, M. B. Nagard and J. B. C. Pettersson, *J. Phys. Chem. B* **104**, 1596 (2000).
- 11) Y. R. Shen, *Nature* **337**, 519-525 (1989).
- 12) P. S. Cremer, X. C. Su, Y. R. Shen and G. A. Samorjai, *J. Am. Chem. Soc.* **118**, 2942-2949 (1996).
- 13) B. S. Day, S. F. Shuler, A. Ducre and J. R. Morris, *J. Chem. Phys.* **119**, 8084-8096 (2003).
- 14) J. Bredenbeck, A. Ghosh, H.-K. Nienhuys and M. Bonn, *Acc. Chem. Res.* **42**, 1332-1342 (2009).
- 15) C. C. Cheng, S. R. Lucas, H. Gutleben, W. J. Choyke and J. T. Yates, *J. Am. Chem. Soc.* **114**, 1249-1252 (1992).
- 16) B. Jackson, M. Persson and B. D. Kay, *J. Chem. Phys.* **100**, 7687-7695 (1994).
- 17) A. M. Zolot, W. W. Harper, B. G. Perkins, P. J. Dagdigian and D. J. Nesbitt, *J. Chem. Phys.* **125**, 021101 (2006).
- 18) Q. Chang, H. M. Cuppen and E. Herbst, *Astronomy & Astrophysics* **469**, 973-983 (2007).
- 19) E. Herbst, *Ann. Rev. Phys. Chem.* **46**, 27-53 (1995).

- 20) K. Willacy and W. D. Langer, *Astrophys. J.* **544**, 903-920 (2000).
- 21) S. M. Fan and D. J. Jacob, *Nature* **359**, 522-524 (1992).
- 22) M. J. Molina, T.-L. Tso, L. T. Molina and F. Wang, *Science* **238**, 1253 (1987).
- 23) G. C. Bond and D. T. Thompson, *Catal. Rev.* **41**, 319-388 (1999).
- 24) P. E. Labinis, R. G. Nuzzo and G. M. Whitesides, *J. Phys. Chem.* **96**, 5097-5105 (1992).
- 25) P. B. Petersen and R. J. Saykally, *Ann. Rev. Phys. Chem.* **57**, 333-364 (2006).
- 26) D. Briggs and M. P. Seah, *Practical Surface Analysis By Auger And X-ray Photoelectron Spectroscopy* (John Wiley & Sons, Chichester, 1983)
- 27) G. M. McClelland, G. D. Kubiak, H. G. Rennagel and R. N. Zare, *Phys. Rev. Lett.* **46**, 831 (1981).
- 28) B. G. Perkins and D. J. Nesbitt, *Proc. Natl. Acad. Sci.* **105**, 12685-12689 (2008).
- 29) B. G. Perkins and D. J. Nesbitt, *J. Phys. Chem. A* **112**, 9324-9335 (2008).
- 30) A. T. J. B. Eppink and D. H. Parker, *Rev. Sci. Instrum.* **68**, 3447-3484 (1997).
- 31) S. P. K. Koehler, Y. Y. Ji, D. J. Auerbach and A. M. Wodtke, *Phys. Chem. Chem. Phys.* **11**, 7540-7544 (2009).
- 32) S. Arepalli, N. Presser, D. Robie and R. J. Gordon, *Chem. Phys. Lett.* **118**, 88-92 (1985).
- 33) D. S. Green, G. A. Bickel and S. C. Wallace, *J. Mol. Spectrosc.* **150**, 388-469 (1991).
- 34) D. Proch and T. Trickle, *Rev. Sci. Instrum.* **60**, 713 (1989).
- 35) C. Romanescu and H. P. Looock, *J. Chem. Phys.* **127**, 124304 (2007).
- 36) M. Korolik, D. W. Arnold, M. J. Johnson, M. M. Suchan, H. Reisler and C. Wittig, *Chem. Phys. Lett.* **284**, 164-170 (1998).
- 37) Q. Ran, D. Matsiev, A. M. Wodtke and D. J. Auerbach, *Rev. Sci. Instrum.* **78**, 104104 (2007).
- 38) C. T. Rettner, J. Kimman and D. J. Auerbach, *J. Chem. Phys.* **94**, 734 (1991).
- 39) J. Kimman, C. T. Rettner, D. J. Auerbach, J. A. Barker and J. C. Tully, *Phys. Rev. Lett.* **57**, 2053-2056 (1986).

- 40) D. Townsend, M. P. Minitti and A. G. Suits, *Rev. Sci. Instrum.* **74**, 2530-2539 (2003).
- 41) R. Sau and R. Merrill, *Surf. Sci.* **34**, 268-28 (1973).
- 42) R. Brako and D. M. Newns, *Surf. Sci.* **117**, 42-52 (1982).
- 43) M. N. R. Ashfold, N. H. Nahler, A. J. Orr-Ewing, O. P. J. Vieuxmaire, R. L. Toomes, T. N. Kitsopoulos, I. A. Garcia, D. A. Chestakov, S.-M. Wu and D. H. Parker, *Phys. Chem. Chem. Phys.* **8**, 26-53 (2005).
- 44) B. R. Ringeisen, A. H. Muentner and G. M. Nathanson, *J. Phys. Chem. B* **106**, 4999-5010 (2002).

BIBLIOGRAPHY

- 1) C. L. Adams, H. Schneider, K. M. Ervin and J. M. Weber, *J. Chem. Phys.* **130**, 074307 (2009).
- 2) S. Albert, K. K. Albert, P. Lerch and M. Quack, *Faraday Discuss.* **150**, 71-99 (2011).
- 3) M. W. Allen, J. R. Unruh, B. D. Slaughter, S. J. Pyszczynski, T. R. Hellwig, T. J. Kamerzell and C. K. Johnson, *J. Phys. Chem. A* **107**, 5660-5669 (2003).
- 4) P. U. Andersson, M. B. Nagard and J. B. C. Pettersson, *J. Phys. Chem. B* **104**, 1596 (2000).
- 5) L. A. Angel and K. M. Ervin, *J. Phys. Chem. A* **110**, 10392-10403 (2006).
- 6) C. S. Anstöter, C. R. Dean and J. R. R. Verlet, *J. Phys. Chem. Lett.* **8**, 2268-2273 (2017).
- 7) T. Aota, T. Ebata and M. Ito, *J. Phys. Chem.* **93**, 3519-3522 (1989).
- 8) S. Arepalli, N. Presser, D. Robie and R. J. Gordon, *Chem. Phys. Lett.* **118**, 88-92 (1985).
- 9) S. Arnold and M. Sulkes, *J. Phys. Chem.* **96**, 4768-4778 (1992).
- 10) X. Asensio, À. González-Lafont, J. Marquet, J. M. Lluch and M. Geoffroy, *Journal of Molecular Structure: THEOCHEM* **913**, 228-235 (2009).
- 11) M. N. R. Ashfold, N. H. Nahler, A. J. Orr-Ewing, O. P. J. Vieuxmaire, R. L. Toomes, T. N. Kitsopoulos, I. A. Garcia, D. A. Chestakov, S.-M. Wu and D. H. Parker, *Phys. Chem. Chem. Phys.* **8**, 26-53 (2005).
- 12) R. Atkinson, C. N. Plum, W. P. L. Carter, A. M. Winer and J. N. Pitts, *J. Phys. Chem.* **88**, 1210-1215 (1984).
- 13) E. R. Batista, P. Ayotte, A. Bilic, B. D. Kay and H. Jonsson, *Phys. Rev. Lett.* **95**, (2005).
- 14) C. W. Bauschlicher, S. R. Langhoff and S. P. Walch, *J. Chem. Phys.* **96**, 450-454 (1992).
- 15) A. D. Becke, *J. Chem. Phys.* **98**, 5648-5652 (1993).
- 16) M. Bendikov, H. M. Duong, K. Starkey, K. N. Houk, E. A. Carter and F. Wudl, *J. Amer. Chem. Soc.* **126**, 7416-7417 (2004).
- 17) G. Berden, W. L. Meerts and E. Jalviste, *J. Chem. Phys.* **103**, 9596-9606 (1995).
- 18) C. E. S. Bernardes and M. E. Minas da Piedade, *J. Phys. Chem. A* **112**, 10029-10039 (2008).

- 19) R. Bersohn, U. Even and J. Jortner, *J. Chem. Phys.* **80**, 1050-1058 (1984).
- 20) P. R. Bevington and D. K. Robinson, *Data Reduction and Error Analysis for the Physical Sciences* (McGraw-Hill, New York, 2003), 3rd edn.
- 21) G. A. Bickel, D. R. Demmer, E. A. Outhouse and S. C. Wallace, *J. Chem. Phys.* **91**, 6013-6019 (1989).
- 22) H. S. Biswal, P. R. Shirhatti and S. Wategaonkar, *J. Phys. Chem. A* **113**, 5633-5643 (2009).
- 23) E. D. Black, *Am. J. Phys.* **69**, 79-87 (2001).
- 24) S. J. Blanksby and G. B. Ellison, *Acc. Chem. Res.* **36**, 255-263 (2003).
- 25) C. Blondel, W. Chaibi, C. Delsart, C. Drag, F. Goldfarb and S. Kröger, *Eur. Phys. J. D* **33**, 335-342 (2005).
- 26) G. C. Bond and D. T. Thompson, *Catal. Rev.* **41**, 319-388 (1999).
- 27) W. T. Borden, *Diradicals* (John Wiley and Sons, New York, 1982)
- 28) F. G. Bordwell and J. Cheng, *J. Amer. Chem. Soc.* **113**, 1736-1743 (1991).
- 29) F. G. Bordwell, X.-M. Zhang, A. V. Satish and J. P. Cheng, *J. Amer. Chem. Soc.* **116**, 6605-6610 (1994).
- 30) M. Born, S. Ingemann and N. M. M. Nibbering, *Mass Spectrom. Rev.* **16**, 181-200 (1997).
- 31) R. Brako and D. M. Newns, *Surf. Sci.* **117**, 42-52 (1982).
- 32) L. M. Branscomb, D. S. Burch, S. J. Smith and S. Geltman, *Phys. Rev.* **111**, 504-512 (1958).
- 33) L. M. Branscomb and S. J. Smith, *Phys. Rev.* **98**, 1127-1128 (1955).
- 34) J. Bredenbeck, A. Ghosh, H.-K. Nienhuys and M. Bonn, *Acc. Chem. Res.* **42**, 1332-1342 (2009).
- 35) B. Breiner, K. Kaya, S. Roy, W.-Y. Yang and I. V. Alabugin, *Org. Biomolec. Chem.* **10**, 3974-3987 (2012).
- 36) D. Briggs and M. P. Seah, *Practical Surface Analysis By Auger And X-ray Photoelectron Spectroscopy* (John Wiley & Sons, Chichester, 1983)
- 37) D. R. Burgess and J. E. Bartmess, *Thermochemical Data in NIST Chemistry WebBook, NIST Standard Reference Database Number 69, Eds. P.J. Linstrom and W.G. Mallard,*

<http://webbook.nist.gov/chemistry/>

- 38) W. Caminati and S. Di Bernardo, *J. Mol. Struct.* **240**, 253-262 (1990).
- 39) J. R. Carney, F. C. Hagemeister and T. S. Zwier, *J. Chem. Phys.* **108**, 3379-3382 (1998).
- 40) J. R. Carney and T. S. Zwier, *J. Phys. Chem. A* **103**, 9943-9957 (1999).
- 41) R. J. Celotta, R. A. Bennett, J. L. Hall, M. W. Siegel and J. Levine, *Phys. Rev. A* **6**, 631-642 (1972).
- 42) A. Chandra and T. Uchimaru, *Int. J. Mol. Sci.* **3**, 407-422 (2002).
- 43) Q. Chang, H. M. Cuppen and E. Herbst, *Astronomy & Astrophysics* **469**, 973-983 (2007).
- 44) C. Chatgililoglu, K. U. Ingold and J. C. Scaiano, *J. Amer. Chem. Soc.* **103**, 7739-7742 (1981).
- 45) P. Chen, *Unimolecular and Bimolecular Reactions Dynamics* (John Wiley & Sons, Chichester, 1994) 371.
- 46) C. C. Cheng, S. R. Lucas, H. Gutleben, W. J. Choyke and J. T. Yates, *J. Am. Chem. Soc.* **114**, 1249-1252 (1992).
- 47) B. Christophe, D. Christian and G. Fabienne, *Journal of Physics B: Atomic, Molecular and Optical Physics* **34**, L281 (2001).
- 48) W. B. Collier, *J. Chem. Phys.* **88**, 7295-7306 (1988).
- 49) J. Cooper and R. N. Zare, *J. Chem. Phys.* **48**, 942-943 (1968).
- 50) J. D. Cox, *Pure Appl. Chem.* **2**, 125-128 (1961).
- 51) P. S. Cremer, X. C. Su, Y. R. Shen and G. A. Samorjai, *J. Am. Chem. Soc.* **118**, 2942-2949 (1996).
- 52) G. E. Davico, R. L. Schwartz, T. M. Ramond and W. C. Lineberger, *J. Amer. Chem. Soc.* **121**, 6047-6054 (1999).
- 53) P. H. Dawson, *International Journal of Mass Spectrometry and Ion Physics* **17**, 423-445 (1975).
- 54) B. S. Day, S. F. Shuler, A. Ducre and J. R. Morris, *J. Chem. Phys.* **119**, 8084-8096 (2003).
- 55) C. H. DePuy and V. M. Bierbaum, *Acc. Chem. Res.* **14**, 146-153 (1981).

- 56) C. H. DePuy, S. Gronert, S. E. Barlow, V. M. Bierbaum and R. Damrauer, *J. Amer. Chem. Soc.* **111**, 1968-1973 (1989).
- 57) P. J. Derrick, L. Åsbrink, O. Edqvist and E. Lindholm, *Spectrochimica Acta Part A: Molecular Spectroscopy* **27**, 2525-2537 (1971).
- 58) V. F. DeTuri and K. M. Ervin, *J. Phys. Chem. A* **103**, 6911-6920 (1999).
- 59) A. L. Devine, M. G. D. Nix, B. Cronin and M. N. R. Ashfold, *Phys. Chem. Chem. Phys.* **9**, 3749-3762 (2007).
- 60) B. Dick, Maximum Entropy Velocity Legendre Reconstruction (MEVELER), 2013, see
61) B. Dick, *Phys. Chem. Chem. Phys.* **16**, 570-580 (2014).
- 62) D. Doehnert and J. Koutecky, *J. Amer. Chem. Soc.* **102**, 1789-1796 (1980).
- 63) B. T. Draine and L. Aigen, *Astrophys. J.* **657**, 810 (2007).
- 64) B. T. Draine, D. A. Dale, G. Bendo, K. D. Gordon, J. D. T. Smith, L. Armus, C. W. Engelbracht, G. Helou, R. C. Kennicutt, Jr., A. Li, H. Roussel, F. Walter, D. Calzetti, J. Moustakas, E. J. Murphy, G. H. Rieke, C. Bot, D. J. Hollenbach, K. Sheth and H. I. Teplitz, *Astrophys. J.* **663**, 866 (2007).
- 65) V. Dribinski, A. Ossadtchi, V. A. Mandelshtam and H. Reisler, *Rev. Sci. Instrum.* **73**, 2634-2642 (2002).
- 66) D. B. Dunkin, F. C. Fehsenfeld, A. L. Schmeltekopf and E. E. Ferguson, *J. Chem. Phys.* **49**, 1365-1371 (1968).
- 67) J. E. Bright Wilson, J. C. Decius and P. C. Cross, *Molecular Vibrations: The Theory of Infrared and Raman Vibrational Spectra* (Dover Publications, Inc., New York, 1980)
- 68) T. Ebata and M. Ito, *J. Phys. Chem.* **96**, 3224-3231 (1992).
- 69) P. C. Engelking, G. B. Ellison and W. C. Lineberger, *J. Chem. Phys.* **69**, 1826-1832 (1978).
- 70) A. T. J. B. Eppink and D. H. Parker, *Rev. Sci. Instrum.* **68**, 3477-3484 (1997).
- 71) K. M. Ervin, PESCAL, Fortran Program for Franck-Condon Analysis of Molecular Photoelectron Spectra, 2010, see <http://wolfweb.unr.edu/~ervin/pes/>
- 72) K. M. Ervin, I. Anusiewicz, P. Skurski, J. Simons and W. C. Lineberger, *J. Phys. Chem. A* **107**, 8521-8529 (2003).
- 73) K. M. Ervin, I. Anusiewicz, P. Skurski, J. Simons and W. C. Lineberger, *J. Phys. Chem. A* **107**, 8521-8529 (2003).

- 74) K. M. Ervin and V. F. DeTuri, *J. Phys. Chem. A* **106**, 9947-9956 (2002).
- 75) K. M. Ervin, S. Gronert, S. E. Barlow, M. K. Gilles, A. G. Harrison, V. M. Bierbaum, C. H. DePuy, W. C. Lineberger and G. B. Ellison, *J. Amer. Chem. Soc.* **112**, 5750-5759 (1990).
- 76) K. M. Ervin, J. Ho and W. C. Lineberger, *J. Phys. Chem.* **92**, 5405-5412 (1988).
- 77) K. M. Ervin and W. C. Lineberger, in *Advances in Gas Phase Ion Chemistry*, edited by N. G. Adams, and L. M. Babcock (JAI Press, Greenwich, 1992), pp. 121-166.
- 78) K. M. Ervin, T. M. Ramond, G. E. Davico, R. L. Schwartz, S. M. Casey and W. C. Lineberger, *J. Phys. Chem. A* **105**, 10822-10831 (2001).
- 79) S. M. Fan and D. J. Jacob, *Nature* **359**, 522-524 (1992).
- 80) S. J. Farlow, *Partial Differential Equations for Scientists and Engineers* (Dover Publications, Inc., New York, 1993)
- 81) C. S. Feigerle, (1983). *Laser Photoelectron Spectroscopy of Transition Metal Negative Ions* (Doctoral Thesis).
- 82) B. J. Fender, D. M. Sammeth and P. R. Callis, *Chem. Phys. Lett.* **239**, 31-37 (1995).
- 83) M. J. Frisch, G. W. Trucks, H. B. Schlegel, G. E. Scuseria, M. A. Robb, J. R. Cheeseman, G. Scalmani, V. Barone, B. Mennucci, G. A. Petersson, H. Nakatsuji, M. Caricato, X. Li, H. P. Hratchian, A. F. Izmaylov, J. Bloino, G. Zheng, J. L. Sonnenberg, M. Hada, M. Ehara, K. Toyota, R. Fukuda, J. Hasegawa, M. Ishida, T. Nakajima, Y. Honda, O. Kitao, H. Nakai, T. Vreven, J. A. Montgomery Jr., J. E. Peralta, F. Ogliaro, M. J. Bearpark, J. Heyd, E. N. Brothers, K. N. Kudin, V. N. Staroverov, R. Kobayashi, J. Normand, K. Raghavachari, A. P. Rendell, J. C. Burant, S. S. Iyengar, J. Tomasi, M. Cossi, N. Rega, N. J. Millam, M. Klene, J. E. Knox, J. B. Cross, V. Bakken, C. Adamo, J. Jaramillo, R. Gomperts, R. E. Stratmann, O. Yazyev, A. J. Austin, R. Cammi, C. Pomelli, J. W. Ochterski, R. L. Martin, K. Morokuma, V. G. Zakrzewski, G. A. Voth, P. Salvador, J. J. Dannenberg, S. Dapprich, A. D. Daniels, Ö. Farkas, J. B. Foresman, J. V. Ortiz, J. Cioslowski and D. J. Fox, *Gaussian 09 Rev. B01*, 2009, see www.gaussian.com
- 84) A. Fujii, E. Fujimaki, T. Ebata and N. Mikami, *J. Amer. Chem. Soc.* **120**, 13256-13257 (1998).
- 85) M. Fujio, R. T. McIver and R. W. Taft, *J. Amer. Chem. Soc.* **103**, 4017-4029 (1981).
- 86) M. Gerhards, B. Kimpfel, M. Pohl, M. Schmitt and K. Kleinermanns, *J. Mol. Struct.* **270**, 301-324 (1992).
- 87) A. J. Gianola, T. Ichino, R. L. Hoenigman, S. Kato, V. M. Bierbaum and W. C. Lineberger,

- J. Phys. Chem. A **108**, 10326-10335 (2004).
- 88) A. Giuliani, J. Delwiche, S. V. Hoffmann, P. Limão-Vieira, N. J. Mason and M.-J. Hubin-Franskin, J. Chem. Phys. **119**, 3670-3680 (2003).
- 89) E. Goldstein, B. Beno and K. N. Houk, J. Amer. Chem. Soc. **118**, 6036-6043 (1996).
- 90) J. R. B. Gomes and M. A. V. R. Da Silva, Int. J. Quantum Chem. **101**, 860-868 (2005).
- 91) J. Gräfenstein, A. M. Hjerpe, E. Kraka and D. Cremer, J. Phys. Chem. A **104**, 1748-1761 (2000).
- 92) D. S. Green, G. A. Bickel and S. C. Wallace, J. Mol. Spectrosc. **150**, 388-469 (1991).
- 93) S. Gronert, Chem. Rev. **101**, 329-360 (2001).
- 94) G. Gryn'ova and M. L. Coote, J. Amer. Chem. Soc. **135**, 15392-15403 (2013).
- 95) R. F. Gunion, M. K. Gilles, M. L. Polak and W. C. Lineberger, Int. J. Mass Spectrom. Ion Processes **117**, 601-620 (1992).
- 96) M. J. Haas and A. G. Harrison, Int. J. Mass Spectrom. Ion Processes **124**, 115-124 (1993).
- 97) M. Haeberlein and T. Brinck, J. Phys. Chem. **100**, 10116-10120 (1996).
- 98) J. Hager, M. Ivanco, M. A. Smith and S. C. Wallace, Chem. Phys. Lett. **113**, 503-507 (1985).
- 99) J. Hager and S. C. Wallace, J. Phys. Chem. **87**, 2121-2127 (1983).
- 100) H. K. Hall and A. B. Padias, Acc. Chem. Res. **23**, 3-9 (1990).
- 101) B. G. Halliwell, John M. C. , *Free Radicals in Biology and Medicine* (University Press, 2nd Ed.;Oxford, 1988)
- 102) B. G. Halliwell, *Free Radicals in Biology and Medicine* (Oxford University Press, Oxford, 1989), 2nd Ed
- 103) H. Handschuh, G. Ganteför and W. Eberhardt, Rev. Sci. Instrum. **66**, 3838-3843 (1995).
- 104) C. Hansch, A. Leo and R. W. Taft, Chem. Rev. **91**, 165-195 (1991).
- 105) W. M. Haynes, *CRC Handbook of Chemistry and Physics* (CRC Press, New York, 2016-2017)
- 106) A. Hellweg and C. Hattig, J. Chem. Phys. **127**, 24307 (2007).

- 107) A. Hellweg, C. Hattig, I. Merke and W. Stahl, *J. Chem. Phys.* **124**, 204305 (2006).
- 108) E. Herbst, *Ann. Rev. Phys. Chem.* **46**, 27-53 (1995).
- 109) G. Herzberg, *Molecular Spectra and Molecular Structure* (Krieger Publishing Co., New York, 1989), 2nd edn.
- 110) B. T. Hill, J. C. Poutsma, L. J. Chyall, J. Hu and R. R. Squires, *J. Am. Soc. Mass Spectrom.* **10**, 896-906 (1999).
- 111) T. L. Hill, *An Introduction to Statistical Thermodynamics* (Dover Publications, Inc., New York, 1986).
- 112) R. Hoffmann, D. B. Boyd and S. Z. Goldberg, *J. Amer. Chem. Soc.* **92**, 3929-3936 (1970).
- 113) J. M. Hollas, *Spectrochimica Acta* **19**, 753-767 (1963).
- 114) D. J. Hopper, *Biochem. J.* **175**, 345-347 (1978).
- 115) H. Hotop and W. C. Lineberger, *J. Phys. Chem. Ref. Data* **14**, 731-750 (1985).
- 116) H. Hou, S. J. Gulding, C. T. Rettner, A. M. Wodtke and D. J. Auerbach, *Science* **277**, 5322 (1997).
- 117) K. N. Houk, J. Liu, N. C. DeMello and K. R. Condroski, *J. Amer. Chem. Soc.* **119**, 10147-10152 (1997).
- 118) D. A. Hrovat and W. T. Borden, *J. Phys. Chem.* **98**, 10460-10464 (1994).
- 119) D.-L. Huang, H.-T. Liu, C.-G. Ning and L.-S. Wang, *J. Chem. Phys.* **142**, 124309 (2015).
- 120) J. Huang, K. Huang, S. Liu, Q. Luo and W. Tzeng, *J. Photochem. Photobiol. A* **188**, 252-259 (2007).
- 121) Y. Huang, C. T. Rettner, D. J. Auerbach and A. M. Wodtke, *Science* **290**, 111 (2000).
- 122) R. Huisgen, *The Journal of Organic Chemistry* **41**, 403-419 (1976).
- 123) E. P. L. Hunter and S. G. Lias, *J. Phys. Chem. Ref. Data* **27**, 413-656 (1998).
- 124) T. Ichino, S. M. Villano, A. J. Gianola, D. J. Goebbert, L. Velarde, A. Sanov, S. J. Blanksby, X. Zhou, D. A. Hrovat, W. T. Borden and W. C. Lineberger, *J. Phys. Chem. A* **115**, 1634-1649 (2011).
- 125) T. Ichino, S. W. Wren, K. M. Vogelhuber, A. J. Gianola, W. C. Lineberger and J. F. Stanton, *J. Chem. Phys.* **129**, 084310 (2008).

- 126) M. Ito, *J. Phys. Chem.* **91**, 517-526 (1987).
- 127) M. Ito and A. Oikawa, *J. Mol. Struct.* **126**, 133-140 (1985).
- 128) B. Jackson, M. Persson and B. D. Kay, *J. Chem. Phys.* **100**, 7687-7695 (1994).
- 129) T. N. V. Karsili, A. M. Wenge, B. Marchetti and M. N. R. Ashfold, *Phys. Chem. Chem. Phys.* **16**, 588-598 (2014).
- 130) A. Kasdan and W. C. Lineberger, *Phys. Rev. A* **10**, 1658-1664 (1974).
- 131) J. B. Kim, P. G. Wenthold and W. C. Lineberger, *J. Phys. Chem. A* **103**, 10833-10841 (1999).
- 132) J. B. Kim, T. I. Yacovitch, C. Hock and D. M. Neumark, *Phys. Chem. Chem. Phys.* **13**, 17378-17383 (2011).
- 133) J. Kimman, C. T. Rettner, D. J. Auerbach, J. A. Barker and J. C. Tully, *Phys. Rev. Lett.* **57**, 2053-2056 (1986).
- 134) G. A. King, A. L. Devine, M. G. D. Nix, D. E. Kelly and M. N. R. Ashfold, *Phys. Chem. Chem. Phys.* **10**, 6417-6429 (2008).
- 135) S. P. K. Koehler, Y. Y. Ji, D. J. Auerbach and A. M. Wodtke, *Phys. Chem. Chem. Phys.* **11**, 7540-7544 (2009).
- 136) M. Korolik, D. W. Arnold, M. J. Johnson, M. M. Suchan, H. Reisler and C. Wittig, *Chem. Phys. Lett.* **284**, 164-170 (1998).
- 137) L. Koziol, V. A. Mozhayskiy, B. J. Braams, J. M. Bowman and A. I. Krylov, *J. Phys. Chem. A* **113**, 7802-7809 (2009).
- 138) K. P. Krishnan Namboodiri, S. Viswanathan, R. Ganesan and V. C. Jyothi Bhasu, *Monatshefte fur Chemie / Chemical Monthly* **113**, 949-963 (1982).
- 139) S. A. Kudchadker, A. P. Kudchadker, R. C. Wilhoit and B. J. Zwolinski, *J. Phys. Chem. Ref. Data* **7**, 417-423 (1978).
- 140) J. Kupper, D. W. Pratt, W. Leo Meerts, C. Brand, J. Tatchen and M. Schmitt, *Phys. Chem. Chem. Phys.* **12**, 4980-4988 (2010).
- 141) M. A. Kurinovich and J. K. Lee, *J. Am. Soc. Mass Spectrom.* **13**, 985-995 (2002).
- 142) C. E. Kuyatt and J. A. Simpson, *Rev. Sci. Instrum.* **38**, 103-111 (1967).

- 143) P. E. Labinis, R. G. Nuzzo and G. M. Whitesides, *J. Phys. Chem.* **96**, 5097-5105 (1992).
- 144) L. D. Landau and E. M. Lifshitz, *Mechanics* (Elsevier Ltd., 2010), 3rd edn., Vol. 1, Course of Theoretical Physics
- 145) D. G. Leopold, A. E. S. Miller and W. C. Lineberger, *J. Amer. Chem. Soc.* **108**, 1379-1384 (1986).
- 146) D. G. Leopold, K. K. Murray, A. E. S. Miller and W. C. Lineberger, *J. Chem. Phys.* **83**, 4849-4865 (1985).
- 147) P. D. Lightfoot, R. A. Cox, J. N. Crowley, M. Destriau, G. D. Hayman, M. E. Jenkin, G. K. Moortgat and F. Zabel, *Atmospheric Environment. Part A. General Topics* **26**, 1805-1961 (1992).
- 148) J. L. Lin, C. Li and W. B. Tzeng, *J. Chem. Phys.* **120**, 10513-10519 (2004).
- 149) M. Lin and J. J. Grabowski, *Int. J. Mass spectrom.* **237**, 149-165 (2004).
- 150) R. Lindh, T. J. Lee, A. Bernhardsson, B. J. Persson and G. Karlstroem, *J. Amer. Chem. Soc.* **117**, 7186-7194 (1995).
- 151) W. C. Lineberger and W. T. Borden, *Phys. Chem. Chem. Phys.* **13**, 11792-11813 (2011).
- 152) W. C. Lineberger, H. Hotop and T. A. Patterson, edited by H. Kleinpoppen, and M. McDowell (Plenum, New York, 1976), pp. 125-132.
- 153) W. C. Lineberger and B. W. Woodward, *Phys. Rev. Lett.* **25**, 424-427 (1970).
- 154) R. J. Lipert and S. D. Colson, *J. Phys. Chem.* **93**, 3894-3896 (1989).
- 155) H.-T. Liu, C.-G. Ning, D.-L. Huang, P. D. Dau and L.-S. Wang, *Angew. Chem. Int. Ed.* **52**, 8976-8979 (2013).
- 156) X. Liu, M. Liu, X. Guo and J. Zhou, *Catal. Comm.* **9**, 1-7 (2008).
- 157) A. Lopez-Calvo and C. E. Manzanares, *J. Phys. Chem. A* **110**, 10427-10434 (2006).
- 158) Y.-J. Lu, J. H. Lehman and W. C. Lineberger, *J. Chem. Phys.* **142**, 044201 (2015).
- 159) K. R. Lykke and B. D. Kay, *J. Chem. Phys.* **92**, 2614-2623 (1990).
- 160) P. J. A. Madeira, P. J. Costa, M. T. Fernandez, J. A. M. Simões and J. P. Leal, *J. Am. Soc. Mass Spectrom.* **19**, 1590-1599 (2008).
- 161) D. C. Magri and M. S. Workentin, *Chemistry – A European Journal* **14**, 1698-1709 (2008).

- 162) M. A. R. Matos, M. S. Miranda and V. M. F. Morais, *J. Chem. Eng. Data* **48**, 669-679 (2003).
- 163) G. M. McClelland, G. D. Kubiak, H. G. Rennagel and R. N. Zare, *Phys. Rev. Lett.* **46**, 831 (1981).
- 164) A. R. McKay, M. E. Sanz, C. R. S. Mooney, R. S. Minns, E. M. Gill and H. H. Fielding, *Rev. Sci. Instrum.* **81**, 123101 (2010).
- 165) T. B. McMahon and P. Kebarle, *J. Amer. Chem. Soc.* **99**, 2222-2230 (1977).
- 166) J. McMurry, *Organic Chemistry* (Brooke/Cole Publishing Company, Belmont, California, 1992)
- 167) M. Meot-Ner, J. F. Liebman and S. A. Kafafi, *J. Amer. Chem. Soc.* **110**, 5937-5941 (1988).
- 168) H. Mizuno, K. Okuyama, T. Ebata and M. Ito, *J. Phys. Chem.* **91**, 5589-5593 (1987).
- 169) M. J. Molina, T.-L. Tso, L. T. Molina and F. Wang, *Science* **238**, 1253 (1987).
- 170) K. K. Morishetti, P. Sripadi, V. Mariappanadar and J. Ren, *Int. J. Mass spectrom.* **299**, 169-177 (2011).
- 171) G. Myszkiewicz, W. L. Meerts, C. Ratzler and M. Schmitt, *Phys. Chem. Chem. Phys.* **7**, 2142-2150 (2005).
- 172) H. Nakai and Y. Kawamura, *Chem. Phys. Lett.* **318**, 298-304 (2000).
- 173) G. M. Nathanson, *Ann. Rev. Phys. Chem.* **55**, 231-255 (2004).
- 174) G. M. Nathanson, P. Davidovits, D. R. Worsnop and C. E. Kolb, *J. Phys. Chem.* **100**, 13007-13020 (1996).
- 175) D. J. Nelson, W. K. Gichuhi, E. M. Miller, J. H. Lehman and W. C. Lineberger, *J. Chem. Phys.* **146**, 074302 (2017).
- 176) P. Neta, R. E. Huie and A. B. Ross, *J. Phys. Chem. Ref. Data* **17**, 1027-1284 (1988).
- 177) D. M. Neumark, *J. Phys. Chem. A* **112**, 13287-13301 (2008).
- 178) D. M. Neumark, K. R. Lykke, T. Andersen and W. C. Lineberger, *Phys. Rev. A* **32**, 1890-1892 (1985).
- 179) Y. Nibu, H. Abe, N. Mikami and M. Ito, *J. Phys. Chem.* **87**, 3898-3901 (1983).

- 180) L. Nie, P. M. de Souza, F. B. Noronha, W. An, T. Sooknoi and D. E. Resasco, *Journal of Molecular Catalysis A: Chemical* **388–389**, 47-55 (2014).
- 181) M. G. D. Nix, A. L. Devine, B. Cronin and M. N. R. Ashfold, *Phys. Chem. Chem. Phys.* **8**, 2610-2618 (2006).
- 182) M. G. D. Nix, A. L. Devine, B. Cronin, R. N. Dixon and M. N. R. Ashfold, *J. Chem. Phys.* **125**, 133318 (2006).
- 183) E. O. Odebunmi and D. F. Ollis, *J. Catal.* **80**, 56-64 (1983).
- 184) A. Oikawa, H. Abe, N. Mikami and M. Ito, *J. Phys. Chem.* **88**, 5180-5186 (1984).
- 185) A. N. Oldani, J. C. Ferrero and G. A. Pino, *Phys. Chem. Chem. Phys.* **11**, 10409-10416 (2009).
- 186) A. M. Oliveira, J. H. Lehman, A. B. McCoy and W. C. Lineberger, *J. Phys. Chem. A* **120**, 1652-1660 (2016).
- 187) H. E. O'Neal and S. W. Benson, *J. Phys. Chem.* **72**, 1866-1887 (1968).
- 188) D. L. Osborn, D. J. Leahy, E. H. Kim, E. de Beer and D. M. Neumark, *Chem. Phys. Lett.* **292**, 651-655 (1998).
- 189) D. S. N. Parker, F. Zhang and R. I. Kaiser, *J. Phys. Chem. A* **115**, 11515-11518 (2011).
- 190) C. S. Parmenter and B. M. Stone, *J. Chem. Phys.* **84**, 4710-4711 (1986).
- 191) S. Penner, *Rev. Sci. Instrum.* **32**, 150-160 (1961).
- 192) B. G. Perkins, T. Haber and D. J. Nesbitt, *J. Phys. Chem. B* **109**, 16396-16405 (2005).
- 193) B. G. Perkins and D. J. Nesbitt, *J. Phys. Chem. B* **110**, 17126-17137 (2006).
- 194) B. G. Perkins and D. J. Nesbitt, *Proc. Natl. Acad. Sci.* **105**, 12685-12689 (2008).
- 195) B. G. Perkins and D. J. Nesbitt, *J. Phys. Chem. A* **112**, 9324-9335 (2008).
- 196) P. B. Petersen and R. J. Saykally, *Ann. Rev. Phys. Chem.* **57**, 333-364 (2006).
- 197) K. Pius and J. Chandrasekhar, *Journal of the Chemical Society, Perkin Transactions 2* 1291-1295 (1988).
- 198) M. Pohl and K. Kleinermanns, *Z. Phys. D: At., Mol. Clusters* **8**, 385-392 (1988).
- 199) D. Proch and T. Trickle, *Rev. Sci. Instrum.* **60**, 713 (1989).

- 200) A. Rajca, Chem. Rev. **94**, 871-893 (1994).
- 201) T. M. Ramond, G. E. Davico, R. L. Schwartz and W. C. Lineberger, J. Chem. Phys. **112**, 1158-1169 (2000).
- 202) E. Ramos-Cordoba and P. Salvador, Phys. Chem. Chem. Phys. **16**, 9565-9571 (2014).
- 203) Q. Ran, D. Matsiev, A. M. Wodtke and D. J. Auerbach, Rev. Sci. Instrum. **78**, 104104 (2007).
- 204) W. T. Read, *Industrial Chemistry* (Chapman and Hall, Limited, London, 1947)
- 205) D. R. Reed, M. Hare and S. R. Kass, J. Amer. Chem. Soc. **122**, 10689-10696 (2000).
- 206) D. R. Reed, M. C. Hare, A. Fattahi, G. Chung, M. S. Gordon and S. R. Kass, J. Amer. Chem. Soc. **125**, 4643-4651 (2003).
- 207) H. M. Relles, D. S. Johnson and J. S. Manello, J. Amer. Chem. Soc. **99**, 6677-6686 (1977).
- 208) C. T. Rettner, J. Kimman and D. J. Auerbach, J. Chem. Phys. **94**, 734 (1991).
- 209) E. C. Richard, R. A. Walker and J. C. Weisshaar, J. Chem. Phys. **104**, 4451-4469 (1996).
- 210) L. S. Richard, C. E. S. Bernardes, H. P. Diogo, J. P. Leal and M. E. Minas da Piedade, J. Phys. Chem. A **111**, 8741-8748 (2007).
- 211) G. H. N. Riddle, J. Vac. Sci. Tech. **15**, 857-860 (1978).
- 212) B. R. Ringeisen, A. H. Muentner and G. M. Nathanson, J. Phys. Chem. B **106**, 4999-5010 (2002).
- 213) C. Romanescu and H. P. Looch, J. Chem. Phys. **127**, 124304 (2007).
- 214) C. C. J. Roothaan, Rev. Mod. Phys. **23**, 69-89 (1951).
- 215) B. Ruscic and J. Berkowitz, J. Phys. Chem. **97**, 11451-11455 (1993).
- 216) B. Ruscic, A. F. Wagner, L. B. Harding, R. L. Asher, D. Feller, D. A. Dixon, K. A. Peterson, Y. Song, X. Qian, C.-Y. Ng, J. Liu, W. Chen and D. W. Schwenke, J. Phys. Chem. A **106**, 2727-2747 (2002).
- 217) M. E. Saecker, S. T. Govoni, D. V. Kowalski, M. E. King and G. M. Nathanson, Science **252**, 1421-1424 (1991).
- 218) A. Sanov, Annu. Rev. Phys. Chem. **65**, 341-363 (2014).

- 219) R. M. B. d. Santos and J. A. M. Simoes, *J. Phys. Chem. Ref. Data* **27**, 707-739 (1998).
- 220) R. Sau and R. Merrill, *Surf. Sci.* **34**, 268-28 (1973).
- 221) L. Serrano-Andrés and B. O. Roos, *J. Amer. Chem. Soc.* **118**, 185-195 (1996).
- 222) R. Shankar, *Principles of Quantum Mechanics* (Springer, 2008), 2nd edn.
- 223) T. E. Sharp and H. M. Rosenstock, *J. Chem. Phys.* **41**, 3453-3463 (1964).
- 224) Y. R. Shen, *Nature* **337**, 519-525 (1989).
- 225) L. Sheps, E. M. Miller and W. C. Lineberger, *J. Chem. Phys.* **131**, 064304 (2009).
- 226) M. W. Siegel, R. J. Celotta, J. L. Hall, J. Levine and R. A. Bennett, *Phys. Rev. A* **6**, 607-631 (1972).
- 227) E. S. Simon, P. G. Papoulias and P. C. Andrews, *Rapid Commun. Mass Spectrom.* **27**, 1619-1630 (2013).
- 228) B. D. Slaughter, M. W. Allen, G. H. Lushington and C. K. Johnson, *J. Phys. Chem. A* **107**, 5670-5680 (2003).
- 229) V. N. Staroverov and E. R. Davidson, *J. Amer. Chem. Soc.* **122**, 186-187 (2000).
- 230) K. M. Stirk, L. K. M. Kiminkinen and H. I. Kenttamaa, *Chem. Rev.* **92**, 1649-1665 (1992).
- 231) E. H. Strickland, J. Horwitz and C. Billups, *Biochemistry (Mosc.)* **9**, 4914-4921 (1970).
- 232) A. Studer and D. P. Curran, *Angew. Chem. Int. Ed.* **55**, 58-102 (2016).
- 233) R. D. Suenram, F. J. Lovas and G. T. Fraser, *J. Mol. Spectrosc.* **127**, 472-480 (1988).
- 234) K. Suzuki, Y. Emura, S.-i. Ishiuchi and M. Fujii, *J. Electron. Spectrosc. Relat. Phenom.* **108**, 13-20 (2000).
- 235) M. Szwarc, *Discuss. Faraday Soc.* **2**, 39-46 (1947).
- 236) R. W. Taft and F. G. Bordwell, *Acc. Chem. Res.* **21**, 463-469 (1988).
- 237) C. K. Teh, J. Sipior and M. Sulkes, *J. Phys. Chem.* **93**, 5393-5400 (1989).
- 238) R. Tembreull and D. M. Lubman, *Anal. Chem.* **56**, 1962-1967 (1984).
- 239) K. Tonokura, T. Ogura and M. Koshi, *J. Phys. Chem. A* **108**, 7801-7805 (2004).

- 240) D. Townsend, M. P. Minitti and A. G. Suits, *Rev. Sci. Instrum.* **74**, 2530-2539 (2003).
- 241) M. J. Travers, D. C. Cowles, E. P. Clifford, G. B. Ellison and P. C. Engelking, *J. Chem. Phys.* **111**, 5349-5360 (1999).
- 242) C.-M. Tseng, Y. T. Lee, C.-K. Ni and J.-L. Chang, *J. Phys. Chem. A* **111**, 6674-6678 (2007).
- 243) M. J. Tubergen and D. H. Levy, *J. Phys. Chem.* **95**, 2175-2181 (1991).
- 244) G. S. Tyndall, R. A. Cox, C. Granier, R. Lesclaux, G. K. Moortgat, M. J. Pilling, A. R. Ravishankara and T. J. Wallington, *Journal of Geophysical Research: Atmospheres* **106**, 12157-12182 (2001).
- 245) C. Unterberg, A. Jansen and M. Gerhards, *J. Chem. Phys.* **113**, 7945-7954 (2000).
- 246) J. M. Van Doren, S. E. Barlow, C. H. Depuy and V. M. Bierbaum, *Int. J. Mass Spectrom. Ion Processes* **81**, 85-100 (1987).
- 247) V. Vanovschi, A. Krylov and P. Wenthold, *Theoretical Chemistry Accounts* **120**, 45-58 (2008).
- 248) G. Varsányi, *Vibrational Spectra of Benzene Derivatives* (Academic Press, New York and London, New York, 1969) 430 pages.
- 249) R. Vianello and Z. B. Maksić, *Tetrahedron* **62**, 3402-3411 (2006).
- 250) D. T. Vier and J. E. Mayer, *J. Chem. Phys.* **12**, 28-34 (1944).
- 251) J. T. Vivian and P. R. Callis, *Biophys. J.* **80**, 2093-2109 (2001).
- 252) L. Wåhlin, *Nucl. Instr. Meth.* **27**, 55-60 (1964).
- 253) C. Wang, D. Wang, Z. Wu, Z. Wang, C. Tang and P. Zhou, *App. Catal. A* **476**, 61-67 (2014).
- 254) C. Wang, Z. Wu, C. Tang, L. Li and D. Wang, *Catal. Comm.* **32**, 76-80 (2013).
- 255) X.-B. Wang, Q. Fu and J. Yang, *J. Phys. Chem. A* **114**, 9083-9089 (2010).
- 256) X.-B. Wang, H.-K. Woo, B. Kiran and L.-S. Wang, *Angew. Chem. Int. Ed.* **44**, 4968-4972 (2005).
- 257) M. L. Weichman, J. B. Kim and D. M. Neumark, *J. Phys. Chem. A* **119**, 6140-6147 (2015).

- 258) P. G. Wenthold, M. L. Polak and W. C. Lineberger, *J. Phys. Chem.* **100**, 6920-6926 (1996).
- 259) P. G. Wenthold and R. R. Squires, *J. Amer. Chem. Soc.* **116**, 6401-6412 (1994).
- 260) P. G. Wenthold, R. R. Squires and W. C. Lineberger, *J. Amer. Chem. Soc.* **120**, 5279-5290 (1998).
- 261) V. M. L. Whiffen and K. J. Smith, *Ener. & Fuels* **24**, 4728-4737 (2010).
- 262) V. M. L. Whiffen, K. J. Smith and S. K. Straus, *App. Catal. A* **419-420**, 111-125 (2012).
- 263) K. B. Wiberg, G. B. Ellison, J. M. McBride and G. A. Petersson, *J. Phys. Chem. A* **117**, 213-218 (2012).
- 264) C. T. Wickham- Jones, K. M. Ervin, G. B. Ellison and W. C. Lineberger, *J. Chem. Phys.* **91**, 2762-2763 (1989).
- 265) N. R. Wijeratne and P. G. Wenthold, *J. Am. Soc. Mass Spectrom.* **18**, 2014-2016 (2007).
- 266) W. C. Wiley and I. H. McLaren, *Rev. Sci. Instrum.* **26**, 1150-1157 (1955).
- 267) K. Willacy and W. D. Langer, *Astrophys. J.* **544**, 903-920 (2000).
- 268) E. B. Wilson, Jr., *Phys. Rev.* **45**, 706-714 (1934).
- 269) H.-K. Woo, X.-B. Wang, B. Kiran and L.-S. Wang, *J. Phys. Chem. A* **109**, 11395-11400 (2005).
- 270) G. P. F. Wood, L. Radom, G. A. Petersson, E. C. Barnes, M. J. Frisch and J. A. Montgomery, *J. Chem. Phys.* **125**, 094106 (2006).
- 271) S. W. Wren, (2011). *Photoelectron Spectroscopy of Organic Anions* (Doctoral Thesis).
- 272) S. W. Wren, K. M. Vogelhuber, T. Ichino, J. F. Stanton and W. C. Lineberger, *J. Phys. Chem. A* **116**, 3118-3123 (2012).
- 273) J. S. Wright, D. J. Carpenter, D. J. McKay and K. U. Ingold, *J. Amer. Chem. Soc.* **119**, 4245-4252 (1997).
- 274) X. Wu, Z.-b. Qin, H. Xie, X.-h. Wu, R. Cong and Z.-c. Tang, *Chin. J. Chem. Phys.* **23**, 373-380 (2010).
- 275) Y. Xie, H. Su and W. B. Tzeng, *Chem. Phys. Lett.* **394**, 182-187 (2004).
- 276) T. I. Yacovitch, E. Garand and D. M. Neumark, *J. Phys. Chem. A* **114**, 11091-11099

(2010).

277) J. Yang, J. Li and Y. Mo, *J. Chem. Phys.* **125**, 174313 (2006).

278) A. Yariv, *Quantum Electronics* (John Wiley & Sons, New York, 1988), 3rd edn.

279) A. M. Zolot, W. W. Harper, B. G. Perkins, P. J. Dagdigian and D. J. Nesbitt, *J. Chem. Phys.* **125**, 021101 (2006).

APPENDIX

FORTRAN PROGRAMS FOR PHOTOELECTRON DATA ANALYSIS

Contained in this appendix are the annotated forms of the FORTRAN programs I wrote to perform data analysis upon the photoelectron spectra collected in this dissertation. Hopefully, these may be useful to others for similar purposes.

```
PROGRAM VARIABLE_SMOOTHING
C BY DAN NELSON, 5/5/2016
C THIS PROGRAM TAKES A PHOTOELECTRON SPECTRUM
C AND SMOOTHS IT TO SOME % OF THE EXPERIMENTAL
C RESOLUTION, AND ASSUMES THAT THE RESOLUTION
C IS A FUNCTION OF ELECTRON KINETIC ENERGY. INPUT
C DATA NEEDS TO BE IN ASCENDING ORDER.
C
C MODIFIED 2/15/17 TO INCLUDE TERMINATING BOUNDARY
C CONDITIONS

IMPLICIT DOUBLE PRECISION (A-H,O-Z)

DIMENSION EBE_IN(10000)
DIMENSION QINT_IN(10000)
DIMENSION EBE_OUT(10000)
DIMENSION QINT_OUT(10000)

OPEN(6,FILE='PES_SMOOTH_INPUT.TXT',STATUS='UNKNOWN')
OPEN(7,FILE='SMOOTHED_DATA.TXT',STATUS='UNKNOWN')
OPEN(8,FILE='SMOOTH_DEBUG.TXT',STATUS='UNKNOWN')

READ(6,*) SMOOTH,QM,QB,NPOINTS
WRITE(8,*) SMOOTH,QM,QB,NPOINTS

C ZERO ARRAYS

DO 11 I=1,10000
    EBE_IN(I)=0.0D0
    QINT_IN(I)=0.0D0
    EBE_OUT(I)=0.0D0
    QINT_OUT(I)=0.0D0
11 CONTINUE
```

```

DO 112 I=1,NPOINTS
    READ(6,*) EBE_IN(I),QINT_IN(I)
112 CONTINUE

WRITE(8,*) EBE_IN(1),QINT_IN(1)
WRITE(8,*) EBE_IN(NPOINTS),QINT_IN(NPOINTS)

DO 23 I=1,NPOINTS
    COUNT=0.0D0
    SUM=0.0D0
    RES=(EBE_IN(I)*QM+QB)/2.0D0
    IF(EBE_IN(I)-SMOOTH*RES.LE.EBE_IN(1)) THEN
        DO 55 K=1,NPOINTS
            IF(EBE_IN(K).LE.(EBE_IN(I)+SMOOTH*RES))
THEN
                IF(EBE_IN(K).GE.(EBE_IN(I)-*
                    SMOOTH*RES).AND.EBE_IN(K)
*
                .LE.(EBE_IN(I)+SMOOTH*RES)) THEN
                    SUM=SUM+QINT_IN(K)
                    COUNT=COUNT+1.0D0
                    WRITE(8,*) SUM, COUNT
                    END IF
                END IF
55 CONTINUE
            END IF
            IF(EBE_IN(I)-SMOOTH*RES.LE.
*
            EBE_IN(1).OR.EBE_IN(I)+SMOOTH
*
            *RES.GE.EBE_IN(NPOINTS)) THEN
                DO 34 J=1,NPOINTS
                    IF(EBE_IN(J).GE.(EBE_IN(I)-SMOOTH
*
                    *RES).AND.EBE_IN(J)
*
                    .LE.(EBE_IN(I)+SMOOTH*RES)) THEN
                        SUM=SUM+QINT_IN(J)
                        COUNT=COUNT+1.0D0
                        END IF
34 CONTINUE
                END IF
                DO 66 L=1,NPOINTS
                    IF(EBE_IN(L).GE.(EBE_IN(I)-SMOOTH*RES))
THEN
                        IF(EBE_IN(L).GE.(EBE_IN(I)-SMOOTH
*
                        *RES).AND.EBE_IN(L)
*
                        .LE.(EBE_IN(I)+SMOOTH*RES)) THEN
                            SUM=SUM+QINT_IN(L)
                            COUNT=COUNT+1.0D0
                            WRITE(8,*) SUM, COUNT
                            END IF

```

```
                END IF
66                CONTINUE
                EBE_OUT(I)=EBE_IN(I)
                QINT_OUT(I)=SUM/COUNT
                WRITE(8,*) EBE_OUT(I),QINT_OUT(I)
23 CONTINUE

                DO 78 I=1,NPOINTS
                WRITE(7,*) EBE_OUT(I),QINT_OUT(I)
78 CONTINUE

                CLOSE(6)
                CLOSE(7)
                CLOSE(8)

                END PROGRAM
```

```

PROGRAM VARIABLE_FWHM_CONVOLUTION
C
C BY DANIEL NELSON, 3/25/2016
C
C THIS PROGRAM READS IN A STICK SPECTRUM (LINE POSITIONS AND
C INTENSITIES) AND THEN MAPS THEM ONTO A CONTINUOUS ELECTRON
C BINDING ENERGY SPECTRUM WHILE CONVOLVING THEM WITH
C GAUSSIANS WHOSE FWHM VARIES LINEARLY
C WITH EBE, AND WHOSE AREA EQUALS THE LINE INTENSITY
C
C IMPLICIT DOUBLE PRECISION (A-H,O-Z)
C
C DECLARE NEEDED ARRAYS AND CONSTANTS
C
C PARAMETER(PI=3.14159265359D0)
C OUTPUT RESOLUTION DETERMINES THE STEPSIZE OF THE OUTPUT
C SPECTRUM IN MEV
C PARAMETER(OUTPUT_RESOLUTION=0.00025D0)
C PARAMETER(EBE_RANGE=4.0D0)
C PARAMETER(N_OUTPUT=EBE_RANGE/OUTPUT_RESOLUTION+1)
C DIMENSION STICKCENTER(50000)
C DIMENSION STICKCENTER_EKE(50000)
C DIMENSION XLINE_INTENSITY(50000)
C DIMENSION FWHM(50000)
C DIMENSION CONVOLVED_INTENSITY(N_OUTPUT)
C DIMENSION EBE_OUTPUT(N_OUTPUT)
C
C FIRST ZERO OUT THE ARRAYS
C
C DO 111 I=1,50000
C
C         STICKCENTER(I)=0.0D0
C         XLINE_INTENSITY(I)=0.0D0
C         FWHM(I)=0.0D0
C         STICKCENTER_EKE(I)=0.0D0
111 CONTINUE
C DO 98 I=1,N_OUTPUT
C         CONVOLVED_INTENSITY(I)=0.0D0
C         EBE_OUTPUT(I)=0.0D0
98 CONTINUE
C
C CALCULATE OUTPUT EBE AXIS
C
C DO 112 I=1,N_OUTPUT
C
C         EBE_OUTPUT(I)=(I-1)*OUTPUT_RESOLUTION
112 CONTINUE

```

```

C
C NEXT OPEN AND READ IN STICK CENTERS, INTENSITIES,
C AND NUMBER OF TRANSITIONS AS WELL AS OUTPUT FILE
C AND DIAGNOSTIC FILE
C
OPEN(6,FILE='VARIABLE_INFO.TXT',STATUS='UNKNOWN')
OPEN(7,FILE='CONVOLVED_OUTPUT.TXT',STATUS='UNKNOWN')
C OPEN(8,FILE='CONVOLVED_DIAG.TXT',STATUS='UNKNOWN')
C
C FIRST READ IN HV AND M AND B
C
READ(6,*) QM,B,N_MAX
C WRITE(8,*) QM,B
C WRITE(8,*) EBE_OUTPUT(1),EBE_OUTPUT(N_OUTPUT)
C WRITE(8,*) STICKCENTER(1),XLINE_INTENSITY(1)
C
C NOW READ IN THE STICK SPECTRUM
C
DO 113 I=1,N_MAX
      READ(6,*) STICKCENTER(I),XLINE_INTENSITY(I)
113 CONTINUE
C
C WRITE(8,*) STICKCENTER(1),XLINE_INTENSITY(1)
C
C NOW CONVERT THE EBE OF THE STICKS TO EKE
C
C NOW CALCULATE THE FWHM OF EACH TRANSITION
C
DO 74 I=1,N_MAX
      FWHM(I)=QM*STICKCENTER(I)+B
74 CONTINUE
C
C WRITE(8,*) FWHM(1),FWHM(N_MAX)
C
C NOW THE MAIN EVENT- CONVOLUTE!
C
DO 79 I=1,N_MAX
      DO 89 J=1,N_OUTPUT
CONVOLVED_INTENSITY(J)=CONVOLVED_INTENSITY(J)+2.0D0
*      *SQRT(LOG(2.0D0)/PI)*XLINE_INTENSITY(I)/FWHM(I)*EXP(-
*      4.0D0*LOG(2.0D0)*(EBE_OUTPUT(J)-
*      STICKCENTER(I))**2/(FWHM(I)**2))
89 CONTINUE

```

```
79  CONTINUE
C
C  NOW WRITE THE OUTPUT SPECTRUM
C
      DO 23 I=1,N_OUTPUT
          WRITE(7,*) EBE_OUTPUT(I),CONVOLVED_INTENSITY(I)
23  CONTINUE
C
C
      CLOSE(6)
      CLOSE(7)
C  CLOSE(8)

      END PROGRAM
```


The next program I wrote with Monika Grutter Kasumaj to simulate the rovibronic spectrum of benzene. While we did not end up utilizing this to analyze an experiment, it is a useful example of how to simulate a relatively complex spectrum.

```
PROGRAM BENZENE_ROVIBRONIC

C   CALCULATES ROVIBRONIC TRANSITIONS OF S1 - S0 IN BENZENE
C   THIS VERSION FOR 6_0^1 TRANSITION

      IMPLICIT DOUBLE PRECISION (A-H,O-Z)

C   G: GROUND STATE E: EXCITED STATE

C   IF JGMAX IS CHANGED, THE NUMBER OF TRANSITIONS
C   CALCULATED CHANGES, THEREFORE THE NUMBER ITRANS
C   THAT IS SENT TO GAUSSIAN_BENZENE_BROADER.F
C   NEEDS TO CHANGE TOO.

PARAMETER (JGMAX=160)
PARAMETER (JEMAX=JGMAX+1)
PARAMETER (JGDIM=(JGMAX+1)**2)
PARAMETER (JEDIM=2*(JEMAX+1)**2)

DIMENSION G(JGDIM)
DIMENSION E(JEDIM)
DIMENSION BOLTZ(JGDIM)
DIMENSION FAVOR(JGDIM)
DIMENSION SPIN(JGDIM)

PARAMETER (MAXTRANS=400000)
DIMENSION TRANS(MAXTRANS)
DIMENSION XINT(MAXTRANS)

PRINT *, JGMAX, JGDIM, JEMAX, JEDIM

C   MOLECULAR PARAMETERS IN S0 GROUND STATE / CM-1

BG=0.18977D0
CG=BG/2.0D0

C   EXCITED STATE S1 6^1 / CM-1 (ZC=C_0'ZETA')

BE=0.18179D0
CE=0.09087D0
```

```

ZC=0.05256D0

C   TEMPJ AND TE ARE THE ADJUSTABLE PARAMETERS HERE.

TE=38606.0D0

TEMPJ=300.0D0
TEMPK=TEMPJ

C   FILE 6 IS THE OUTPUT STICK SPECTRUM,
C   WHICH CORRESPONDS TO THE INPUT INTO
C   GAUSSIAN_BENZENE_BROADER.F

OPEN(6,FILE='25KS.DAT',STATUS='UNKNOWN')
OPEN(8,FILE='GROUND.DAT',STATUS='UNKNOWN')
OPEN(9,FILE='EXCITED.DAT',STATUS='UNKNOWN')
C   OPEN(10,FILE='NOFAVOR.DAT',STATUS='UNKNOWN')
OPEN(12,FILE='NSSW.DAT',STATUS='UNKNOWN')

C           BOLTZMANN CONSTANTS

           QKB=1.3806504D-23
           PLANCK=6.62606896D-34
           C0=299792458
           C0G=29.9792458

C   INITIALIZING

DO 111 I=1,MAXTRANS

           TRANS(I)=0.0D0
           XINT(I)=0.0D0
111 CONTINUE

C   GROUND STATE LEVELS

DO 1 J=0,JGMAX

DO 2 K=-J,J

           G((J+1)**2-(J-K))=0.0D0
           BOLTZ((J+1)**2-(J-K))=0.0D0
           FAVOR((J+1)**2-(J-K))=0.0D0
           SPIN((J+1)**2-(J-K))=0.0D0
2   CONTINUE
1   CONTINUE

```

```

QSUM=0.0D0

DO 3 J=0,JGMAX

DO 4 K=-J,J

      G((J+1)**2-(J-K))=BG*J*(J+1)+(CG-BG)*K**2

C   BOLTZ((J+1)**2-(J-K))=
C   *   EXP(-(PLANCK*C0*100*G((J+1)**2-(J-K)))/(QKB*TEMP))

      BOLTZ((J+1)**2-(J-K))=
      *   EXP(-(PLANCK*C0*100*(BG*J*(J+1)))/(QKB*TEMPJ))*
      *   EXP(-(PLANCK*C0*100*((CG-BG)*K**2))/(QKB*TEMPK))

QSUM=QSUM+BOLTZ((J+1)**2-(J-K))

C   WRITE(8,*) G((J+1)**2-(J-K)),J,K

      IF(K.EQ.J) THEN

PRINT *,BOLTZ((J+1)**2-(J-K)),J,K,QSUM
END IF

4   CONTINUE
3   CONTINUE

C   FAVOR LOWER K OVER HIGHER K STATES

DO 333 J=0,JGMAX

DO 444 K=-J,J

      IF(J.EQ.0) THEN

          FAVOR((J+1)**2-(J-K))=1.0D0
      ELSE

          FAVOR((J+1)**2-(J-K))=1.0D0
      END IF

      WRITE(10,*) FAVOR((J+1)**2-(J-K)),J,K

444 CONTINUE
333 CONTINUE

C   INCLUDE NUCLEAR SPIN STATISTICAL WEIGHTS

```

```

DO 876 J=0,JGMAX
DO 864 K=-J,J

    KK=ABS(K)

    IF (MOD(KK,6).EQ.0) THEN

        IF (KK.EQ.0) THEN

            IF (MOD(J,2).EQ.0) THEN

                SPIN((J+1)**2-(J-K))=7.0D0

            ELSE

                SPIN((J+1)**2-(J-K))=3.0D0
            END IF

        ELSE

            SPIN((J+1)**2-(J-K))=10.0D0
        END IF
    END IF

    IF (MOD(KK,6).EQ.1) THEN

        SPIN((J+1)**2-(J-K))=11.0D0
    END IF

    IF (MOD(KK,6).EQ.2) THEN

        SPIN((J+1)**2-(J-K))=9.0D0
    END IF

    IF (MOD(KK,6).EQ.3) THEN

        SPIN((J+1)**2-(J-K))=14.0D0
    END IF

    IF (MOD(KK,6).EQ.4) THEN

        SPIN((J+1)**2-(J-K))=9.0D0
    END IF

    IF (MOD(KK,6).EQ.5) THEN

```

```

                SPIN((J+1)**2-(J-K))=11.0D0
            END IF

C            WRITE (12,*) SPIN((J+1)**2-(J-K)),J,K

864 CONTINUE
876 CONTINUE

C    EXCITED STATE LEVELS

        DO 5 I=1,JEDIM

                E(I)=0.0D0
5        CONTINUE

        DO 6 J=0,JEMAX

                DO 7 K=-J,J

                        DO 8 L=1,-1,-2

                                IF(L.GE.0) THEN
                                        IL=1
                                ELSE
                                        IL=0
                                END IF

                                E(2*((J+1)**2-(J-K))-IL)=
                                + BE*J*(J+1)+(CE-BE)*K**2+2*ZC*K*L

                                WRITE (9,*) E(2*((J+1)**2-(J-K))-IL),J,K,L
8        CONTINUE
7        CONTINUE
6        CONTINUE

C    ROVIBRONIC TRANSITIONS
C    (SYMM. SEL. RULES: DELTAK=+-1 AND SAME DIRECTION AS L)

        ITRANS=0

        DO 10 J=0,JGMAX

                DO 11 K=-J,J

                        DO 12 JE=0,JEMAX

                                DO 13 KE=-JE,JE

```

```

        DO 14 L=1,-1,-2
C      ADD FACTOR FOR (K,KE) (0,1) AND (1,0) TRANSITIONS
      GS=1.0D0
      IF (K.EQ.0) THEN
        IF (ABS(KE).EQ.1) THEN
          GS=2.0D0
        END IF
      END IF
      IF (ABS(K).EQ.1) THEN
        IF (KE.EQ.0) THEN
          GS=1.0D0
        END IF
      END IF
C      SELECT SPECIFIC STATES HERE (DIAGNOSTICS)
      IF (1.EQ.1) THEN
C      IF (J.EQ.3) THEN
C      DELTAK=K'-K''=+1 AND L=+1
      IF (KE.EQ.K+1.AND.L.EQ.1) THEN
        IL=1
C      Q-BRANCH
        IF (JE.EQ.J) THEN
C      PRINT *,J,K,JE,KE,L,'UPPER'
        ITRANS=ITRANS+1
        TRANS(ITRANS)=TE+E(2*((JE+1)**2-(JE-KE))-IL)-G((J+1)**2-
*      (J-K))
        XINT(ITRANS)=(2*J+1)*BOLTZ((J+1)**2-(J-K))/QSUM
*      *((J+1+K)*(J-K)*1.0/(2*J*(J+1)))
*      *SPIN((J+1)**2-(J-K))

```

```

*      *FAVOR ((J+1)**2-(J-K)) *GS*1.0

C      PRINT *, (J+1+K) * (J-K) * (2*J+1) *1.0 / (4*J*(J+1))
C      PRINT *, J, K
      END IF

C      P-BRANCHES

      IF (JE+1.EQ.J) THEN

      ITRANS=ITRANS+1

      TRANS (ITRANS)=TE+E (2* ((JE+1)**2-(JE-KE)) -IL) -G ((J+1)**2-
*      (J-K))

      XINT (ITRANS) = (2*J+1) *BOLTZ ((J+1)**2-(J-K)) /QSUM
*      * ((J-1-K) * (J-K) *1.0 / (2*J*(2*J+1)))
*      *SPIN ((J+1)**2-(J-K))
*      *FAVOR ((J+1)**2-(J-K)) *GS*1.0
      END IF

C      R-BRANCHES

      IF (JE-1.EQ.J) THEN

      ITRANS=ITRANS+1

      TRANS (ITRANS)=TE+E (2* ((JE+1)**2-(JE-KE)) -IL) -G ((J+1)**2-
*      (J-K))

      XINT (ITRANS) = (2*J+1) *BOLTZ ((J+1)**2-(J-K)) /QSUM
*      * ((J+2+K) * (J+1+K) *1.0 / (2*(J+1)*(2*J+1)))
*      *SPIN ((J+1)**2-(J-K))
*      *FAVOR ((J+1)**2-(J-K)) *GS*1.0
      END IF
      END IF

C      DELTAK=K'-K' '=-1 AND L=-1

      IF (KE+1.EQ.K.AND.L.EQ.-1) THEN

      IL=0

C      Q-BRANCH

      IF (JE.EQ.J) THEN

```

```

C   PRINT *, J, K, JE, KE, L, 'LOWER'

      ITRANS=ITRANS+1

      TRANS (ITRANS)=TE+E (2* ((JE+1)**2-(JE-KE)) -IL) -G ((J+1)**2-
*      (J-K))

      XINT (ITRANS) = (2*J+1) *BOLTZ ((J+1)**2-(J-K)) /QSUM
*      * ((J+1-K) * (J+K) *1.0 / (2*J*(J+1)))
*      *SPIN ((J+1)**2-(J-K))
*      *FAVOR ((J+1)**2-(J-K)) *GS*1.0

C   PRINT *, (J+1+K) * (J-K) * (2*J+1) *1.0 / (4*J*(J+1))
C   PRINT *, J, K
      END IF

C   P-BRANCHES

      IF (JE+1.EQ.J) THEN

      ITRANS=ITRANS+1

      TRANS (ITRANS)=TE+E (2* ((JE+1)**2-(JE-KE)) -IL) -G ((J+1)**2-
*      (J-K))

      XINT (ITRANS) = (2*J+1) *BOLTZ ((J+1)**2-(J-K)) /QSUM
*      * ((J-1+K) * (J+K) *1.0 / (2*J*(2*J+1)))
*      *SPIN ((J+1)**2-(J-K))
*      *FAVOR ((J+1)**2-(J-K)) *GS*1.0
      END IF

C   R-BRANCHES

      IF (JE-1.EQ.J) THEN

      ITRANS=ITRANS+1

      TRANS (ITRANS)=TE+E (2* ((JE+1)**2-(JE-KE)) -IL) -G ((J+1)**2-
*      (J-K))

      XINT (ITRANS) = (2*J+1) *BOLTZ ((J+1)**2-(J-K)) /QSUM
*      * ((J+2-K) * (J+1-K) *1.0 / (2*(J+1)*(2*J+1)))
*      *SPIN ((J+1)**2-(J-K))
*      *FAVOR ((J+1)**2-(J-K)) *GS*1.0
      END IF
      END IF

```



```

        END IF

14    CONTINUE
13    CONTINUE
12    CONTINUE
11    CONTINUE
10    CONTINUE

C     'ITRANS' CORRESPONDS TO 'NB' IN GAUSSIAN_BENZENE_BROADER.F

C     PRINT *,ITRANS
      DO 44 I=1,ITRANS
          IF (XTRANS(ITRANS) .GE. SOMEVALUE) THEN

              WRITE(6,*) TRANS(I),0.0D0
              WRITE(6,*) TRANS(I),XINT(I)
              WRITE(6,*) TRANS(I),0.0D0
          END IF
44    CONTINUE

      CLOSE(12)
      CLOSE(10)
      CLOSE(9)
      CLOSE(8)
      CLOSE(6)

          END PROGRAM

```